Università degli Studi di Roma Sapienza
Università degli Studi di Roma Tor Vergata
Istituto Nazionale di Astrofisica (INAF)

FACOLTÀ DI SCIENZE MATEMATICHE FISICHE E NATURALI
XXXVI cycle of Ph.D. Course in
Astronomy, Astrophysics and Space Science

Upgraded optical aberration correction techniques for Advanced Virgo plus: commissioning toward O4 and mitigation of non-axisymmetric optical defects

Supervisor:
Prof. Viviana Fafone
Co-supervisors:
Dr. Matteo Lorenzini
Dr. Alessio Rocchi

Ph.D. Candidate:
Claudia Taranto

Anno Accademico 2022–2023

To the men of my life
my husband Marco,
my father Romano,
my nonno Nando,
unwavering pillars of support,
always proud of me.

"You'll stay with me?"
"Until the very end," said James.
"They won't be able to see you?" asked Harry.
"We are part of you," said Sirius. "Invisible to anyone else."
- *J.K. Rowling, Harry Potter and the Deathly Hallows*

Contents

Introduction

On September 14^{th}, 2015, a momentous event in the realm of astrophysics occurred when a transient gravitational wave signal emanated from the coalescence of a binary system of intermediate-mass black holes was detected for the first time by the two LIGO detectors. This landmark discovery, officially announced to the scientific community by the LIGO and Virgo collaborations on February 11, 2016, inaugurated an entirely new tool for the exploration of the cosmos. However, the study of gravitational waves traces its origins back to 1916 when Albert Einstein postulated their existence within his General Relativity theory. Over the course of a century, numerous attempts were made to observe these elusive ripples of space-time, all met without success. Gravitational waves, due to the extreme weakness of their effects, presented an extraordinary challenge to detection. The earliest venture into gravitational wave measurement was pioneered by Joseph Weber in the 1960s, employing resonant antennas capable of detecting signals in the range of approximately 1000 Hz. In the 1980s, the Michelson interferometer was proposed as a means to reveal gravitational waves, extending the detection spectrum from 10 Hz to 10000 Hz. The core principle underlying interferometric detection involves measuring the phase shift induced by gravitational waves at the interferometer's output. Among the gravitational wave interferometers presently in operation, the most sensitive instruments are the American LIGO detectors and their European counterpart, Virgo, situated in Cascina, Pisa, at the EGO. Between 2002 and 2010, these interferometers reached their design sensitivity without detecting any gravitational signal. In 2012, a new plan of technological enhancement for both LIGO and Virgo started, aimed at increasing the observable volume of the universe by a factor of 1000 compared to the first generation. It was through these second-generation interferometers, known as Advanced LIGO and Advanced Virgo, that gravitational waves emitted by binary systems of black holes and neutron stars were detected for the very first time. The collaborative network of ground-based interferometric detectors, Advanced LIGO and Advanced Virgo, has since detected ninety gravitational wave signals during the initial three observing runs. The plan for Advanced detectors has been developed by alternating observing phases with upgrade phases. The enhancement plan for Advanced Virgo after O3 has been reorganized into two phases, collectively referred to as Advanced Virgo+. At present, Advanced Virgo+ is engaged in the commissioning of Phase I upgrades in preparation for the start of the observing run O4. In the medium term, a Phase II of upgrades will follow O4, aiming to reach O5 with a binary neutron star range of 200 Mpc.

The sensitivity of terrestrial gravitational interferometers is constrained by a combination of external noise sources, such as seismic noise, and intrinsic noises inherent to the apparatus, such as thermal and quantum noise. Among the various improvements introduced in the second-generation detectors, a key strategy involves increasing the laser power to mitigate quantum noise at higher frequencies. However, this power increase severely worsen the absorption of optical power by the mirrors, leading to thermal expansion

and thermal lensing effects. These effects introduce deviations from the interferometer's nominal optical configuration, thereby compromising its performance. Consequently, the implementation of a Thermal Compensation System (TCS) in charge of recovering the optimal functionality of the interferometer upon input power increase is a central item in the Advanced Virgo+ upgrade process.
The thesis is centred on the TCS commissioning, in preparation of Advanced Virgo+ joining the observing run O4. Additionally, this work involves the development of a new actuator aimed at compensating for non-axisymmetric optical defects, as part of preparations for the upcoming observing run O5.

The **first chapter** deals with a snapshot of the derivation of the gravitational wave equation from the General Relativity field equation. Following a concise overview of the main sources, the chapter narrows its focus to explore some aspects of gravitational wave science and highlights the most significant detections among the ninety identified during the past three observing runs of the gravitational wave interferometers network.

The **second chapter** is devoted to the description of the interaction of a gravitational wave with a mass distribution and provides an overview of the interferometric detection technique. It proceeds with an examination of the various sources of noise that constrain the sensitivity of interferometric detectors, along with the strategies implemented within Advanced Virgo+ to mitigate these constraints. The chapter concludes with a brief overview of the future prospects for Advanced Virgo+ and the next generation of detectors, Einstein Telescope and the Laser Interferometer Space Antenna.

The **third chapter** is dedicated to the description of the aberration sources and their impact on the interferometer performance. Sensors and actuators composing the TCS are described. The chapter concludes with the future prospects for TCS.

Within the **fourth chapter**, an exhaustive account of the activities conducted on the Virgo site for the preliminary commissioning of the TCS is presented. All the tests performed on the TCS actuators in order to make them fully capable to compensate the optical aberrations and cold defects are detailed. Conclusively, the chapter shows the impact of TCS on the interferometer.

In the last and **fifth chapter**, we get into the core of the R&D activity, with the characterization of a prototype of a deformable mirror in the INFN laboratories at the University of Rome Tor Vergata. The deformable mirror is used to apply a phase imprint on the laser beam impinging on it in order to obtain the heating pattern required for a complementary correction of the non-axisymmetric aberrations. The final part of the chapter describes how, starting from the characterization, a Modified Gerchberg-Saxton based algorithm has been developed to extract the phase to be applied by the deformable mirror; the results of the experimental tests are finally described.

Chapter 1

Gravitational Waves Science

On September 14^{th}, 2015 at 09:50:45 UTC a **G**ravitational **W**ave (GW) signal originated by the final part of the inspiral phase of two intermediate mass **B**lack **H**ole (BH) was detected. It was the first direct observation ever of GWs, whose existence was theorized by Albert Einstein one century before in 1916. Thanks to the network of the ground-based interferometric detectors Advanced LIGO and Advanced Virgo, ninety GW signals have been detected in the first three observing runs. This chapter focuses on some aspects of GW science and on the main detections published so far.

1.1 Theoretical hints

The existence of GWs was theorized by Albert Einstein in 1916 [1] as a consequence of **G**eneral **R**elativity (GR), the theory that describes the gravitational interaction no longer as a force - as done in the Newtonian mechanics - but as a consequence of the space-time curvature induced by the presence of massive objects. This is encoded in the *Einstein's equations* that can be written as a linear combination of the *Ricci tensor* $R_{\mu\nu}$ and the *Ricci scalar* R:

$$G_{\mu\nu} = R_{\mu\nu} - \frac{1}{2} g_{\mu\nu} R = \frac{8\pi G}{c^4} T_{\mu\nu}, \tag{1.1}$$

where the *Einstein's tensor* $G_{\mu\nu}$ describes the space-time geometry, $T_{\mu\nu}$ is the energy-momentum tensor field, G is the gravitational constant, c the speed of light and $g_{\mu\nu}$ is the metric tensor field evaluated at the given point in space-time x^{μ}. Although equation 1.1 is not linear, in the *weak field limit* the theory can be linearized by writing $g_{\mu\nu} = \eta_{\mu\nu} + h_{\mu\nu}$, where $|h_{\mu\nu}| << 1$ is a perturbation of the geometry of Minkowski space-time $\eta_{\mu\nu}$. In this framework, we can simplify equation 1.1 introducing the *trace-reversed* metric $\bar{h}_{\mu\nu} = h_{\mu\nu} - \frac{1}{2}\eta_{\mu\nu} h$ (h is the trace of $h_{\mu\nu}$) and applying the *Lorenz gauge* condition $\partial^{\nu} \bar{h}_{\mu\nu} = 0$. By doing so, we get [2]:

$$\Box \bar{h}_{\mu\nu} = -\frac{16\pi G}{c^4} T_{\mu\nu}. \tag{1.2}$$

Far from the sources, $T_{\mu\nu} = 0$, so one can impose additional conditions which lead to a wave equation for $h_{\mu\nu}$:

$$\Box h_{\mu\nu} = 0. \tag{1.3}$$

This equation describes the field propagation in vacuum and its simplest solution is a monochromatic plane wave:

$$\bar{h}_{\mu\nu} = Re[A_{\mu\nu} e^{i k_{\alpha} x^{\alpha}}], \tag{1.4}$$

where $A_{\mu\nu}$ is the polarization tensor, k_α are the components of the *wave vector* that is defined as $\vec{k} = \left(\frac{\omega}{c}, 0, 0, k_z\right)$ - for a wave travelling along z axis - and ω is the wave pulsation. To satisfy equation 1.3, the two conditions $k^\alpha k_\alpha = 0$ and $k_\mu A^\mu_\nu = 0$ - which define the **T**ransverse and **T**raceless (TT) gauge - must be accomplished. The solution expressed by equation 1.4 is the GW and the two conditions defined above tell us that the wave propagates at the speed of light and is transverse. Considering a wave travelling along the z axis, in the TT gauge we get:

$$h^{TT}_{\mu\nu} = \begin{pmatrix} 0 & 0 & 0 & 0 \\ 0 & h_+ & h_x & 0 \\ 0 & h_x & -h_+ & 0 \\ 0 & 0 & 0 & 0 \end{pmatrix} e^{ikz}, \tag{1.5}$$

where h_+ and h_x describe the two GW polarizations predicted by GR, called *plus* and *cross* respectively. Their effect is shown in Figure 1.1.

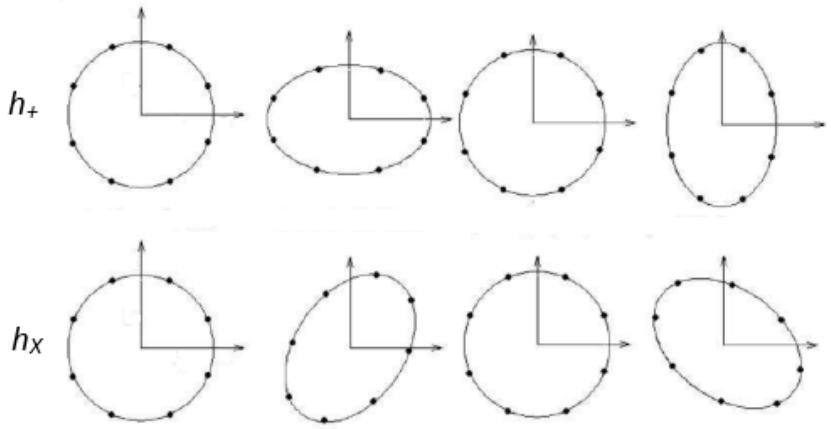

Figure 1.1: *Effect of the two polarization states of a GW on a circular distribution of free-falling TM for a wave propagating perpendicularly to the plane.*

According to momentum and angular momentum conservation laws, the emission of GWs is associated to the variations of the *quadrupole moment* Q_{ij} of a mass distribution, defined as:

$$Q_{ij} = \int_V \rho(\vec{x}) \left(x_i x_j - \frac{1}{3}\delta_{ij}|\vec{x}|^2 \right). \tag{1.6}$$

The power emitted in GWs (luminosity) depends on the third time derivative of the quadrupole moment Q_{ij} according to the formula:

$$L = \frac{1}{5}\frac{G}{c^5}\langle \dddot{Q}^{ij} \dddot{Q}_{ij} \rangle. \tag{1.7}$$

Finally, the amplitude of a wave emitted at a distance r from the source is:

$$h_{ij} = \frac{2}{r}\frac{G}{c^4}\frac{d^2}{dt^2}Q_{ij}. \tag{1.8}$$

The order of magnitude with which they should be detected on Earth is around 10^{-21}. GW sources are usually categorised according to the duration and spectral content of the emitted signals:

- Compact binary systems: pairs of compact object like BH-BH, BH-**N**eutron **S**tar (NS) or NS-NS. The emitted signals are characterized by three phases which correspond to three different stages in their dynamic evolution:
  i) the *inspiral*, with a signal having an increasing frequency and amplitude, often referred to as a chirp;
  ii) the *merger*, which describes the strong-field dynamical regime of the two compact objects coalescence;
  iii) the *ring down* signal which describes the final settling down of the remnant object.
  As reported later, the detection and inference of the parameters of the progenitor and remnant depend on the strength of the signal, the systems' characteristic masses and spins, the signal frequency and the sensitivity of the GW detectors.

- Burst or unmodelled sources: generic short-duration signals - typically less than a second - from the merger phase of a compact binary system and those from **S**uper**N**ovae (SN) and cosmic strings. The latter are hypothesized to originate from topological fluctuations in the early universe [3].

- Continuous sources: they originate persistent GW signals related to a mass quadrupole moment varying in time in a periodic or semi-periodic manner. The prototypical **C**ontinuous **W**aves (CW) sources are spinning neutron stars with some degree of asymmetry with respect to their rotation axis. More exotic sources of CWs are clouds of ultra-light bosons [4], which could grow around spinning BHs due to a super-radiance process and which are expected to dissipate through the emission of CWs over seconds to several minutes.

- **GW stochastic background**: defined as the incoherent superposition of GWs emitted by astrophysical or cosmological sources too faint or distant to be resolved individually. The figure of merit for this background is the fractional energy density spectrum [5]:
  $$\Omega_{GW}(f) = \frac{f}{\rho_c}\frac{d\rho_{GW}}{df}, \tag{1.9}$$
  where $d\rho_{GW}$ is the energy density in the frequency interval from f to $f + df$, $\rho_c = \frac{3H_0^2c^2}{8\pi G}$ is the critical energy density required to close the universe and H_0 is the Hubble constant.

1.2 Science Case

The sensitivity increase of the ground-based detectors has made it possible to increase the number of detections and to access new sources as the NS-BH systems. This process will be more and more significant thanks to the developments foreseen in the forthcoming years: new sources and new physics will be possibly accessible such as SN explosions [6], newly born or millisecond pulsars [7], the birth of NSs from SN [8], the astrophysical background of populations of compact object mergers [9], Dark Matter either around BHs [10] or through its direct interaction with the detectors themselves [11]. Moreover, the improved **I**n**t**er**f**erometer (ITF) will enable the discovery of thousands of **B**inary **B**lack **H**ole (BBH) and NS mergers over their lifetime, allowing for not only a detailed demographic census of the formation and fate of such systems but also for itemized source characterisation.

In the upcoming sections, some aspects of the science that has been performed and that can still be carried out will be discussed.

1.2.1 The physics and astrophysics of black holes

We have learned that BHs of stellar mass can form binaries and that these binaries orbit and inspiral as predicted by GR emitting GWs. The rate density of these mergers has been measured up to a redshift of $z \sim 1$ along with the masses and angular momenta of the involved BHs [12]. Nevertheless, significant questions about their origin and nature remain open, including how BHs form such systems and the extent to which GR accurately describes these BHs and their detailed mass distribution. Discovering more BBH mergers with high **S**ignal-to-**N**oise **R**atio (SNR) will allow us to have a better understanding of their properties and enable a precise characterization. In particular, observing more events similar to GW190521[1] and GW190814 will be invaluable for probing the presence of a *lower mass gap* that separates NSs from stellar-mass BHs ($\sim 2.5\ M_\odot$) and a *higher mass gap* around $\sim 50\ M_\odot$ possibly related to (pulsational) pair-instability supernovae [9]. Finally, the reliable characterization of a BH merger with high SNR requires an accurate model of the GW waveform parametrized by the properties of the binary system. The continued operation of ground-based detectors will be essential in providing motivation and fresh data to advance the development of these waveform models.

1.2.2 Multimessenger astrophysics

Joint observations with multiple messengers provide additional science that is not possible to get with single channel observations only. By combining the GW and **G**amma-**R**ay **B**urst (GRB) data, the long-hypothesized association between NS mergers and GRBs was established, and an important constraint was set on the speed of gravity. The combination of the GW and optical observations allowed to verify the processes responsible for the formation of heavy elements in the universe [13]. The GW, GRB and radio data provided important information on the properties of the relativistic jet emitted after the merger. The GW and X-ray data were used to probe the nature of the post-merger remnant. Despite the huge amount of information obtained with GW170817, we still lack a complete understanding of the formation processes of **B**inary **N**eutron **S**tar (BNS) systems. Moreover, we do not entirely understand the structure of a NS and its impact on the gravitational, **E**lectro**M**agnetic (EM) and neutrino emissions produced by a BNS merger. The physical processes taking place during and after the merger, in particular the mechanism responsible for the production of a relativistic jet, require more observations as well, in order to be better understood. There is also a whole class of plausible multimessenger observations which have not been exploited yet, such as the observation of a core-collapse SN in the GW, EM and neutrino channels or a persistent GW signal associated with a pulsar. The next subsections will briefly describe some of the science cases related to multimessenger observations.

Kilonovae, gamma-ray bursts and fast radio bursts

GRBs are highly-energetic flashes of gamma-rays emitted in the energy band between tens of keV to several MeV. They are currently detected at a rate of ~ 1 per day by

[1] The GW events have a name starting with the prefix GW and the following three pairs of numbers indicate the year, month and day of observation, respectively.

observatories like Fermi and Swift [14]. Their observed duration covers several orders of magnitude, from fractions to hundreds of seconds. Those lasting more than ∼2 s (long GRBs) are generally understood as being produced by the collapsing cores of massive stars [15]. Those lasting less than ∼2 s (short GRBs) only represent a small fraction and they are typically associated with NS mergers [15] or, even more rarely, with magnetar flares [15], although potential exceptions to this classification have been identified [16]. In general, understanding the properties and the origin of a particular GRB using only gamma-ray information is challenging. EM follow-up observation can occasionally provide a robust association of the source with a particular galaxy and/or a reliable spectral characterization, which is a crucial information to identify the physical process at the origin of the GRB. The observation of a GW signal coming from the same source of a GRB can provide an independent spatial localization of the source and can immediately identify the physical process undergoing at the source as well, making the classification of the GRB unambiguous or at least strongly constraining it. Even a GW non-detection can constrain the possible processes at the origin of a GRB [17]. The sensitivity of GW detectors is not sufficient to reach the redshifts typically associated with GRBs yet. Moreover, the relatively short GW observing runs imply that the majority of GRBs are not covered by GW observations at all. Improving the sensitivity would increase the maximum observable redshift by an order of magnitude for BNS mergers, pushing it into the short GRB source population. This would greatly enlarge our chance of either detecting the GW emission from short GRBs that originate from BNS mergers or improving our understanding of the small population of short GRBs that are not produced by NS mergers.

Extreme compact objects and their equations of state

The GWs emitted by the inspiral of a compact binary are not dependent from the composition and structure of the compact objects, instead their internal properties become important during the last few orbits of the inspiral. Before the merger, the tidal field of an object induces deformations on the companion, which transfer orbital energy into the structure of the object, accelerating the rate of the inspiral and therefore slightly affecting the GW phase. This effect is described by the *tidal deformability parameter* $\widetilde{\Lambda}$ [18]. It can be inferred from the GW signal and, in the case of NSs, it can be directly related to the **E**quation **o**f **S**tate (EoS) of matter at (supra)nuclear densities.

Neutron stars and pulsars

The signal's amplitude for a CW emitted by a non-accreting and spinning NS, with an asymmetry with respect to its rotation axis, can be expressed as [19]:

$$h_0 = \frac{4\pi^2 G}{c^4}\frac{\varepsilon I_{zz} f^2}{d} \approx 1.06 \times 10^{-26}\left(\frac{\varepsilon}{10^{-26}}\right) \times \left(\frac{I_{zz}}{10^{38}\ \mathrm{kg\ m^2}}\right)^2 \left(\frac{1\ \mathrm{kpc}}{d}\right), \tag{1.10}$$

where d is the distance from the source, f is the GW frequency which is twice the spin frequency of the NS in the prototypical case of a star rotating around one of its principal axes of inertia f_s, i.e. $f = 2f_s$, ε is the ellipticity of the star $\varepsilon = \frac{I_{xx}-I_{yy}}{I_{zz}}$ and I_{zz} is the moment of inertia of the star with respect to the principal axis aligned with the rotation axis. There are two ways to study the CWs from spinning NSs: the first one depends on the amount of sources' information we have; while the second method is based on the information we assume to have. For "targeted" searches, we use accurate measurements

of the main parameters, namely position, spin frequency and its derivative and, in case of binary systems, the Keplerian parameters [20] obtained from EM observations. Data from the detector's network can be coherently combined in order to increase the sensitivity of the analysis. At the other end, there are all-sky searches for NSs without an EM counterpart, in which a portion of the parameters' space as large as possible is explored. Searches covering intermediate cases are also routinely carried out. For instance, narrow-band searches slightly extend the parameters' space around the EM-inferred parameters of known pulsars, in order to account for possible small - fraction of a Hertz - mismatches among the EM and GW emission [21]. "Directed" searches assume the source position is known, while the star's rotational parameters are not, as in the case of the supernova remnants. All-sky and directed searches typically use data from different detectors, with the aim of suppressing the false alarm probability. Although no CWs have been detected so far, interesting upper limits on the star's ellipticity have been put [22, 23]. These can be interpreted as constraints on the residual initial star's deformation frozen after crust solidification or as due to an inner magnetic field not aligned to the rotation axis. Accreting NSs, like Low-Mass X-ray binaries systems, are also considered promising sources of CWs. In such systems, angular momentum is being added by the accreted matter while some may be lost to GW emission as a consequence of accretion-induced thermal or compositional asymmetries on the star surface. A torque equilibrium between these two effects has been invoked to explain the observed spin frequencies [24], all of which are much smaller than the possible maximum value for a NS. If the torque-balance condition is verified, the resulting CW amplitude is [24]:

$$h_{0,torque-balance} \approx 3.4 \times 10^{-26} \left(\frac{3.4\ \mathrm{M}_\odot}{M}\right)^{\frac{1}{4}} \left(\frac{r_m}{10\ \mathrm{km}}\right)^{\frac{1}{4}} \left(\frac{F_{X,-7}}{4}\right)^{\frac{1}{2}} \left(\frac{R}{10\ \mathrm{km}}\right)^{\frac{1}{2}} \left(\frac{600\ \mathrm{Hz}}{f}\right)^{\frac{1}{2}}, \tag{1.11}$$

where $F_{X,-7}$ is the X-ray flux in units of 10^{-7} erg s^{-1} cm^{-2} and $r_m \geq R$ is the torque lever arm, typically taken as the radius at which the NS magnetic field starts to disrupt the accretion flow. Analysis of O2 data [24] based on cross-correlation among LIGO detectors has set upper limits near or slightly below the torque-balance limit in the band 40-180 Hz. Going below this limit allows to set constraints on the mass-radius-magnetic field plane or implies that the accretion torque is weaker than assumed so it will be important to make this analysis with more sensitive data.

Long-transient signals

The long-transient signals are the semi-periodic GW with duration from hours to days. If the signal lasts ∼one day, or longer, the same modulations present in standard CW searches must be taken into account. Their duration can be due to the amplitude decreasing in time until it drops below the detection threshold or/and to a very fast spin-down, which rapidly brings the signal frequency outside the sensitivity range of the detectors [25, 26]. In the latter case, the signal amplitude is given by equation 1.10 and, if the ellipticity is determined by the interior magnetic field of the NS [27], we may write as an order of magnitude:

$$\varepsilon_B \approx 2 \times 10^{-4} \left(\frac{B_t}{10^{16}\ \mathrm{G}}\right)^2 \left(\frac{R}{10\ \mathrm{km}}\right)^4 \left(\frac{M}{1.4\ \mathrm{M}_\odot}\right)^{-2}, \tag{1.12}$$

where B_t is the toroidal component of the interior magnetic field, whose geometry is expected to play a crucial role. Furthermore, the frequency and amplitude evolution of the

signal will carry the signature of the relative strengths of the EM and GW torques, which depend on the exterior-to-interior magnetic field ratio and on the time-dependent angle between the magnetic and spin axes [26]. There is a general consensus that $\sim$ millisecond spin at the birth is needed in order to trigger the amplification of the NS B-field to large-enough values for inducing a significant distortion of the NS [27]. As a result, a $\sim$ hours-long signal with a starting frequency $f_0 \sim [0.5 \div 2]$ kHz and decreasing frequency would be expected. The ellipticity may be very large $\varepsilon \sim 10^{-1}$, as a consequence of a secular bar-mode instability being excited in a newborn NS [28]. The instability arises at a rotation-to-binding energy ratio $\frac{T}{|W|} \geq 0.14$, strictly requiring a $\approx$1 ms spin. Its growth time is $> 10^4$ s if it is driven by GWs alone, however a strong magnetic dipole spin-down acting on a timescale $\sim 10^3$ s may represent a more effective energy sink capable of accelerating the mode growth [29]. For this to work, the NS must possess a $B_d \sim 10^{15}$ G [30] hence its spin-down may power a bright EM counterpart during the growth phase of the bar. The subsequent GW signal is expected to last $\sim [10^3 \div 10^4]$ s and does not track the NS spin but a lower frequency ($\sim [\div 200]$ Hz) characteristic of the bar. In an alternative scenario, the ellipticity may be due to the fall-back material settling on the NS surface soon after its birth and forming an accretion column near the magnetic poles. The accretion-induced ellipticity will reach smaller values than in the previous case and the signal is expected to have a shorter duration as the accretion column can only be sustained for a limited time ($\leq [\div 100]$ s) [30]. Furthermore, the accreted mass may cause the gravitational collapse of the NS in an even shorter timescale. The fall-back material will, on the other hand, add angular momentum to the NS, keeping its spin close to maximal for the whole signal duration, despite the GW-induced spindown [30]. As a result, this scenario predicts a $\sim$50 s long signal with an increasing frequency at $f \sim [1 \div 2]$ kHz.

Supernova explosions

SN that can emit GWs are the type II ones, which are produced starting from the gravitational collapse of the core and the consequent violent explosion of star with a mass higher than 10 $M_\odot$. During the collapse phase, gravitational emission due to an asymmetrical collapse occurs, associated with a strong neutrino emission. Despite the growing understanding of the collapse process, the explosion mechanism is not fully understood yet. Understanding the collapse means to be able to directly probe SN's inner dynamics. Neutrinos and GWs leave the core around the time of collapse and can be used to directly probe the SN engine. Since they bring complementary information, future detections of neutrinos will allow us to probe mainly the thermodynamic properties of the collapsed core while GWs will allow us to understand the dynamics of moving matter. Because of turbulence, SN explosions are stochastic in nature and so are the predicted GW signals [31]. Moreover, the distribution of matter in SN explosions does not deviate much from spherical symmetry this means that even though these explosions are very powerful, only a small fraction of the energy is emitted as GWs. SN explosions are quite rare: the rate of SN explosions in the Milky Way is expected to be about 2 per century. While optical telescopes probe a large number of galaxies detecting several such explosions per year, the GW signals that SNs produce are expected to be weak, so that the detection range of current detectors does not even cover the whole Milky Way. For these reasons, detecting GW transients from SN explosions is quite challenging.

1.2.3 Cosmology

The Standard Cosmological model is a successful one whose predictions have passed many precise observational tests in both the early and late-time universe [32]. Despite its successes, the Standard Cosmological model still suffers from some important experimental and theoretical difficulties. On the experimental side, there are discrepancies between different independent measurements of the Hubble constant [33]. On the theoretical one, the nature of the two largest energy components of the universe, i.e. **D**ark **E**nergy (DE) and **C**old **D**ark **M**atter (CDM), still remains unknown.

The Hubble constant

Since they directly provide the source luminosity distance, GWs open a new avenue to study cosmology [34]. For example, there is the possibility to improve the measurement of H_0 with BNSs and BBHs observable during the next observing runs. In order to provide a redshift estimation three different methodologies could be used:

1. the source host galaxy is identified by its EM counterpart as in the case of GW170817 [35];
2. galaxy surveys are exploited to identify possible hosting galaxy for the GW events [36];
3. the implicit redshift information coming from the relation between source-frame masses and detector-frame masses [37] is considered.

The common denominator to forecast the measurement of H_0 with these approaches is the population of BNS and BBH that we expect to detect in the future.

Sub-solar mass primordial BHs

Primordial **B**lack **H**ole (PBH) could have formed during the early life of the Universe due to different mechanisms including the gravitational collapse of large inhomogeneities created during inflation, phase transitions and the collapse of topological defects like cosmic strings [38]. PBHs could constitute a fraction of dark matter [39], or even the entirety for some specific PBH mass ranges. Regardless of this, the discovery of PBHs would shed light on cosmology and on the new physics processes responsible for their formation. The detection of sub-solar mass BHs would represent a clear indication of their primordial origin. Latest searches have covered the range from 0.2 to 1 $M_\odot$ and a mass ratio $q > 0.1$ [40], allowing to set an upper limit on the merger rate of sub-solar binary systems. This can be translated in a constraint on the fraction of dark matter made of PBHs [39], for given PBH formation models.

1.2.4 Tests of General Relativity

The dynamics of merging binaries in the framework of GR is a well-posed problem that can be solved to predict the evolution of any binary system. The solution of Einstein's equations is however a formidable task that is tackled either via sophisticated analytical methods, carried out only under certain conditions e.g. weak field, or via direct numerical simulation.

Parametric tests

The main idea behind any parametric test of GR is to introduce a perturbation around the GR solution, controlled by one or more phenomenological parameters $\overrightarrow{\delta p}$ and constrain the magnitude of the perturbation by inferring the value of the perturbation parameter from the data [41]. The problem is always formulated in a way that GR can be defined as the locus of the parameter space $\overrightarrow{\delta p} = 0$. Using the 3.5 **P**ost-**N**ewtonian (PN) waveform phase model in GR, the frequency-domain GW signal from merging BBH can be written as [42]:

$$h(f) = A(f)e^{i\Phi(f)}, \tag{1.13}$$

with the phase for the inspiral:

$$\Phi(f) = \sum_{k=0}^{7} \left(\varphi_k + \varphi_k^{(l)} log(f)\right) f^{\frac{k-5}{3}}, \tag{1.14}$$

where each of the PN coefficients φ_k and $\varphi_k^{(l)}$ is a known function of the physical parameters of the system. Perturbing around GR implies the introduction of the effective PN coefficients:

$$\hat{\varphi_k} = \varphi_k(1 + \delta\varphi_k), \tag{1.15}$$

so that GR is uniquely defined by $\delta\varphi_k = 0, \forall k \in [0, 7]$. This method has been applied to the detected signals [41].

Black hole remnants

Since the GW150914 detection, several BBHs showed the signature of a ring down and this allowed to construct catalogues of remnant properties. However, a key ingredient for definitive tests of the merger remnant is missing. Tests of the so-called no-hair theorem[2] require the detection of multiple ring down modes [43]. The ring down waveform can be expressed as a superposition of damped sinusoids, labeled in GR by their projection over spherical harmonics:

$$h(t) = \sum_{nlm} A_{nlm} e^{i\omega_{nlm}(t-t_{lmn})}, \tag{1.16}$$

where the amplitude A_{lmn} is typically unknown for a merger process, while the complex frequencies ω_{nlm} are known functions of the BH mass and spin. When expressed in this way the ring down signal is dominated by the $(n, l, m) = (0, 2, 2)$ mode for regions of the parameter space that are most commonly probed by BBH systems. Despite unconfirmed claims to the contrary, no higher order mode has been detected yet in any BBH ring down. Higher SNR in the ring down phase of BBH systems could allow the detection of higher order modes. However, the detection probability is critically dependent on the inclination angle and on the mass ratio. Given the detection bias towards face-on and equal mass systems, this implies that it is unlikely that higher modes will be actually detected even with the improved sensitivity.

[2]The no-hair theorem states that a BH in GR is characterized by only three observable properties – its mass, angular momentum and electrical charge.

1.2.5 Dark Matter

The nature of dark matter remains unknown and several possible candidates have been proposed and discussed in the literature. There is a growing sense of "crisis" in the dark matter particle community, which arises from the absence of evidence for the most popular candidates for dark matter particles - such as weakly interacting massive particles, axions and sterile neutrinos - despite the enormous effort that has gone into searching for these particles [44]. What we are quite confident about is that most of dark matter must be non-baryonic and interact very weakly with ordinary matter. Overall, dark matter candidates span about ninety orders of magnitude in mass, going from "fuzzy" dark matter with mass around 10^{-22} eV to stellar mass PBHs. A very promising alternative model of dark matter is that of the dark matter scalar field. Dark matter may induce apparent temporal variations in the physical "constants", including the EM fine-structure constant and fermion masses. In particular, a coherently oscillating classical dark-matter field may induce apparent oscillations of physical constants in time, while the passage of macroscopic dark-matter objects - such as topological defects - may induce apparent transient variations in the physical constants. Several new signatures of the aforementioned types of dark matter can arise due to the geometric asymmetry created by the **B**eam **S**plitter (BS) in a two-arm laser ITF [45]. It has been shown that GW detectors and ITFs in general, built for other scientific purposes, can put very good limits on this type of dark matter [46]. GW ITFs could be use as dark matter detectors through two main paths:

- the detection of GWs emitted by dark matter, like:
  - the emission of continuous GWs from ultra-light boson clouds around spinning BHs [47];
  - the coalescence of PBHs [38].
- The direct interaction of dark matter with the detector hardware, i.e.
  - the differential strain induced by dark photons impinging on detector optics [48];
  - the change of the mirror diffraction index due to scalar dark matter particles [49].

Boson Clouds

The ultra-light bosons would appear around rotating BHs as a consequence of quantum fluctuations [50]. They would then scatter off and extract angular momentum from the BHs, and - being confined by the gravitational field - form macroscopic clouds, i.e. boson condensates, through a superradiance process [47]. After the BH spin decreases below a certain threshold, the superradiance process stops and the cloud may leave an imprint on GW detectors in two different ways:

1. the cloud depletes over time mainly through annihilation of bosons into gravitons (for weak boson self-interactions), producing a long-duration quasi-monochromatic GW signal [51];
2. if the cloud forms around a BH in a binary system, it can affect the inspiral phase in a potentially measurable way [52].

Direct interaction of dark matter with detectors

Ultra-light dark matter, i.e. $\ll 1$ eV, can couple with interferometric detector components, producing an observable signal that would produce a differential strain measurable by analysing the data with the same standard techniques used to detect GW signals. The detectors are sensitive to the mass scale set by the particle field frequency $f_0 = \frac{m_b c^2}{h}$ where m_b is the particle mass in the range $[10^{-14} \div 10^{-11}]$ eV for ground-based detectors. The interaction between dark matter and normal matter would result in a stochastic and narrow band differential strain which can be searched using data analysis techniques adapted from CW and stochastic GW searches. Recent results obtained in the analysis of Advanced LIGO, Advanced Virgo and GEO600 data [53] have already provided interesting limits on the dark matter coupling constant to normal matter, competitive - over a large mass range - with experiments aiming at measuring a violation of the Equivalence Principle.

1.3 GW detections

In this section, a description of the sources detected so far, is reported together with a brief survey of the existing ground-based ITFs.

- **L**aser **I**nterferometer **G**ravitational Wave **O**bservatory (LIGO) is a USA observatory, founded in 1984, as a joint project between the California Institute of Technology (Caltech) and the Massachusetts Institute of Technology. Its construction began in 1994. It now consists of two ITFs, each with two 4-km-long-arms, one located in Livingston (Louisiana) and the other one in Hanford (Washington State).

- Virgo was born as a French-Italian interferometric ground-based detector, funded by INFN and CNRS. It is located in Cascina, near Pisa, on the site of the **E**uropean **G**ravitational **O**bservatory (EGO). Many others countries joined the experiment since its foundation: Netherlands, Poland, Hungary, Spain, Germany, Belgium and Greece are part of the Virgo Collaboration today. The length of the Virgo arms is 3 km. The name of the experiment is referred to the Virgo cluster because the sensitivity goal for Virgo was $h \sim [10^{-21} \div 10^{-22}]$ corresponding to GWs amplitude for a NS-NS merger at 15 Mpc which is the distance of the Virgo cluster from the Earth.

- **Ka**mioka **Gra**vitational Wave Detector (KAGRA), is located underground at the Kamioka Observatory, which is near the Kamioka section of the city of Hida in Japan. The arms' length of the detector is 3 km. It is the first GW observatory in the world built underground and the first making use of cryogenic mirrors.

- GEO600 is located near Hannover, Germany, with an arms' length of 600 m. It is designed and operated by scientists from the Max Planck Institute for Gravitational Physics, along with partners in the United Kingdom.

The ground-based detectors alternate observing periods (or *runs*), in which the ITF takes data, and phases of technological improvements, where upgrades are installed and commissioned on the instrument. Every upgrade ends with a *commissioning* period whose the goal is the achievement of the best working point both in terms of duty cycle and sensitivity. Till now, three observing runs have been completed:

- During the **first observing run O1**, from September 12, 2015, to January 19, 2016, the two LIGO - Virgo was still in the upgrade phase - detected three GW signals emitted by the coalescence of a BBH;

- The **second observing run O2** took place from November 30, 2016 to August 25, 2017 with the two Advanced LIGO ITFs. In the time interval between O1 and O2 the sensitivity of both LIGO detectors was improved. As a result, the BNS range, i.e. the average distance to which these signals could be detected, reached 80 Mpc at the beginning of O2 and about 100 Mpc at the end of the observation period. The Advanced Virgo detector, the upgraded version of Virgo, joined O2 on August 1, 2017, with a BNS range of about 25 Mpc. At the end of the second run, the total number of confirmed detections was eleven - ten of which from BBH systems and one from a BNS systems. All of them were reported in the *Gravitational Wave Transient Catalog 1* (GWTC-1) [54];

- The **third observing run** was divided in two phases **O3a** and **O3b**, respectively. O3a started on April 1, 2019 and it was suspended on September 30, 2019, for maintenance and upgrades. During this period, forty-four new GW events were detected and reported in the *Gravitational Wave Transient Catalog 2* (GWTC-2) [55]. In particular, a second BNS system GW190425 was detected [56]. O3b began on November 1, 2019 and due to the COVID-19 pandemic was forced to end prematurely on March 27, 2020. KAGRA joined LIGO and Virgo for the final part of O3b and on April 2020 completed its observing period jointly with GEO600. Thirty-five new gravitational wave events were observed during O3b and they have been reported in the *Gravitational Wave Transient Catalog 3* (GWTC-3) [57], bringing the total number of detections to ninety - see Figure 1.2.

A snapshot of the ninety sources detected so far is shown in Figure 1.3. Most of them consisted in coalescing BHs, a few were BNS systems and two were mixed systems, i.e., BH-NS. The GWs emitted in the last orbits of the inspiral are observed together with the subsequent coalescence resulting in the formation of a single body. In the following, the noteworthy events are summarized - see Table 1.1.

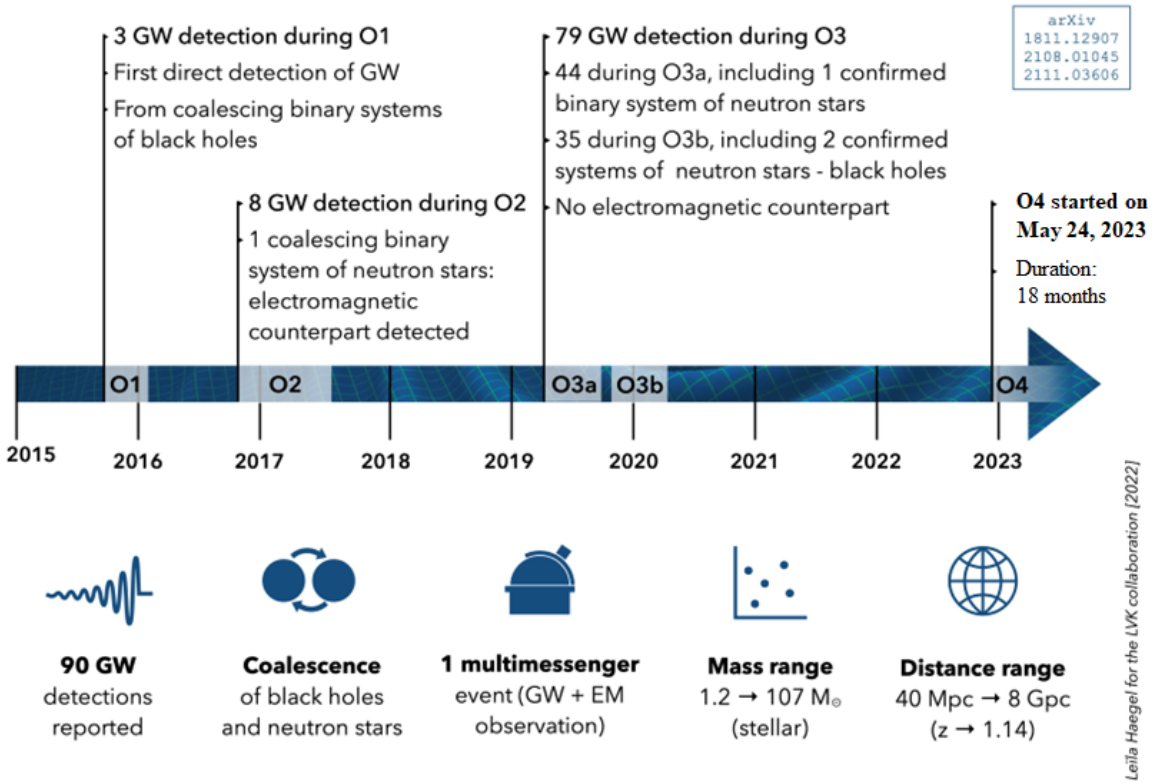

Figure 1.2: *State of the art of GW detections related to the interferometric ground-based detectors observing runs.*

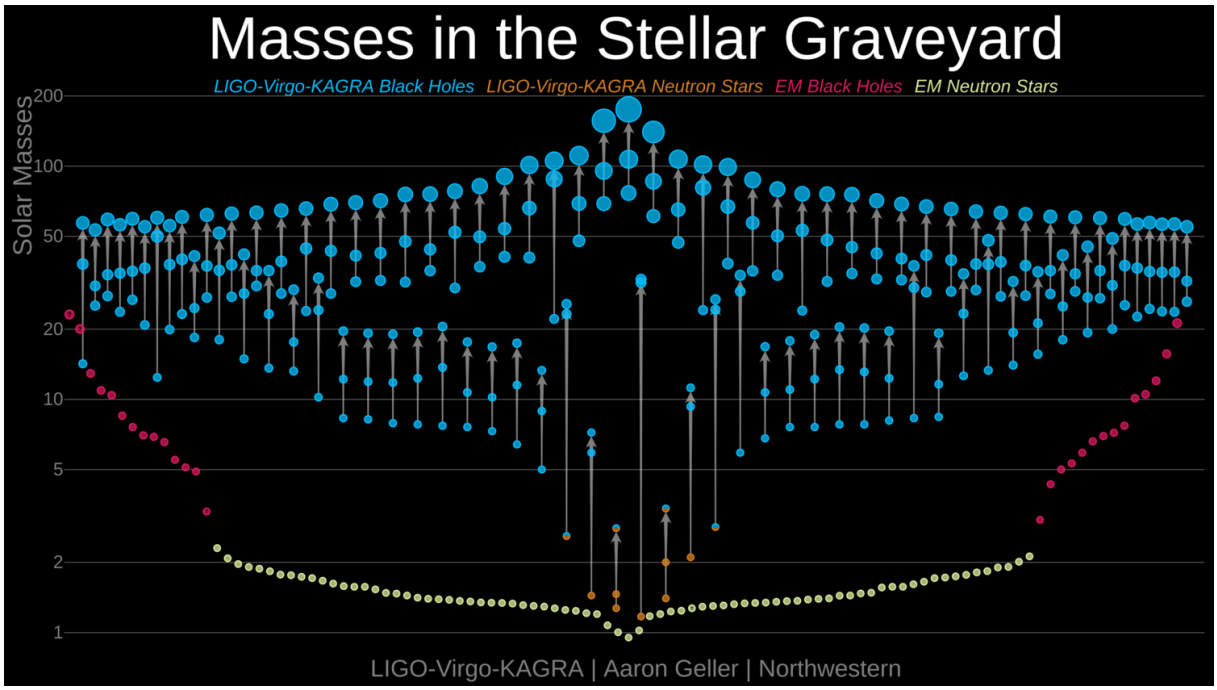

Figure 1.3: *The snapshot shows the masses of all compact binaries detected in the first three observing runs, with BHs in blue and NS in orange. Also, stellar mass BHs (purple) and NSs (yellow) discovered with EM observations are shown. Credit: LIGO/Virgo/Northwestern Univ./Aaron Geller.*

GW event Time (UTC)	Initial Masses ($M_\odot$)	Final Mass ($M_\odot$)	Luminosity Distance (Mpc)
GW150914 09:50:45	36^{+5}_{-4} 29^{+4}_{-4}	62^{+4}_{-4}	430^{+150}_{-170}
GW170814 10:30:43	$30.7^{+5.7}_{-3.0}$ $25.3^{+2.8}_{-4.2}$	$53.4^{+3.2}_{-2.4}$	540^{+130}_{-210}
GW170817 12:41:04	$1.17 \div 1.60$	$2.74^{+0.04}_{-0.01}$	40^{+8}_{-14}
GW190412 05:30:44	$29.7^{+5.0}_{-5.3}$ $8.4^{+1.8}_{-1.0}$	$37.0^{+4.1}_{-3.9}$	730^{+140}_{-170}
GW190521 03:02:29	85^{+21}_{-14} 66^{+17}_{-18}	142^{+28}_{-16}	5300^{+2400}_{-2600}
GW190814 21:10:39	23.2^{+11}_{-10} $2.59^{+0.08}_{-0.09}$	$25.6^{+1.1}_{-0.9}$	241^{+41}_{-45}
GW200105 16:24:26	$8.9^{+1.2}_{-1.5}$ $1.9^{+0.3}_{-0.2}$	$10.4^{+2.7}_{-2.0}$	280^{+110}_{-110}
GW200115 04:23:10	$5.7^{+1.8}_{-2.1}$ $1.5^{+0.7}_{-0.3}$	$7.8^{+1.4}_{-1.6}$	300^{+150}_{-100}

Table 1.1: *List of noteworthy binary merger events with measured masses and luminosity distances.*

1.3.1 First direct detection: GW150914

GW150914 was observed by the two LIGO detectors [58] while Virgo was still in the upgrade phase. The waveform predicted by GR was observed for the final part of the inspiral phase of two intermediate (stellar) mass BHs, the fusion of the binary system and the damping of the resulting rotating BH, see figure 1.4.
This observation is important not only as the first ever detected GW but also because it proved the existence of BHs heavy as tens of solar masses, the fact that they can form binary systems and that such systems can merge within the lifetime of the universe. Furthermore, it is a powerful test of GR in presence of very strong gravitational fields. GR states that any accelerating masses will produce GWs. However, in order to detect them, the objects have to be extremely massive and to move very fast. For GW150914, the waves were produced by two BHs, orbiting each other close to the half of the speed of light, and finally merging into a single BH. GW are emitted through all these stages. The theoretical predictions of this process have been worked out from GR and have been used to translate the received pattern of waves into an understanding of what produced them. Moreover, the different features of the observed signal can also be compared with GR's predictions.
The detection of GW150914 was announced to the World on February 11^{th}, 2016 with several worldwide joint press conferences by the LIGO and Virgo Collaborations. The Royal Swedish Academy of Sciences decided to award the Nobel Prize in Physics 2017 *"for decisive contributions to the LIGO detector and the observation of gravitational waves"* to Rainer Weiss, Barry C. Barish and Kip S. Thorne. The prize, given in record time, was the ultimate recognition of the importance of this discovery in the history of not just astrophysics but of science at large.

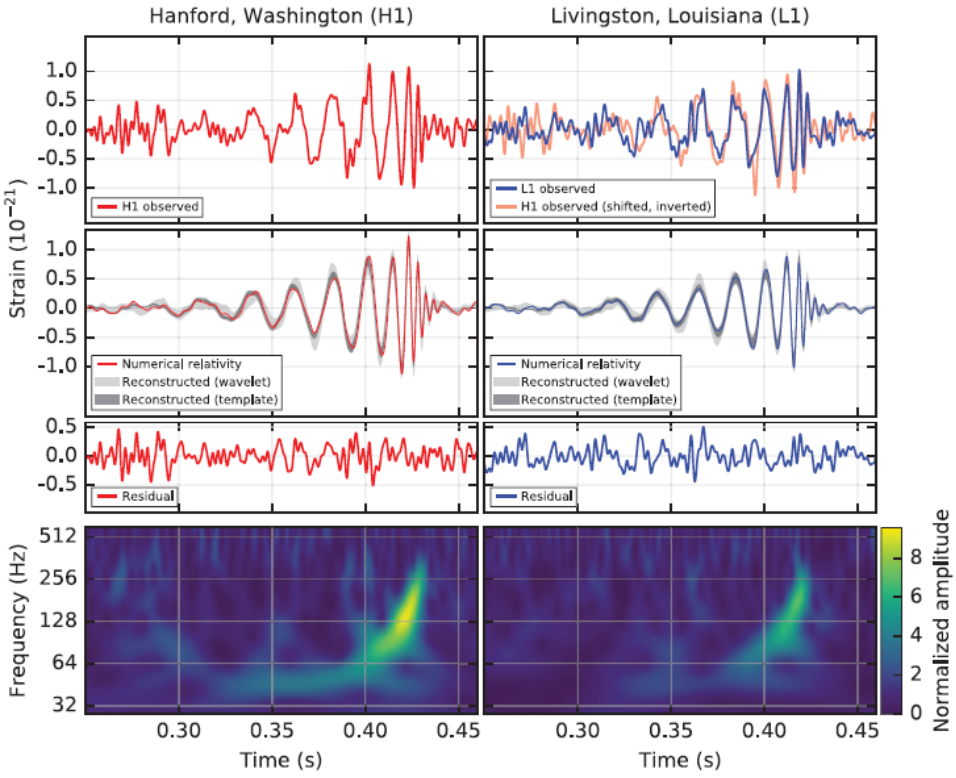

Figure 1.4: *The GW event GW150914 observed by the LIGO detectors of Hanford (H1) and Livingston (L1) [58]. The times are shown compared to September 14, 2015 09:50:45 UTC. For visualization, all time series are filtered with a 35-350 Hz bandpass filter.* ***First line****: Measured signal; GW150914 first came to L1 and* $6.9^{+0.5}_{-0.4}$ *ms later to H1.* ***Second line****: Expected signal.* ***Third line****: Residuals of the difference between the two waveforms presented above.* ***Fourth line****: Signal frequency as time changes.*

1.3.2 Three-detector observation: GW170814

GW170814 is a signal from the coalescence of two BHs observed in all three Advanced detectors. The signal was first observed by the Advanced LIGO Livingston detector and then by the Advanced LIGO Hanford and Virgo detectors with a delay of ∼8 ms and ∼14 ms, respectively [59]. It was detected with a high confidence and within 30 seconds from its arrival an alert was then generated and sent to the telescopes which signed a **M**emorandum **o**f **U**nderstanding (MoU) with LIGO-Virgo. For GW170814, the false alarm probability is estimated to be less than 1 in 27000 years. Advanced Virgo also detected this event, as demonstrated by two independent analyses. The first method compared two models: first assuming GW170814 detected by all three detectors and then assuming the signal detected only by Advanced LIGO. The second method has looked for un-modelled GW signals with a frequency which increases over time, i.e. the chirp signal produced by the merger of two compact objects, without assuming that particular waveform.

The sky localization of a source can be estimated using the differences in the arrival times of the signal that reaches the detectors. The time difference will be associated with a circle in the sky consistent with the positions [60]. With a network of three detectors, we can get three time differences and therefore three circles intersecting at two points, while with four or more detectors, all circles intersect at a single point. Because the arrival times

have uncertainties, this means that those circles are actually bands that cover a more or less wide region of the sky when they intersect. Figure 1.5 summarizes the GW170814 source's sky localization provided by the analysis. In many cases, the most probable volume in which the source is located may contain only a limited number of galaxies, thus simplifying the search for a counterpart visible with telescopes. For GW170814, twenty-five telescopes tried to observe the source but no EM counterpart was observed. As in the previous detections, GR tests have been carried on and the results are consistent with the theoretical predictions of Einstein's theory and similar to those already previously obtained.

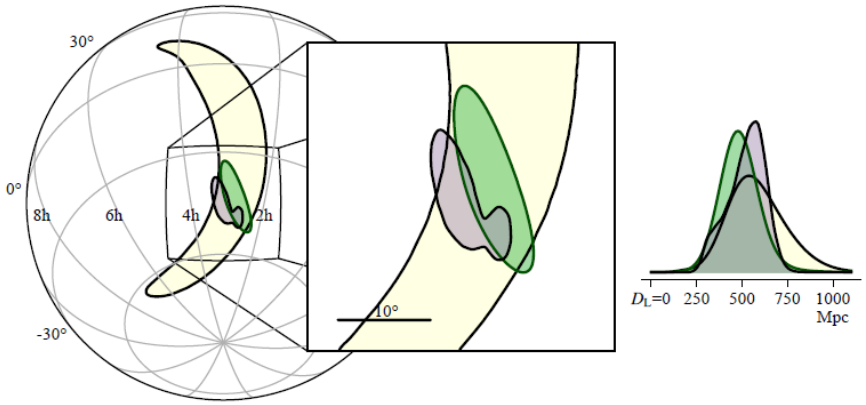

Figure 1.5: *Localization of GW170814: the left part of the figure compares the sky regions selected from different analyses as the most likely to contain the source of GW170814. These are called 90 % confidence regions as they are defined by a 90 % probability that the source lies within them. The area in yellow corresponds to the rapid localization based only on the data of the two LIGO ITFs. Adding Virgo gives the green area, which is smaller than more an order of magnitude: 100 deg^2 versus 1160. Finally, the purple region is the result of parameter estimation from the full analysis. The right side of the figure compares the probability distributions for the source luminosity distance. Adding Virgo cuts the tails off of the distribution that correspond to the larger distances, finding the most probable distance of the source to be 540 Mpc.*

1.3.3 Gravitational waves from a binary neutron star inspiral: GW170817

GW170817 is the first observation of a BNS inspiral made by Advanced LIGO and Advanced Virgo. The signal was detected with a network SNR of 32.4 and a false alarm rate estimate of less than one per 80000 years. The combination of data from the LIGO and Virgo detectors allowed a precise sky localization to an area of 28 deg^2 [61]. The signal was clearly visible in both Advanced LIGO detectors, but not in Advanced Virgo. This aspect was very important for the localization since the signal comes from a blind spot in the Virgo pattern.
A γ-ray counterpart was observed 1.7 s after the coalescence time [13] and consistent with the localization and distance inferred from GW data [62]. The coincident observation of a GW signal and of a GRB seems confirming the long-held hypothesis that BNS mergers are linked to short-γ-ray bursts.
This event represents the first multimessenger detection. Telescopes from all over the

world were pointed towards the sky area identified by the GW to make further observations related to this source, thus performing the first follow up campaign ever done. This has allowed us to carry out studies on the fundamental physics of gravity, astrophysics, and cosmology. The observed arrival times are used to investigate the speed at which GWs propagate, the Lorentz invariance, and to test the equivalence principle through the Shapiro's time delay [13]. Furthermore, the GW signal gives a direct measurement of the luminosity distance of the source which - along with a redshift measurement - can be used to infer cosmological parameters independently of the cosmic distance scale. Using the association with the galaxy NGC 4993 to infer the redshift and the luminosity distance directly measured, the Hubble constant has been derived to be $H_0 = 70^{+12}_{-8}$ km s^{-1} Mpc^{-1} [63] which can be compared with the value from other methods.

1.3.4 Imprints of higher order multipoles: GW190412

At the time of the event GW190412, both the LIGO detectors and Advanced Virgo were in operation. This binary is different from previously observed ones most notably due to its asymmetric masses: a ~ 30 M$_\odot$ BH merged with a ~ 8 M$_\odot$ BH companion. The more massive BH rotated with a dimensionless spin magnitude between 0.22 and 0.60 at 90% confidence level [64]. Signal models that include higher order multipoles are needed in order to infer the strongest constraints on GW190412's source properties. Indeed, if the data contain significant imprints of different multipoles, the appropriate models can fit the data better than dominant-mode models leading then to a higher statistical likelihood. Conversely, if the data would not contain imprints of higher multipoles, using more complex models allows us to disfavor configurations in which clear imprints are predicted. A violation from general relativity may arise from how the signal is generated by the source; additionally, the form of the signal may be tested by checking the consistency of independently obtained estimates of parameters between the inspiral and merger-ring down parts of the full BBH waveform. By enhancing the sensitivity of the detectors and extending the observation time, we will obtain a more comprehensive insight into the BBH population. Subsequent observations of similar binary systems, and potentially those with even more extreme mass ratios, will further refine the comprehension of their prevalence and may offer insights into the mechanisms governing their formation.

1.3.5 Binary black hole merger with a total mass of 150 M$_\odot$: GW190521

Advanced LIGO and Advanced Virgo observed the short duration GW signal, GW190521, with a three-detector network signal-to-noise ratio of 14.7 and an estimated false-alarm rate of 1 in 4900 years [65]. Both objects are much more massive than any other BH detected, their masses are 85 and 66 M$_\odot$ – and the smaller BH is larger than most massive remnants of other mergers. The mass of the final BH is 142 M$_\odot$, making this a direct observation of the formation of a so called *intermediate-mass BH* [66]. The mass emitted into GW energy is about 8 M$_\odot$. The frequency at which the BH merger signal reaches its maximum is inversely proportional to the total mass of the binary system; for this event the peak frequency was about 60 Hz, confirming that the source originating this signal was a pair of very large BHs, see figure 1.6. The large individual and total masses of GW190521 and the low likelihood that the primary originated from a stellar collapse - given theoretical constraints on supernova physics - make the detection particularly

interesting for astrophysics [67]. The remnant ring down signal is compatible with the waveform generated by solving GR equations. As the low frequency sensitivity improves for Advanced LIGO and Advanced Virgo, further massive binary BH events should be observed, since mergers at lower frequencies imply sources of higher masses [2].

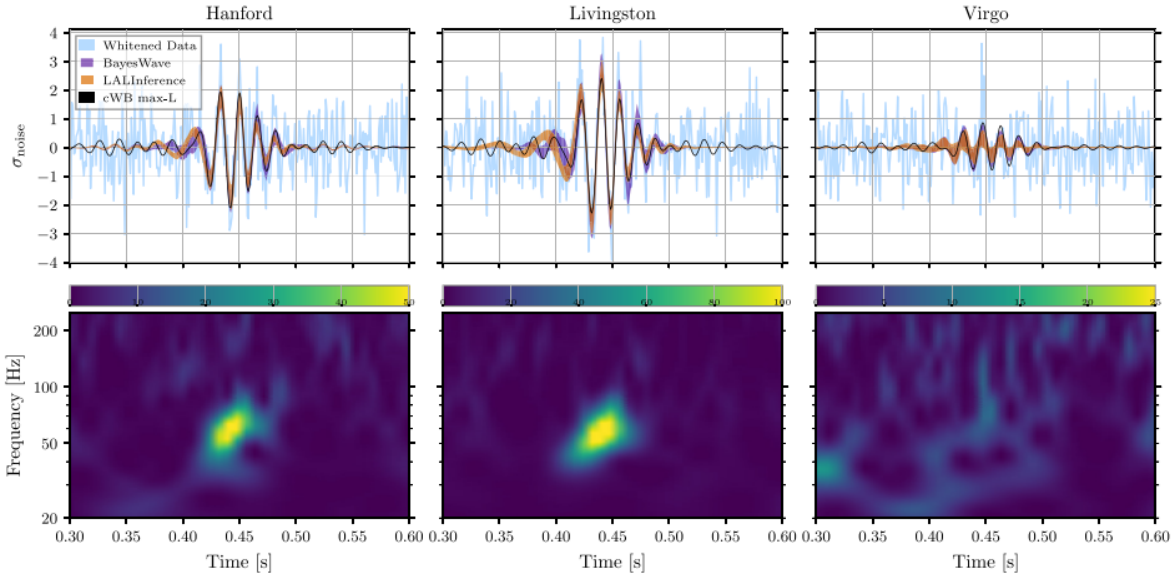

Figure 1.6: *The GW event GW190521 observed by the LIGO Hanford (left), LIGO Livingston (middle), and Virgo (right) detectors. Times are shown relative to May 21, 2019 at 03:02:29 UTC. The top row displays the time-domain detector data after whitening by each instrument's noise amplitude spectral density (light blue lines); the point estimate waveform from the CWB search [68] (black lines); the 90% credible intervals from the posterior probability density functions of the waveform time series, obtained via Bayesian inference with a binary BH waveform model (orange bands), and with a generic wavelet model (purple bands). The ordinate axes are in units of noise standard deviations. The bottom row displays the time frequency representation of the whitened data.*

1.3.6 Coalescence of a BH with a compact object: GW190814

The GW signal GW190814 has a SNR of 25 in the three-detector network. The source has the most unequal mass ratio measured with GWs so far, i.e. $0.112^{+0.008}_{-0.009}$ [69]. The nature of the secondary component is unclear, the lack of measurable tidal deformations and the absence of an EM counterpart are consistent with either a NS or a BH. The final mass $25.6^{+1.1}_{-0.9}$ $M_\odot$ and the final dimensionless spin $0.28^{+0.02}_{-0.02}$ of the merger remnant are estimated under the assumption that the secondary is a BH [69]. Because of the lower primary spin and the smaller orbital contribution due to the asymmetric masses, the final spin resulted to be lower than the ones measured in previous merges. Therefore, GW190814 can be used to test GR in a region of parameters space previously unexplored with strong-field tests. The asymmetric nature of a system excites the higher multipole moments of the gravitational signal, which allows us to test the multipolar structure of gravity. These tests assume GW190814 to be a (quasi-circular) BBH merger and look for inconsistencies between the observed signal and predictions of the theory. According to the no-hair conjecture [70], the multipole moments of a Kerr's BH are completely described by its mass and spin angular momentum. At leading order in spin, the spin-induced quadrupole

moment scalar is $Q = -\kappa a^2 m^3$, where (m, a) are the mass and dimensionless spin of the compact object, respectively, and κ is a dimensionless deformation parameter. Kerr's BHs have $\kappa = 1$, while $\kappa \sim [2 \div 14]$ for NSs - depending on the EoS. For Kerr BHs in GR, $\kappa_1 = \kappa_2 = 1$, where κ_1, κ_2 are the individual deformation parameters of the primary and secondary compact objects in the binary, respectively. Hence, an accurate measurement of κ would deepen the nature of the compact object. For compact binaries, the spin-induced quadrupole moment terms appear at second post-Newtonian order. Since κ_1 and κ_2 are strongly degenerate in the gravitational waveform [71], a linear symmetric combination of these quantities $\kappa_s = (\kappa_1 + \kappa_2)/2$ is measured instead, which is 1 for a BBH according to GR. The result from the analysis of the data shows that GW190814 is consistent with a BBH source as described by GR. However, the possibility for the secondary object to be a NS is not completely ruled out, depending on the maximum mass supported by the unknown NS EoS. The source's asymmetric masses, the non-detection of an EM counterpart and the lack of a clear signature of tides or spin-induced quadrupole effects in the waveform do not allow to distinguish between a BBH or a NSBH. Instead, we rely on comparisons between m_2 and different estimates of the maximum NS mass, M_{max}, to indicate the source classification preferred by data: if $m_2 > M_{max}$, then the NSBH scenario is untenable [72]. While some candidate EoSs from nuclear theory can support nonrotating NSs with masses of up to ~ 3 $M_\odot$, such large values of M_{max} are disfavored by the relatively small tidal deformabilities measured in GW170817, which correlate with smaller internal pressure gradients as a function of density and hence a lower threshold for gravitational collapse. By adopting a phenomenological model for the EoS, conditioning it on GW170817 and extrapolating the constraints to the high densities relevant for the maximum mass, it is found that $M_{max} \leq 2.3$ $M_\odot$. Similarly, the EoS inference reported in [64], based on an analysis of GW170817 with a spectral parameterization for the EoS, implies an upper bound of $M_{max} \leq 2.43$ $M_\odot$, with tenuous but non-zero posterior support beyond 2.6 $M_\odot$. Comparison with the m_2 posterior probability suggests that the secondary component of GW190814 is probably more massive than this prediction for M_{max}. Finally, the NS M_{max} is constrained by studies of the merger remnant of GW170817 [73]. Although no postmerger gravitational waves has been observed, modeling of the associated kilonova suggests that the merger remnant collapsed to a BH after a brief supramassive or hypermassive NS phase which it was stabilized by uniform or differential rotation. Assuming this to be the ultimate fate for the merger remnant implies that no NS can be stable above ~ 2.7 $M_\odot$ and it places a more stringent constraint on NSs that are not rotationally supported. The precise mapping from the collapse threshold mass of the remnant to M_{max} depends on the EoS. By developing approximate prescriptions based on sequences of rapidly rotating stars for a range of candidate EoSs, M_{max} has been bounded below approximately $[2.2 \div 2.3]$ $M_\odot$ [74]. Overall, these considerations suggest that GW190814 is probably not the product of a NSBH. Nonetheless, due to the current uncertainty in M_{max}, the possibility that the secondary component is a NS cannot be completely discarded.

1.3.7 NS–BH coalescences: GW200105 and GW200115

GW200105 and GW200115 are the first confident observations of NSBH mergers [75]. The coincident detection of GW200115 by the three detectors - Advanced LIGO Hanford, Advanced LIGO Livingston and Advanced Virgo - provide high confidence to be an astrophysical GW event. On the contrary, when GW200105 was detected, Hanford

was not in observing mode. Because of the small SNR in Virgo too, it was effectively a single-detector event in LIGO Livingston. The source component masses of GW200105 and GW200115 make it likely that these events originated both from NSBH coalescences - see Figure GW2001. Their secondary masses are consistent with the observed NS mass distribution in the Milky Way, as well as population synthesis predictions for secondary masses in merging NSBHs [76]. No evidence of measurable tides or tidal disruption for either of the two signals has been observed and no EM counterparts to either detection have been identified. As such, there is no direct evidence that the secondaries are NSs and our observations are consistent with both events to be a BBH merger. However, given the properties and distances of the two events, the absence of tidal measurements and EM counterparts is to be expected. Moreover, the comparisons of the secondary masses to the maximum allowed NS mass yield a probability $p(m_2 \leq M_{max})$ of $[89\% \div 96\%]$ and $[87\% \div 98\%]$ for the secondaries in GW200105 and GW200115 [75], respectively, being compatible with NSs. The effective inspiral spin parameter of GW200105 is strongly peaked around zero, i.e. $\chi_{eff} = -0.01^{+0.11}_{-0.15}$, while for the second event, GW200115 $\chi_{eff} = -0.19^{+0.23}_{-0.35}$. For GW200115, the spin component parallel to the orbital angular momentum of the primary is $\chi_{1,z} = -0.19^{+0.24}_{-0.50}$ and we find support for negatively aligned primary spin ($\chi_{1,z} < 0$) at 88% probability. More negative values of $\chi_{1,z}$ in GW200115 are correlated with particularly small primary masses reaching into the lower mass gap. We find $p(3\ \mathrm{M}_\odot < m_1 < 5\ \mathrm{M}_\odot) = 30\%(27\%)$ under the high-spin (low-spin) parameter estimation priors [77]. No conclusive evidence was found for spin-induced orbital precession in either system. Regarding the merger rate density of NSBH binaries, it has been estimated with two approaches.

- Assuming that GW200105 and GW200115 are representative of the entire NSBH population, we find $\Re_{NSBH} = 45^{+75}_{-33}\ \mathrm{Gpc}^{-3}\ \mathrm{yr}^{-1}$.
- Assuming a broader range of allowed primary and secondary masses and considering all triggers in O3, we find $\Re_{NSBH} = 130^{+112}_{-69}\ \mathrm{Gpc}^{-3}\ \mathrm{yr}^{-1}$.

These are the first direct measurements of the NSBH merger rate. Both estimates are broadly consistent with the rate predicted from NSBH formation in isolated binaries or via young star clusters [78]. Formation channels in dense star clusters (globular or nuclear) and triples predict lower rates than those inferred from the two events and are unlikely to be the dominant NSBH formation channels. The observations of GW200105 and GW200115 are consistent with predictions for merging NSBHs and observations of BHs and NSs in the Milky Way [79]. Given their significantly unequal component masses, future observations of NSBH systems will provide new opportunities to study matter under extreme conditions, including tidal disruption, and to search for potential deviations from GR.

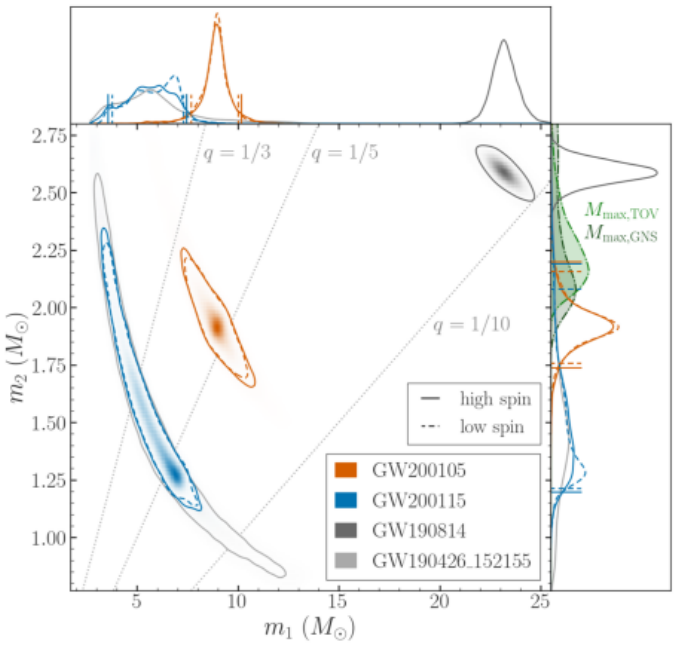

Figure 1.7: *Component masses of GW200105 (red) and GW200115 (blue), represented by their two- and one-dimensional posterior distributions. Colored shading and solid curves indicate the high-spin prior, whereas dashed curves represent the low-spin prior. The contours in the main panel, as well as the vertical and horizontal lines in the top and right panels, respectively, indicate the 90% credible intervals. Also shown in gray are two possible NSBH events, GW190814 and the marginal candidate GW190426_152155, the latter overlapping GW200115. Lines of constant mass ratio are indicated in dashed gray. The green shaded curves in the right panel represent the one-dimensional probability densities for two estimates of the maximum NS mass, based on analyses of nonrotating NSs and Galactic NSs.*

Chapter 2

Advanced Virgo +

At the end of O3, both Advanced LIGO and Advanced Virgo started the integration of new upgrades in order to further improve their sensitivity. For Advanced Virgo, an improvement by a factor of two is expected. This phase of improvement will bring the detectors to a new stage - **A**dvanced Ligo + (A+) and **Ad**vanced **V**irgo + (AdV+), respectively. The AdV+ Project is realized in two phases named Phase I and Phase II:

- Phase I concerns upgrade of the detector in view of the observing period O4 (started in May 2023) and R&Ds for Phase II. The goal of AdV+ Phase I is to improve the sensitivity to the coalescence of BNS systems up to 100 Mpc [80];
- Phase II will start at the end of O4 (January 2025) and aims to upgrading the instrument in order to reach a sensitivity to BNS of the order of 200 Mpc [80].

This chapter describes the interferometric detection technique, the main noise sources that limit the sensitivity and the operability of the ground-based detectors with a focus on the strategies adopted to mitigate them. An overview of the ITF's working point, its optical layout and the future plans for AdV+ and beyond and for the third generation of detectors are discussed as well.

2.1 Interaction of GWs with test masses

The motion of a single particle is not enough for the detection of a GW. Its effect is detectable with at least two particles [2]. To understand how a GW interacts with free-falling TMs we need to introduce the *geodesic equation* and the *geodesic deviation equation*. The former is:

$$\frac{d^2x^\mu}{d\tau^2} + \Gamma^\mu_{\nu\rho}(x)\frac{dx^\nu}{d\tau}\frac{dx^\rho}{d\tau} = 0, \tag{2.1}$$

with the Christoffel symbol $\Gamma^\mu_{\nu\rho} = \frac{1}{2}g^{\mu\sigma}\left(\partial_\nu g_{\sigma\rho} + \partial_\rho g_{\sigma\nu} - \partial_\sigma g_{\nu\rho}\right)$. The equation 2.1 is the classical equation of motion of a free-falling TM in the curved space described by the metric tensor $g_{\mu\nu}$ with τ *proper time*. Let's consider two geodesic parametrized by $x^\mu(\tau)$ and by $x^\mu(\tau) + \xi^\mu(\tau)$, respectively and which are separated by the distance $\xi^\mu(\tau)$. If $|\xi^\mu|$ is much smaller than the typical scale of the variation of the gravitational field, taking the difference between the two geodesics, expanding to first order in ξ and rewriting in terms of covariant derivative $\frac{D^2\xi^\mu}{D\tau^2}$, we get the geodesic deviation:

$$\frac{D^2\xi^\mu}{D\tau^2} = -R^\mu_{\nu\rho\sigma}\xi^\rho\frac{dx^\nu}{d\tau}\frac{dx^\sigma}{d\tau}. \tag{2.2}$$

From equations 2.1 and 2.2 we can understand how TMs at rest behave for an observer in the TT gauge:

$$\frac{d^2x^i}{d\tau^2} = -\left[\Gamma^{\mu}_{\nu\rho}(x)\frac{dx^\nu}{d\tau}\frac{dx^\rho}{d\tau}\right] = -\left[\Gamma^{i}_{00}\left(\frac{dx^0}{d\tau}\right)^2\right]. \tag{2.3}$$

Considering the weak field approximation $g_{\mu\nu} = \eta_{\mu\nu} + h_{\mu\nu}$ with $|h_{\mu\nu}| << 1$ and expanding to first order in $h_{\mu\nu}$, the Christoffel symbol becomes $\Gamma^i_{00} = \frac{1}{2}(2\partial_0 h_{0i} - \partial_i h_{00}) = 0$. If at the time $\tau = 0$ $\frac{dx^i}{d\tau} = 0$ also $\frac{d^2x^i}{d\tau^2} = 0$ at any time. Therefore the particles at rest before the arrival of the wave remain at rest also after its arrival and their separation coordinates remain constant as well. From equation 2.2 it can be demonstrated that, in the TT frame, the separation ξ^i between the coordinates of the two TMs initially at rest does not change because the reference system itself expands with the coordinates [2]. Thus, since the theory is invariant under coordinate transformations the TT gauge shows that the physical effects are not described by the coordinates. The effects of the passing GW can only be detected by monitoring the proper distance between TMs. Thus, we can consider two events with space-time coordinates $(t, x_1, 0, 0)$ and $(t, x_2, 0, 0)$ and with $L = x_2 - x_1$ a constant coordinate distance. If the wave propagates along the z axis with pulsation ω and it is *plus* polarized, it can be demonstrated that the the proper distance between the two events changes with time as:

$$s = (x_2 - x_1)\left[1 + h_+\cos(\omega t)\right]^{1/2} \approx L\left[1 + \frac{1}{2}h_+\cos(\omega t)\right], \tag{2.4}$$

thus a GW induces an oscillating effect on the proper distance between free falling particles. Generally, if the spatial separation between the two events is given by a vector $\mathbf{L}$, the proper distance is given by $s^2 = L^2 + h_{ij}(t)L_iL_j$ and - to first order in h - we have $s \simeq L + h_{ij}\left(\frac{L_iL_j}{2L}\right)$, deriving twice with respect to the proper time:

$$\ddot{s} \simeq \frac{1}{2}\ddot{h}_{ij}\frac{L_i}{L}L_j. \tag{2.5}$$

Writing $\frac{L_i}{L} = n_i$ and defining s_i from $s = n_i s_i$ and using the fact that - to lowest order in h - $L_j = s_j$, we get the geodesic equation in terms of proper distances:

$$\ddot{s}_i \simeq \frac{1}{2}\ddot{h}_{ij}L_j \simeq \frac{1}{2}\ddot{h}_{ij}s_j \tag{2.6}$$

So, the effect of a GW is proportional to the adimensional *GW amplitude* h, which is obtained by integrating equation 2.6:

$$h = 2\frac{\Delta L}{L}, \tag{2.7}$$

where ΔL is the variation of the proper distance between the masses.

2.2 Interferometric detection

In the interferometric detectors, these TMs are mirrors placed at the ends of the arms of a *Michelson ITF* - see Figure 2.1.

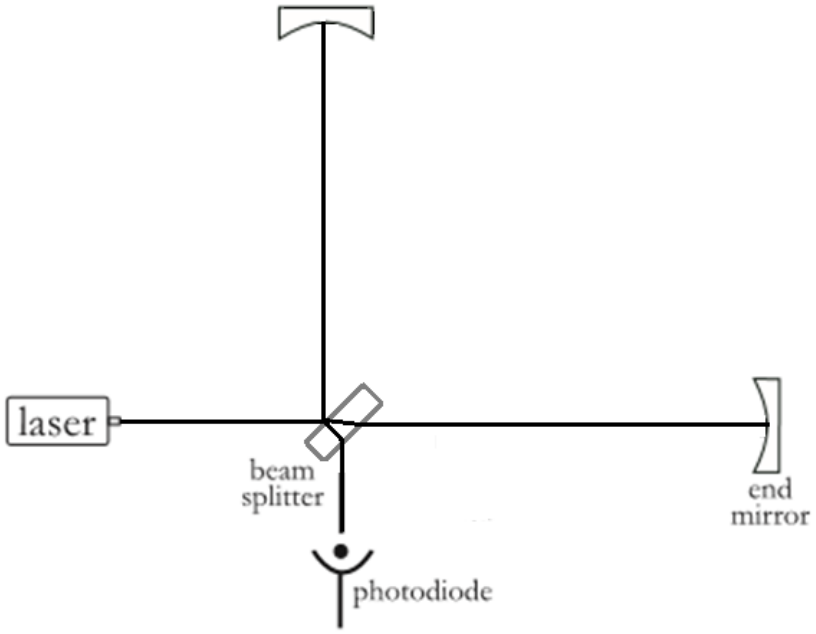

Figure 2.1: *Michelson ITF layout.*

The monochromatic light beam, is split by a BS in two beams having same amplitude and propagating in two arms orthogonal each other. Then, both beams are reflected back by the mirrors at the end of the arms and they recombine on the BS. The interference pattern is detected by a **P**hoto**d**iode (PD). In the presence of a GW, one arm is increased in length while the other is shortened - see Figure 2.2 - and so the beam at the output of the detector accumulates a phase shift due to the difference in the optical path length between the two arms.

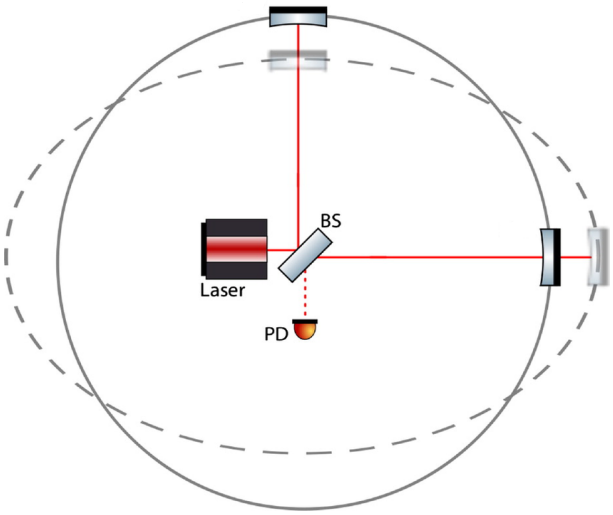

Figure 2.2: *Simplified schematic of Michelson ITF acting as a GW detector and the effect of a plus polarized wave passing perpendicular through the plane of the ITF.*

At the input of a Michelson ITF, the EM field is $\psi_{in} = \psi_0 e^{i\omega_L t} e^{i\phi_L} e^{ik_L x}$, with ψ_0 the amplitude of the input beam, ω_L the laser pulsation, ϕ_L the initial phase and $k_L = \frac{2\pi}{\lambda_L}$ the wave vector where λ_L is the beam wavelength.

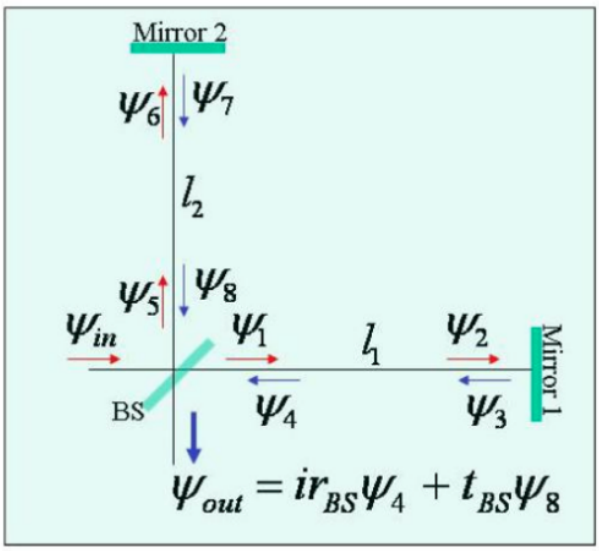

Figure 2.3: *The EM fields at different locations in the ITF, considering r_{BS} and t_{BS} the reflection and the transmission coefficients of the BS respectively, and r_1, r_2 the reflection coefficients of mirror 1 and 2.*

The EM fields in the ITF can be written as follow - see Figure 2.3 notation:

$$\begin{cases} \psi_1 = t_{BS}\psi_{in} \\ \psi_2 = e^{ik_L l_1}\psi_1 \\ \psi_3 = ir_1\psi_2 \\ \psi_4 = e^{-ik_L l_1}\psi_3 \end{cases} \quad \begin{cases} \psi_5 = ir_{BS}\psi_{in} \\ \psi_6 = e^{-ik_L l_2}\psi_5 \\ \psi_7 = ir_2\psi_6 \\ \psi_8 = e^{-ik_L l_2}\psi_7 \end{cases} . \tag{2.8}$$

The output signal is $\psi_{out} = ir_{BS}\psi_4 + t_{BS}\psi_8$ and then the output power can be calculated as:

$$P_{out} = |\psi_{out}|^2 = P_{in} r_{BS}^2 t_{BS}^2 \left(r_1^2 + r_2^2\right)\left(1 + \frac{2r_1 r_2}{r_1^2 + r_2^2}\cos\left(2k_L \Delta L\right)\right), \tag{2.9}$$

where $\Delta L = l_2 - l_1$ and $P_{in} = |\psi_{in}|^2$. If we consider k_L and define $\Delta\phi_L$ as the phase shift, we get:

$$\Delta\phi_L = 2k_L \Delta L = \frac{4\pi}{\lambda_L}\Delta L. \tag{2.10}$$

Starting from the reflection coefficients r_1 and r_2, mentioned above, we can define the quantity $C = \frac{P_{max} - P_{min}}{P_{max} + P_{min}} = \frac{2r_1 r_2}{r_1^2 + r_2^2}$, the so-called *contrast*, where P_{max} is the power measured by the detection PD when the interference between the beams recombining on the BS is constructive, while P_{min} is the power recorded in destructive-interference conditions (ideally equal to zero). For a symmetrical ITF usually $C \approx 1$. We can rewrite equation 2.9 as:

$$P_{out} = P_{in} r_{BS}^2 t_{BS}^2 \left(r_1^2 + r_2^2\right)\left(1 + C\cos\left(\Delta\phi_L\right)\right). \tag{2.11}$$

As shown in equation 2.11 the output power depends on the optical path difference between the arms of the Michelson ITF. Now, let's consider the passage of a plus-polarized monochromatic GW - assumed to be a plane wave - $h_+(z,t)$ that propagates along the z axis, i.e. perpendicular to the ITF plane with the arms along the x and the y axes. So, the phase shift $\Delta\phi_L$ can be expressed as:

$$\Delta\phi_L = \Delta\phi_{off} + \Delta\phi_{GW} = 2k_L(\Delta L) - 2k_L h_+ L, \tag{2.12}$$

where $\Delta\phi_{off}$ can be considered as an offset term and $\Delta\phi_{GW}$ is the phase shift induced by the GW passage. The output power can then be rewritten - taking into account the effect of a GW - as:

$$P_{out} = P_{in} r_{BS}^2 t_{BS}^2 \left(r_1^2 + r_2^2\right) \left(1 + C\cos\left(\Delta\phi_{off} + \Delta\phi_{GW}\right)\right). \tag{2.13}$$

Equation 2.13 shows that the output power variation due to the passage of a GW is proportional to its amplitude h_+, to the reflectivity of the mirrors, to the contrast, to the arms length. The optimization of these parameters is the key for detecting such a weak signal - in the best-case scenario, the TMs of the ITF would be barely perturbed with a displacement in their positions on the order of 10^{-21} m. The frequency response of the detector to gravitational radiation is strictly connected to the laser light travel time in the arms. Consider again a plus-polarized plane wave propagating along the z axis with pulsation ω_{GW} and amplitude h_0:

$$h_+(t) = h_0 e^{i\omega_{GW} t}. \tag{2.14}$$

The space time interval ds^2, according to the equation $ds^2 = -c^2dt^2 + dx^2 + dy^2 + dz^2$, is given by:

$$ds^2 = -cdt^2 + \left[1 + h_+\right] dx^2 + \left[1 - h_+\right] dy^2 + dz^2. \tag{2.15}$$

Calculating the round-trip time of a laser beam in the arms [81], we get:

$$\tau_x = \frac{2L}{c}\left[1 + \frac{h_0}{2}\frac{\sin\left(\omega_{GW}\frac{L}{c}\right)}{\omega_{GW}\frac{L}{c}} e^{i\omega_{GW}\frac{L}{c}}\right], \tag{2.16}$$

$$\tau_y = \frac{2L}{c}\left[1 - \frac{h_0}{2}\frac{\sin\left(\omega_{GW}\frac{L}{c}\right)}{\omega_{GW}\frac{L}{c}} e^{i\omega_{GW}\frac{L}{c}}\right]. \tag{2.17}$$

It should be noticed that one can transform one polarization state into the other through a rotation of 45°, thus if we considered cross-polarized plane wave we would obtain analogous results.
When the two beams return to the BS, they are not synchronized - so we can define:

$$\Delta\tau = \tau_x - \tau_y = \frac{2L}{c} h_0 \frac{\sin\left(\omega_{GW}\frac{L}{c}\right)}{\omega_{GW}\frac{L}{c}} e^{i\omega_{GW}\frac{L}{c}}, \tag{2.18}$$

which can be rewritten as a phase difference for a laser with wavelength λ_L:

$$\delta\Phi(t) = \frac{4\pi L}{\lambda_L} h \frac{\sin\left(\omega_{GW}\frac{L}{c}\right)}{\omega_{GW}\frac{L}{c}} e^{i\omega_{GW}\frac{L}{c}}. \tag{2.19}$$

Its modulus - normalized to the GW amplitude - is plotted in Figure 2.4, which highlights the presence of frequencies at which the ITF is insensitive. Indeed, if a GW travels through the detector having frequency greater than $\frac{c}{2L}$, the response of the ITF starts to decrease. From equation 2.19, we can see that $\delta\Phi$ is maximum when $\sin\left(\omega_{GW}\frac{L}{c}\right) = 1$ - so when $\left(\omega_{GW}\frac{L}{c}\right) = \frac{\pi}{2}$. Therefore, rearranging the terms we get $L = \frac{c}{4f}$ and so we see that, for a GW having a frequency of 100 Hz, the optimum length which maximizes the detection of its signal is $L \sim 750$ km. In section 2.4.2 we will discuss the implementation of optical cavities in the simple Michelson arms in order to maximize the **O**ptical **P**ath **L**ength (OPL) of the light inside the ITF.

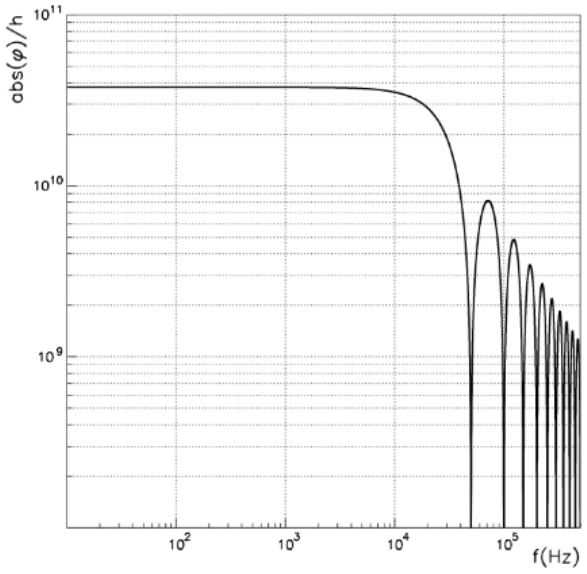

Figure 2.4: *Frequency response of an ITF with 3* km *arm long and a laser source of* $\lambda_L = 1064$ nm *plotted in logarithmic scale. For frequencies multiple of* $c/(2L) = 50$ kHz *the ITF is blind.*

2.3 Noise sources

When designing a ground-based ITF, all noise sources that can affect the sensitivity of the instrument must be taken into account in order to plan how to minimize them and to estimate the noise budget. Noises are divided into two categories [2]:

- **Fundamental noises**: Fluctuations due to the intrinsic properties of matter that cannot be removed;
- **Disturbances**: Signals of external origin with respect to the investigated system, that can be reduced by using ad hoc filters or specific shielding techniques.

The noise appears as a random signal, for which an analytical description as a function of time is not possible but it can be described in terms of statistical quantities. When we consider noise, what matter most it is not its absolute value but the one compared to the signal. The SNR is defined as the ratio of the mean squared value of the signal to the mean squared value of the noise:

$$SNR = \frac{\langle s^2(t) \rangle}{\langle n^2(t) \rangle}. \tag{2.20}$$

To determine the sensitivity of an instrument, the following quantities are used:

- **Noise Power Spectral Density (PSD)** $S_n(f)$ - in units of $\frac{1}{\text{Hz}}$ because h is dimensionless and the noises are compared to the signal - defined as:

$$\langle n^2(t) \rangle = \int_0^\infty S_n(f) df; \tag{2.21}$$

- **Amplitude Spectral Density (ASD)** is given by $\sqrt{S_n(f)}$ and it is in units of $\frac{1}{\sqrt{\text{Hz}}}$.

For each frequency range, different noise sources are dominant. The *sensitivity curve* of the ITF is obtained by quadratically adding the PSDs of all the noises. It represents the minimum intensity of the gravitational signal detectable by an ITF, i.e. it corresponds to SNR=1. In figure 2.5 the sensitivity curve for AdV+ Phase I detector is shown [80].

- In the frequency range $[10 \div 30]$ Hz the dominant noises are the technical noises;
- in the mid-frequency band $[30 \div 300]$ Hz the mirror thermal noise due to the **H**igh **R**eflectivity (HR) coating dominates;
- at the higher frequencies, the shot noise prevails.

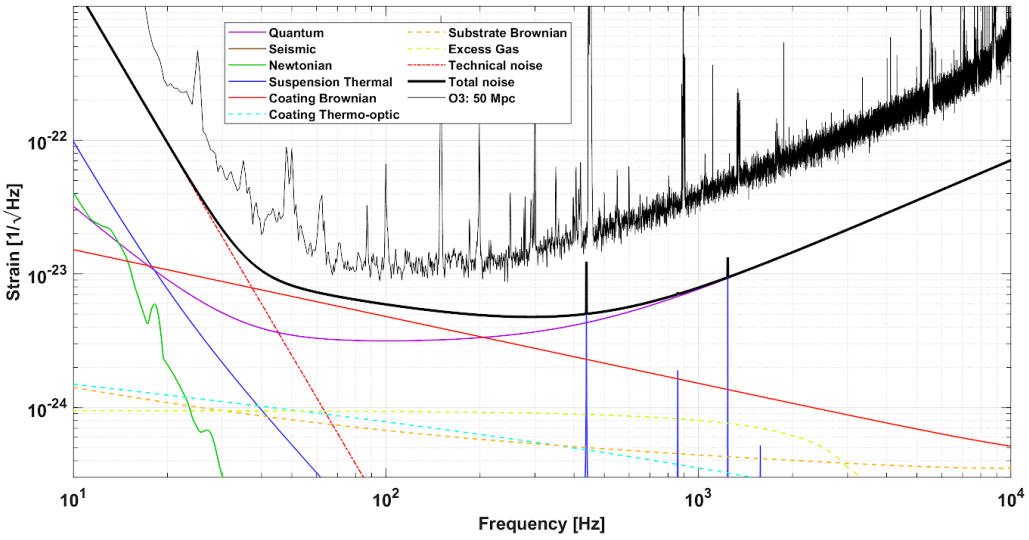

Figure 2.5: *Projected best sensitivity of AdV+ during Phase I. For comparison the sensitivity at the beginning of O3 is also shown [80].*

2.3.1 Quantum noise

The so-called *quantum limit* arises from two effects due to the corpuscular nature of light, the *shot noise* and the *radiation pressure noise* described in the following sections.

Shot noise

The effect of the quantum nature of photons is to introduce an uncertainty in measuring the output power, thus the GW signal. The optical power at the output of the ITF is related to the number of photons collected in a certain interval of time τ via $P_{out} = \frac{\langle N \rangle \hbar\omega}{\tau}$, where $\langle N \rangle$ is the mean number per counting interval, ω the pulsation of the light and $\hbar\omega$ the energy of a photon. The photons follow a Poissonian probability distribution $p(N) = \frac{\langle N \rangle^N e^{-N}}{N!}$ with standard deviation $\Delta N = \sqrt{\langle N \rangle}$. From the definitions of P_{out} and ΔN and remembering that $\omega = \frac{2\pi c}{\lambda}$, we can calculate the fractional uncertainty in the measurement of the number of photons as:

$$\frac{\Delta N}{\langle N \rangle} = \frac{1}{\sqrt{\langle N \rangle}} = \frac{\Delta P_{out}}{P_{out}} = \sqrt{\frac{2\pi\hbar c}{\tau P_{out} \lambda}}. \tag{2.22}$$

This kind of noise is the so-called *shot noise*. It can be demonstrated that the apparent change of distance between the input and the end mirror of the **F**abry-**P**erot (FP) arm cavity induced by the fluctuations of the number of detected photons is [2]:

$$\Delta L = \left|\frac{dL}{dP_{out}}\right| \Delta P_{out} = \left|\frac{dL}{dP_{out}}\right| \frac{\Delta N}{\langle N \rangle} P_{out}. \tag{2.23}$$

If the ITF working point is the half-fringe, i.e. $P_{out} = \frac{P_{in}}{2}$, then:

$$\Delta L_{shot} = \sqrt{\frac{\hbar c \lambda}{4\pi P_{in}}}. \tag{2.24}$$

The ASD associated to the shot noise is given by:

$$\tilde{h}_{shot} = \frac{\Delta \tilde{L}_{shot} \omega}{L} = \frac{1}{L}\sqrt{\frac{\hbar c \lambda}{2\pi P_{in}}}. \tag{2.25}$$

As can be seen from the equation 2.25, $\tilde{h}_{shot}$ scales as the inverse of the root of the input power. Therefore, increasing the P_{in}, $\tilde{h}_{shot}$ decreases.

Radiation pressure noise

The shot noise conjugate effect is the *radiation pressure noise*. It arises because the photon flux reaching the mirrors fluctuates - because of the Poissonian probability distribution - generating then a stochastic force $F_{rad} = \frac{P_{in}}{c}$ acting on the mirror and mimicking the effect of a GW passage. The fluctuation of this force in the frequency domain is:

$$\Delta \tilde{F}_{rad}(\omega) = \frac{\Delta \tilde{P}_{in}}{c} = \sqrt{\frac{2\pi \hbar P_{in} \tau}{\lambda}}, \tag{2.26}$$

where $\Delta P_{in} = \hbar \omega \Delta n = \sqrt{\frac{2\pi \hbar P_{in} \tau}{\lambda}}$. The corresponding fluctuations of the position of a mirror with mass M is:

$$\Delta \tilde{L}_{rad}(\omega) = \frac{\Delta \tilde{F}_{rad}}{M\omega^2} = \frac{1}{M\omega^2}\sqrt{\frac{2\pi \hbar P_{in} \tau}{c\lambda}}. \tag{2.27}$$

Therefore, the strain noise due to the radiation pressure is:

$$\tilde{h}_{rad}(\omega) = \frac{2\Delta \tilde{L}_{rad}(\omega)}{L} = \frac{1}{M\omega^2 L}\sqrt{\frac{8\pi \hbar P_{in} \tau}{c\lambda}}. \tag{2.28}$$

As we see from equation 2.28 the radiation pressure noise contribution can be reduced by decreasing the laser power, thus acting in the opposite direction with respect to the shot noise. Therefore, a good compromise in the choice of input power value is needed.

Quantum Limit

The optical read-out noise is the sum in quadrature of the two components of the quantum noise, i.e the two term expressed in equations 2.25 and 2.28, respectively:

$$\tilde{h}(\omega) = \sqrt{\tilde{h}^2_{shot} + \tilde{h}^2_{rad}}. \tag{2.29}$$

The minimum for $\tilde{h}$ is found with a power that puts the shot noise equal to radiation pressure noise and correspond to:

$$\tilde{h}_{SQL}(\omega) = \frac{1}{\pi\omega L}\sqrt{\frac{\hbar}{M}}, \tag{2.30}$$

which is also called the *standard quantum limit*. The radiation pressure does not represent the main contribution at low frequencies of the ITF sensitivity, where we have seen technical noises dominate. Instead, the dominant contribution at high frequencies is precisely the shot noise, which can be improved with higher input power.

2.3.2 Seismic noise

The vibrations induced by seismic, oceanic and human activities transmitted to the TMs through their mechanical supports are called *seismic noise*. The absence of an universal model for the seismic noise constitutes the main limit in quantifying the sensitivity of terrestrial detectors at low frequencies. Its intensity can change by orders of magnitude from place to place and, in the same place, from day to day. Therefore, it is necessary to reduce the contribution of the seismic noise to improve the ITF performance in the range $[10 \div 30]$ Hz. In section 2.6.1 we will see the solution adopted in Virgo for this purpose.

2.3.3 Newtonian noise

The *gravity gradient* or *Newtonian noise* is due to the local mass distribution fluctuations that couples with the TMs via gravitational interaction. For example, a seismic surface wave propagating close to the detector can induce an unwanted movement/oscillation of the TMs - see Figure 2.6. This noise limits the sensitivity of ground-based ITF below 20 Hz. A complex network of accelerometers has been developed to characterize this noise in order to subtract it from the sensitivity [82], since, due to the gravitational nature of the interaction, this noise source cannot be shielded by any means. However, the only way to attenuate this type of noise is by making ITFs in space in order to broaden the observation range to lower frequencies, in fact the scientific community of GWs is already focused on the design of **L**aser **I**nterferometer **S**pace **A**ntenna (LISA) the first GW detector in space - see section 2.9.

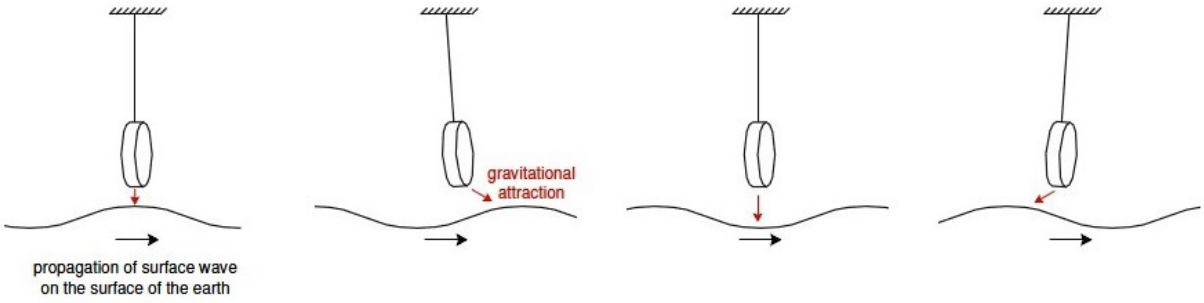

Figure 2.6: *Time-lapsed schematic illustrating the gravitational force on a suspended mass by the propagation of a surface wave through the ground.*

2.3.4 Thermal noise

A linear system left to evolve freely under conditions of thermodynamic equilibrium at a certain temperature T shows a fluctuation in the values of the descriptive variables. The existence of a relationship between the physical processes responsible for the dissipation and fluctuation is described by the Callen and Welton's *fluctuation-dissipation theorem* [83]. It states that in a thermodynamic linear[2] and dissipative[3] system at the equilibrium, the power spectrum of a variable which describes the system is:

$$S_x^2 = \frac{4k_B T}{\omega^2} Re\left\{Y\left(\omega\right)\right\}, \tag{2.31}$$

where T is the system temperature, ω is the observation frequency, k_B is the Boltzmann constant and $Y(\omega)$ is the *admittance* defined as the inverse of the impedance Z. The power spectrum given by equation 2.31 is called *thermal noise* which limits the ITF sensitivity in the frequency band $[10 \div 300]$ Hz, and in the detectors has two different components: *suspension thermal noise* and *mirror thermal noise* [2].

Suspension thermal noise

This noise is due to the vibrations of the wires used to suspend the TMs which results in a displacement noise as:

- *Pendulum thermal fluctuations*: a swinging motion in the suspension with a horizontal displacement of the TM;
- *Vertical thermal fluctuations*: a vertical motion of the suspensions. Due to the curvature of the Earth the vertical directions for the input and end mirrors are not the same. This results in an horizontal-vertical coupling of the angle $\theta = \frac{L}{2R_{Earth}} \sim 2 \cdot 10^{-4}$;
- *Violin modes*: Vibrations described in terms of the fluctuations of the normal modes of the wire. They are responsible for the set of lines in the sensitivity plot shown in Figure 2.5.

Mirror thermal noise

This noise is due to dissipation processes inside the TMs themselves. The effect can be distinguished in:

- *Brownian motion of the mirrors*: it is given by the Brownian motion of the mirror atoms caused by their kinetic energy at a certain temperature T;
- *Thermo-elastic fluctuations*: in a finite volume, the temperature fluctuates and this fluctuation generates displacement noise because of the expansion of the material. This happens both in the mirror bulk and in the coating;
- *Thermo-refractive fluctuations*: the temperature fluctuations induce also fluctuations in the refraction index of the mirrors.

[2]The dissipated power is quadratic in the amplitude of the stress.
[3]Subjected to a stress it absorbs energy irreversibly.

2.4 Strategies to improve the sensitivity

In section 2.3, we have seen the main sources of noise present in an ITF. We focus now on describing the techniques adopted to maximize the response of the detector to the GW passage and to minimize all noises affecting the ITF sensitivity.

2.4.1 Dark fringe working point and frontal modulation technique

The passage of a GW in an ITF produces a phase shift $\delta\phi_{GW}$. We now describe how to extract it from the detector output. The output power trend as a function of phase ϕ is represented in Figure 2.7.

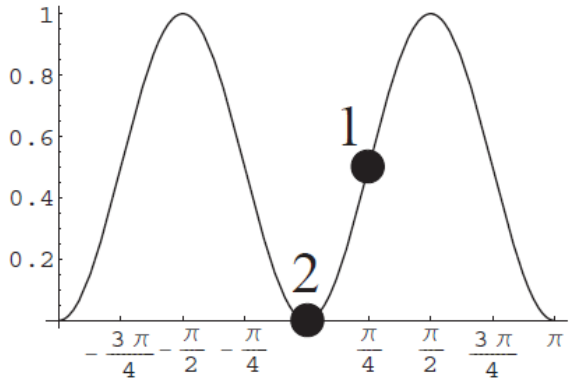

Figure 2.7: *Behaviour of the output power of the ITF in function of phase ϕ. The points denoted by 1 and 2 are the two possible working points. The point 1 corresponds to a phase of $\phi = \frac{\pi}{4}$ and it is the half dark fringe. The point 2 is the dark fringe point and its phase is zero.*

One might think that the best working point is at $\phi = \frac{\pi}{4}$ - where $\frac{\partial P}{\partial \phi}$ is maximum - and so that the sensitivity of a small displacement in ϕ due to the passage of a GW is the highest. But at this working point, we are very sensitive to fluctuations in the input power P_{in} of the laser as well [2]. Therefore, by measuring the output power P_{out} at this working point, it is impossible to determine whether the variation obtained is due to a variation induced by the passage of a GW $\delta\phi_{GW}$ or by the fluctuation of the laser power. When looking for a very small effects, a good experimental strategy is to build a so-called *null instrument*, i.e. if the signal is absent, a zero output is recorded. This method allows the detector to be insensitive to calibration uncertainties that otherwise could be confused with the small signal we are looking for. Therefore, the best working point is the so-called *dark fringe*. With no GW signal the output is zero and we are insensitive to the laser power fluctuations. But the variation of the output power induced by the GW is $\Delta P = \mathcal{O}(h^2)$ and a quadratic effect is invisible to our detector since it would be of the order of 10^{-42}. To get out of this problem the idea is to apply phase modulation to the input laser light - the so-called *Frontal Modulation technique* [2] - using an **E**lectro **O**ptical **M**odulator (EOM) placed at the input of the ITF. The modulator is a crystal with a variable refractive index that introduces a phase shift on the beam proportional to the voltage applied to it. The EM field of the laser is $\psi(t) = \psi_{in} e^{i\omega_L t}$, with ω_L the laser frequency and ψ_{in} the input beam amplitude. By applying a voltage $V = V_0 \sin(\Omega t)$ - Ω

is the modulation frequency - to the EOM, the EM field after becomes:

$$\psi'(t) = \psi_{in} e^{i(\omega_L t + m\sin(\Omega t))}. \tag{2.32}$$

The equation 2.32 can be expanded as a sum of Bessel functions $J_n(m)$:

$$\psi'(t) = \psi_{in} \sum_{n=-\infty}^{+\infty} J_n(m) e^{i(\omega_L + n\Omega)t}, \tag{2.33}$$

where m is the modulation depth and n is an integer. For $m \ll 1$, only the first terms of the expansion are non negligible:

$$\psi'(t) \approx \psi_{in} \left[J_0(m) e^{i\omega_L t} + J_1(m) e^{i(\omega_L + \Omega)t} + J_{-1}(m) e^{i(\omega_L - \Omega)t} \right], \tag{2.34}$$

where the first term J_0 represents the **Ca**rrier (CA) and the other two correspond to the first upper and lower **S**ide**B**and (SB) with frequencies $\omega_\pm = \omega_L \pm \Omega$ and wave numbers $k_\pm = \frac{\omega_\pm}{c} = \left(\frac{1}{\lambda_L} \pm \frac{1}{\lambda_{mod}} \right)$, where λ_L is the laser wavelength - see Figure 2.8.

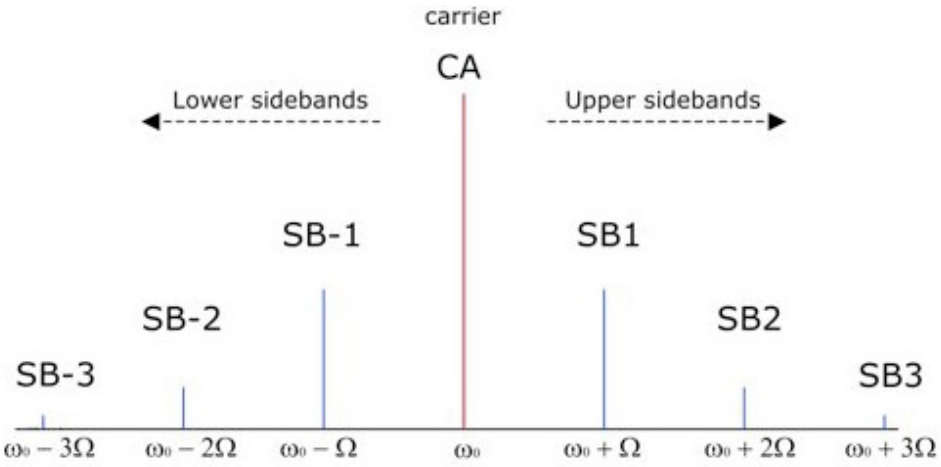

Figure 2.8: *Modulation of the incoming laser beam phase. The CA frequency ω_0 and the first few SBs $\omega_0 \pm n\Omega$ are shown.*

If the two arms length are exactly equal, both the CA and the SBs destructively interfere, resulting in an output EM field equal to zero. Instead, we can set a difference in the arms length $\Delta L = n\lambda_L$ - in this way, the CA is on the dark fringe, while the SBs are not [2]. ΔL is the so-called *Schnupp asymmetry*. So, the output power P_{out} contains the contributions of the beating between the CA and the SBs - this term is linear in h and oscillates with a frequency Ω. Thanks to working in the dark fringe, the translation to a higher frequency makes the signal insensitive to the laser power fluctuations and with the modulation technique, by introducing a small asymmetry between the detector arms, the GW signal can be extracted from the component demodulated at Ω which is linear in h. The use of the SBs is called *heterodyne readout*. However, the CA is cleaner than the radio-frequency SBs because it is filtered by both the **P**ower **R**ecycling **C**avity (PRC) - see section 2.4.3 - and the arms. This coupled-cavity pole is only a few Hertzs. The radio-frequency SBs originate from some type of imperfect radio-frequency oscillator, which results in both amplitude and phase noise contaminating the radio-frequency readout signal [84, 85]. Thus, the heterodyne readout has been replaced by the detection scheme called *DC readout*, in which a small differential detuning is introduced in the ITF and then a small amount of CA light at the output is exploited as a local oscillator field.

2.4.2 Fabry-Perot cavities

As seen in the equation 2.19, the sensitivity of a GW ITF improves by increasing its arms length. However, because it is unfeasible to build arms hundreds-of-km long, *Fabry-Perot* cavities are added in the Michelson ITF arms to increase the light optical path. This cavity consists of two mirrors placed at distance L between them and with reflectivity r_1 and r_2, respectively. When the resonance condition[4] is satisfied, the EM field resonates, traveling for many round trip before exiting from the cavity and constructive interference of all these rays occurs. In this way, the effective length traveled by the laser radiation is much bigger than the one of the arms. The increase of the OPL due to the resonant cavity is related to a parameter called *Finesse* F and defined as [2]:

$$F = \frac{\pi\sqrt{r_1 r_2}}{r_1 r_2}. \tag{2.35}$$

Thus, the effective path length L_{eff} travelled by beam inside a FP cavity of length L is:

$$L_{eff} = L\frac{2F}{\pi}, \tag{2.36}$$

where $\frac{2F}{\pi}$ is the *optical gain*. The average time taken by a photon to exit the cavity is the *storage time* τ_s [86]:

$$\tau_s = \frac{2L}{c}\frac{1}{1-r_1^2} \sim F\frac{L}{c\pi}, \tag{2.37}$$

assuming $r_2 = 1$ since the beam impinges on the second mirror i.e. the **E**nd **T**est **M**ass (ETM), which has a very high reflectivity. In the presence of a GW, the effective path length travelled by the beam is:

$$L_{eff}^{GW} = L\frac{4F}{\pi}\frac{1}{\sqrt{1+\left(\frac{\nu_{GW}}{\nu_c}\right)^2}}, \tag{2.38}$$

where ν_{GW} is the frequency of incident gravitational wave and $\nu_c = \frac{1}{2\pi\tau_s} = \frac{c}{2FL}$ is the cutoff frequency of the cavity (or cavity pole). Now, with the FP cavity the phase shift becomes:

$$\Delta\phi_{FP} = h_0 L\frac{2\pi}{\lambda_L}\frac{4F}{\pi}\frac{1}{\sqrt{1+\left(\frac{\nu_{GW}}{\nu_c}\right)^2}}. \tag{2.39}$$

Therefore, the detector with FP cavities in the arms is more sensitive to GWs with respect to a simple Michelson ITF by a factor equals to optical gain:

$$\frac{\Delta\phi_{FP}}{\Delta\phi_M} = \frac{2F}{\pi}. \tag{2.40}$$

2.4.3 Dual-recycled interferometer

As we have seen, the best working point for the ITF is the dark fringe condition - in which very low power impinges on the detection PD, while most of it is reflected towards the laser. In order to not lose this reflected power, another mirror - the **P**ower **R**ecycling

[4] The distance between the two mirrors is equal to a multiple of half wavelength.

Mirror (PRM) - has been added between the laser and the BS forming a new cavity called PRC. Its optical gain is:

$$G_{PR} = \left(\frac{t_{PR}}{1 - r_{PR} \cdot r_{ITF}} \right)^2 , \tag{2.41}$$

where t_{PR} is the transmissivity of the PRM, r_{PR} its reflectivity, and r_{ITF} is the reflectivity of the whole ITF. In this way, the power circulating increases by a factor G_{PR} and, as a consequence, the sensitivity by a factor $\sqrt{G_{PR}}$ - see equation 2.25. This configuration is the so-called *Power-Recycled*.
To shape the detector's frequency response in order to increase the sensitivity in a specific frequency region, another cavity has been added - the **S**ignal **R**ecycling **C**avity (SRC) - by placing another mirror - the **S**ignal **R**ecycling **M**irror (SRM) - between the BS and the output port, as shown in Figure 2.9. This ITF configuration is called *Dual-Recycled*. Adjusting the SRM position on a microscopic scale allows to change the frequency of the best sensitivity, optimizing then the ITF for different astrophysical sources [87].

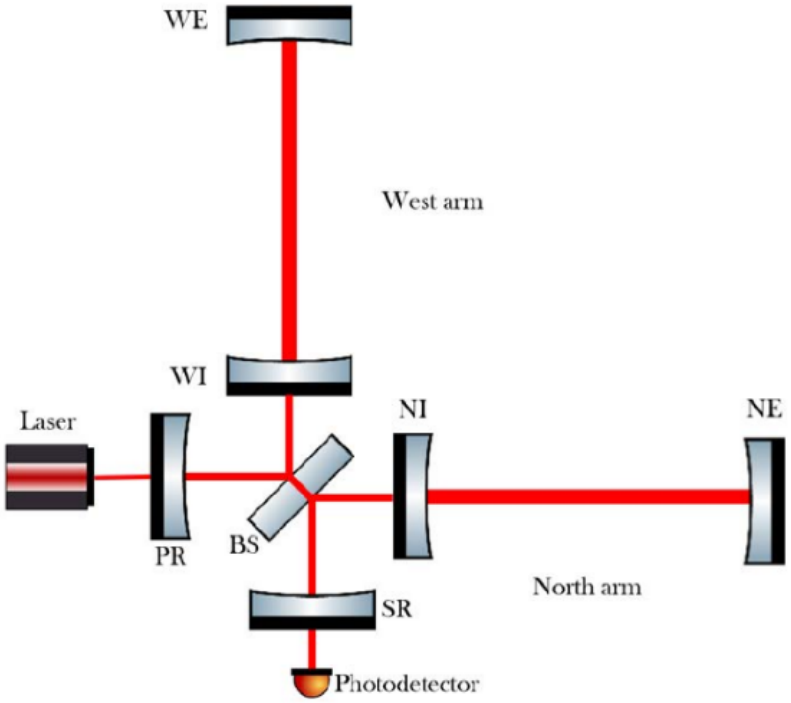

Figure 2.9: *Layout of the dual-recycled ITF with FP cavities in the arms, PRM and SRM: PR indicates the power recycling mirror, SR the signal recycling mirror and input mirror and end mirror form the FP optical cavities in each arm.*

2.5 Interferometer's working point

The working point of a dual-recycled FP Michelson ITF can be summarized by the following statements:

1. the PRC, SRC and FP optical cavities must be in resonance;
2. the output of the ITF must be in the destructive interference - i.e., dark fringe condition.

The achievement of this configuration - from the uncontrolled mirrors to the final working point - takes place through a complex procedure called *lock acquisition* [88] which uses a digital feedback control system and several PDs - see section 2.6.3 for more details. In this way, it is possible to act on the longitudinal and angular positions of the mirrors. To check the ITF status, five longitudinal **D**egree **o**f **F**reedom (DoF) are defined and controlled - see Figure 2.10 - with dedicated picometer precision signals:

- **MICH**: the length difference between the two input mirrors of the FP cavities from the BS $l_X - l_Y$. This DoF defines the dark fringe condition;
- **DARM**: the differential length of the FP arms $\frac{L_X - L_Y}{2}$. This is the most important DoF, since it contains the GW signal;
- **CARM**: the average (common) length of the FP arms $\frac{L_X + L_Y}{2}$. It is used for stabilizing the frequency of the main laser and the arms length;
- **PRCL** and **SRCL**: the length of the PRC and SRC $l_p + \frac{l_X + l_Y}{2}$ and $l_s + \frac{l_X + l_Y}{2}$, respectively, where l_p is the distance between the PRM and the BS and l_s is the distance between the SRM and the BS. They are responsible for improving the optical response of the ITF.

The FP and power-recycling cavities need to be kept on resonance to maximize the optical path travelled by the light inside the ITF.

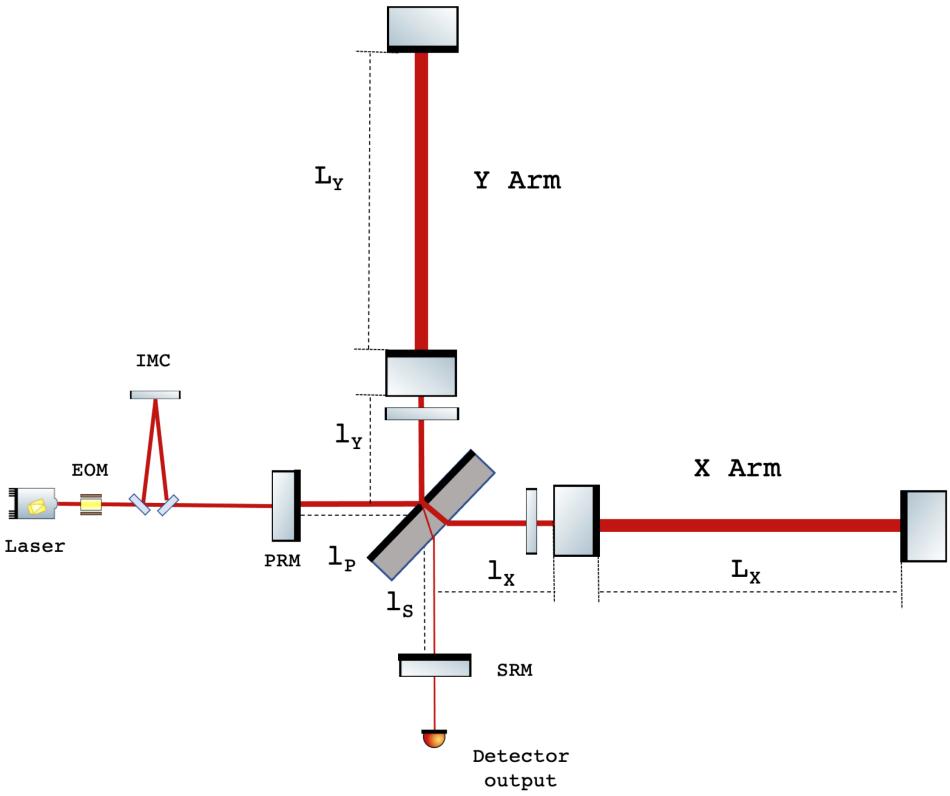

Figure 2.10: *Dual-recycled FP Michelson ITF configuration: the thickness of the red lines indicating the beam path, is proportional to the amount of power circulating into the detector.*

The longitudinal DoFs are controlled by using the **P**ound-**D**rever-**H**all (PDH) technique [89, 90] - the output of different PDs located in strategical parts of the detector are used to extract the error signals for each DoF by measuring the beating between the CA and the radio-frequency SBs. The CA resonates in all the optical cavities but it is anti-resonant in the SRC and the SBs are anti-resonant in the FP cavities and resonant in the recycling cavities. Once the longitudinal DoFs controls are engaged, different angular controls act to overlap the input laser beam to the optical cavity axis. At the first stage, the angular motions in pitch and yaw of each mirror are controlled using optical lever signals provided by an auxiliary probe beam. This type of control is defined local since it is independent from the main laser beam pointing and from the mutual position of the optics. During the last steps of the lock acquisition sequence, such control is replaced with an angular global control scheme reaching the nano-radian accuracy. This control is based on error signals provided by quadrant PDs installed in key places of the laser beam path, encoding tilt and shift information about the cavity angular DoFs. Once the dark fringe is achieved, the effects induced by the radiation pressure arise in the FP arm cavities inducing an optical spring between the cavity mirrors [88]. Thus, in this condition, a basis of Common and Differential DoFs are introduced to describe the global misalignment of the optical cavities, that is schematised in Figure 2.11. The error signals associated with these DoFs satisfy the required accuracy [88] for the optics' orientation control needed to ensure a robust and reliable working point to acquire scientific data.

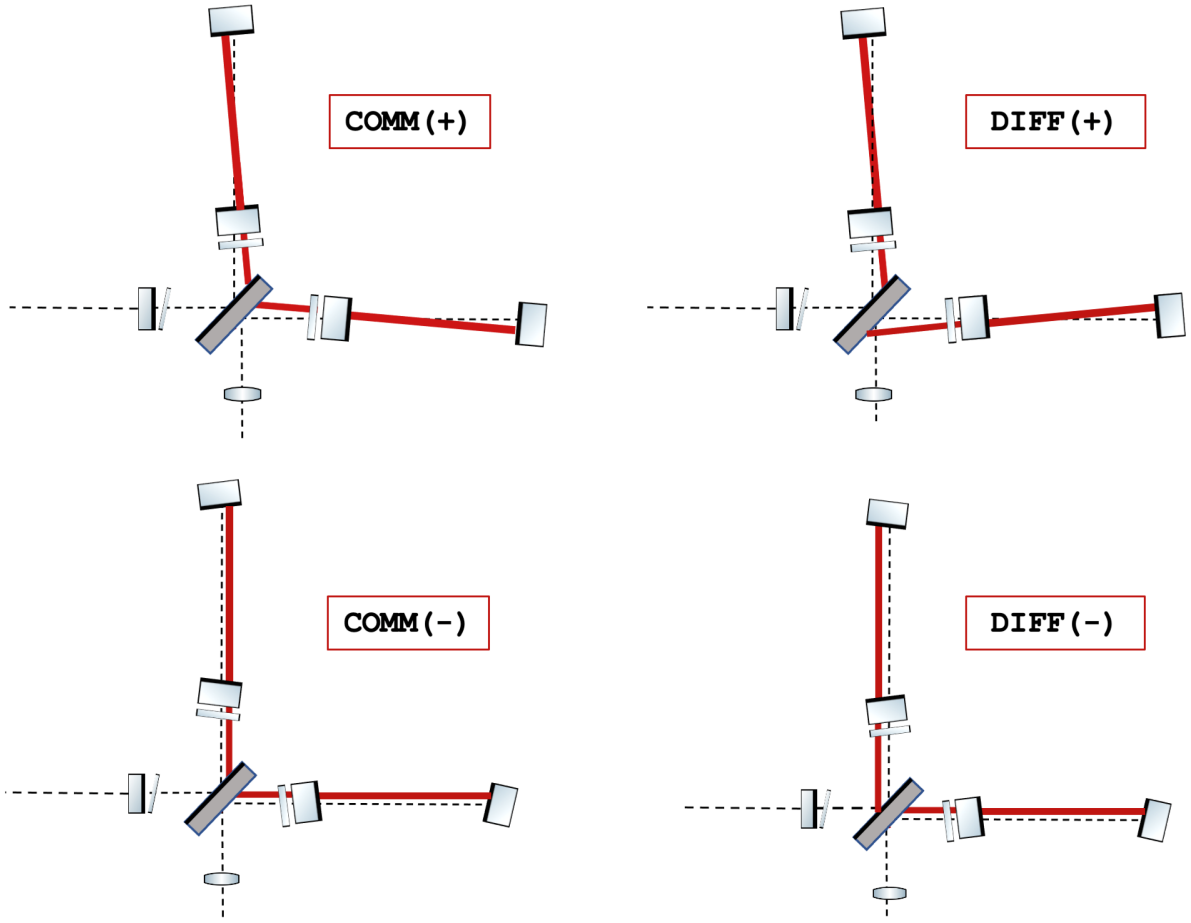

Figure 2.11: *Schematic view of the angular DoFs used to describe the ITF alignment once reached the dark fringe working point.*

- **COMM(+)**: common tilt of the arm cavities, i.e. the two beams recombine in the same spot on the BS mirror;
- **DIFF(+)**: differential tilt of the arm cavities, i.e. the two beams recombine on the two opposite sides of the BS mirror;
- **COMM(-)**: common shift of the arm cavities, i.e. the effect is two beams recombining in the same spot on the BS mirror;
- **DIFF(-)**: differential shift of the arm cavities, i.e. the effect is two beams recombining on the two opposite sides of the BS mirror.

The **I**nterferometer **S**ensing and **C**ontrol (ISC) subsystem is responsible for the achievement and the maintaining of the correct working point of the detector through the lock acquisition procedure, described in [91].

2.6 Optical configuration

The two FP cavities are 3-km long each and labelled as North and West according to their geographical orientation. In the arms, the input and the end mirrors are called **N**orth **I**nput (NI)/**W**est **I**nput (WI) and **N**orth **E**nd (NE)/**W**est **E**nd (WE), respectively. The design mirror's **R**adius **o**f **C**urvature (RoC) is 1420 m and 1683 m for the input and end mirrors, respectively, and they have been designed to maximize the beam spot size on the cavity mirrors in order to reduce the coating thermal noise [80]. With this configuration, the cavity waist is near its center and the beam radius is about 49 mm on the **I**nput **T**est **M**ass (ITM) and 58 mm on ETM [80]. The input mirrors have a design reflectivity of 98.6%, while the end ones of 99.9995%. The Finesse F value is 450 and the pole frequency is at 55 Hz. The distances between the BS and the two input mirrors differ by the Schnupp asymmetry, equal to 0.23 m.
The SRM has a design RoC of 1430 m and a transmissivity of 40%, while PRM reflectivity is 95% resulting in a design finesse of the PRC of $\sim$ 48 [80]. The PRM RoC is 1430 m and the length of the cavity is equal to 11.952 m, pushing the PRC stability condition very close to the instability limit [88]. The same situation occurs for the SRC. The decision to have marginally stable cavities was imposed by infrastructure limitations. The marginally stable geometry of the recycling cavities makes them extremely sensitive to optical aberrations, that degrade the quality of the error signals making the ITF working point not stable. Therefore, the implementation of a system keeping the optical aberrations under control is crucial to run the ITF. In the chapter 3 we will focus on the **T**hermal **C**ompensation **S**ystem (TCS), being the cornerstone of this thesis.
The AdV+ Phase I optical layout is shown in Figure 2.12 and in the following section a brief description of the most important subsystems that compose the GW detector will be provided.

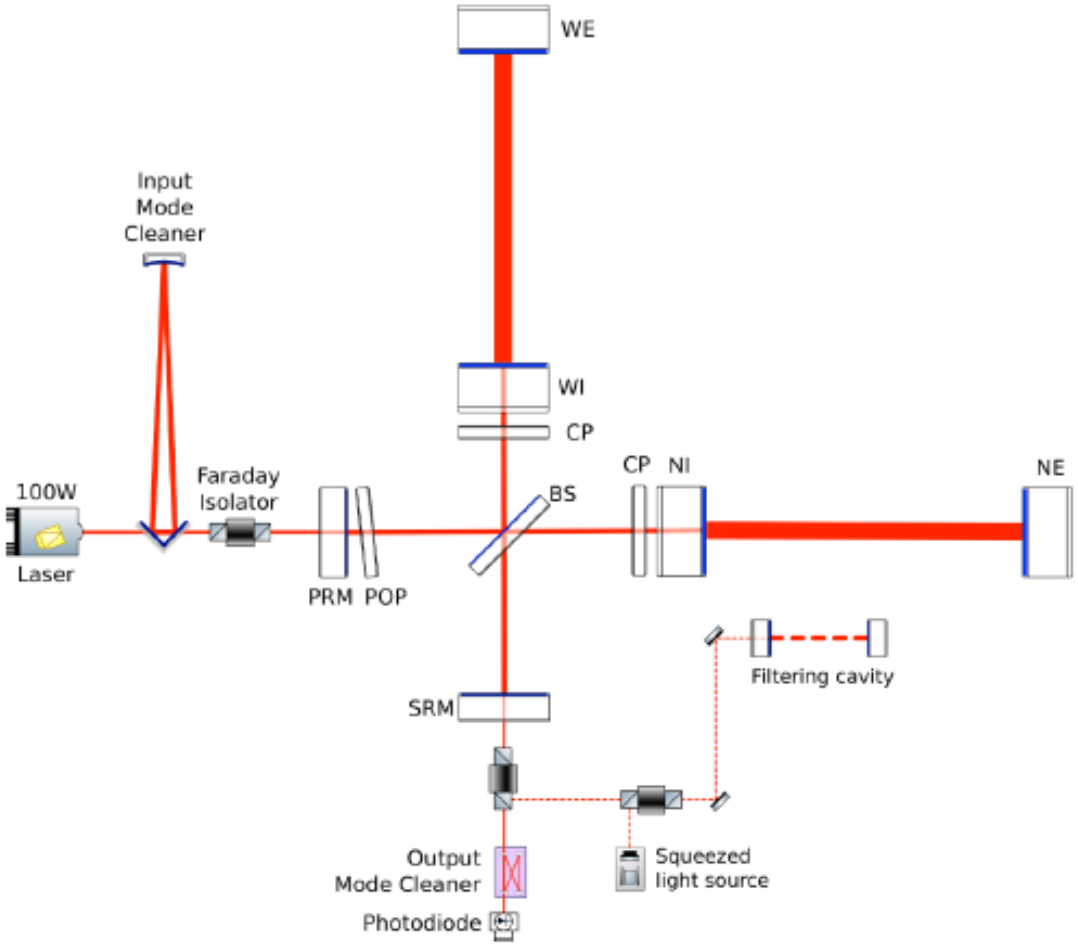

Figure 2.12: *AdV+ Phase I optical layout.*

2.6.1 Mirrors and suspensions

The core optics of AdV+ have been designed to minimize the losses that increase the mirror thermal noise and the power absorption that causes the heating of the mirror itself. They are made of a new type of high-purity fused silica: Suprasil 3002 for the input mirrors, Suprasil 312 for the end mirrors and Suprasil 3001 for the BS. The choice of this material is due to the need for a very low bulk absorption 0.2 $\frac{\text{ppm}}{\text{cm}}$, and its transparency to 1064 nm which is the ITF main laser wavelength [80]. To avoid the scattering of the fundamental light mode into the higher order ones, the surface of the optic is polished to a **R**oot **M**ean **S**quare (RMS) level better than 0.5 nm. Moreover, in order to reduce the optical losses in the cavities, a HR coating consisting of alternating layers of silicon dioxide SiO_2 and tantala pentoxide Ta_2O_5 is deposited on the HR surface of the mirror pointed towards the FP cavity. On the other side of the mirror, an **A**nti-**R**eflective (AR) coating is deposited to minimize the power losses at the cavity entrance. The arm cavity mirrors have a diameter of 35 cm and a thickness of 20 cm. The BS has a diameter of 55 cm and a thickness of 6.5 cm. In order to reduce the seismic noise, a seismic isolation system - the *Superattenuator*, shown in Figure 2.13 - has been developed. It is composed of three basic components: the *inverted pendulum*, the *chain of seismic filters* and the *mirror suspension*. The mirror is placed in the lower part of the superattenuator. The suspension wires are made of fused silica - the same material of the mirrors. Because

fused silica has small loss angles and the monolithic suspension eliminates the friction in the contact points [87], it allows to reduce the thermal noise of the pendulum.

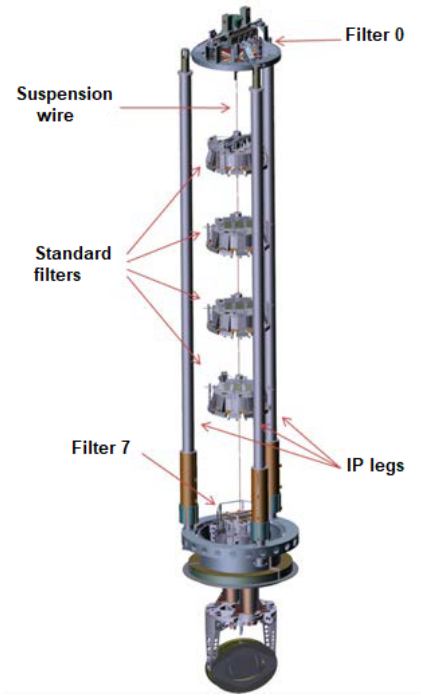

Figure 2.13: *View of the mechanical structure of the AdV+ Superattenuator.*

2.6.2 Injection

The **Inj**ection (INJ) subsystem - which is schematically shown in Figure 2.14 - takes care of adapting and conditioning the laser beam - emitted by a **Nd:YAG** solid state laser at $\lambda = 1064$ nm - to the ITF.

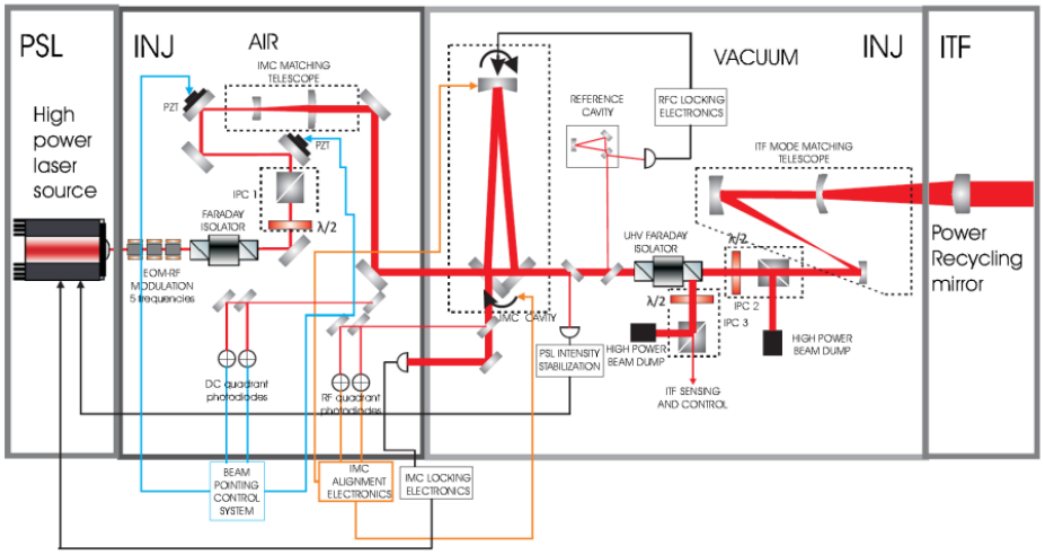

Figure 2.14: *Optical scheme of the INJ subsystem, directly connected to the main laser source [92].*

The system is composed of a **P**re-**S**tabilized **L**aser (PSL) stage and of two suspended optical benches - one in air and the other one in vacuum. The laser system is based on a high-power oscillator configuration, i.e. the master laser emitting 500 mW is amplified up to 100 W by two solid state amplifiers. The power-amplified laser beam propagates through a bow-tie pre-mode cleaner cavity 308-mm long, which cleans the spatial profile and reduces the jitter of the laser beam [93]. The beam impinges then on the EOM, that generates the SBs used to keep the ITF in the right working point. For this purpose, five different modulation frequencies are used: 6 MHz, 8 MHz, 22 MHz and 56 MHz [88]. After the EOM, the beam propagates through the **I**nput **M**ode **C**leaner (IMC) - a triangular cavity 144-m long with a very large finesse of $F \sim 1200$ - that suppress the amplitude of the higher order modes and lets only the fundamental mode to be transmitted. The IMC input and output mirrors are mounted on the bench, while the end mirror - at the top of the triangle - is connected to the others via a vacuum pipe. In this part of the INJ there is the **R**eference **F**requency **C**avity (RFC), a triangular cavity 30-cm long for the pre-stabilization of the laser frequency, with a $F \sim 900$. Then, the beam passes through the *Faraday Isolator* that prevents the beam reflected back from the ITF to reach the laser. Then the beam propagates through the **M**ode-**M**atching **T**elescope (MMT) to tune the optical parameters of the input beam before entering in the ITF. The MMT is composed by two off-axis parabolic mirrors and a diverging lens used in combination with the AR surface of the PRM to match the beam to the ITF at the best of 99%. The power available to the detector after the propagation through the INJ system is more than 65 W [93].

2.6.3 Detection

The error signals are extracted from different PDs and quadrant PDs positioned on the various detection benches that fall under the responsibility of the **Det**ection (DET) sub-system. The PDs detect all signals used to control the ITF and to keep it in the optimum working point. For example, the quadrant PDs are used to control the angular degrees of freedom of the mirrors. At the detector output, on the DET benches, a *bow-tie* cavity - the **O**utput **M**ode **C**leaner (OMC) - is placed in series to select the fundamental mode and remove all the higher order ones and also to filter out the SBs. A PD labelled **B1p** is installed before the OMC. The beam filtered out by OMC encodes only the valuable information about the GW signal and it is measured by the a PD labelled **B1** installed after the OMC. The PDs are placed on dedicated suspended optical benches. By looking at Figure 2.15, it is possible to have a clear view of the whole read-out scheme which is fundamental to extract both the GW strain and the error signals needed to control the ITF.

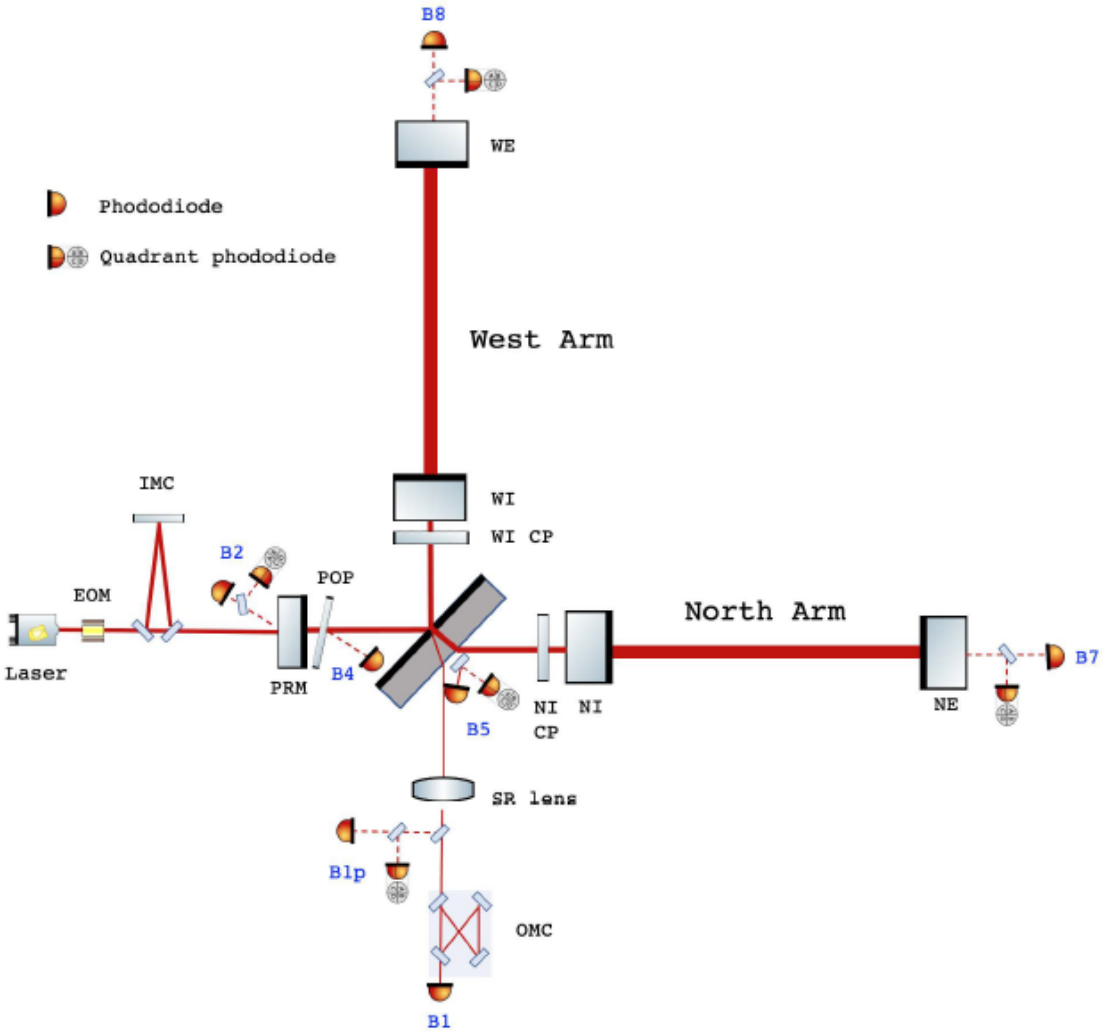

Figure 2.15: *Scheme of the PDs used in AdV+.* ***B2*** *monitors the power reflected by the PRC, while* ***B4*** *the power inside.* ***B5*** *measures the power reflected by the North FP arm, while* ***B7*** *and* ***B8*** *the power transmitted from the North and West FP arm, respectively.*

2.6.4 Vacuum system

The gas density fluctuations cause a variation of the air refractive index, resulting in a subsequent fluctuation of the beam intensity and in a variation in the OPL of the light. To eliminate these problems, a vacuum system consisting of towers and pipes was implemented - see Figure 2.16. With a volume of 7000 m^3 AdV+ pipes are the largest ultra-high vacuum system in Europe. In Advanced Virgo the vacuum level has been improved by a factor of about 100 with respect to Virgo to be compliant with the sensitivity. This improvement is achieved thanks to the installation of four large cryotraps - one at each tube extremity - to stop the migration of water molecules from the towers hosting the mirrors to the tubes.

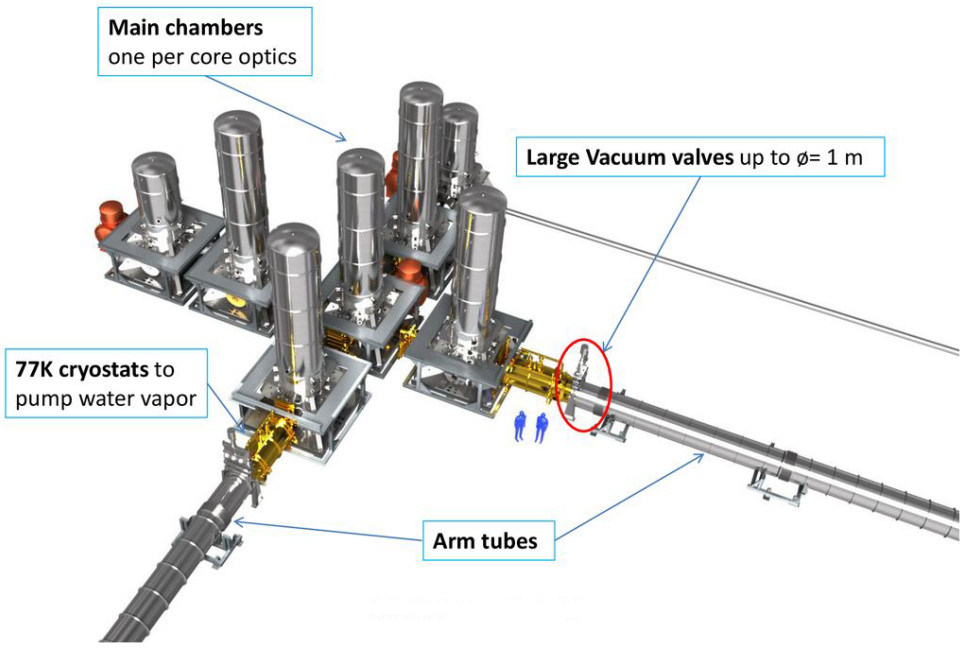

Figure 2.16: *Advanced Virgo vacuum system scheme.*

2.6.5 Squeezed states of light

In order to get an intuitive understanding of quantum noise described in section 2.3.1, we can use a rather simple graphical tool often referred to as the *quadrature picture* or *the ball on a stick picture* [94]. In general we can describe an electric field $\vec{E}$ at a position $\vec{r}$ and at the time t by:

$$\vec{E}(\vec{r},t) = E_0 \left[a(\vec{r})e^{-i\omega t} - a^*(\vec{r})e^{+i\omega t}\right] \vec{p}(\vec{r},t), \tag{2.42}$$

where a is the complex amplitude of an EM field, ω its angular frequency and $\vec{p}$ the polarization. We can introduce the following two new properties:

$$X_1(\vec{r}) = a^*(\vec{r}) + a(\vec{r}) \; and \; X_2(\vec{r}) = i\left[a^*(\vec{r}) - a(\vec{r})\right]. \tag{2.43}$$

X_1 and X_2 are usually referred to as the *amplitude* and *phase quadrature*, respectively. Using the quadrature representation we can rewrite equation 2.42 to express the EM field in terms of X_1 and X_2:

$$\vec{E}(\vec{r},t) = E_0 \left[X_1 cos(\omega t) - X_2 sen(\omega t)\right] \vec{p}(\vec{r},t). \tag{2.44}$$

In close analogy to equation 2.43 we can introduce the so-called *quadrature operators* which are the foundation of a description of light fields in the realm of quantum mechanics as:

$$\widehat{X}_1(\vec{r}) = \widehat{a}^\dagger(\vec{r}) + \widehat{a}(\vec{r}) \; and \; \widehat{X}_2(\vec{r}) = i\left[\widehat{a}^\dagger(\vec{r}) - \widehat{a}(\vec{r})\right], \tag{2.45}$$

where $\widehat{X}_1(\vec{r})$ and $\widehat{X}_2(\vec{r})$ are the *amplitude quadrature operator* and *phase quadrature operator*, respectively. To display the quadrature operators, we can use the ball on the stick picture - see Figure 2.17.

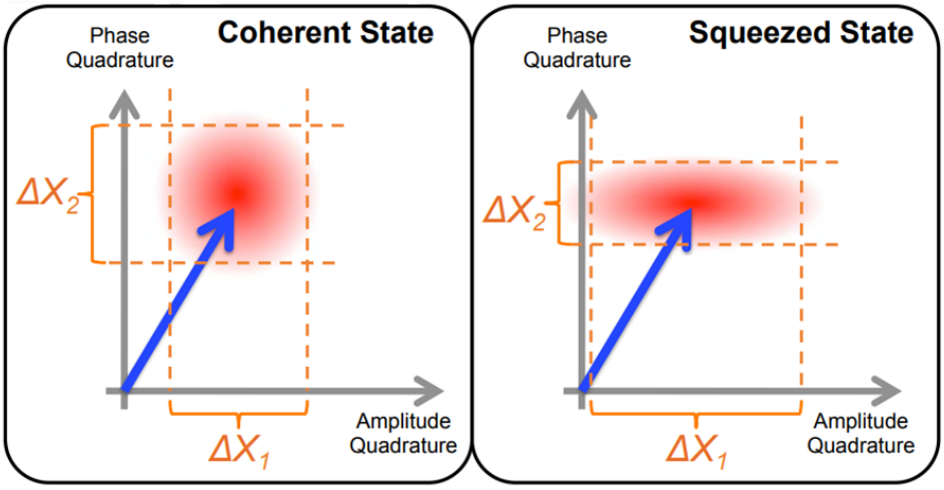

Figure 2.17: *Graphical representation in the quadrature picture of a coherent state (left) and a squeezed one (right).*

The left-hand side of Figure 2.17 shows an example of a coherent light field. A coherent state has the product of the uncertainties - given by Heisenberg's principle - which is minimal and the uncertainties in the two quadratures are equal to each other. The light field consists of a huge number of photons and we continuously perform measurements over a finite duration to determine the *light states*. Each measurement is represented by a single dot in the $\widehat{X}_1$, $\widehat{X}_2$ plane, and the solid arrow points at the center of the ball which is the highest probability to encounter the field in this state if a measurement is carried out. The ball indicates the probability distribution of the light state. So, the coherent part of a light field is represented by the arrow and the noise of the field is represented by the ball. The quantum nature of light forbids us to reduce the area of the ball below a certain limit, this limit is a consequence of the *Heisenberg Uncertainty Principle*. The uncertainty principle dictates the minimal area, but we have the freedom to manipulate its shape. The technique used is the *squeezing* [95]. The right-hand side of Figure 2.17 shows a light field squeezed in phase quadrature, i.e. the uncertainty of the light state is reduced in one quadrature - the phase quadrature in this case - while one has to pay the price of a proportionally increased uncertainty in the orthogonal quadrature - the amplitude quadrature in this case. Squeezed states of light can be used to improve the quantum noise that limits sensitivity of GW detectors [94]. In AdV+ the squeezing technique has been improved with respect to O3 thanks to the addition of the **F**ilter **C**avity (FC) that allows to increase sensitivity not only at high frequencies by beating the shot noise, but also at low frequencies by beating the radiation pressure. This is the so-called frequency-dependent squeezing [96].

2.7 The future of Advanced Virgo +

As previously described, AdV+ is an upgrade of Advanced Virgo to be realized in two phases named Phase I and Phase II, respectively. The installation of AdV+ Phase I upgrades took place between the observing runs O3 and O4 with the main goal to reduce the ITF sensing noise by implementing the following improvements:

- the signal recycling technique;

- increase of the laser power injected into the ITF;
- injection of frequency-dependent squeezed vacuum states.

The installation of AdV+ Phase II will take place between the observing runs O4 and O5 and it will be focused on the reduction of the mirror thermal noise. To do so, the beam on the end mirrors will be enlarged to about 20 cm in diameter while keeping the same size in the central area of the ITF. Thus, larger optics will have to be used for the end mirrors, which will be 55 cm in diameter and 100 kg in weight [80]. The change in the beam divergence will require to replace also the two cavity input mirrors, the PRM and the SRM. The AdV+ Phase II optical layout and the sensitivity of project are shown in Figure 2.18.

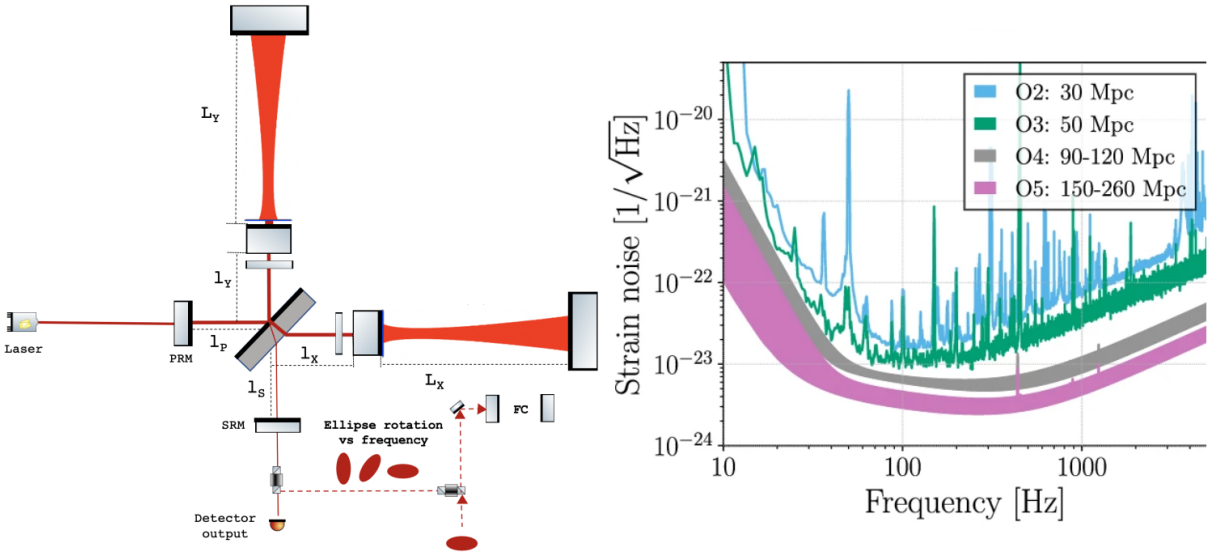

Figure 2.18: *On the left: AdV+ Phase II optical layout. On the right: The purple band shows the range of sensitivities achievable AdV+ Phase II i.e. O5. For comparison the sensitivity of Advanced Virgo in O2 and O3 and the design sensitivity of AdV+ in O4 are also shown.*

Looking at the future plans of the GW community, there will be a decade of potential observations to be filled in between the end of O5 and the beginning of third generation detectors data taking. The Virgo Collaboration intends to keep on improving the sensitivity of its instrument until it reaches the limits set by the site infrastructure. Virgo$_{nEXT}$ is a post-O5 upgrade project with the target of getting an ultimate sensitivity in terms of BNS range of about 500 Mpc, gaining an additional factor of two in sensitivity with respect to AdV+ Phase II. The following improvements in the optical configuration are under consideration [97]:

- stable recycling cavity;
- target input power of 250 W, resulting in ∼1.5 MW circulating in the cavities;
- larger ITM in order to reduce quantum noise in the range $[10 \div 40]$ Hz and to mitigate the parametric instabilities.

The Virgo$_{nEXT}$ optical layout and the sensitivity of project are shown in Figure 2.19.

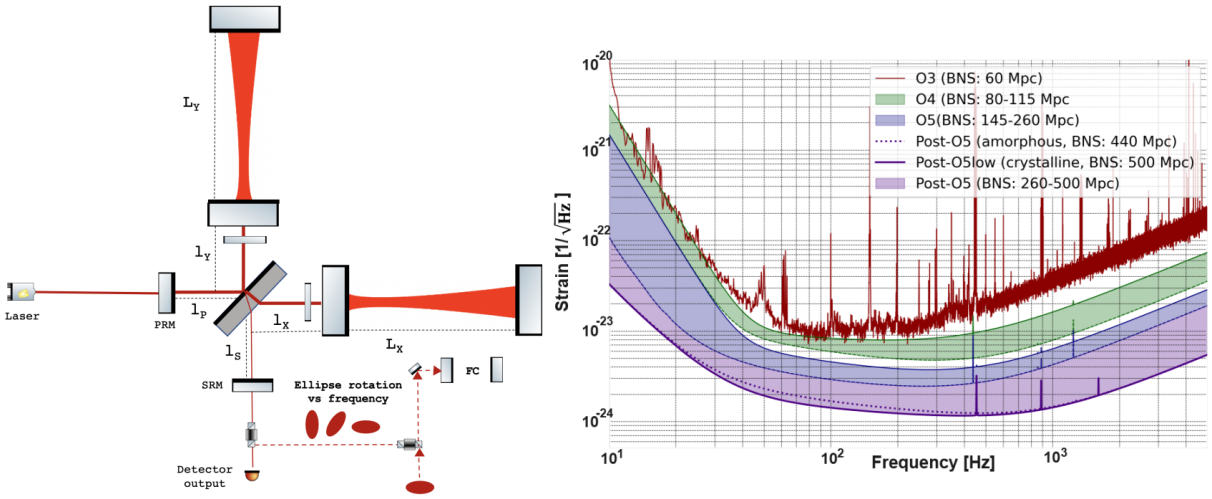

Figure 2.19: *On the left: Virgo$_{nEXT}$ optical layout. On the right: The purple band shows the range of sensitivities achievable Virgo$_{nEXT}$. For comparison the sensitivity of Advanced Virgo in O3 and the design sensitivity of AdV+ in O4 and O5 are also shown. The dotted curve in the purple band shows the best sensitivity achievable by Virgo$_{nEXT}$ with improved amorphous coatings.*

2.8 Einstein Telescope

The scientific community of GWs is already focused on the design of *third generation* GW detectors, capable of improving sensitivity and of extending the low frequency bandwidth. A ground-based detector is limited by seismic noise in the low frequency region, to reduce it, the detector must be placed underground. The **E**instein **T**elescope (ET) will be a large underground and cryogenic ITF, designed to improve the sensitivity of a factor of 10 compared to second generation ITFs and, therefore, to enlarge the detection volume by a factor of 1000. To reduce the effect of the residual seismic motion - thus allowing a better sensitivity at low frequencies between 3 and 100 Hz - ET will be located underground at a depth of about $[100 \div 200]$ m. It will consist of three nested detectors, each composed by two ITFs - the so-called xylophone configuration. The topology of each ITF will be the dual-recycled Michelson layout, with FP arm cavities with a length of about 10 km. The xylophone configuration of each detector devotes one ITF to the detection of the low-frequency components - $[2 \div 40]$ Hz - of the GW signal while the other is dedicated to the high-frequency ones. The foreseen sensitivity is shown in Figure 2.21. Therefore, each ITF will adopt different technologies to optimize the sensitivity in the frequency region of interest. In the former **E**instein **T**elescope **l**ow-**f**requency (ET-LF), operating at cryogenic temperature, the thermal, seismic, gravity gradient and radiation pressure noise sources will be the main ones to be suppressed; in the latter **E**instein **T**elescope **l**ow-**h**igh (ET-HF), the sensitivity at high frequencies will be improved through high laser power circulating in the FP cavities. The use of cryogenic technology its fundamental to reduce the thermal noise contributions. For ET-LF, the suspensions and the mirrors will be cooled down to 20 K. In order to reduce mechanical losses, the mirrors' substrates of the low frequency detector will be made of silicon instead of fused silica. The laser wavelength will also be from 1064 nm to 1550 nm, since the silicon is transparent to this wavelength. The full discussion is detailed in [98].

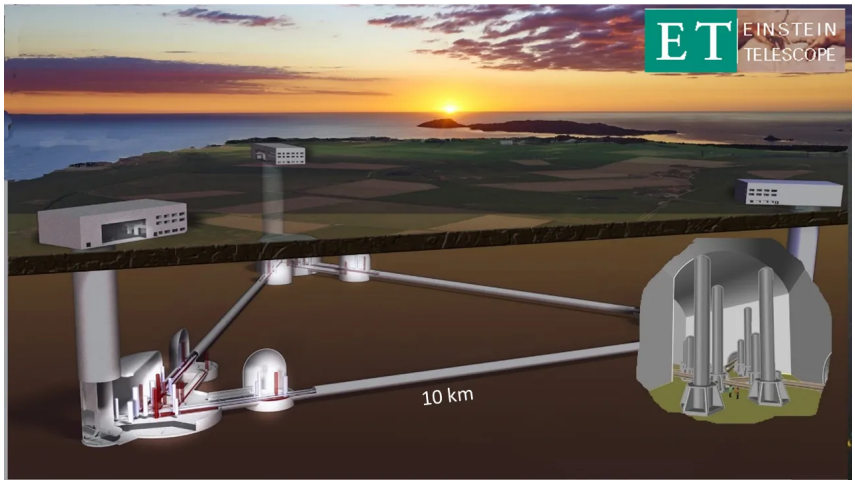

Figure 2.20: *Representation of the possible design for the ET detector.*

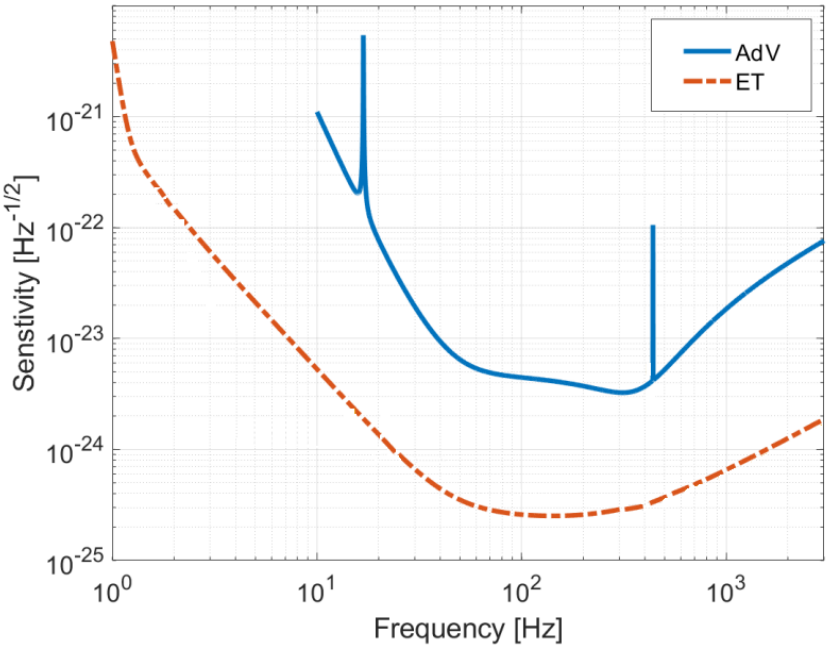

Figure 2.21: *Foreseen sensitivity curve for the ET in orange. Advanced Virgo sensitivity curve in blue is also shown for reference.*

2.9 Laser Interferometer Space Antenna

Laser **I**nterferometer **S**pace **A**ntenna (LISA) is a mission funded by the European Space Agency to develop the first GW detector in space. The launch is currently scheduled for 2037 [99]. LISA will consist of three spacecrafts arranged in a triangular configuration, each separated from the others by 2.5 millions km. The detector will be placed in the Lagrangian point L1 at approximately 50 millions km away from the Earth. In each spacecraft two telescopes, two lasers and two TMs will be installed and arranged in two optical groups pointing towards the other two spacecrafts [100]. Each of them will behave like a zero drag satellite floating around the masses in order to remove non-gravitational

forces and it will be connected to the others by high-precision laser beams that form the arms of the ITF. The sensitivity of this detector will be mainly focused on the very low frequency region, between 0.1 mHz and 1 Hz. This will allow LISA to see sources undetectable by ground-based detectors, such as supermassive BH mergers or extreme mass ratio inspirals. LISA Pathfinder was launched on December 3, 2015 as a proof-of-concept that tests that the noise characteristics of free-floating TMs within the spacecraft are small enough compared to an expected GW signal. Completing its mission in July, 2017, LISA Pathfinder has shown that the residual noise levels surpassed the original requirements by a factor of ~ 100 [101]. The LISA Pathfinder mission even outperformed the requirements for the full LISA mission, demonstrating that key technology for LISA is well underway.

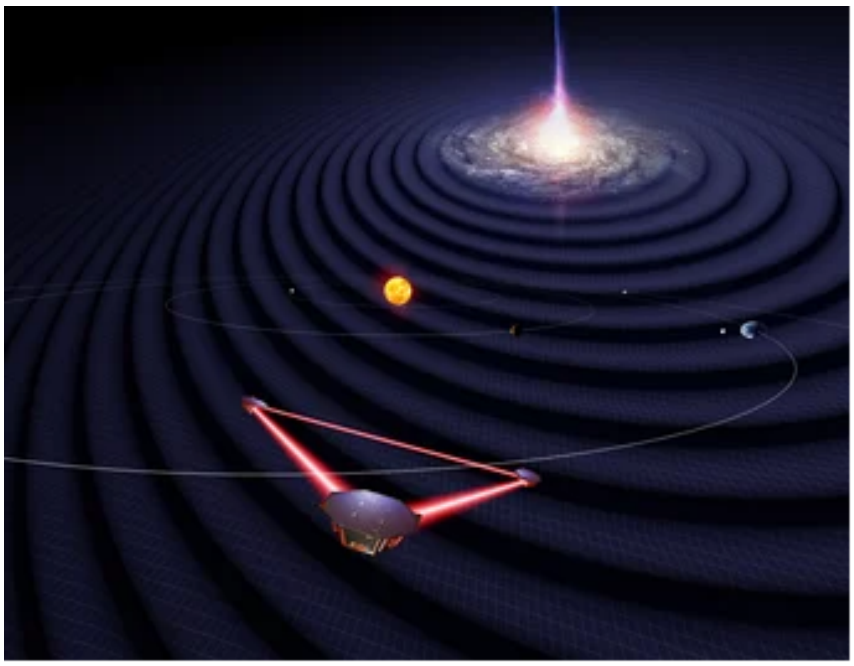

Figure 2.22: *Artist's impression of the LISA mission satellites in the solar system observing GWs from a distant galaxy. Credit: University of Florida - Simon Barke*

Chapter 3

Wavefront distortions and their compensation

As discussed in Chapter 2, the increase of the input power is required to improve the detector sensitivity at high frequency. The absorption of the laser power in the mirror substrate and coatings causes a thermal expansion of the optic itself along the optical axis and an inhomogeneous increase of the OPL of the light due to the mirror refractive index dependency on temperature. These effects induce **W**avefront **D**istortion (WD) in the beam propagating inside the ITF. This chapter examines the physical mechanisms by which WDs occur, their effects on the ITF performance and the AdV+ approach to correct them.

3.1 Wavefront distortions

A WD is a deviation from an ideal surface of equal phase (wavefront) of an EM field accumulated after reflection from or transmission through an optical element [102]. Figure 3.1 illustrates an EM field E_{in} impinging on an optic with refractive index n_0, undergoing reflection and transmission.

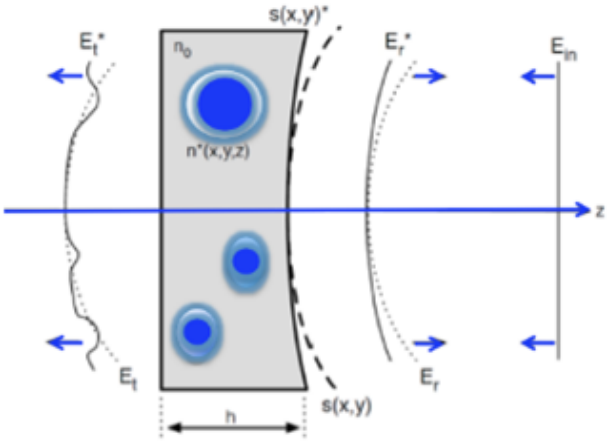

Figure 3.1: *Because of reflection from or transmission through an optic suffering of surface distortions $s^*(x,y)$ and refractive index inhomogeneities $n^*(x,y,z)$ (blue regions), an incident EM field E_{in} accumulates WDs in reflection E_r^* and transmission E_t^*. For the sake of comparison, the wavefront of the ideal reflected field E_r (dotted line) and the wavefront of the ideal transmitted field E_t (dotted line) are also shown.*

If the design surface of the optic $s(x, y)$ is distorted into the actual surface $s^*(x, y)$, the wavefront of the reflected field E_r^* differs from the expected wavefront E_r, whereas the transmitted field, influenced by the potential presence of local fluctuations $n^*(x, y)$ in the refractive index of the material (pictured as shaded regions), is changed from the ideal wavefront E_t to the distorted wavefront E_t^*. From a mathematical point of view, the information about WD is encoded in the phase of the reflected and transmitted fields. For the reflected wave, the field is:

$$E_r^* = E_r e^{2ik[s(x,y)-s^*(x,y)]}, \tag{3.1}$$

where $k = \frac{2\pi}{\lambda}$ and λ is the wavelength of the laser. Thus, the WD $\Delta WD_r(x, y)$ after the reflection can be defined as:

$$\Delta WD_r(x, y) = s(x, y) - s^*(x, y), \tag{3.2}$$

while the distortion accumulated in the propagation inside the optics is evaluated as:

$$\Delta WD_t(x, y) = \int_0^h (n^*(x, y, z,) - n_o)\, dz. \tag{3.3}$$

3.2 Sources of wavefront distortions

There are two main sources of WD in an interferometric detector [103]:

- *Imperfections*: introduced by the mirrors' manufacturing process these are the *static distortions* or *cold defects* which are both time and state-of-the-detector independent. With state-of-art polishing techniques, it is possible to obtain deviations in surface curvature from the design value of the order of 1 m per 1000 m of a typical curvature radius - which is not critical and doesn't limit the detector performance. But other defects - such as errors in the surface shape and spatial variations in the refractive index of the substrates - may instead affect the detector performance since they can not be removed during the manufacturing process. Somewhat halfway between this category and the following one, we encounter imperfections of various kinds that lead to non-uniform absorptions. These imperfections give rise to WDs containing high spatial frequencies and dimensions typically smaller than the Gaussian beam diameter that impacts the optics. In Section 3.4.5, we will discuss an example;

- *Power absorption*: the non-zero absorption of the laser power in the substrate and in the coatings of the test masses creates a temperature gradient inside the optics. After a transient period, a steady-state temperature distribution will settle down in the optic volume. This generates a non-uniform OPL distortion and a change in the HR surface RoC, eventually resulting in a degradation of the ITF performance and response.

In the advanced detectors, hundreds of kWs of optical power impinge on the HR surface of the arm cavity mirrors and few kWs cross the substrates. Although the absorption coefficients of coating and substrates are extremely low, several tens of mW will be absorbed by the ITF's optics. The time constant for the temperature distribution to reach a steady state depends on the thermal diffusivity of the material and on the characteristic size of

the heat distribution applied to the optic. As mentioned before, the thermal effects can develop in transmission or in reflection: the ITMs are influenced by both of them, while in the ETMs the substrate is outside of the FP cavity, and then the thermal lensing within it is not felt by the ITF.

3.2.1 Thermally induced wavefront distortions

Wavefront distortions in transmission

For an optic with thickness h and refractive index n at uniform temperature T_0, the OPL is defined as $OPL_0 = nh$. The absorption of power in the optic raises its temperature resulting in an OPL increase and in an expansion of the optics along its axis - see Figure 3.2. Absorption can happen within the volume of the mirror or within the optical coating. The latter is the dominant heating source for the ITMs, despite the small HR coating aborption coefficient (less than 1 ppm), due to the high power circulating in the arms.

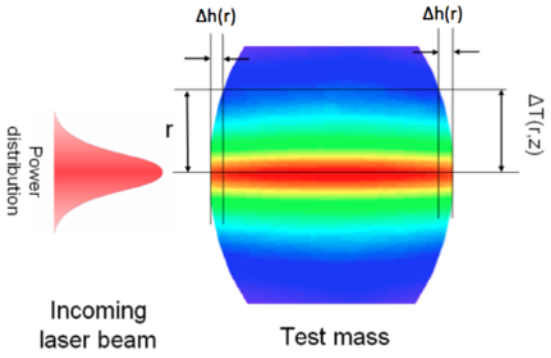

Figure 3.2: *Increase of OPL of a TM crossed by a laser beam:* $\Delta T(r, z)$ *is the temperature profile and* $\Delta h(r)$ *the thermal expansion.*

The OPL increase can happen in three ways [103]:

- **Thermo-optic effect**, due to the variation of the local refractive index when the temperature changes by a quantity ΔT:

$$\Delta OPL_{TL}(x, y) = \frac{dn}{dT} \int_0^h \Delta T dz, \tag{3.4}$$

  where $\frac{dn}{dT}$ is the thermo-optic coefficient;

- **Thermo-elastic deformation**, due to a non-zero thermal expansion coefficient α, that induces a change of the shape of the mirror equal to:

$$\Delta OPL_{TE}(x, y) \sim \alpha(1 + \sigma)(n - 1) \int_0^h \Delta T dz, \tag{3.5}$$

  where σ is the *Poisson's ratio*[5].

[5]It is the property of each material, dependent on the temperature, which measures the degree to which the material sample is transversely shrink or expands in the presence of a longitudinal one-way stress, so $\sigma = -\frac{transverse\ deformation}{longitudinal\ deformation}$.

- **Elasto-optic effect**, due to the local refractive index change due to the mechanical strain caused by the thermal expansion:

$$\Delta OPL_{EO}(x,y) \sim -\alpha p_{11} \int_0^h \Delta T dz, \tag{3.6}$$

where p_{11} is the component of the elasto-optic tensor along the probe beam polarization axis.

In fused silica, the main properties of which are shown in Table 3.1, the elasto-optic effect is negligible compared to the other two effects [103]. Summing up all the non-negligible contributions, the OPL variation in transmission can be written as:

$$\Delta OPL_T(r,\theta) = \left(\frac{dn}{dT} + \alpha(1+\sigma)(n-1)\right) \int_0^h \Delta T(r,\theta,z) dz, \tag{3.7}$$

where $\Delta T(r,\theta,z)$ is the temperature change of each point of coordinate (r,θ,z) with respect to T_0.

Material Properties	**Fused Silica**
Refractive index n	1.45
Thermo-optic coefficient dn/dT	$10 \cdot 10^{-6}$ K^{-1}
Optical absorption at 1064 nm	0.2 ppm/cm
Density	2202 kg/m^3
Thermal conductivity K_c	1.38 W/mK
Specific heat C	740 J/(kg·K)
Thermal expansion coefficient α	$0.55 \cdot 10^{-6}$ K^{-1}
Poisson's ratio σ	0.17

Table 3.1: *The main Fused Silica properties [104, 105].*

Wavefront distortion in reflection

Any inhomogeneous mirror heating induces a volume thermal expansion, resulting in a change of the shape of the mirror itself. As a consequence of the absorption of laser power, a bump appears in the center of the TM so its profile is no longer spherical and its RoC changes - see Figure 3.3.

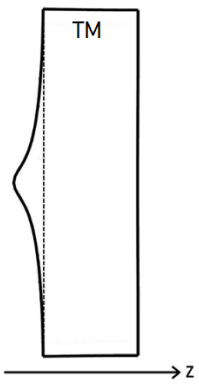

Figure 3.3: *Thermo-elastic deformation of a mirror due to a Gaussian beam partially absorbed by its surface.*

This WD on upon surface reflection is due to the **thermo-elastic deformation** and the total variation of the OPL in reflection is given by:

$$\Delta OPL_R(r,\theta) \sim 2\alpha(1+\sigma)\int_0^h \Delta T(r,\theta,z)dz. \tag{3.8}$$

The factor 2 is an inherent characteristic of reflection, as it involves both the outgoing and the returning path of a reflected beam, and deformation affects both.

3.2.2 Analytical solution: Hello-Vinet theory

The analytical solution for a cylindrical mirror shined by a Gaussian beam has been computed by Hello-Vinet [106]. The laser circulating in the ITF has a Gaussian profile and its intensity is given by:

$$I(r,z) = \frac{2P}{\pi w^2} e^{-2\frac{r^2}{w^2}}, \tag{3.9}$$

where P is the power, w is the beam spot size[6] and r the radial coordinate. Because the intensity profile and the mirror geometry are cylindrically symmetric, the problem is modelled by using a set of cylindrical coordinates. In the most general case, the time evolution of the temperature field is given by the Fourier equation:

$$\rho C\frac{\partial T}{\partial t} - \kappa\nabla^2 T = H, \tag{3.10}$$

where ρ is the density, C the specific heat, κ the thermal conductivity and H accounts for volume heat absorption within the mirror. Considering the steady state and assuming $H = 0$ that is, taking into account only the dominant coating absorption, equation 3.10 becomes the Laplace equation:

$$\nabla^2[\Delta T(r,z)] = 0, \tag{3.11}$$

which can be solved by imposing boundary conditions that are depicted by the interchange of radiative heat and the absorption of heat within the coatings. A general solution can be expressed as:

$$\Delta T(r,z) = \sum_n \left(A_n e^{k_n z} + B_n e^{-k_n z}\right) J_0(k_n r), \tag{3.12}$$

where $J_0(k_n r)$ are Bessel functions, A_n, B_n and k_n are constants to be determined with appropriate boundary conditions. Once the latter have been determined it is possible to analitically express the temperature field increase in a cylindrical mirror absorbing a fraction of the power stored in a Gaussian laser beam [107].

3.2.3 Numerical approach: Finite Element Analysis

In addition to the analytical approach, the thermal effects in the optics can be evaluated also with the **F**inite **E**lement **A**nalysis (FEA) method [108]. This tool is very useful when dealing with systems lacking any symmetry or with materials having high anisotropy or inhomogeneity. In FEA simulations, a complex shape is divided into a large number of simpler elements defined by their nodes. The properties of each node are connected to those of the closest nodes through both a polynomial equation that characterizes the boundary conditions i.e., the thermal conduction and radiation and the equation that

[6] The spot size is the radius of the $\frac{1}{e^2}$ contour after the wave has propagated at a distance z.

describes the physical processes i.e., the heat conduction. Then, a system of equations describing the entire system is numerically solved. The main tool used to perform this type of FEA simulations is ANSYS [109], which is provided with an easy data transfer interface toward the other two softwares used: Zemax [110] and Matlab [111]. To estimate the temperature profile inside an optical component due to surface/volume power absorption, thermal conduction and radiation are included in the codes. There are two possible types of analysis:

- *coupled*: Fourier's equations and thermal expansion incorporate stress and temperature and are simultaneously solved;
- *uncoupled*: The thermal lensing and thermoelastic deformation can be evaluated from the temperature distribution within the optics, which is a faster and more straightforward approach, albeit with some approximation.

3.3 Consequences of thermal effects

As we have seen, the WD is a consequence of a change in the optical system of the ITF. These deviations are not within the optical system itself - which remains constant - but rather in the behaviour of the system, which deviates from ideality due to sources of aberration. Furthermore, ITFs for GWs employ various resonant optical cavities. The stability of an optical cavity refers to its ability to maintain a confined beam of light within it consistently and without divergence. In other words, a stable optical cavity can keep the optical beam within specific parameters, determined by mirrors RoC and cavity length, and prevent uncontrolled spreading or divergence [103]. The effects due to WDs can be divided into the following categories:

- *Reduction of the GW signal amplification*: the power scattered out of the fundamental mode after reflection on a distorted mirror represents a loss in the cavity which reduces its finesse and therefore the amplification of the GW signal;
- *Increase of noise at the output port* due to:
  - Reduction in the power at the BS: any common-mode WD in the ITF arms - i.e., the component of the distortion that is symmetric about the front surface of the BS - reduces the mode-matching into the PRC. Therefore, the power at the BS is reduced and the shot noise limit worsens;
  - Increase of the carrier power leaking toward the dark port: any differential-mode WD in the arms of the ITF - i.e., the component of the distortion that is anti-symmetric about the front surface of the BS - reflects light out of the dark port adding shot noise to the measurement;
- *ITF stability and robustness reduction*:WD can originate power losses in the main control loops, resulting in a lower SNR on the PDs and then in fainter error signals that could make the ITF uncontrollable, reducing then the ITF observing time.

Optical simulations of the ITF can include aberration effects to evaluate their influence on the ITF. The EM fields propagating inside the detector can not be simply derived from analytical models, especially in presence of asymmetries as mirror's defects. Thus, complex optical simulation tools have been developed to study the ITF behaviour. In

particular, **F**ast **F**ourier **T**ransform (FFT)-based optical simulations are exploited in OSCAR [112]. OPL variation due to cold defects or thermal effects can be included in the model to evaluate their impacts on the ITF performances.

3.4 Thermal Compensation System

In the previous section, we discussed how WDs degrade the performance of a GW detector. Therefore, a system to monitor and correct these distortions is needed. The adopted strategy to compensate for the thermal effects is to locally introduce a complementary distortion along the main laser path thus restoring the ITF optimum performance. This is the basis of the *Thermal Compensation System* design. The correction provided by the TCS concerns:

- OPL distortions at the level of ITMs - thermal lensing, mirror figure errors, inhomogeneity of the substrate refraction index - which generate WDs in the signal recycling and power recycling cavities;
- Profile variation of the highly reflective surface - due to thermoelastic deformation - in both ITMs and ETMs, affecting the FP cavity;
- Correction of manufacturing error of the ITMs, ETMs and recycling cavities mirrors RoC.

The impact of the thermal effects depends on the optical configuration of the ITF. As seen in section 2.5, in AdV+ the requirements regarding the compensation of thermal effects are more stringent with respect to Advanced LIGO being the recycling cavities marginally stable. The requirements for the TCS accuracy are defined in the AdV+ design document [80]. They result from the general requirement that the aberration-induced recycling cavity gain drop should not surpass 50% of the design value. These requirements are summarized in Table 3.2 [113].

Parameter	**Requirement**
RC residual OPL RMS	< 2 nm
TM RoC precision	± 2 m

Table 3.2: *AdV+ TCS requirements.*

Considering a nominal coating absorption of 0.7 ppm, at 125 W of input power, the thermo-elastic deformation increases the radius of curvature by about 40 m and the focal length of the thermal lensing induced by the Gaussian beam heating is around 10 km. Thus, the TCS must be able to decrease the RoC of the mirrors by 40 m and to generate a divergence lens with a 10-km focal length in order to restore the nominal ITF configuration. Following the accuracy requirements and the needed actuation dynamics, the TCS sensors and actuators have been defined. They will be described in the next sections.

Evaluation of the requirements

Before delving into the discussion of TCS sensors and actuators, it is necessary to introduce an analysis method, the Gaussian weighted fit, and two figures of merit for evaluating

the requirements, the Gaussian weighted RMS and the coupling losses, based on the idea that the effect of any optical distortion is only relevant if sensed by the ITF beam, which has a Gaussian intensity distribution.
Typically, a weighted fit involves assigning a *weight* to each experimental data point, determining its significance within the fitting process. In our specific scenario, where all wavefront points share the same error, the objective of the **Gaussian weighted fit** is to assign greater weight to data points corresponding to the laser beam's presence. To achieve this, we utilize weights derived from a unit Gaussian profile matching the main laser beam's width. For example, a Gaussian weighted RoC is obtained by applying a parabolic fit where the data points are weighted using the laser profile. This procedure may be dispensable for spherical wavefronts but becomes crucial when dealing with aspherical wavefronts, as is the case with YAG thermo-elastic deformation or YAG thermal lensing.
The **Gaussian weighted RMS** is used to quantify the deviation from an ideal wavefront surface, calculated within a given diameter and weighted by the main beam of the ITF and it is defined as:

$$RMS = \sqrt{\sigma_g^2} = \sqrt{\frac{\sum_{m,n} G(x_m, y_n) \left[h(x_m, y_n) - h_g\right]^2}{\sum_{m,n} G(x_m, y_n)}}. \tag{3.13}$$

Considering that:

- (x_m, y_n) are the mirror coordinates;
- $h(x_m, y_n)$ is the WD;
- $h_g = \frac{\sum_{m,n} G(x_m,y_n) h(x_m,y_n)}{\sum_{m,n} G(x_m,y_n)}$;
- $G(x_m, y_n) = \frac{2}{\pi \omega_{YAG}^2} e^{-2\frac{x_m^2+y_n^2}{\omega_{YAG}^2}}$ is the ITF normalized beam intensity;
- ω_{YAG} is the main beam radius impinging on the mirror. For the ITMs of AdV+ $\omega_{YAG} \sim 49$ mm and for the ETMs $\omega_{YAG} \sim 58$ mm.

The coupling losses L is the fractional power scattered out from the fundamental mode, defined as $L = 1 - A^* A$ where:

$$A = \frac{\langle E_0 | E \rangle}{\langle E_0 | E_0 \rangle} = \frac{\langle E_0 | e^{i\frac{2\pi}{\lambda} h(x,y)} | E_0 \rangle}{\langle E_0 | E_0 \rangle} \iint e^{i\frac{2\pi}{\lambda} h(x,y)} |E_0(x,y)|^2 dx dy, \tag{3.14}$$

with E_0 is the EM field in the cavity unaffected by optical distortions, $h(x, y)$ is the value of the OPL at point (x, y), λ is the wavelength of the main laser and E is the distorted field. Considering that the EM field can be described by a set of basis modes $|U_{mn}\rangle$ and the scattering of the EM field between modes is expressed mathematically by the matrix $M_{mnpq} = \langle U_{pq} | e^{ik\Delta W} | U_{mn} \rangle$ [102] where m, n, p and q are the mode matrix indices, ΔW is the wavefront variation and the basis $|U_{mn}\rangle$ are arbitrary, L can be written as:

$$S_{00,00} = 1 - M_{00,00}^2 = 1 - |\langle U_{00} | e^{ik\Delta W} | \rangle U_{00}|^2. \tag{3.15}$$

If $M_{00,00}^2 = 1$, the TEM00 mode is not affected by any WD, and in this case $k\Delta W \ll 1$ so that the previous equation can be linearized. It is possible to define a function

$IFO(S_{00,00})$, depending on the ITF configuration, that connects the power scattered from the fundamental mode in **H**igher-**O**rder **M**ode (HOM)s with the decrease of the SNR due to thermal effects. This function can be expressed as $\Delta SNR = IFO(S_{00,00})$. The maximum acceptable loss of SNR, ΔSNR_{max}, is around the 10% of the total SNR [102], then $IFO(S_{00,00}) < \Delta SNR_{max}$.

3.4.1 Local sensing: Hartmann Wavefront Sensor

The **H**artmann **W**avefront **S**ensor (HWS) is a differential sensor devoted to detect WDs with an extremely high sensitivity. It uses a probe beam, emitted by an auxiliary light source, which investigates the optics under test. The HWS measures changes in the wavefront with respect to an initial reference wavefront. The probe beam is a **S**uper**L**uminescent **E**mitting **D**iode (SLED) characterized by a broadband emission and a short coherence length which prevents stray beams from producing interference, thus enhancing the figure of merit of the sensor [114]. The probe beam is injected from the source into an afocal telescope in order to match the size of sampled optics - of the order of tens of cm - and then upon back-reflection to be shrinked to the optimal size for the wavefront sensor, as shown in Figure 3.4.

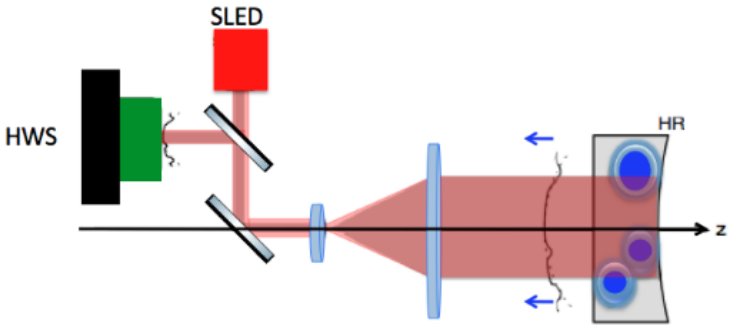

Figure 3.4: *A probe beam is injected through an imaging telescope and interrogates a distorted optic. It is back-reflected from the HR surface and returns such as the HR surface of the optic is imaged onto the HWS. According to the needs, the setup can be arranged in collinear or off-axis arrangements - see Figure 3.6.*

The wavefront sensor is positioned on the conjugate plane of the optic under test so that the WD is directly mapped from the optic to the sensor. Map coordinates on the HWS are rescaled from the optic surface coordinates using the optical magnification. The working principle of the HWS [114] is shown in Figure 3.5.

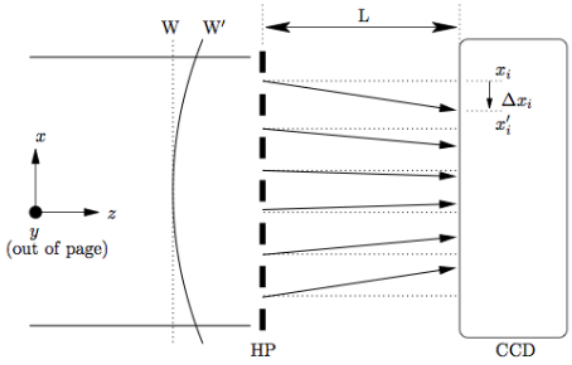

Figure 3.5: *An aberrated wavefront W' impinges on a HP. The resulting rays propagate at distance L, normal to the wavefront, and are incident on a CCD. The spot position x_i is determined by the centroid of that spot's intensity profile. The gradient of the wavefront at the i-th aperture is given by the displacement x'_i from the reference position x_i divided by L.*

The front surface of the sensor is the so-called **H**artmann **P**late (HP) containing a series of holes that split the incoming wave into a series of beams. These beams propagate up to the CCD - positioned at a know distance L behind the HP - forming a dots pattern on the CCD. The resulting image is acquired and the position of the centroid of the i-th dot, x'_i, is determined by an image analysis algorithm. The displacement of the centroid of each point Δx_i with respect to a reference provides a direct measurement of the incident wavefront local gradient, which is evaluated using:

$$\frac{\partial \Delta W}{\partial x} = \frac{\Delta x_i}{L}. \tag{3.16}$$

This gradient can then be numerically integrated to reconstruct the WD induced in the optical element under analysis [115]. The HWSs are excellent to measure both the effect of the thermal lensing inside the TMs and the thermo-elastic effect on their HR surfaces. The measurement of thermal lensing is defined *on-axis*, because the probe beam (λ=790 nm) impinges perpendicularly to the WI and NI TMs - see figure 3.6 (left). Two different HWSs each with its own probe beam - are placed on the INJ and DET benches, respectively. The probe beam is overimposed to the main laser after being expanded by a factor M=11 (for the WI) and M=13.5 (for the NI). Then, the SLED passes through the TM and is reflected back by its HR surface toward the sensor along the outward path. This is a double-pass measurement, performed in order to increase the signal to noise ratio by a factor 2. For the thermo-elastic case, the probe beam (λ=880 nm) hits the HR surface with an angle of incidence of 45° in the so-called *off-axis* configuration - see Figure 3.6 (right). Then it propagates up to a perpendicular mirror reflecting the beam back toward the HR surface. The probe beam reaches the sensor after two bounches on the TM performing - as in the on-axis case - a double-pass measurement. For the off-axis setup, the expanding telescope has a magnification of M=7. Both the on-axis and off-axis HWS sources and their optics are placed in dedicated areas around the towers hosting the TMs.

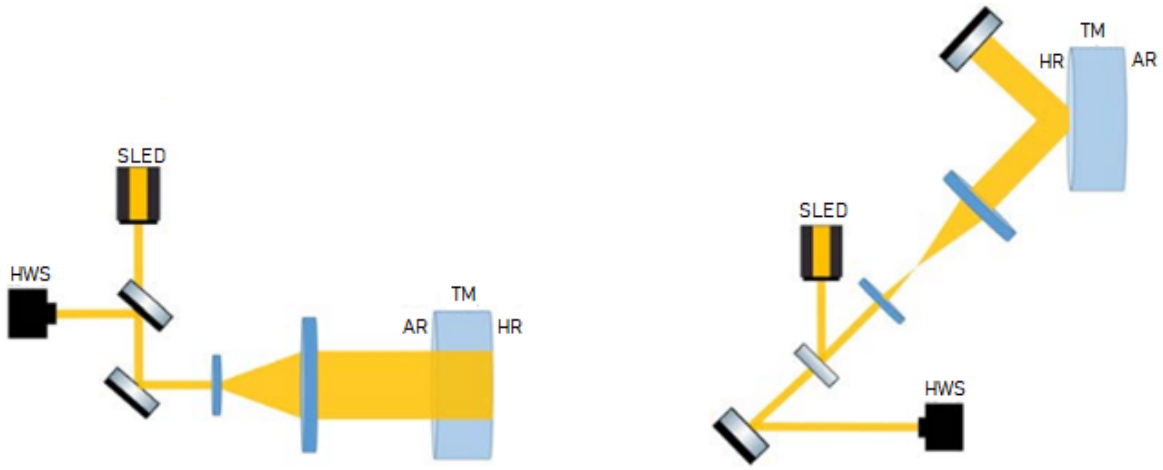

Figure 3.6: *Left: on-axis setup for the evaluation of the thermal lensing effect in the ITMs. Right: off-axis setup for the estimation of the thermoelastic deformation in all the TMs.*

3.4.2 Global sensing: Phase Camera

Phase **C**amera (PC) simultaneously measures the amplitude and phase of both the CA and the SBs circulating into the detector. They provide the global status of the EM field in the ITF [116], while the HWSs provide information on local aberrations only.
The coupled cavities make it difficult to disentangle the contributions from the individual optics, therefore these sensors are considered as complementary to the HWS. In fact, the PC produces maps obtained by the beating of two beams: the pick-off beam - picked up in the PC position and that contains the information about the fields in the ITF - and a reference beam collected from the laser before it is injected in the ITF. The beam resulting from the recombination of the two is scanned over a PD. The heterodyne technique is used to independently record the information in the CA, in the upper and in the lower SBs at different frequencies. Two PCs are installed in AdV+ - see Figure 3.7:

- one used to monitor the presence of aberrations in the PRC;
- one used to check the aberration budget in the beam at the output of the detector.

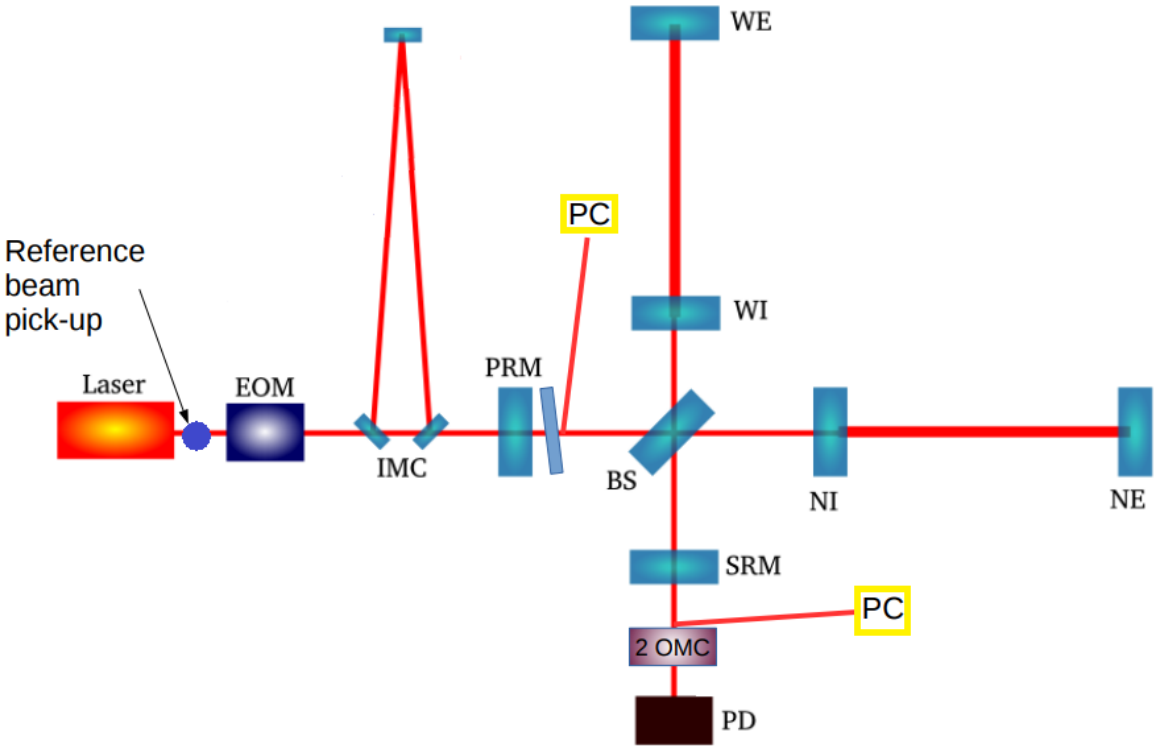

Figure 3.7: *Sketch of the phase cameras position in AdV+.*

3.4.3 Actuators: Ring Heater

The purpose of the **R**ing **H**eater (RH) is to correct the radius of curvature of each HR surface restoring its nominal value. Both thermal deformations due to absorbed power and static curvature errors due to uncorrect polish can be compensated in this way [117]. The RH is a ring-shaped apparatus encircling an optical component. When electrical power is dissipated within a RH to increase its temperature through Joule effect, it radiates heat and generates a thermal gradient in the mirror volume. This leads to the periphery becoming warmer than the central region. A negative lens and a surface curvature change are induced respectively because of the action of thermo-optic and thermo-elastic effects. The heating power is transferred from the RH to the mirror barrel by radiation from two borosilicate glass rings heated by Joule effect, while a polished copper shield around the rings increases the overall efficiency by reflecting the dispersed radiation toward the mirror - see Figure 3.8. Since only a small fraction of the emitted power reaches the optic, the two heaters alone are not enough. By adding a copper reflecting shield around the rings, the amount of emitted power that reaches the mirror increases improving the dynamics allowing the heaters to run at lower temperature too. The heater is a coil of Nichel Crome (NiCr) wire wrapped around a fused silica ring with emissivity $\epsilon \sim 0.9$, 7-mm thick. The RH is composed by two heaters, each of them with a resistance of $\sim 50\ \Omega$, allowing the maximum emitted power to be 24 W. In the two rings the current flows in the opposite directions, to mitigate the stray magnetic field generated by the coils which could interfere with the local control system of the TMs. The RH is positioned around the TM at distance of 18 cm from the HR face, where the maximum actuation efficiency on the HR surface RoC is expected. The RHs have multiple advantages, including a very low injected noise and both the induced elastic deformation and the induced thermal lensing

are perfectly spherical. However, utilizing the RH entails extended periods to achieve the steady state condition, typically spanning several hours. The application of a rapid control system, informed by the RH's transfer function, can significantly shorten these time frames. Furthermore, the deployment of the RH leads to the notable formation of a diverging thermal lensing in the input mirrors.
In Advanced Virgo five ring heaters encircled the ITMs, ETMs and the PRM. During the upgrade phase for AdV+, a new RH has been installed around the SRM. The PRM's RH is not used because it unexpectedly exhibits a significant thermal coupling with the mirror's control coils for degrees of freedom. Consequently, in designing the RH for the SRM, a single-heater ring configuration was adopted to ensure a more compact solution, even though it results in a reduction in dynamic capabilities. Two others smaller RHs have been installed around the mirrors of the FC [80].

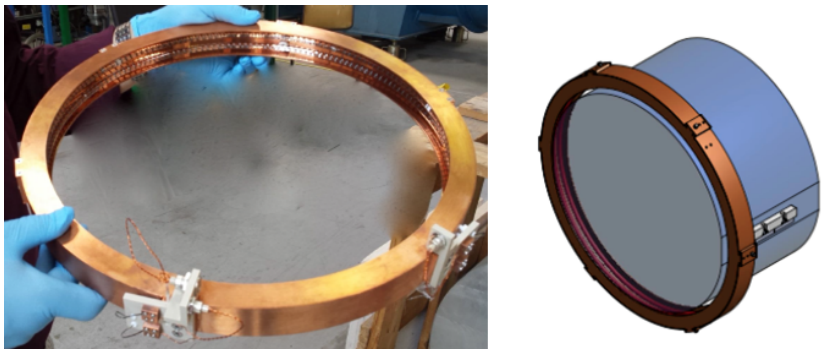

Figure 3.8: *Left: AdV+ RH composed by 2 fused silica rings and a copper shield. Right: sketch of the RH around the test mass.*

3.4.4 Actuators: CO_2 laser projectors

CO_2 lasers are used to compensate the thermal lensing generated by the main laser beam in the input TMs substrate by shining a heating pattern suited to generate a complementary lens. CO_2 laser wavelength $\lambda = 10.6$ μm is completely absorbed by the fused silica. However, the heating pattern is not directly projected on the ITMs but on an additional transmissive optic [118] called **C**ompensation **P**late (CP) to prevent noise coupling to the laser relative intensity noise in the range $[50 \div 100]$ Hz [119]- see Figure 3.9. Two CPs are installed in the recycling cavities, 20 cm from the relative ITM toward the BS. This distance is optimal to minimize the radiative coupling between the CP and the related ITM.

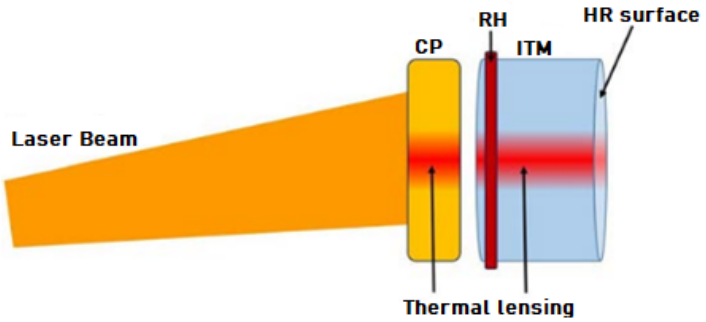

Figure 3.9: *Actuation of the CO_2 laser on the CP, placed at a distance of 20 cm from the ITM. The RH is also shown.*

The beam is injected in the ITF through a viewport made of Zinc Selenide (ZnSe), a material that is transparent to CO_2 radiation. The CO_2 source is mounted on external optical benches where a suitable layout allows for shaping the beam according to the specific actuator's requirements. The current set up of the CO_2 benches includes two spatial beam filters to improve the beam quality of the CO_2 lasers[7]. However, this solution reduced considerably the available power (50%) and then the actuation dynamics. To overcome this issue, a CO_2 Mode Cleaner to improve the beam quality is being prototyped for AdV+ Phase II [120].
The CO_2 laser optical bench layout is designed to shape the source beams into two different heating patterns::

- **C**entral **H**eating (CH): an axi-symmetric centred pattern. It is needed to mitigate the impact of thermal transients when the ITF undergoes a state change, with loss of arm cavity locking. For this purpose, it consists of a Gaussian beam shined in the center of the CP, generating a converging lens - the same sign as produced by self-heating in the optics due to the main laser beam - and it is designed to have the radius on the CP equal to the main laser beam. The CH is automatically engaged when the power stored in the arm cavities drops, to maintain the thermal state of the input optics. Correspondingly, the lock acquisition procedure is designed to switch off the CH actuator when arm cavities are locked again. The CH optical layout integrated in the CO_2 bench is shown in Figure 3.12.

- **D**ouble **A**xicon **S**ystem (DAS): an axi-symmetric annular correction. Its compensation is performed by heating the periphery of the mirror, in order to produce a complementary OPL that of the main laser inside the CP and restore an aberration-free transmission.

[7] In AdV+, the utilized sources maintain a HOM content in the beam of no less than 5%.

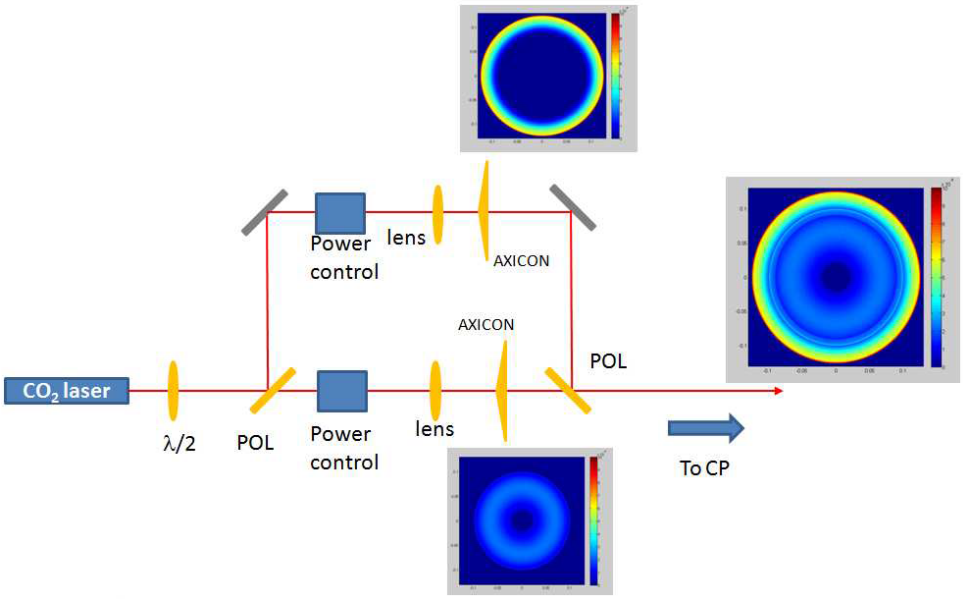

Figure 3.10: *Conceptual design of a DAS.*

Figure 3.10 shows a conceptual design of the DAS. The DAS actuation is performed with the generation of an annular heating pattern that is achieved by means of the use of a particular type of optical element, the *axicon*, i.e. a lens with a conical surface that converts a Gaussian laser beam in an annular one. The process involves a linearly polarized CO_2 beam passing through a $\lambda/2$ plate, which rotates the incident polarization. A fixed polarizer POL then splits the incident polarization into two orthogonal components. Each of these beams proceeds through a non-polarization-rotating power control, a focusing lens, and the axicon. Finally, the beams are recombined using a polarizer. This configuration ensures there is no interference between the beams during recombination. The design allows for the modification of each axicon pattern by adjusting the distance between the focusing lens and the axicon itself. With this setup, it becomes possible to create a heating pattern that closely approximates the optimal one, as depicted in the left plot of Figure 3.11.

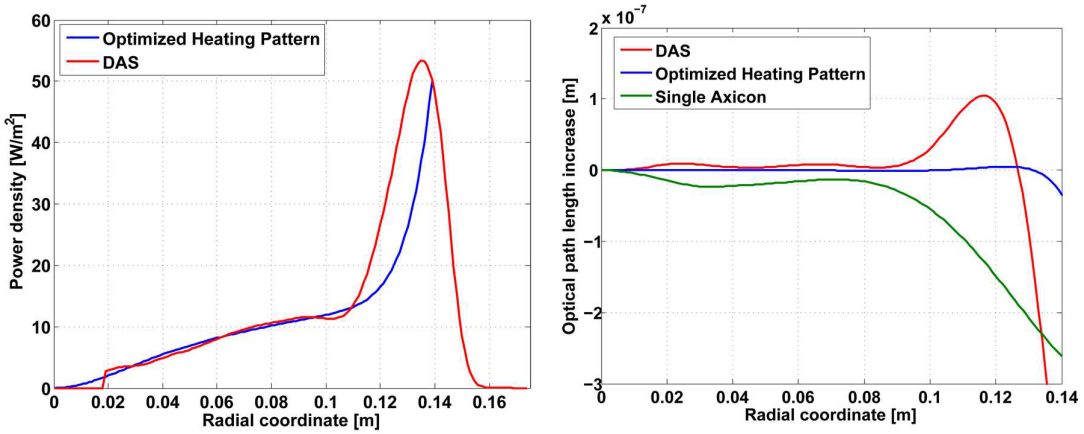

Figure 3.11: *On the left: the DAS heating pattern (red) compared to the optimized heating pattern (blue). On the right: corresponding OPL increase (optimized heating pattern is in blue and the DAS is in red). Also the OPL given from a single axicon system (green) is reported for comparison.*

The right plot in Figure 3.11 displays a comparison of the increase in OPL for the optimized heating pattern, the single axicon system, and the DAS. The enhancement achieved by the DAS in comparison to the single axicon system can be quantified as a tenfold reduction in coupling losses, resulting in approximately 300 ppm instead of 3000 ppm. The RMS calculated with the DAS compensation amounts to 3 nm. Importantly, the DAS has the capability to correct various forms of axisymmetric aberrations, not only thermal lensing but also the symmetrical effects of cold defects, such as substrate refraction index inhomogeneities. Thus, the DAS is composed by two concentric annuli: the inner annulus is small and thick, while the outer one is larger but thinner. The DAS optical layout integrated in the CO_2 bench is shown in Figure 3.12.

CO_2 benches

The TCS has two twin CO_2 benches positioned near the vacuum towers that house the NI and WI mirrors. The optical layout for both the CH and DAS is accommodated on the CO_2 bench, and its optical configuration is depicted in Figure 3.12. In the figure, there is a legend denoting the optics used on the CO_2 bench. The red line represents the DAS beam, the blue one corresponds to the CH beam, while the green segment is the portion common to both actuators. The current setup of the CO_2 benches includes a spatial beam filter to enhance the beam quality of the CO_2 lasers. The primary source is a 50 W CO_2 laser, which is presently reduced by 50% through spatial filtering and is exclusively used for the DAS actuator in anticipation of the power increase in O4. As the DAS operates while the ITF is in operation, the laser chosen is characterized by a very low **R**elative **I**ntensity **N**oise (RIN) [80]. The CH line is generated from a secondary source with more relaxed RIN requirements, as it typically operates only when the ITF is not in its working point. The CH line is mounted on a small breadboard located above the optics in the upper right corner of the bench, represented by the grey rectangle with a dashed black outline. As depicted in Figure 3.12, the two DAS rings' beams recombine on the POL4 optic, and then recombine with the CH on the **BS** of **R**ecombination (BS-REC) before entering the ITF through the ZnSe Viewport after passing through the **H**ot **M**irror (HM). These two mirrors are used for the alignment of the CO_2 beam.

- the DAS rings can be monitored since a motorized flip mirror on the DAS branch deflects the beam towards a telescope that images the beam onto a CO_2 beam profile. This is highlighted in the yellow zone in Figure 3.13.

- The second diagnostic branch employs an infrared camera to observe the heating profile of the actuators from the same distance as the CP. It consists of two mirrors composing a periscope. The first mirror is a motorized flip mirror positioned after the HM that deviates the beam toward another added mirror. Using this two mirrors is possible to divert the beam projecting it onto a black cardboard screen placed at the same distance as the CP. This is emphasized with the green zone in Figure 3.13 and a more detailed sketch of this diagnostic system can be seen in Figure 3.14.

The complete overview of the TCS subsystem is shown in Figure 3.15.

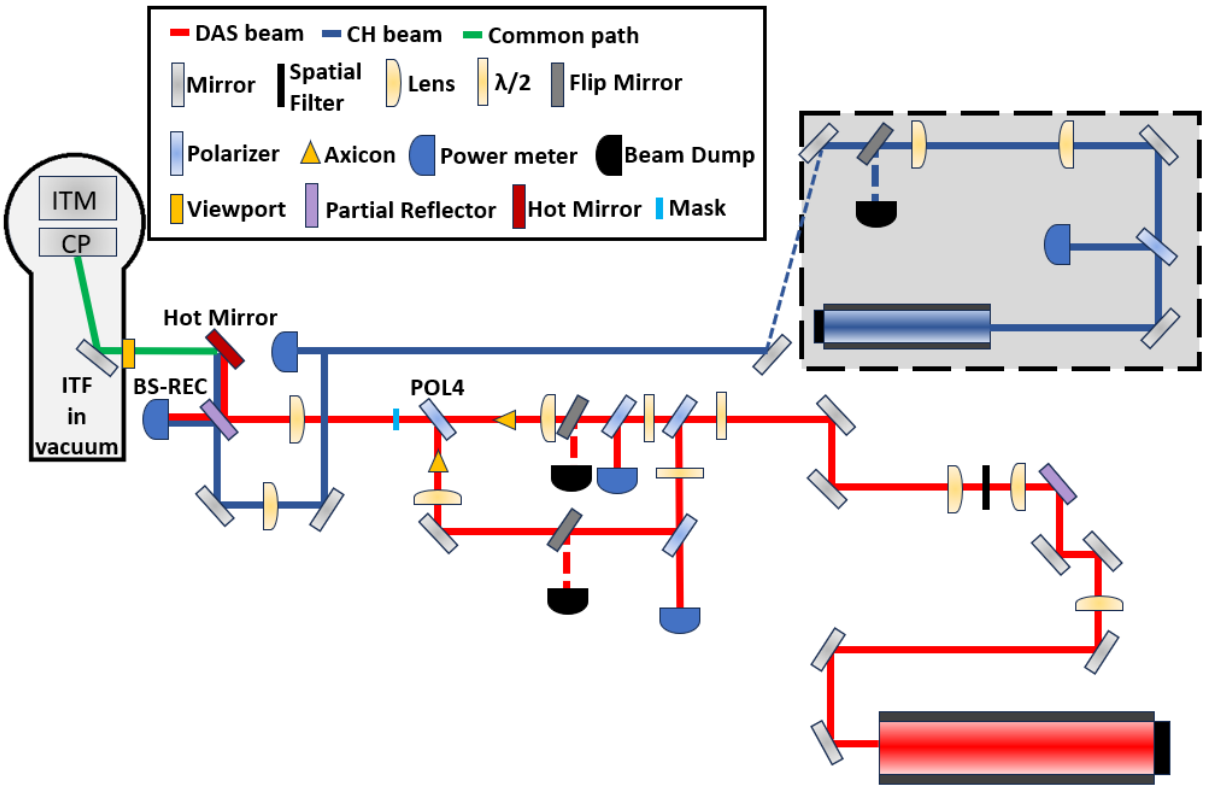

Figure 3.12: *CO_2 bench layout of AdV+.*

To this layout, two diagnostic branches are added:

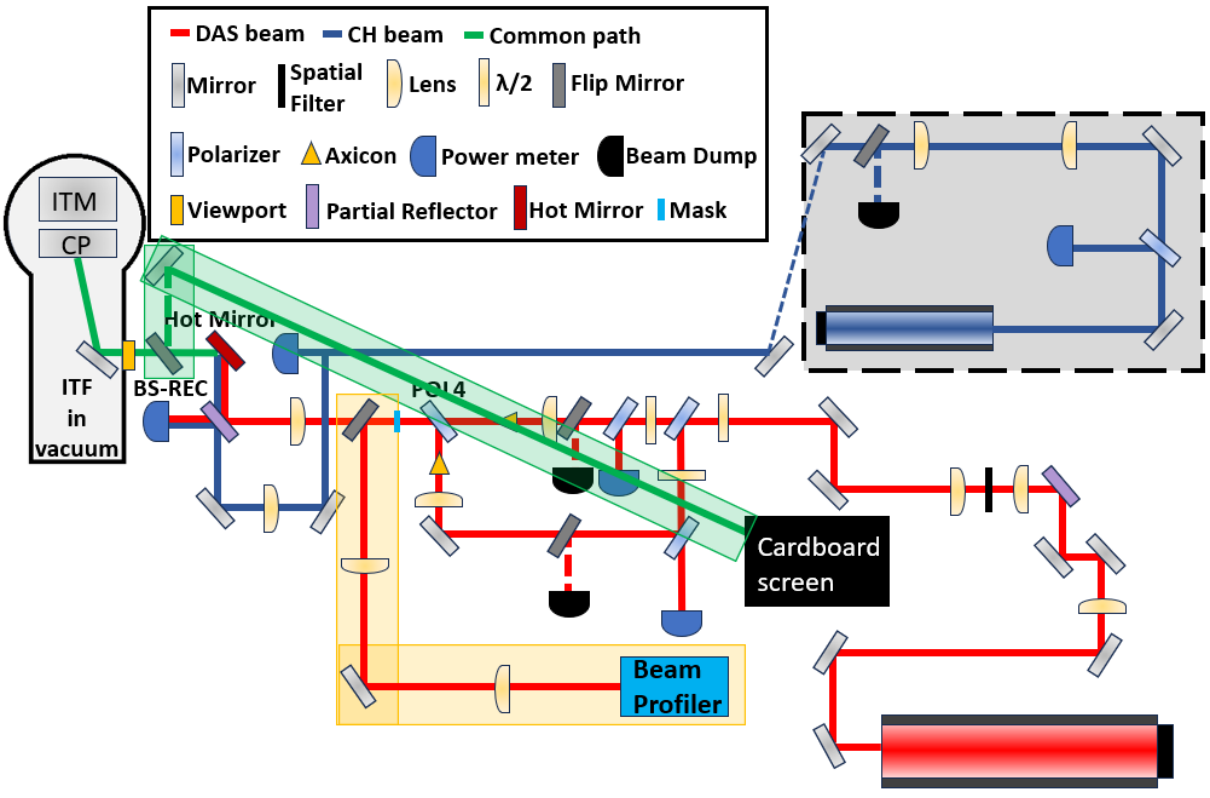

Figure 3.13: *CO_2 bench layout of AdV+ with the two diagnostic branches.*

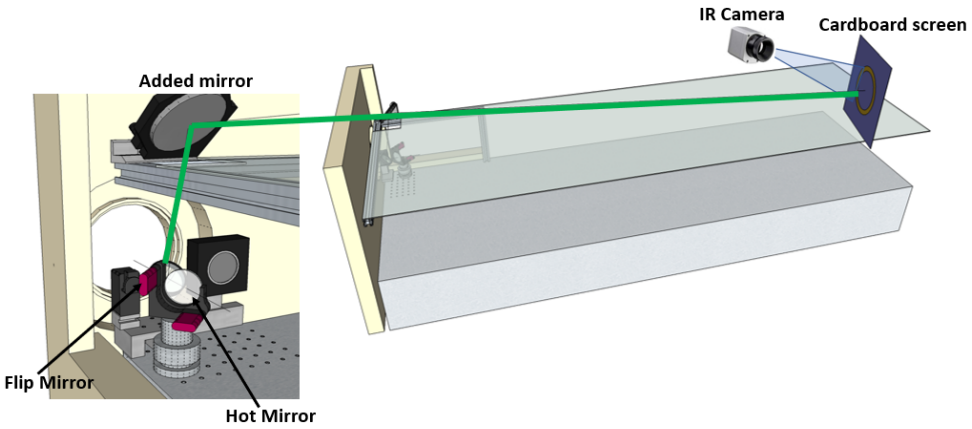

Figure 3.14: *Sketch of the additional optical as the flip mirror and an added mirror needed to propagate the CO_2 laser on the black cardboard screen and the infrared camera.*

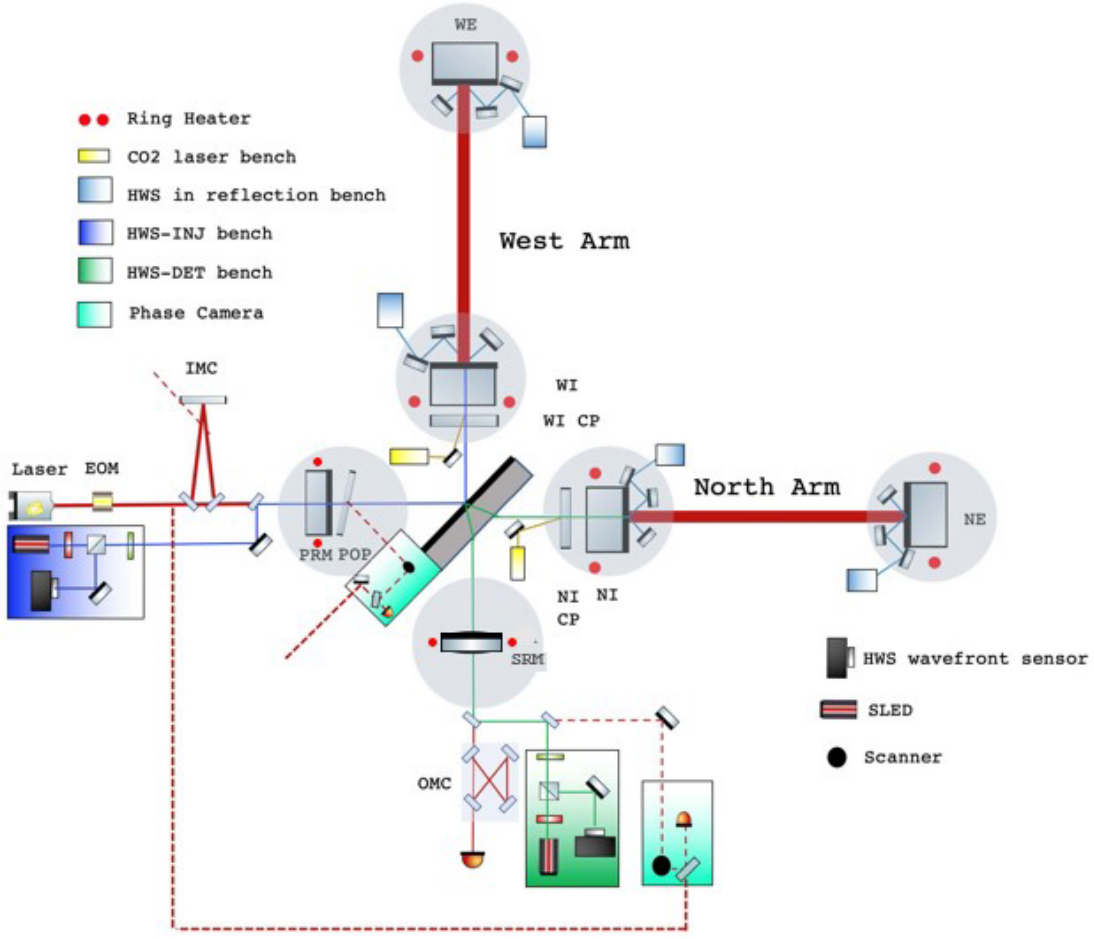

Figure 3.15: *Scheme of the Advanced Virgo TCS superimposed on ITF optical layout. The blue and green beams (HWS-INJ and HWS-DET) represent the two HWS probe beams in transmission that allow measuring the thermal lensing of the WI and NI test masses, respectively. The HWSs devoted to the measurement of the thermo-elastic deformation are shown in light-blue. The phase camera pickoff beam is represented by dashed red line. The red circles represent the RH actuators and the yellow rectangles the CO_2 laser benches. The grey circles identify the vacuum chambers hosting the ITF core optics.*

3.4.5 Compensation of non-axisymmetric optical defects

The actuators described so far are capable of compensating for axisymmetric optical defects. The input powers that Advanced Virgo has worked with so far did not reveal the need to correct non-axisymmetric optical defects as they were not yet significant. Nevertheless, a reference solution at the time of drafting the Technical Design Report for Advanced Virgo had already been considered and it was the **S**canning **S**ystem (SS). It is a system dedicated to the correction of non-axisymmetric WD of ITM, such as those caused by non-uniform absorptions. The optic is scanned point by point following a raster scan model with an area of $16 \cdot 16$ cm^2. The desired heating pattern, deflected by galvo mirrors, impinges on well defined scan points of the CP storing a certain amount of power on each of them. This method has the advantage of concentrating the actuation effect on a single frequency and not on a broadband, however this actuation method introduces noise in the sensitive bandwidth of the detector through several coupling mechanisms [121]. For this reason, it was never actually used. However, during the commissioning phase in preparation for the O3 observing run, small but highly absorbing areas randomly present on the surfaces of the Advanced Virgo mirrors were identified, the so-called **P**oint **A**bsorber (PA) [122]. Thus, the study and development of an actuator to correct these PAs became necessary.

Point Absorber actuator

The PAs were discovered and analyzed for the first time on the optics of LIGO ITFs [123]. They cause non-uniform absorptions, which generate WDs containing high-spatial frequencies and typical dimensions smaller than the Gaussian beam diameter impinging on the optics. The main effects of these points consist in thermo-elastic deformations and lenses in the mirror substrates. These effects impact the ITF operation at full power mainly because they contribute to the generation of optical loss by scattering light out of the cavity fundamental mode and furthermore, their presence reduces the sensitivity of the ITF directly through a decrease in the PRC gains and indirect interactions with the feedback control system [123]. The PAs studied so far on LIGO mirrors appear to be embedded in the HR surface coating and cannot be removed with standard cleaning techniques. However, at least in one case in AdV+, PAs seemingly due to external contaminations disappeared after a mirror cleaning during a suspension breaking recovery [124]. Thus, a dedicated system to compensate the effects of PAs on core optics on the ITF has been developed. Following the same strategy adopted by the other TCS actuators, this new device induces a complementary distortion [125]. The underlying idea of the actuator design involves creating the appropriated correction profile using a binary mask illuminated by a black-body thermal radiation obtained using a ceramic heater, almost entirely absorbed by the mirror. The profile is projected onto the surface under investigation through a system of lenses and mirrors. To better ensure flexibility and control, the actuator is designed to be installed out vacuum with a specific angle of incidence to avoid interfering with the ITF operation - see Figure 3.16. The final technical drawing - comprising the tower and the optical components - is shown in Figure 3.17. For the moment, only the actuator of the NI TM has been installed and it is in the commissioning phase in preparation for O4 run.

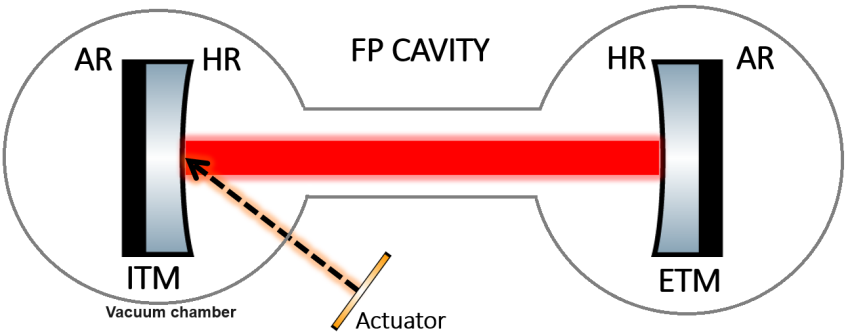

Figure 3.16: *Schematic view of a generic FP cavity with the actuator installed out vacuum with a specific angle of incidence.*

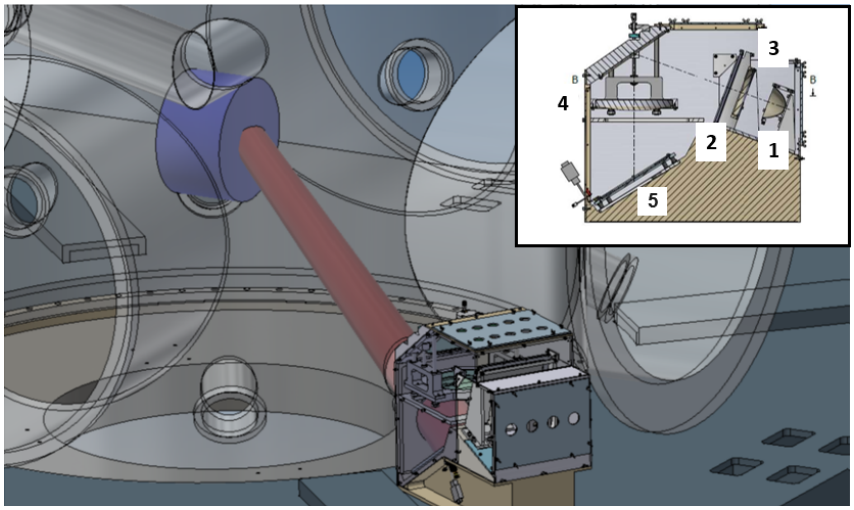

Figure 3.17: *Sketch of the PAs actuator in spatial relationship with the vacuum chamber and the mirror. The inset shows a section of the actuator, with details of the thermal source (1), the mask (2), the two Germanium lenses (3 and 4) - responsible for focusing and magnification - and the steering mirror (5).*

3.5 Future plans for the Thermal Compensation System

The improvements that will be made to the TCS are motivated by the request for a continuous power increase in the ITF. If on one side this leads to an improvement in the sensitivity of the instrument, on the other hand it makes the study, the control and the compensation of the thermal effects inside the optics even more crucial. The ITF input power increase proposed for the next observing run O5 and the installation of larger TMs will require further modifications of the present TCS setup. The investigations for prototyping and validation of the upgrades have already started in order to be ready in due time for AdV+ Phase II installation. The main activities concern:

- **Mode Cleaner cavity for CO_2 laser**: the efficiency of the TCS CO_2 actuators is directly related to the quality of the laser beam. The higher is the Gaussianity of the beam, the closer is the DAS corrective heating pattern to the design. Currently,

the quality of the compensating pattern is still far from the optimal shape due to the presence of non-axisymmetric HOMs in the source beam. Uncompensated residual distortions will become in the future a serious limitation to the TCS capability to handle thermal aberrations with higher circulating powers. It is then mandatory to implement a device to significantly improve the laser beam quality. The reference solution is to design and prototype a mode cleaner cavity for the CO_2 laser. Considering that the power available after the spatial beam filter is less than the nominal source power, the mode cleaner would also increase the available power in order to have a requirement of the power throughput $\geq 85\%$ [120];

- **New Hartmann wavefront sensing**: current HWS setup demonstrated a shot-to-shot reproducibility of $\lambda/1450$ at 820 nm - which improves to $\lambda/15500$ with averaging - and an overall accuracy of $\lambda/6800$ [126]. Recently, the DALSA Teledyne Company has put out of production the Pantera 1M60 CCD, which is the core of the present HWS. It is then necessary to start looking for a new device with good performances in terms of different parameters like sensitive area, noise, fill factor, frame rate, dynamics and saturation power. What is also needed is to design a new Hartmann plate and spacers in order to maximize the performances of the wavefront sensor, by optimizing their parameters over the new sensing element, and guarantee or overcome the sensitivity of the present device;

- **RH prototype for large TMs**: the proposed strategy to improve the AdV+ Phase II sensitivity getting the best from the current Virgo infrastructure is to reduce the coating thermal noise by expanding the beam on the ETMs. The future TM dimensions will be 55 cm in diameter and 20 cm in thickness. The increase of TMs dimensions implies a new design of the RHs already installed. The basic idea is to realize a larger RH exploiting the same working principle: two borosilicate glass (Pyrex) formers, each with a NiCr wire coil wound around, heated by Joule effect and surrounded by a polished copper shield;

- **DC actuator for the correction of non-axisymmetric aberrations**: to tackle the non-axisymmetric distortions, the TCS baseline solution for Advanced Virgo was the SS, as seen in section 3.4.5. DC actuators as **M**icro **E**lectro-**M**echanical **S**ystems (MEMS) or **D**eformable **M**irror (DM) can be an alternative solution. In the framework of adaptive optics for interferometric detectors, these devices would be used to perform high precision laser beam shaping. In fact, with a DM it is possible to modify the phase of an impinging Gaussian laser beam so to obtain, on the image plane, an intensity profile matching the desired one. This solution has the advantage of the DC operation (no noise is introduced) and the flexibility to adaptively modify the corrective pattern. Chapter 5 is fully dedicated to it being one of the cornerstones of this thesis.

Chapter 4

Commissioning of the AdV+ TCS toward O4

In the previous chapters, we have seen why the TCS is so important to keep the ITF in its working point. The high input power and the marginal stability of the recycling cavities make the thermal effects more relevant, the commissioning phase of TCS is crucial to improve the performance of the ITF. In this chapter the activities performed on the AdV+ TCS are reported in detail. In the first part all the work performed on-site for the TCS sensing and actuation pre-commissioning phase will be described. In the second part all the tests performed on the TCS actuators in order to make them fully capable to compensate the optical aberrations and cold defects are detailed. Finally, the TCS effects on the ITF will be shown.

4.1 HWSs pre-commissioning

As described in section 3.4.1, the sensor implemented in AdV+ to monitor the thermal state of the mirror are the HWSs. The two on-axis HWSs and their SLED probe beams at 790 nm are hosted on the INJ and DET areas, called **E**xternal **I**njection **B**ench (EIB) and **E**xternal **D**etection **B**ench (EDB), to sense the thermal lenses on the WI and NI mirrors, respectively. They propagate overimposed to the main laser beam through the PRC and SRC up to the HR surfaces of the input mirrors that reflects the beam toward the HWSs allowing for a double pass measurement. The arrangement of the HWS setup optics on EIB and EDB are shown in Figure 4.1 and 4.2. The HWS probe beams needed to be aligned on the mirrors in as such way that they are reflected back toward the sensor itself. Then, the centring of the HWS beam on the center of the mirror has to be verified and eventually optimized. Both of these activities are fundamental to make the sensor fully operational. The technique that has been applied to recover the back-reflected beam on the HWS involves the overlapping of HWS beams on the green beam used to control the FP cavities during the acquisition of the working point of the ITF [127]. During this operation, the HWS reflected beam is monitored through a CCD replacing the HWS. The alignment is obtained by applying iterative shift and tilt of the beam acting on the optics along the probe beam path, EIB_Har_M0 and POL1 on EIB and EDB_Har_M1 and EDB_Har_M2 on EDB.

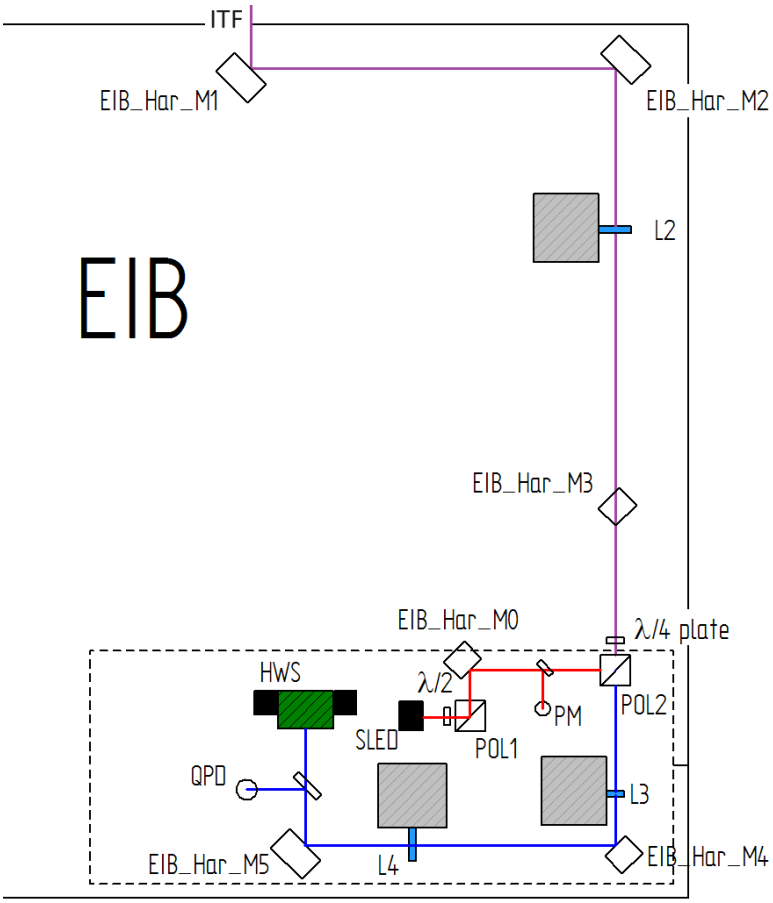

Figure 4.1: *Optical layout of the HWS setup on EIB. The red and blue lines represent the path of the ongoing beam and back-reflected one, respectively. The violet line indicates the common path between the two beams.*

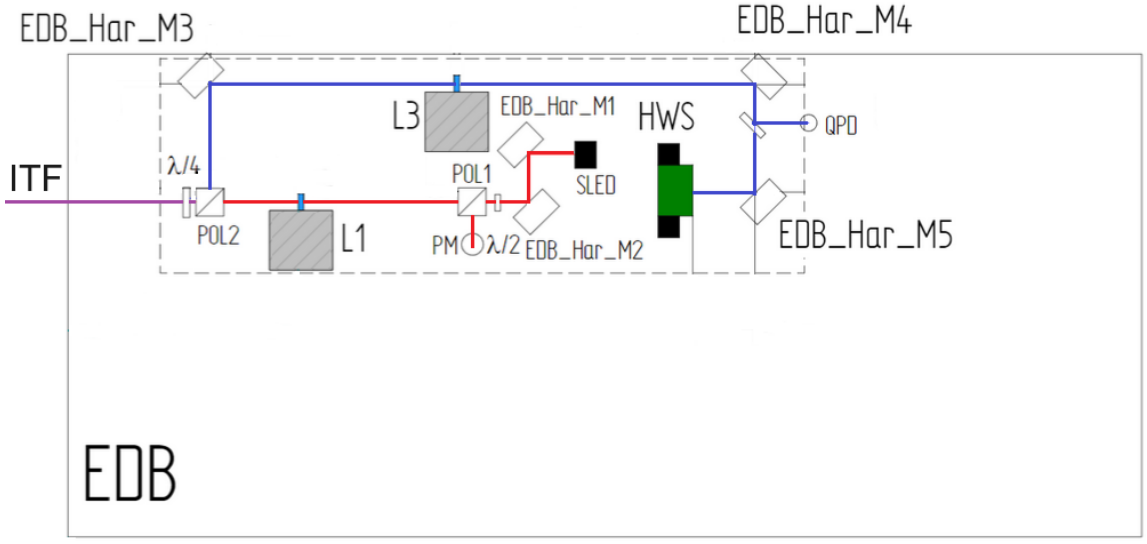

Figure 4.2: *Optical layout of the HWS setup on EDB. The red and blue lines represent the path of the ongoing beam and back-reflected one, respectively. The violet line indicates the common path between the two beams.*

An example of the results of this procedure application is shown in Figure 4.3.

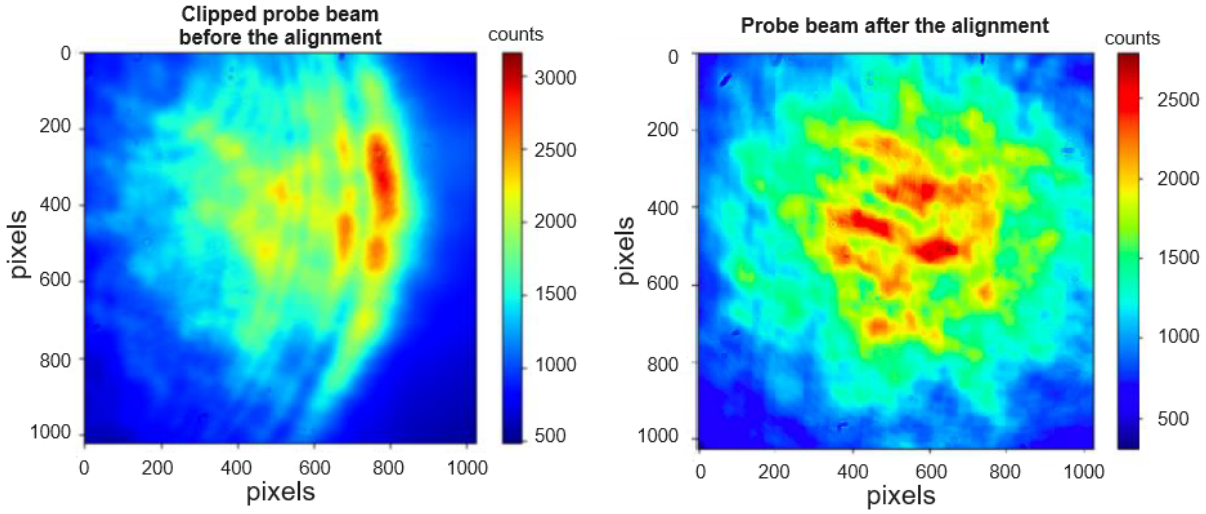

Figure 4.3: *CCD image before and after the recovery of a clipped beam.*

Once completed this phase, the alignment of the HWS beam center on the mirror needs to be checked. The most suitable actuator for achieving this purpose is the RH, as it is geometrically centred around the mirror. The quasi-perfect spherical diverging lens induced by the RH in the mirror substrate causes a spherical wavefront aberrations in the HWS beam, measured by the sensor. The coordinates of the maximum of the OPL identify the center of the mirror in the HWS reference frame. In Figure 4.4-left it is shown an example of this HWS wavefront map when the NI RH has been switched on. In this case the center of the mirror is in the bottom part of the HWS beam limiting the observable areas of the mirror close to the center. Thus, in order to improve the centring of the HWS beam, the EIB_Har_M0 on EIB and EDB_Har_M1 on EDB are used to steer the beam. An example of HWS beam fully commissioned and ready to be used is visible in Figure 4.4-right.

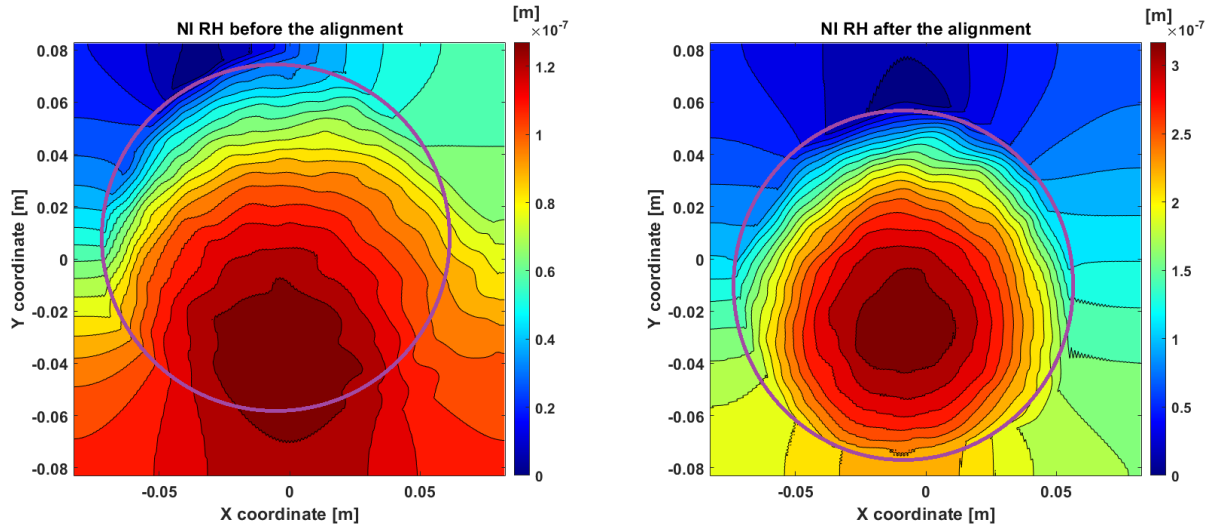

Figure 4.4: *HWS-DET maps with the NI RH switched on before and after the alignment procedure. The violet circle represents the areas of significance on the sensor, which are identified by the locations where the contour lines break.*

4.2 Actuators pre-commissioning

With the HWS fully operational, the CO_2 laser actuators have been commissioned.

4.2.1 Alignment

The first pre-commissioning phase for the CO_2 actuators involved the relative alignment of the DAS rings, and then of the DAS and the CH. Then they need to be aligned on the center of the CP.
The relative alignment among the actuators is obtained using the diagnostic system described in section 3.4.4. The heating induced by the CO_2 projected on the black cardboard screen is recorded by the infrared camera. An example of the infrared camera images set is shown in Figure 4.5. This system is periodically used to verify the relative alignment between the actuators and their positioning.

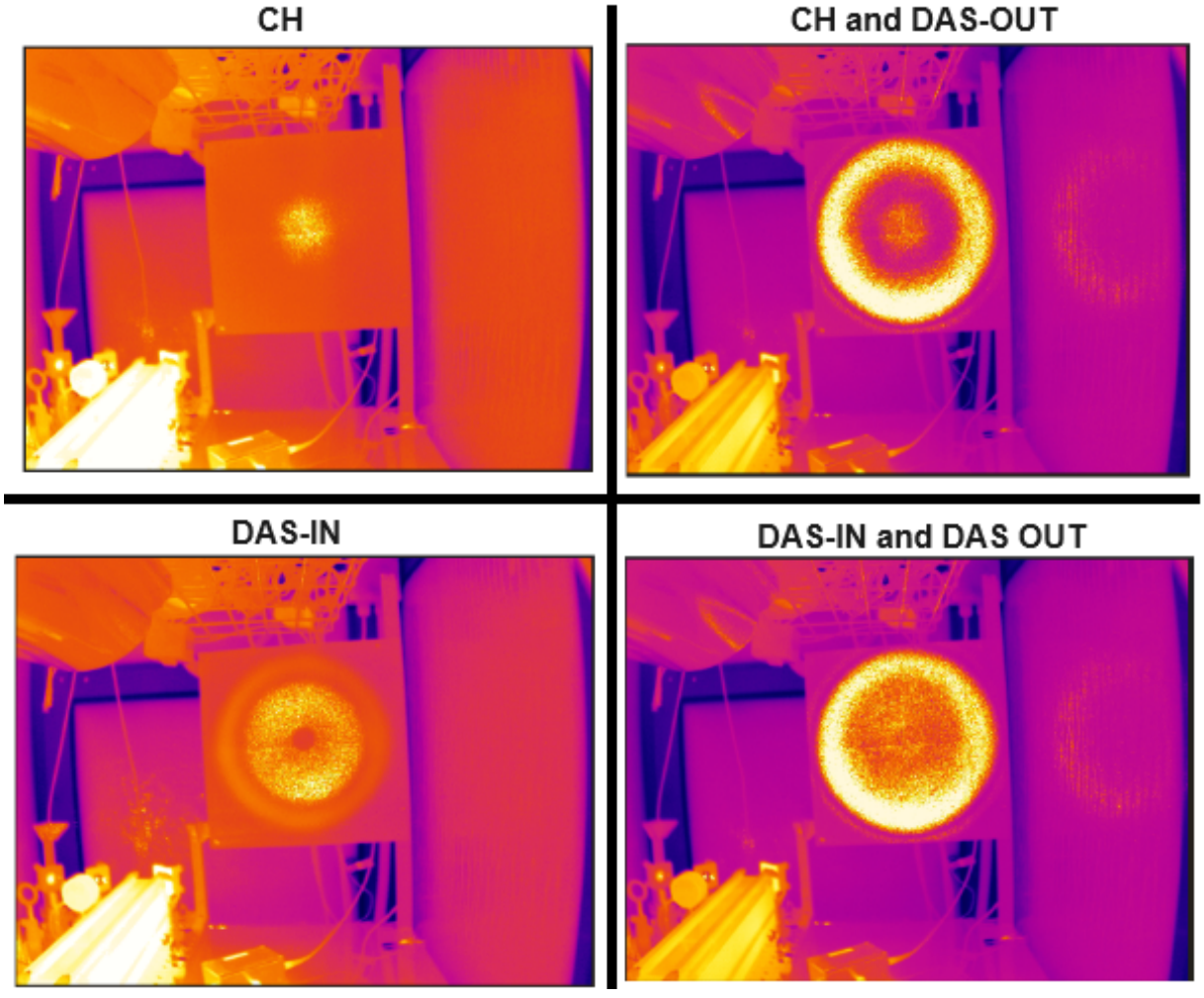

Figure 4.5: *Images acquired with the infrared camera of all actuators, they are used to check their position.*

Given the scheme in Figure 3.12, the relative alignment between the two DAS rings is obtained by tilting POL4 in order to overimpose the **DAS-Out**er ring (DAS-OUT) on the **DAS-In**ner ring (DAS-IN). Once the two rings composing the DAS are aligned, the BS-REC can be used to overimpose the DAS beams on the CH one. Once the alignment

of the DAS and CH is finalized, the centring on the CP is performed by using the HWS. In particular, the CH actuator is used since its time constant is shorter than the DAS one ∼1 hour instead of ∼2 hours. The barycentre coordinates of the OPL induced by the RH and CH wavefront map are estimated and compared. The actuators are considered aligned when the differences between the coordinates are within 5 mm. The HM is used to move the actuators together in order to align them on the CP if needed. The BS-REC and the HM are motorized in order to perform some alignment check and eventually, to adjust it without a direct intervention on the CO_2 benches.

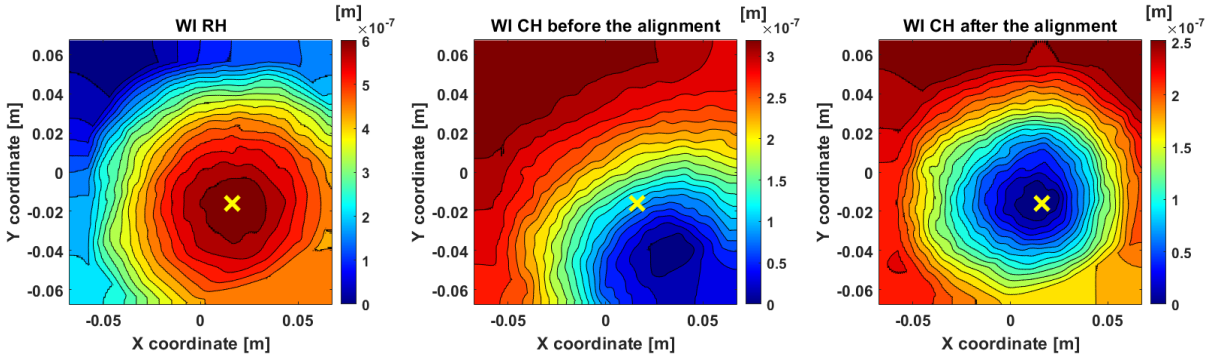

Figure 4.6: *HWS maps of WI RH and CH before and after the actuators alignment procedure. Left: in the HWS map the red area is the OPL induced on the WI by the RH and the yellow cross indicates the WI's center. Middle: in the HWS map the blue area is the OPL induced on the WI by the CH before the alignment. Right: in the HWS map the blue area is the OPL induced on the WI by the CH after the alignment procedure.*

4.2.2 DAS power distribution

The efficiency of the TCS CO_2 actuators is directly related to the quality of the laser beam: the higher is the Gaussianity of the beam, the better is the quality of the corrective heating pattern. The CO_2 lasers used in Advanced Virgo TCS exhibit a very good power stability, much less prone to room temperature fluctuations than the Virgo+ lasers. However, CO_2 lasers typically emit beams with a larger content of HOMs with respect to solid state lasers. As already mentioned above, in order to improve the beam shape of the laser, a spatial beam filter has been placed on the optical benches. This led to an improvement of the beam shape, at the cost of a consistent reduction of the available laser power. However, the quality of the resulting compensating pattern is still far from the optimal shape and the DAS rings can present an asymmetry of the power distribution. The power distribution of the DAS-OUT is measured with a CCD near the mask used to shield the bright spot of the laser, while the power distribution of the DAS-IN is measured by the CO_2 beam profiler after the diagnostic telescope - see Figure 3.13. Starting from these measurements, it is possible to deduce the OPL induced by the DAS rings, shown in Figure 4.7, which will be useful for the characterization of the actuator. If needed the power distribution is corrected by acting on the mirror before the lens-axicon doublet along the optical path of the DAS-OUT and by moving the lens before the axicon on the DAS-IN. The power distribution and the alignment check have been repeated several times during the commissioning phase, allowing us to refine the procedure and have the actuators centred on the CP within a 5 mm tolerance. This well-established procedure can be repeated whenever it is deemed necessary to check the status of the actuators.

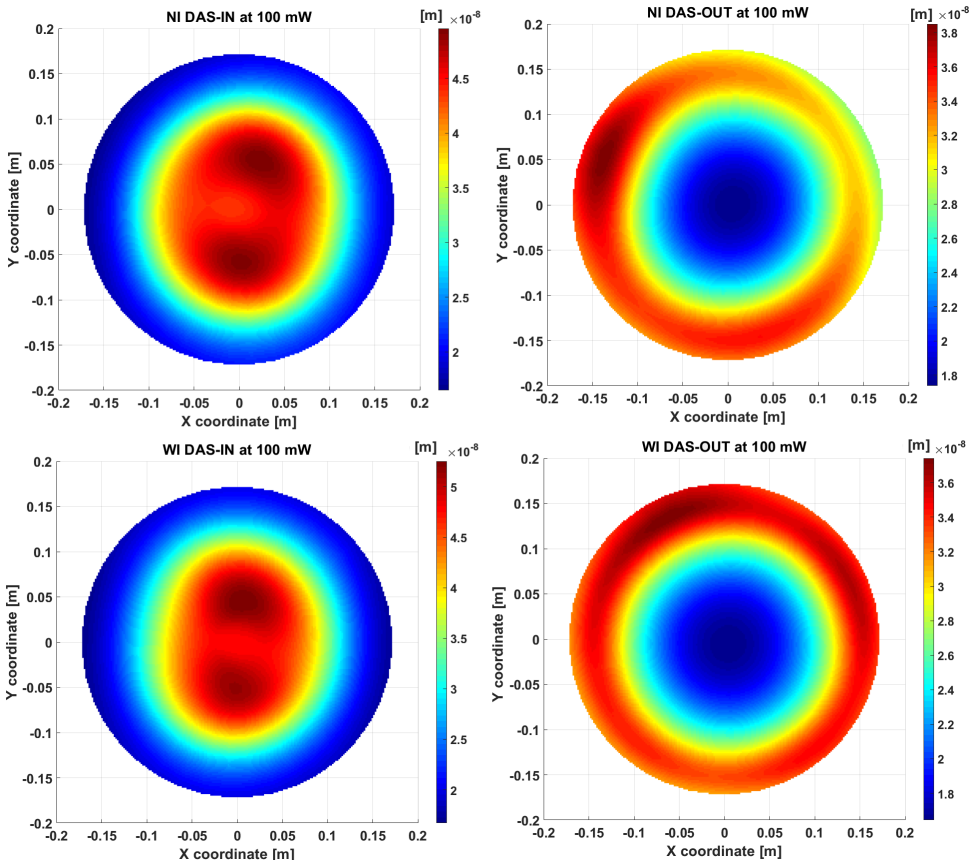

Figure 4.7: *OPL induced by the actuator NI and WI DAS rings.*

4.2.3 Actuators' characterization

The actuator's dynamic characterization is fundamental to develop the best thermal compensation strategy. Indeed, the OPL induced by each actuator was measured to be included in the optical simulations, which are fundamental to tune the working point of the thermal actuators taking care of the cold defects and compensating for the thermally driven effects. As already mentioned, the DAS is used to null the temperature gradient in the optic caused by the main laser beam, while the purpose of the CH is to mimic it. In general, the parameter used to quantify the thermal effect and thus OPL induced by the thermal actuator in the optics is the *Gaussian weighted curvature*. This quantity can be easily estimated for the CH beam, characterized by a Gaussian intensity profile, but not for the DAS, as will be discussed later.

CH's characterization

The CH-induced OPL maps acquired with the HWS are processed in order to evaluate the Gaussian weighted curvature. The procedure applied to extrapolate the curvature induced by the CH and DAS is described in the following:

1. the barycentre of the wavefront map is calculated;
2. the row and the column of the barycentre are selected;
3. a Gaussian weighted fit is done - both for the column and for the row - implementing 1D quadratic fit with Gaussian weights of Matlab;

4. the curvature corresponds to the coefficient of quadratic term of the Gaussian weighted fit;

5. the final curvature is the average between the curvature extracted by the barycentre row and the column one.

The 1D Gaussian weighted curvatures induced by CH thermal lensing have been extracted from the HWS maps at different powers - see Table 4.1. For example, the curvatures induced by the NI CH at 670 mW and by WI CH at 650 mW as a function of time are shown in Figure 4.8.

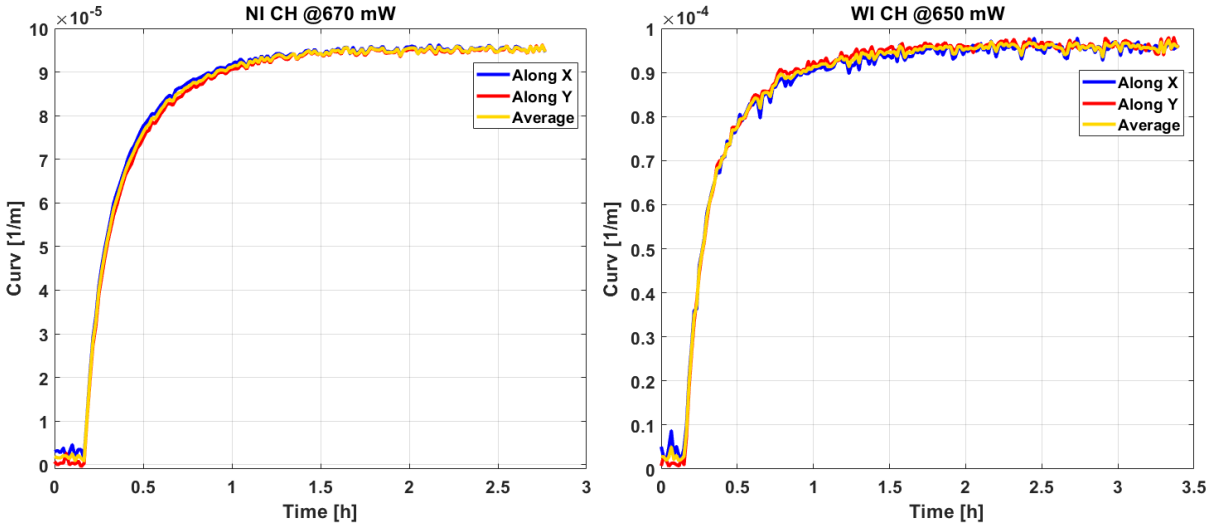

Figure 4.8: *On the left: 1D Gaussian weighted curvatures induced by NI CH on the CP at 670 mW. On the right: 1D Gaussian weighted curvatures induced by WI CH on the CP at 650 mW. The blue lines represent the curvature extracted from the barycentre row and the red lines from the column one. The yellow lines are the average values.*

Test Mass	Power [W]	Duration	Steady state value [1/m]
NI	0.115 ± 0.010	2 h 35 min	$(0.18 \pm 0.02) \cdot 10^{-4}$
NI	0.160 ± 0.010	3 h 28 min	$(0.24 \pm 0.02) \cdot 10^{-4}$
NI	0.220 ± 0.010	2 h 21 min	$(0.36 \pm 0.04) \cdot 10^{-4}$
NI	0.670 ± 0.010	2 h 47 min	$(1.0 \pm 0.1) \cdot 10^{-4}$
WI	0.086 ± 0.010	3 h 34 min	$(0.11 \pm 0.01) \cdot 10^{-4}$
WI	0.220 ± 0.010	3 h 08 min	$(0.34 \pm 0.04) \cdot 10^{-4}$
WI	0.446 ± 0.010	2 h 51 min	$(0.66 \pm 0.07) \cdot 10^{-4}$
WI	0.650 ± 0.010	3 h 25 min	$(0.95 \pm 0.09) \cdot 10^{-4}$

Table 4.1: *List of measurements performed with the NI and WI CHs at different powers. Their respective durations are indicates in the second column. In the third one the curvature values reached at steady state. The errors associated to the power and to the curvature values depends on the power meters, and on the uncertainty on the magnification of the HWS telescopes of the order of* $\pm 5\%$.

The CH dynamics is obtained by plotting the values reached by the curvature at steady state as a function of power. The resulting trend is shown in the figure 4.9.

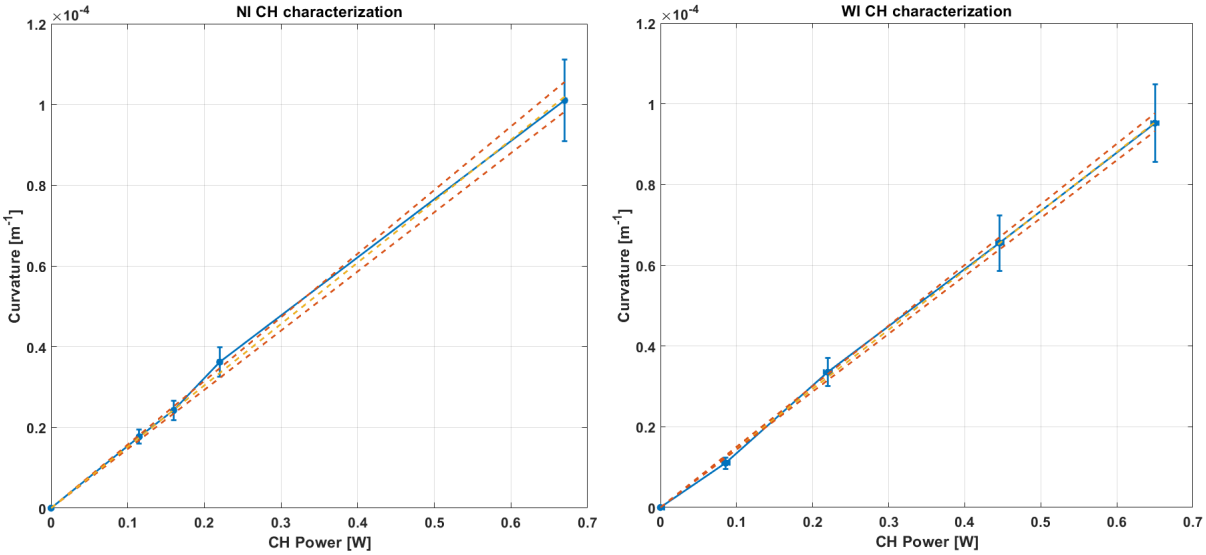

Figure 4.9: *Dynamics of NI CH on the right and of WI CH on the left. The blue points are the data shown in Table 4.1, the yellow lines represent the linear fit* $f(x) = a \cdot x$ *and the red lines are the 95% confidence bounds. For the NI CH, the quadratic term is* $a = 1.41 \cdot 10^{-4} \frac{1}{m \cdot W}$ *with the confidence bounds* $[1.36 \div 1.46] \cdot 10^{-4} \frac{1}{m \cdot W}$*, while for the WI CH,* $a = 1.47 \cdot 10^{-4} \frac{1}{m \cdot W}$ *with the confidence bounds* $[1.43 \div 1.50] \cdot 10^{-4} \frac{1}{m \cdot W}$*. Moreover, the NI and WI power-to-curvature coefficients agree within the errors.*

Considering a reasonable power uncertainty of approximately ±10 mW, a comparison between the steady state measured maps and Hello-Vinet analytical solution - see section 3.2.2 - indicates that the effective beam size on the North and West CPs is (60 ± 1) mm [128] instead of 50 mm. This CH beam size appeared to be consistent assuming an error in the positioning of the CH telescope lenses of about 2%. Thus, a reasonably agreement between the experimental data and the simulations is observed, see Figure 4.10.

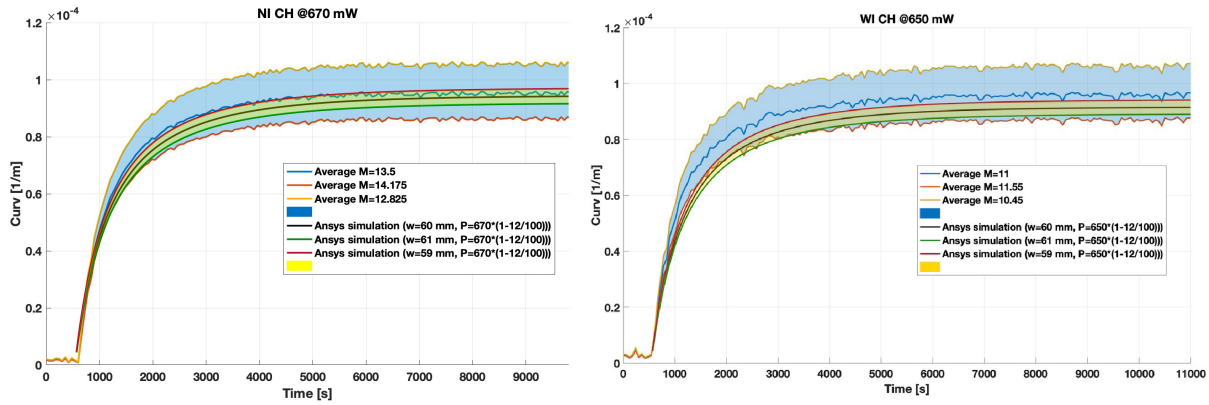

Figure 4.10: *Comparison between experimental data rescaled by the magnification factor M on the CP represented by yellow, red and blue lines and the ANSYS simulations represented by violet, green and purple, for the NI CH on the right and for the WI CH on the left.*

DAS's characterization

As anticipated, the OPL induced by the DAS cannot be parametrized using the Gaussian weighted curvature. Each DAS is made of two independent contributions - the power of DAS-IN and the DAS-OUT one - thus the system is not uniquely determined and the significance of the curvature is not the same over the full parameter space [129]. To verify the reliability of the OPL maps obtained by FEA simulations the HWS measurements have been done. Thus, the inner and outer rings have been characterized separately measuring the OPL induced on the CP by varying the applied power. Firstly, it has been confirmed that the OPL induced by the ring scales linearly with the power. An example is shown in Figures 4.11 and 4.12, the RMS of the difference between rescaled maps computed as $map(P_1) - map(P_2) \cdot \frac{P_1}{P_2}$ - where the power $P_1 > P_2$ - should be compatible with zero.

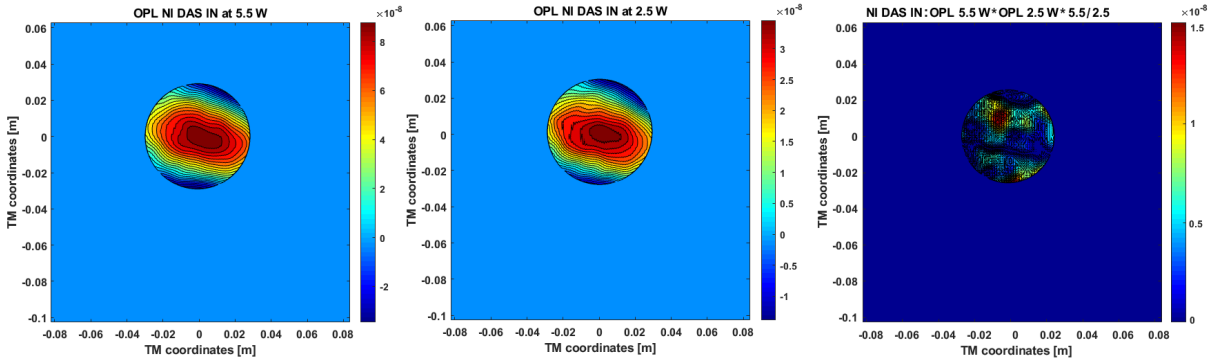

Figure 4.11: *On the left: OPL maps measured by HWS of the NI DAS-IN at 5.5 W. On the middle: OPL maps acquired by HWS of the NI DAS-IN at 2.5 W. The difference between the two rescaled maps gives* $RMS = 1.5 \cdot 10^{-9} m$.

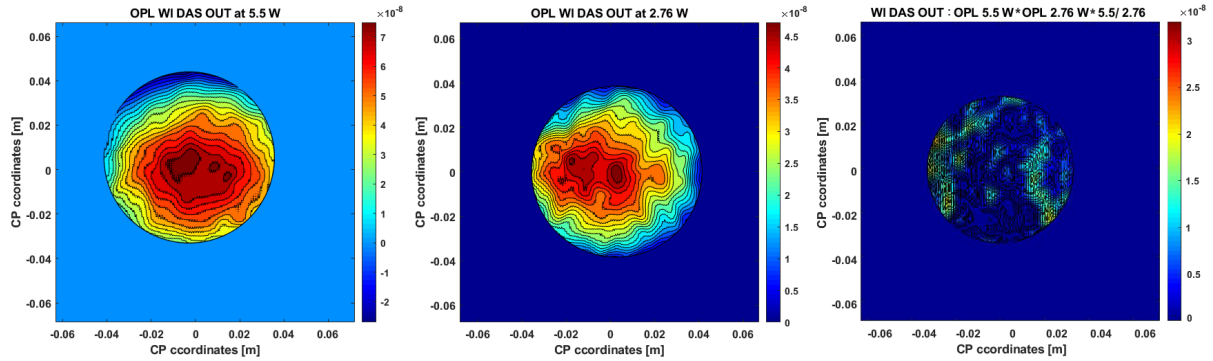

Figure 4.12: *On the left: OPL maps measured by HWS of the WI DAS-OUT at 5.5 W. On the middle: OPL maps acquired by HWS of the WI DAS-OUT at 2.76 W. The difference between the two rescaled maps gives* $RMS = 3.4 \cdot 10^{-9} m$.

Unfortunately, since the areas probed by the HWS is small compared to the CP surface i.e., the HWS probe beam radius is ∼100 mm compared to 175 mm of the ITF optics, the HWS map contains a small portion of the mirror. However, comparing the central part of the OPL maps in Figure 4.7 with the ones measured by HWS in Figure 4.13 for the case involving the NI DAS-IN and Figure 4.14 for the case involving the WI DAS-OUT, a very good agreement is obtained.

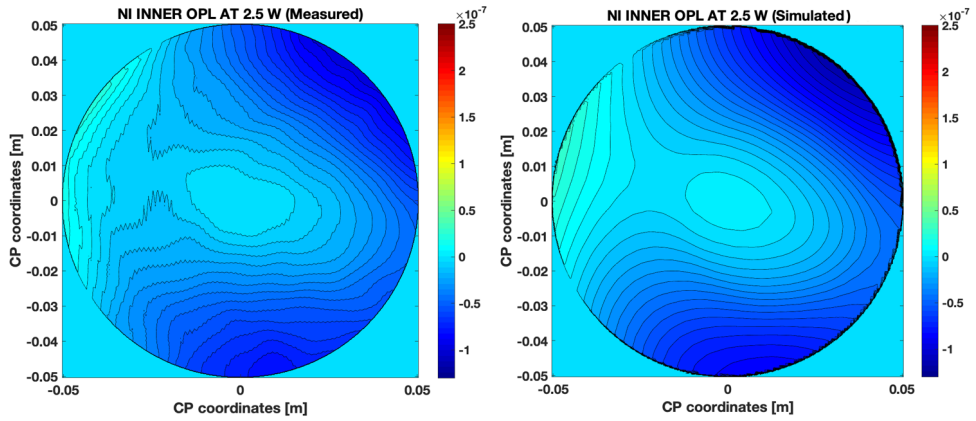

Figure 4.13: *On the left: the measured OPL induced by NI DAS-IN at 2.5 W. On the right: the simulated one. The RMS of the difference between experimental and simulated maps is* $8.55 \cdot 10^{-9}$ *m.*

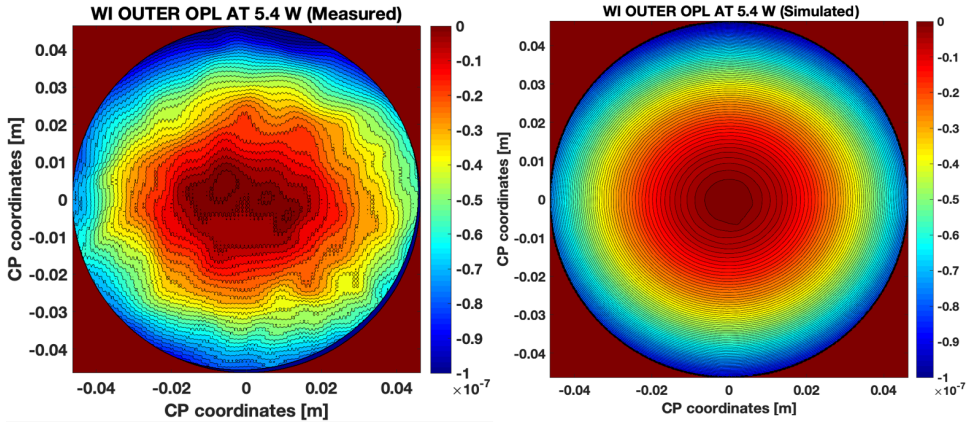

Figure 4.14: *On the left: the measured OPL induced by WI DAS-OUT at 5.4 W. On the right: the simulated one. The RMS of the difference between experimental and simulated maps is* $8 \cdot 10^{-9}$ *m.*

A new actuator: CHRoCC

During the commissioning phase, the need of the use of a new thermal actuator - referred to as **C**entral **H**eating **R**adius **o**f **C**urvature **C**orrection (CHRoCC) - was highlighted to match the PRC and SRC[8]. The CHRoCC projects a thermal radiation emitted by ceramic heater within an elliptical reflector, to induce a converging lens inside the optics. Two different CHRoCCs are installed in the ITF, one shines the POP and the other one the HR surface of the SRM. The CHRoCC creates a converging lens on the POP, that means decreasing the PRM RoC or makes SRM RoC larger in order to equalize with current PRM RoC. A scheme of the actuation is shown in figure 4.15.

[8]The RH installed around the PRM was designed to lower the mirror RoC from 1477 m to the design value of 1430 m, but for practical reason related to the overheating of the mirror suspension system, it has been decided to keep it off.

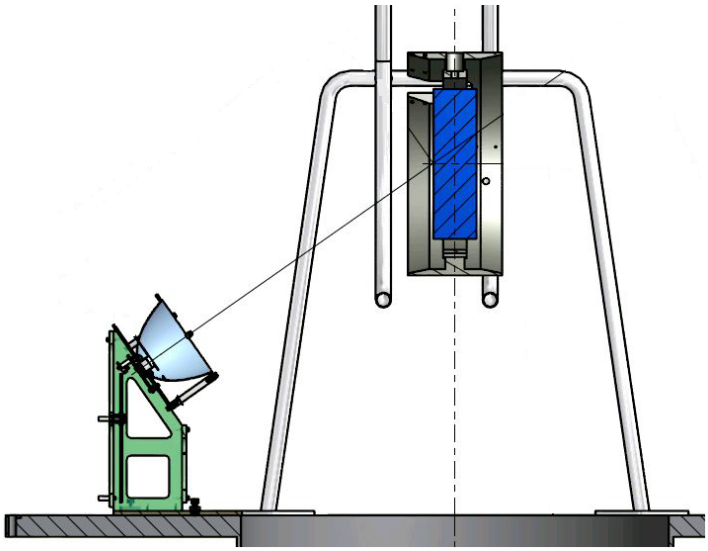

Figure 4.15: *The scheme of the actuation of the CHRoCC actuator.*

The CHRoCCs alignment on the center of the optics have been checked by using the same procedure applied for the TCS actuators described in section 4.2.1, namely comparing the barycentre coordinates of the OPL maps measured by HWS switching on the PRM RH and PRM CHRoCC shown in Figure 4.16. From this measurement, it resulted that the CHRoCC is aligned within 5 mm.

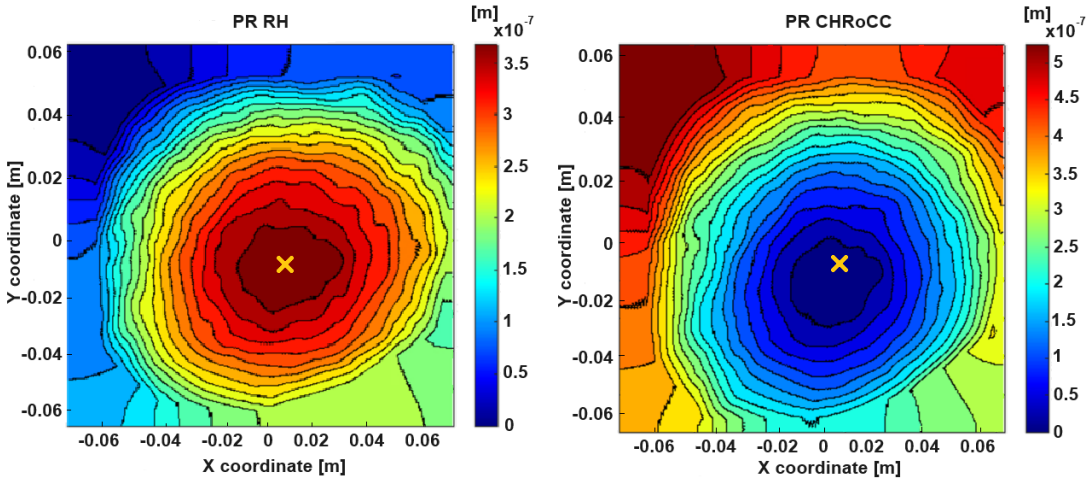

Figure 4.16: *Left: in the HWS map the red area is the OPL induced on the PRM by the RH and the yellow cross indicates its barycentre. Right: in the HWS map the blue area is the OPL induced on the PRM by the CHRoCC the yellow cross indicates the RH's barycentre.*

The procedure used for the characterization of the CH has been also applied for the PRM CHRoCC characterization. The 1D Gaussian weighted curvatures induced by CHRoCC thermal lensing for different powers are summarized in Table 4.2. The CHRoCC dynamic is shown in Figure 4.17. Given the cold PRM RoC that is equal to 1477 m and the design PRM RoC equal to 1430 m, the focal length needed to decrease the PRM RoC is 45 km corresponding to a curvature of $1.12 \cdot 10^{-5} \frac{1}{\mathrm{m}}$, a $D = 2.24 \cdot 10^{-5} \frac{1}{\mathrm{m}}$. Thus, the power to be applied to the actuator is $P = 783$ mW.

Power [W]	**Curvature [1/m]**$\cdot 10^{-5}$	**Dioptres [1/m]**$\cdot 10^{-5}$	**Focal length [km]**
1.6268	2.19 ± 0.003	4.38 ± 0.06	22.8 ± 0.3
2.4264	3.39 ± 0.03	6.78 ± 0.06	14.8 ± 0.1
2.8820	4.11 ± 0.04	8.22 ± 0.08	12.2 ± 0.1
3.6351	5.25 ± 0.06	10.5 ± 0.1	9.52 ± 0.09
4.1838	6.04 ± 0.04	12.08 ± 0.08	8.28 ± 0.06

Table 4.2: *List of all measurements performed with the PRM CHRoCC at different powers. In the second column the curvature value at steady state are listed. In the third column the dioptres $D = 2 \cdot Curvature$ are included. Finally, in the last column the focal lengths $f = 1/D$ are itemized. The curvature uncertainty is related to the uncertainty of $\pm 5\%$ on the magnification of the HWS telescopes.*

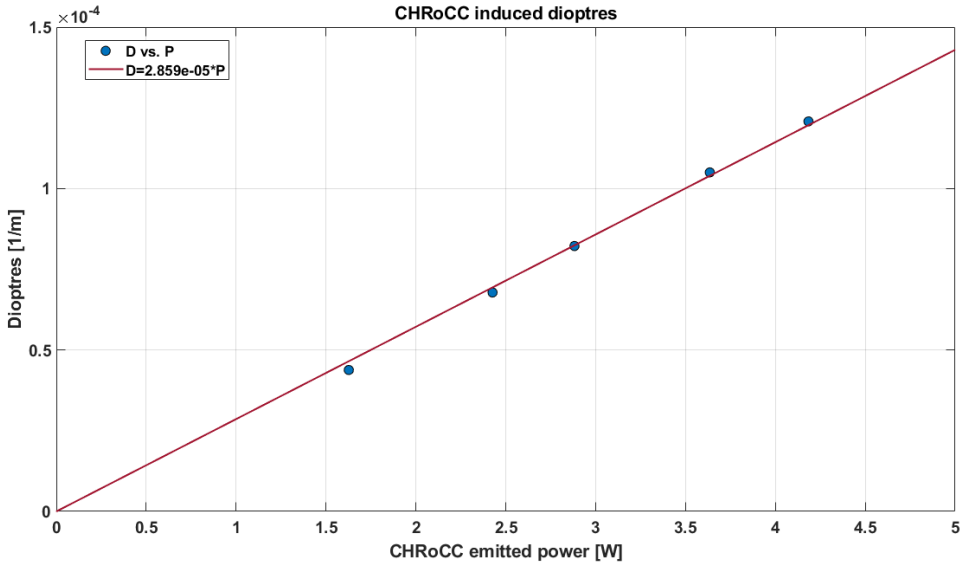

Figure 4.17: *Dynamics of PRM CHRoCC. The blue points indicates the dioptres shown in Table 4.1, the red line represents the linear fit $f(x) = a \cdot x$ with $a = (2.86 \pm 0.07) \cdot 10^{-5} \frac{1}{m \cdot W}$.*

4.3 NI CP cold lens estimation and correction

The most offending cold lens in AdV+ optics is the NI CP converging lens with a focal length declared by the LMA equal to ∼75 km - see Figure 4.18. The consequence of cold defects is that the cavities are prone to generating HOMs, which are subsequently recycled due to the low stability of the recycling cavities. This results in a mismatch of cavity modes between the TEM00 laser mode and the TEM00 mode in the PRC and SRC, causing the coupling coefficient between them to become less than one [130]. Therefore, compensating for cold defects is crucial for bringing the ITF to its optimal working point. During the commissioning phase toward O4, a measurement campaign has been performed to measure the NI CP cold lens. Firstly, the mode matching measurements performed on both North and West cavities provides the direct estimation of the cold focal length of ∼30 km, a factor 2 lower than the declared one.

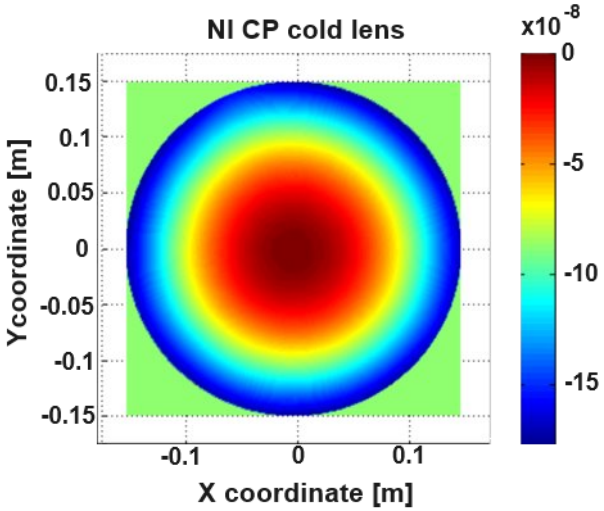

Figure 4.18: *NI CP cold lens map.*

Once the focal length of the NI CP is determined, the NI DAS actuators power has been settled in order to generate the diverging lens needed to compensate for the cold one. As starting point, the DAS power was determined by minimizing the Gaussian weighted RMS of the total OPL increase computed by summing the cold lens OPL to the DAS OPL maps scanned over inner and outer rings power. The values of 0.075 W and 2 W for the inner and outer ring, respectively, have been identified [131]. These values are in agreement with the power settings resulting from the DAS power tuning performed during the commissioning activity. The DAS powers currently injected into the ITF are 0.08 W and 1.8 W for the NI DAS-IN and DAS-OUT, respectively.

4.4 ITMs coating absorption estimation

The power circulating in the FP cavities and the power absorbed by the optics are given by the two following equations 4.1 and 4.2, respectively [132]:

$$P_{cav} = \frac{P_{YAG}}{2}\frac{2G_{PR}F}{\pi}, \tag{4.1}$$

$$P_{abs} = P_{cav}\alpha, \tag{4.2}$$

where P_{YAG} is the ITF input power, G_{PR} is the CA gain for the PRC, F is the finesse and α is the HR coating absorption coefficient of the mirror. Therefore, an accurate estimate of the absorption coefficient is essential for characterizing the main laser thermal effects. The data from the two HWS setups in the recycling cavity have been used for the optical characterization of the ITMs, namely to measure the average optical absorption level. Due to the optical layout of the HWS probe beams in the recycling cavities, also the CP, BS, PRM and SRM thermal lens are probed, but their contribution is expected to be negligible, due to the low power hitting these optics compared to that stored in the arm cavities. The adopted strategy to perform the HWS measurements of the main ITF beam thermal effect is described below:

1. the ITF is brought to the final working point, also known as CARM null - see section 2.5.

2. After reaching the steady state in ∼2 hours, the HWS reference wavefront is acquired and the HWS "live" acquisition starts;

3. After that, the ITF is disengaged from its working point without misaligning the mirrors.

In all measurements, the curvature extracted from the HWS phase maps has been compared to FEA simulations, where the absorption level was kept as a free parameter. Finally, the best fit has been evaluated by a χ^2 minimization procedure. The absorption values have been measured in some occasions with different input power - see Table 4.3. The estimated HR coating absorption remained constant over the years.

ITM	**2023 measurements of α [ppm]**	**2018 measurements of α [ppm]**
NI	0.60 ± 0.09	0.65 ± 0.05
WI	0.29 ± 0.03	0.36 ± 0.07

Table 4.3: *The absorption coefficients of the ITMs performed in 2018 and 2023.*

Figures 4.19 and 4.20 show the last comparison between the measured curvature and FEA simulations for both NI and WI mirrors, respectively.

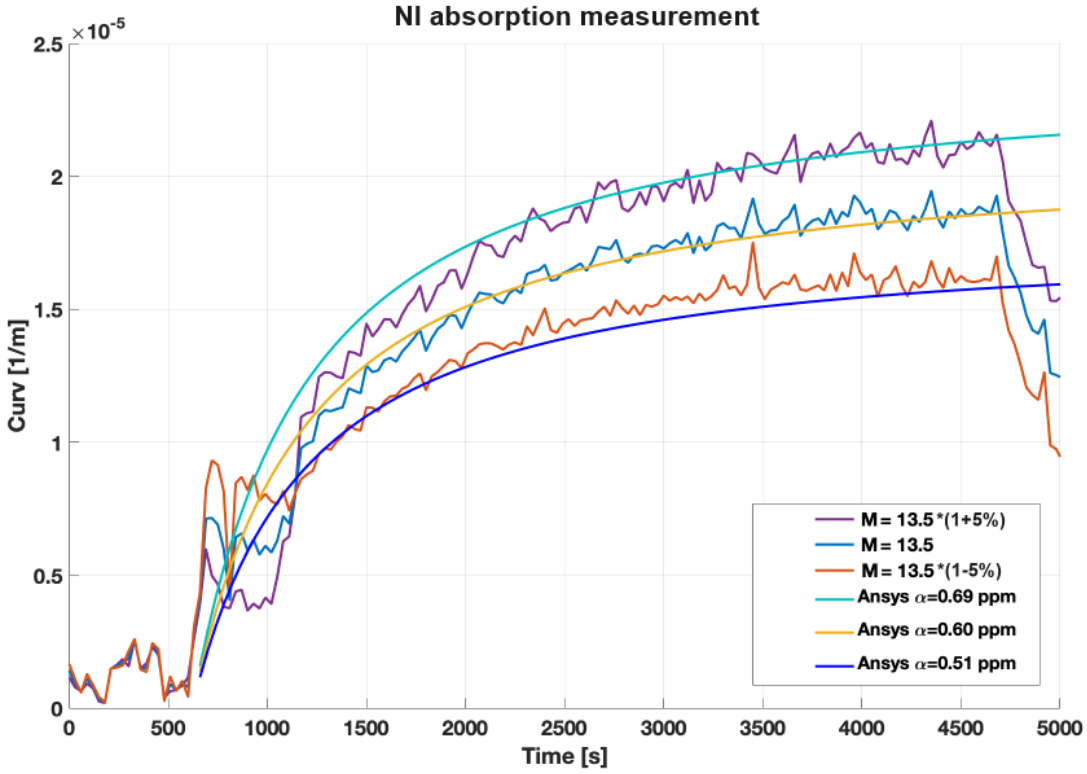

Figure 4.19: *The NI YAG measured curvature with $P_{input} = 33$ W compared to the ANSYS simulation. The light blue line is the measured curvature considering the magnification $M = 13.5$. The violet and orange lines are the measured curvature considering the uncertainty in the HWS-DET magnification telescope of ±5%, respectively. The green, yellow and blue lines are the ANSYS simulations with different absorbed powers. The mean value of the curvature at the steady state is $(1.8 \pm 0.3) \cdot 10^{-5}$ $\frac{1}{m}$.*

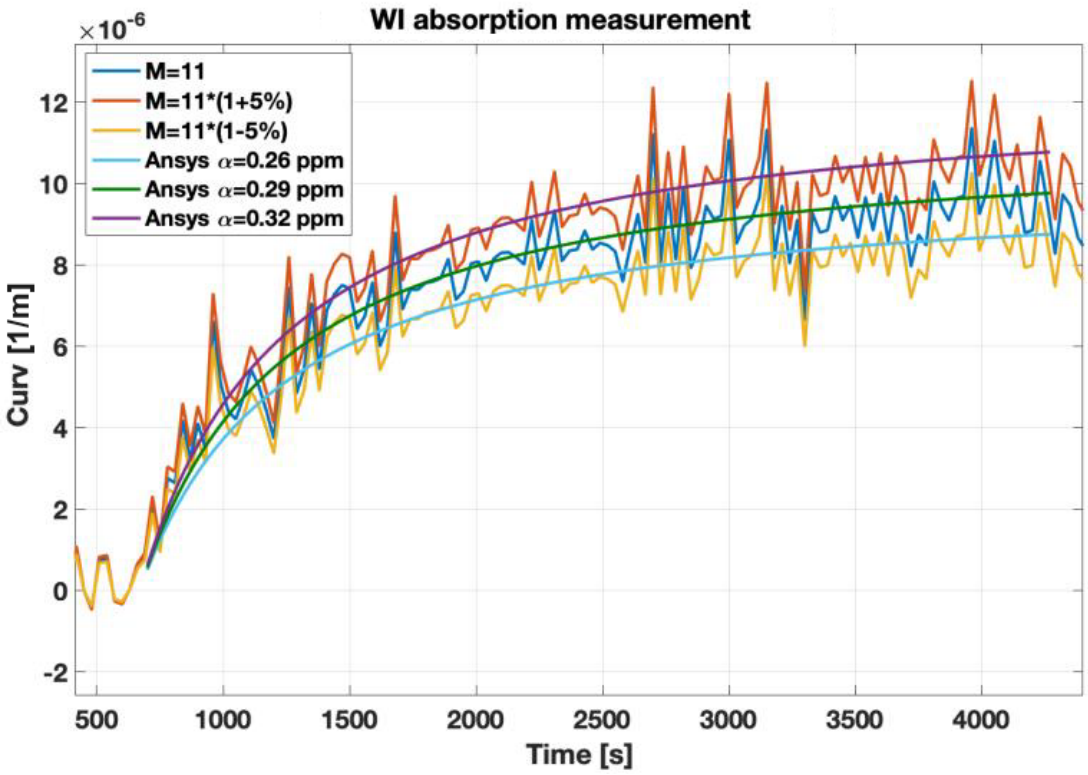

Figure 4.20: *The WI YAG measured curvature with* $P_{input} = 33$ *W compared to the ANSYS simulation. The blue line is the measured curvature considering the magnification* $M = 11$*. The orange and yellow lines are the measured curvature considering the uncertainty in the HWS-INJ magnification telescope of* $\pm 5\%$*, respectively. The light blue, green and violet lines are the ANSYS simulations with different absorbed powers. The mean value of the curvature at the steady state is* $(9.2 \pm 0.8) \cdot 10^{-6}\ \frac{1}{m}$.

Given the OPL induced by the main laser the CH power needed to mimic it can be identified following the CH characterization shown in section 4.2.3. Figures 4.21 and 4.22 show the 1D Gaussian weighted curvatures induced by NI and WI CH, respectively, at the powers required to mimic the YAG effect. The average curvature values at the steady state align with those of the main laser.

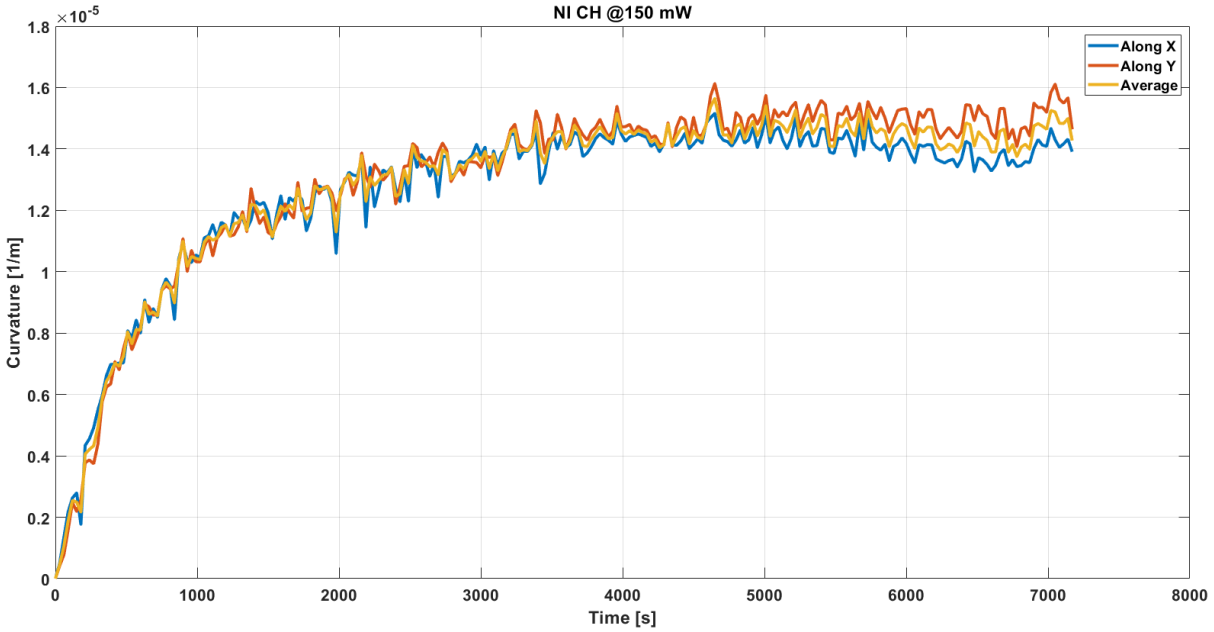

Figure 4.21: *The 1D Gaussian weighted curvatures induced by NI CH - at 150 mW - thermal lensing extracted from the HWS-DET maps. The blue line represents the curvature extracted from the barycentre row and the red line from the column one. The yellow line is the average curvature. The mean value of the curvature at the steady state is* $(1.5 \pm 0.1) \cdot 10^{-5}\ \frac{1}{m}$ *in agreement with the YAG value - see figure 4.19.*

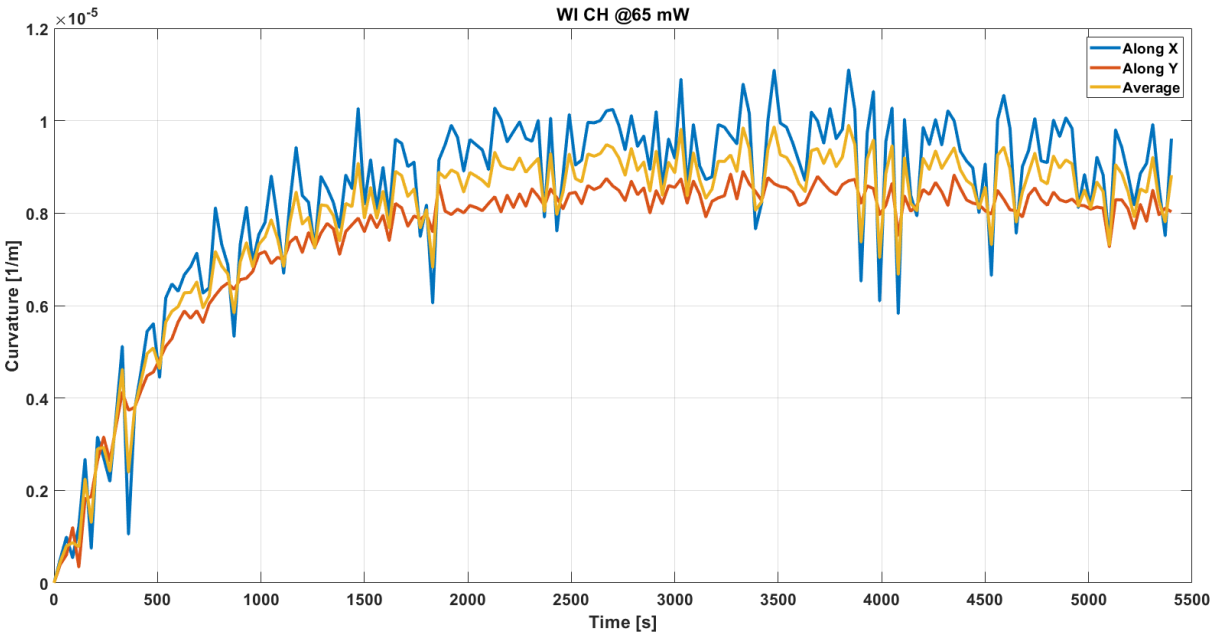

Figure 4.22: *The 1D Gaussian weighted curvatures induced by WI CH - at 65 mW - thermal lensing extracted from the HWS-INJ maps. The blue line represents the curvature extracted from the barycentre row and the red line from the column one. The yellow line is the average curvature. The mean value of the curvature at the steady state is* $(8.8 \pm 0.5) \cdot 10^{-6}\ \frac{1}{m}$ *in agreement with the YAG value - see figure 4.20.*

Once identified the CH power need to mimic the YAG effect, the HWS measurement

is used to identify the DAS powers allowing to compensate for the thermal effects induced by the main laser beam. To perform this verification, starting from a "cold" mirror i.e., with the TCS actuators turned off, the CH is switched on at its nominal power. When its curvature reaches the steady state, the DAS is switched on and DAS-IN and DAS-OUT powers tuning is carried out until the wavefront measured by the HWS becomes flat again i.e., when the curvature returns to zero. An example of this measurement is shown in the figure 4.23.

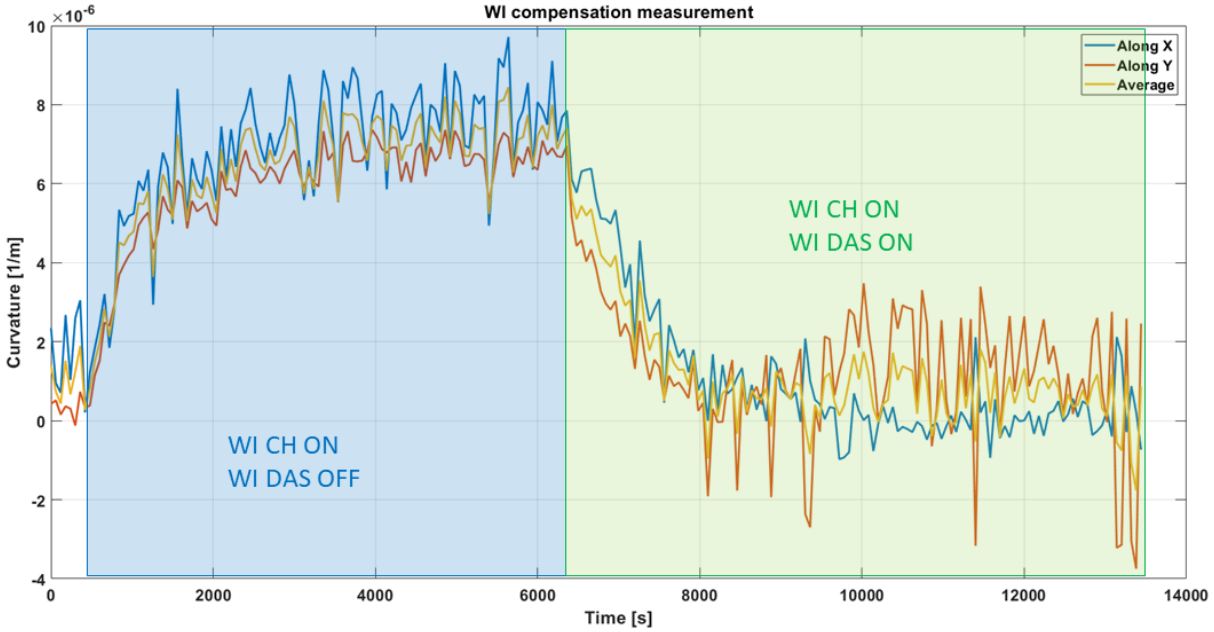

Figure 4.23: *The 1D Gaussian weighted curvatures induced by WI CHat 65 mW and compensated by WI DAS at 68 mW the inner ring and at 1.41 W the outer one. The blue line represents the curvature extracted from the barycentre row and the red line from the column one. The yellow line is the average curvature.*

4.4.1 Superposition between the main laser beam and CO_2 actuators

Once the cooling phase needed to estimate the absorption value ends, the CH is switched on in order to further check the superposition between the CO_2 actuators and the main laser beam. An example of this type of measurement is shown in Figures 4.24 and 4.25. In both YAG figures, the presence of PAs is clearly evident - top left relative to the center for the NI case, and above the center for the WI one. The barycentre coordinates are identified and compared using the same technique described in section 4.2.1. If the difference between them is higher than 5 mm the steering HM on the CO_2 bench is used to superimpose the CO_2 actuators on the main laser beam.

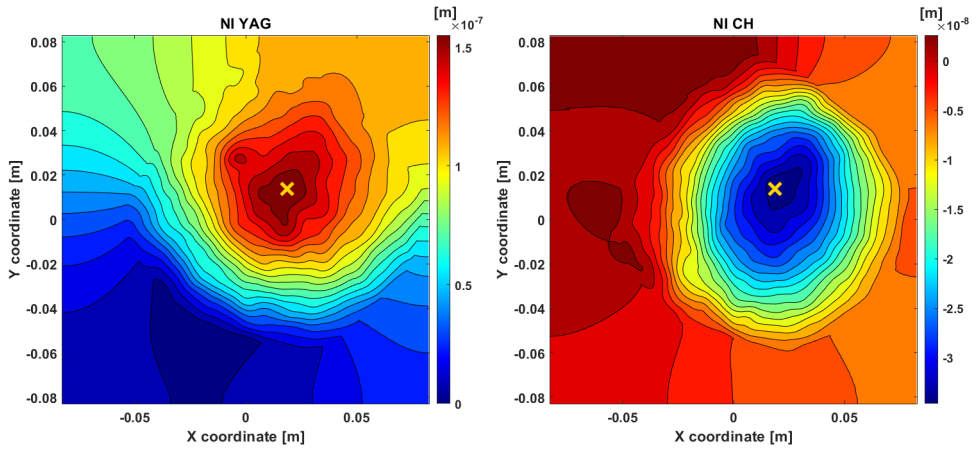

Figure 4.24: *Left: in the HWS map the red area is the OPL induced on the NI by the main laser in its cooling phase and the yellow cross indicates its barycentre. Right: in the HWS map the blue area is the OPL induced on the NI by the CH the yellow cross indicates the YAG's barycentre.*

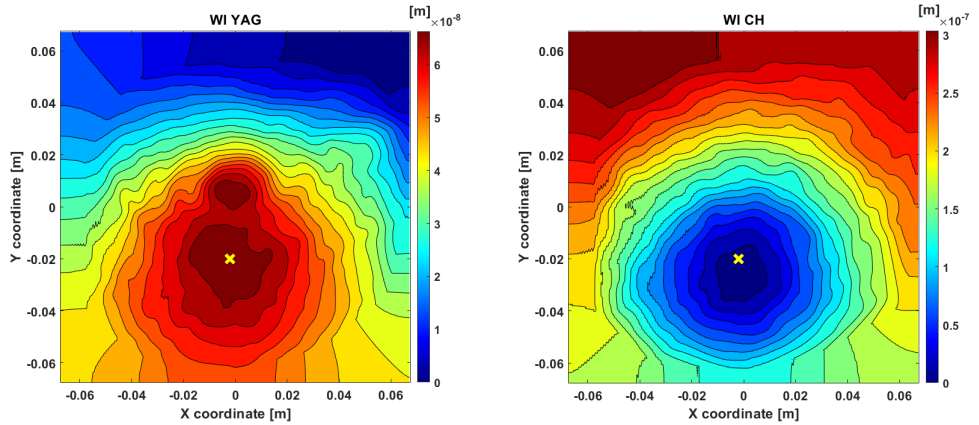

Figure 4.25: *Left: in the HWS map the red area is the OPL induced on the WI by the main laser in its cooling phase and the yellow cross indicates its barycentre. Right: in the HWS map the blue area is the OPL induced on the WI by the CH the yellow cross indicates the YAG's barycentre.*

4.5 Commissioning phase

As previously discussed, Gaussian weighted curvature cannot be considered a comprehensive parameter for assessing the quality of compensation. This test represents only an initial phase of the DAS powers tuning. In order to determine the effective compensation of the main ITF beam thermal effects it is crucial to characterize the global ITF working point. The phase of commissioning is a highly intricate and sensitive process due to the number of the observables that need to be taken into account. This complexity arises from the fact that on one hand, bringing the ITF close to its nominal condition is essential to allow to the other subsystems to work properly and on the other hand, even slight tuning of the actuator powers need an adjustment of the alignment loops and, consequently, of the working point of the ITF. A long period has been spent evaluating the impact of each thermal actuator on the ITF working point identifying the main figures of merit to

drive the TCS tuning and establishing their order of priority. The main figures of merit are listed below, the positions of the mentioned PDs is shown in Figure 2.15:

- the dark fringe power which is measured by B1p PD and we want to minimize it;
- the power circulating in the FP cavities obtained by the powers measured by B7 and B8 PDs that should be the maximum possible;
- the amplitude of the SBs in the recycling cavity detected by B4 PD, it should also be as high and stable as possible;
- the matching of the input beam and the FP cavities;
- the **C**ommon **M**ode **R**ejection **F**actor (CMRF), it quantifies the ITF ability to suppress a reject common mode noise. This noise includes all disturbances that affect both arms of the ITF equally.

Depending on the figure of merit to be considered, specific thermal actuators are employed. It is important to emphasize that all actuators directly or indirectly influence all the observables described above, but some actuators have a more direct impact than others. Furthermore, for some actuators such as the DAS and the ETM RHs, there is a further difficulty linked to the fact that they impact some figures of merit rather than others if tuned in a *common* or *differential* way. In the *common* tuning, the same power change is applied on both ITF arms, while in the *differential* one, the actuator power is increased in one arm and, simultaneously, decreased by the same amount in the other arm. When the goal is to increase the quantity of SBs in the recycling cavity, the preferred thermal actuators are those that act on the optics present in the recycling cavity, namely the CHRoCC, *common* DAS, and SRM RH. Enhancing the matching between the input beam and the FP cavities is primarily achieved by acting on the CHRoCC, DAS (*common*, *differential* or simply acting individually on NI or WI). On the other hand, to ensure that the PRC and SRC are identical and perfectly matched, the main actuators used are the PRM CHRoCC and the SRM RH. The optimization of the CMRF is accomplished through the *differential* DAS. The *common* RHs of the end mirrors are crucial to maximize the power in the FP cavities while the *differential* RHs to equalize them in order to improve the destructive interference reducing the power measured at the dark fringe. It should be noted that not only thermal actuators have an impact on these figures of merit, but also the alignment control loops of all ITF optics whose operation is influenced by the thermal actuators themselves. Thus, the ITF working point is the result of a complex interplay between the sensing and control system and the thermal compensation one. In the following, some emblematic examples of the TCS tunings are described.

4.5.1 Tuning of the DAS powers

As already mentioned, the *differential* tuning of the DAS provides the ability to optimize the CMRF. It was also discussed how the optics alignment can impact the observables used to tune the thermal actuators. Specifically, in this point, it has been observed that BS misalignment - tilting it along its vertical axis TY - can compensate for a non-perfect DAS *differential* tuning. In Figure 4.26, it is shown how that prior to employing *differential* tuning (blue curve), the CMRF reached zero, but it required setting an offset on the BS TY tilt equal to $-2 \cdot 10^{-3}$. Performing the DAS *differential* tuning the offset on the BS

tilt needed to bring the CMRF to zero is -8 · 10^{-4} (red curve), a reduction of 2.5 times compared to the initial setting.

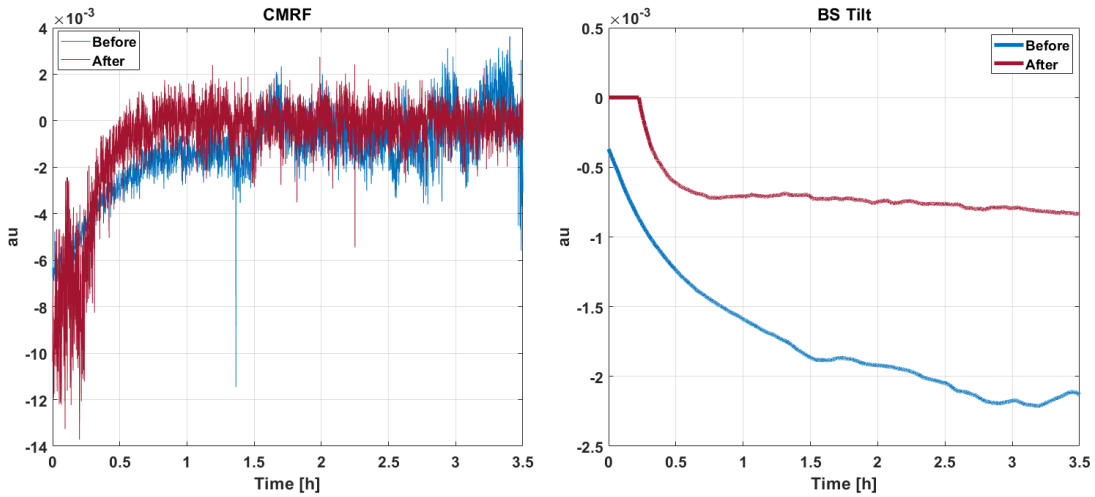

Figure 4.26: *On the right: the CMRF vs time before (blue curve) and after (red curve) acting with the DAS differential tuning. On the left: the BS TY tilt vs time is shown. The blue curve is before acting with the DAS differential tuning and the red curve is after.*

An example of the DAS *common* tuning performed to increase the amplitude of the SBs circulating in the PRC and SRC is described. In Figure 4.27, the SBs level - both the 56 MHz and the 6 MHz - measured by B4 before and after the DAS *common* tuning. It can be observed that the effect of the DAS *common* tuning was twofold: the SBs level stabilizes earlier after reaching the ITF working point, compared to the pre-tuning situation. Second one is that the SBs level is higher at the steady state after tuning the DAS.

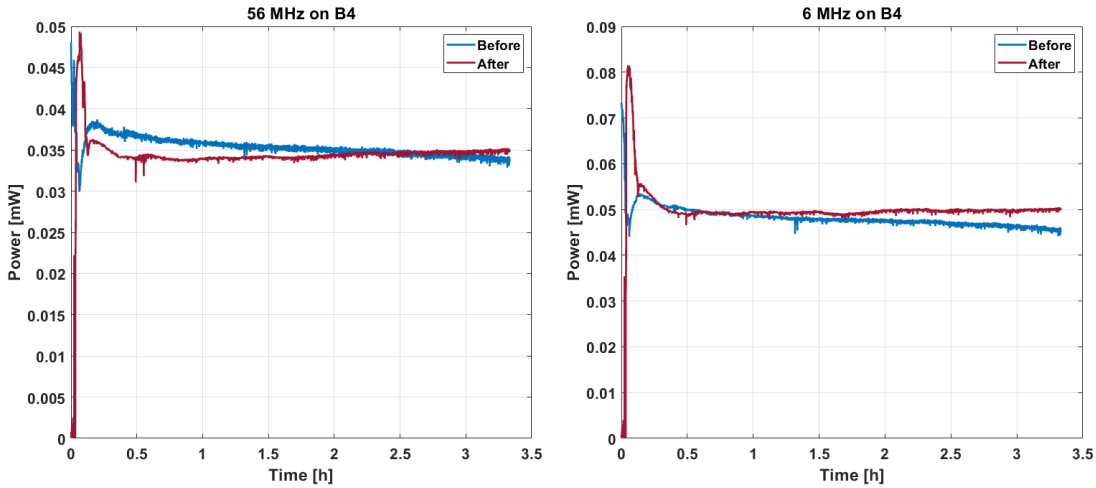

Figure 4.27: *Behaviour of the 56 MHZ (left) and 6 MHz (right) SBs after the acquisition of the final working point of the ITF. The blue curve is before acting with the DAS common tuning and the red curve is after.*

4.5.2 Tuning of the ETM RH powers

The need to re-optimize the operating point of the ITF for each tuning step raises an issue because the curvature induced on the TM by the RH requires more than 10 hours to reach the steady state; this long transient makes a significant impact on the commissioning time. Thus, a new strategy aiming at the reduction of the actuation time of the RHs has been implemented for the first time. It is found that by applying a time varying voltage on the ring heater, the steady state can be reached in less than two hours [133]. The new strategy allowed us to carry out the tuning of the ETMs RHs powers observing the effects on the ITF almost in real-time.
As previously discussed, the tuning of the ETMs' RHs powers has a big impact on both the dark fringe and the power circulating in the FP cavities. Figure 4.28 shows the behaviour of these two figures of merit during one of the ETM RH tuning phase with 25 W as input power. It results in a reduction of the power on the dark fringe by 25% and in an increase of the power circulating in the arms equal to 7% for the West arm and 5% for the North arm. In this new RH working point, a process of optimization of the alignment loops parameters took place. The combination of both of this actions led to an improvement in the sensitivity curve as seen in Figure 4.29.

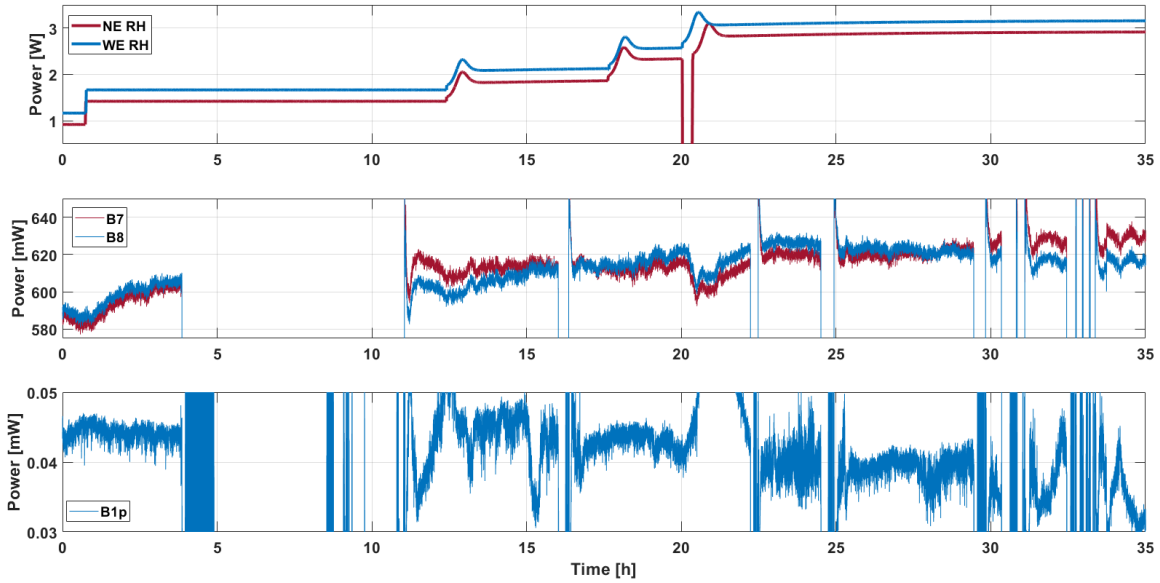

Figure 4.28: *First plot: the powers of the ETMs RHs changed over time. The red line represents the power of the NE RH and the blue line represents the power of the WE RH. Second plot: the power detected by B7 and B8 i.e. the power transmitted from the North (red line) and West (blue line) FP arm, respectively. Third plot: the power detected by B1p, thus it is the dark fringe.*

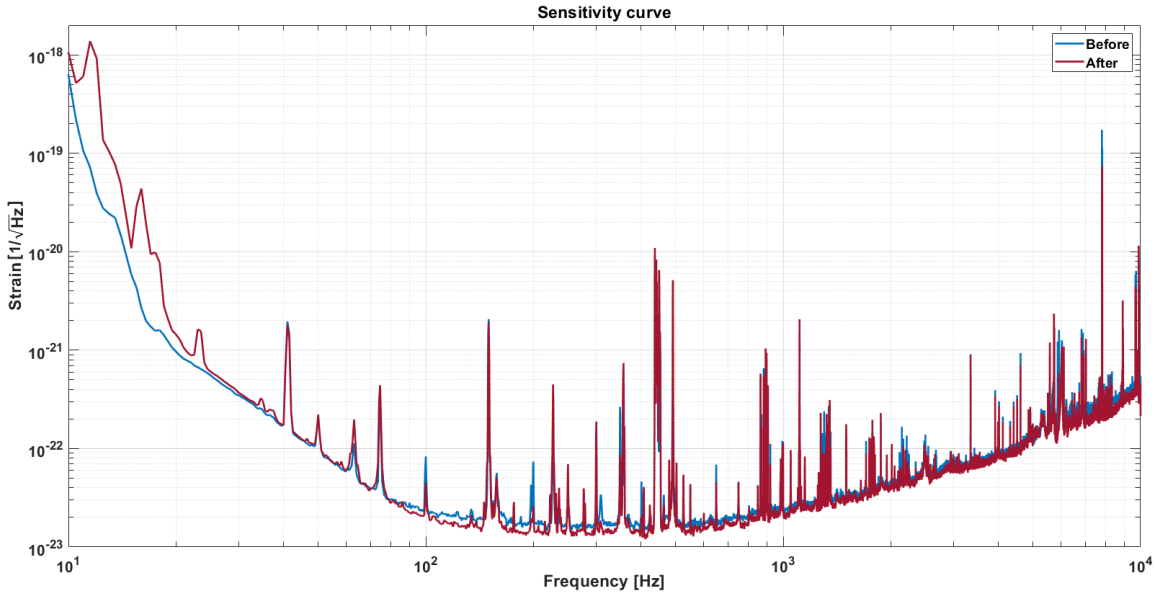

Figure 4.29: *The blue curve represents the sensitivity curve of AdV+ Phase I before the tuning of the TCS actuators powers and the red curve is the one after the tuning and is also the best sensitivity curve achieved to date.*

The achievement of this result was facilitated by improving the tuning procedures for the TCS actuator powers and gaining a better understanding of the relevant observables. Despite the intricacies involved in attaining this outcome, it can be asserted that the TCS procedures are now clearly defined and can be applied to all input powers in which thermal effects are significant.

Chapter 5

Correction of non-axisymmetric aberrations

The relevance of residual aberrations, uncompensated by the axisymmetric actuators of the TCS, is destined to increase with the injected power. Already for O5, with marginally stable recycling cavities, the residual aberration component could become incompatible with the requirements. Consequently, a dedicated compensation method needs to be foreseen. The use of a DM capable of modelling the intensity profile of a CO_2 beam has been proposed for the implementation of a non-axisymmetric actuator. This is a versatile method that operates statically, thus avoiding the introduction of coupled frequency noise. There are many companies in the market that produce DMs, typically designed for adaptive optics applications in astronomy. In the first part of this chapter, I will describe the characteristics that guided the selection of the most suitable DM model for our application, presenting its experimental characterization. A **Mo**dified **G**erchberg-**S**axton (MoG-S) algorithm based on the measured influence function matrix has been developed to extract the phase to be applied by the DM to obtain the heating pattern required for a complementary wavefront correction of the non-axisymmetric aberrations. The MoG-S simulations of the DM-based system and the results of the experimental tests will be described.

5.1 Use of Deformable Mirrors

In the previous chapter, we examined how the TCS deals with aberration corrections using the RH, CH and DAS. All of these actuators provide axisymmetric correction, leaving a residual uncompensated aberration pattern. An example of a simulated residual OPL distortion after the correction of the axisymmetric optical aberrations in the plane of the CP is shown in figure 5.1. In the current operational configuration of AdV+, the non-axisymmetric residual OPL distortion budget can be neglected, but with the power increase foreseen in view of the observing run O5, their impact will grow to the extent that it will no longer meet the general requirements of the TCS. The TCS requirements are reported in Table 3.2 and it is important to add a requirement on spatial frequency. The study was conducted using two sets of maps featuring cold non-symmetric defects, which were provided by LMA. Optical simulations revealed the necessity of flattening the OPL within an 8 cm radius for a probe beam with a 5 cm waist. Therefore, the analysis was performed within a 16 cm by 16 cm area, employing a scanning spot with a 1 cm diameter. The results of the optimization procedure show that the residual OPL RMS is

reduced by a factor of 20 for spatial frequencies below 40 m^{-1} [134].

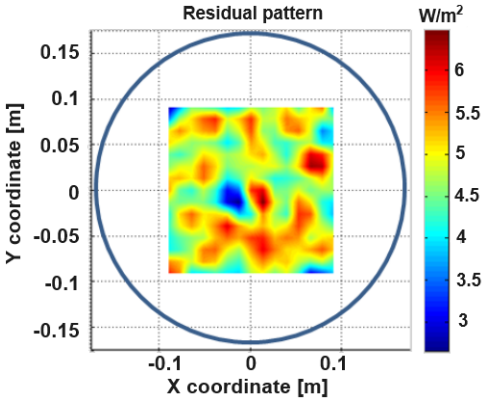

Figure 5.1: *Residual pattern simulated after the correction of the axisymmetric optical aberrations.*

The non-axisymmetric aberrations can be corrected in a manner similar to the approach used with the DAS by projecting an optimal heating profile onto the CP to generate a complementary OPL. To create this profile, a CO_2 beam is employed, and its optimal shape is achieved through beam shaping techniques. A possible solution was the SS, but as discussed in section 3.4.5, it introduces noise in the sensitivity range of the detector. In order to avoid this issue, DMs have been studied as possible future actuators [118]. DMs can be used to apply a phase imprint upon reflection to a CO_2 laser beam to obtain the desired asymmetric intensity pattern onto a given plane located at the CP surface. To produce the phase imprint, a reflective membrane is deformed to accumulate an OPL(x, y) on the reflected beam that depends on the position (x, y). This deformation is achieved through actuators located below the DM reflecting membrane - actuators number and geometrical arrangement depend on the DM model and specific applications. A basic scheme of the actuation principle is shown in figure 5.2. The great advantage of these systems is that the applied correction is static and adaptive, so it does not introduce noise in the detector beyond the laser's RIN.

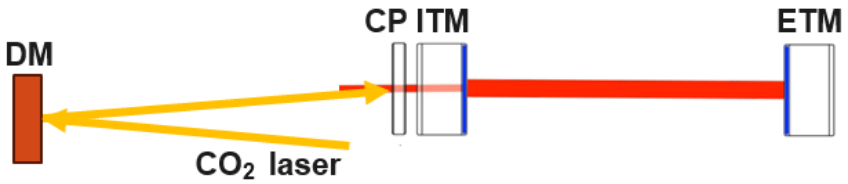

Figure 5.2: *Actuation scheme of the DM-mediated aberration correction in AdV+ Phase II.*

DMs are used in astronomy to correct for time-dependent phase distortions caused by atmospheric turbulence. They are looped to wavefront sensors that measure residual optical distortions by tracking the deviation of a light beam coming from a guide star. The information gathered by the sensors is then used as an error signal to feed the necessary adjustments to the shape of the DM. The mirror continuously adapts to counteract distortions, allowing telescopes to capture sharper and more detailed images of celestial objects. In the case of AdV+ Phase II, the use of the DM is somewhat different from astronomic applications, being used to act on slowly varying (or static) aberrations. The

first notable difference is that we use it to recreate an intensity pattern in a specific plane, on the CP one, instead of correcting directly the phase profile. However, the significant distinction is that the DM will be not necessarily controlled by wavefront sensor, so it will be used in an open-loop configuration. This is because the corrections are not real-time but are statically applied once we know the pattern to shine. When a correction change is required, that is when the budget of residual optical aberrations is refreshed by modifications in the ITF working conditions. Due to these factors, it becomes imperative to provide a DM that can afford the desired pattern's stability for an extended duration. We therefore accomplished a comprehensive market inquiry in which different DMs were compared to select the most suitable model on the basis of the following requirements:

- the **number of actuators** should be such that there is at least one actuator per cm within the CP area that includes the YAG beam, which is approximately $R = 8$ cm;
- the minimum **pupil diameter** as an excessively narrow pupil results in excessive power absorbed per unit area;
- the type of **coating**;
- **stability** and **reproducibility** (hysteresis effect), even if the mechanical hysteresis can be corrected using a particular technique called *Degauss*. It consists in applying a damped oscillating field closed to the working point in order to erase all the hysteresis effect.

Following these requirements and subsequent comparisons among available models, we have chosen two for purchase and characterization, as detailed in the following section.

5.2 Characterization of prototypes

Two different models of DMs have been selected, purchased and characterized. The two models were characterized in terms of stability and reproducibility. The first one is a DM, model DMP40 provided by Thorlabs company. The model is 10 mm in pupil diameter, coated with protected silver[9], with 40 piezoelectric actuators placed under its membrane and a damage threshold of 4 W per cm of diameter for a wavelength range of [450nm $\div$ 2μm]. Piezoelectric actuators offer sub-nm precision, rapid real-time response, and a wide range of adjustment in DM systems. They are known for their low power consumption, long-term durability, and compactness. Furthermore, they operate without mechanical friction, ensuring a stable response over time. Each of the actuators on the DM could be activated applying to the relative electrode a voltage between 0 V and 200 V. With voltage values higher than 100 V the actuator rises, while with values lower than 100 V the actuator lowers and 100 V is the flat condition - see figure 5.3. The mirror commands are sent using a software provided by the company connected to a driver linked to the DM. The DMP40 software incorporates a hysteresis compensation and provide a "Relax" feature in order to eliminate or at least to minimize the creep effect of piezoelectric materials i.e., the continuing material expansion or shrinking after a voltage change was applied that impact the stability and the reproducibility. However, a noticeable weakness becomes apparent when examining the limited versatility of the actuator mapping.

[9] "Protected silver" is a term used in optics technology to describe a silver surface coating that has been shielded or protected by a transparent or protective layer to prevent oxidation, allowing the reflector to maintain its reflective properties over time.

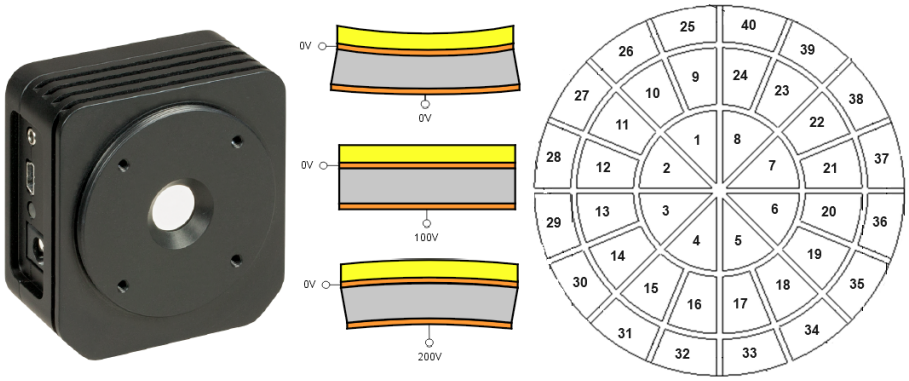

Figure 5.3: *On the left: a photo of the DMP40 Thorlabs DM. In the centre: the working of the actuators applying a voltage to a piezo segment. On the right: actuators mapping.*

The second DM characterized is the model DM97-15 developed by ALPAO company [135]. It consists in a gold-coated membrane with 97 magnetic actuators, a pupil diameter of 13.5 mm - see Figure 5.4 - and a damage threshold of 0.5 W per cm of diameter at the specific CO_2 laser wavelength 10.6 μm. The magnetic actuators, when compared to piezoelectric ones, are better suited when a quick response and long-term stability are required. Furthermore, the gold coating has several advantages, such as higher reflectivity, chemical stability ensuring long-term optical performance without degradation, and the ability to maintain its reflective properties even at high temperatures. The mirror commands are grouped in an array of values through a Matlab code - the array dimension is equal to the number of actuators - and the commands are transmitted to a dedicated driver connected to the DM. For each actuator an actuation value from -1 to 1 is required, with -1 corresponding to the maximum lowering, 1 to the maximum raising and 0 to the no-actuation point. ALPAO DMs have almost no hysteresis effect, less than 2%. Furthermore, the ALPAO DM provides a *high stability option*. In standard DMs, possible drift sources could act as the mechanical creep that is the tendency of a material to deform over time under a constant stress. The creep of the DM is defined as the displacement of the DM relative to the desired shape. Drift comes from the polymer material used to make the actuator springs. The high stability option provides non-polymer springs with state-of-the-art stability for the most demanding open-loop applications.

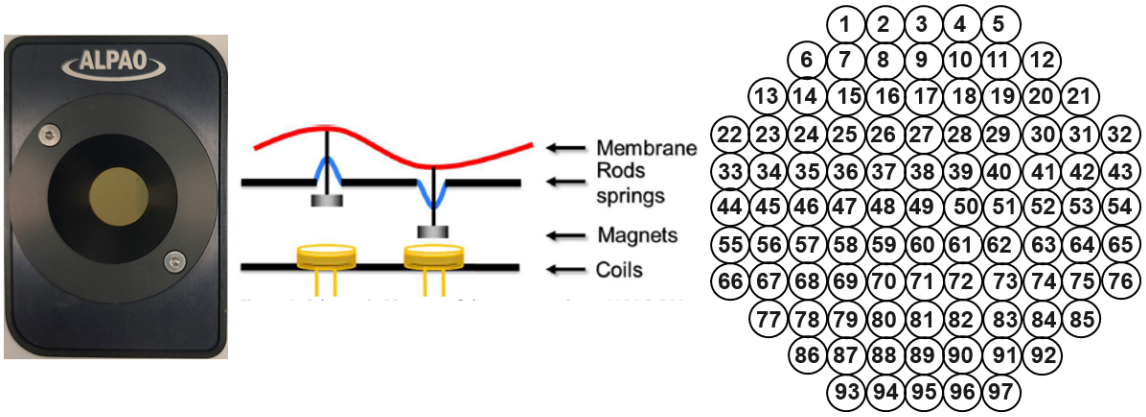

Figure 5.4: *On the left: a photo of the ALPAO DM. In the centre: schematic diagram of the working principle of the actuators. On the right: actuators mapping.*

5.2.1 Sensing optical layout design

To provide a predictive model for the surface deformation of the DM membrane in response to the actuation signals it is necessary to measure the response for each individual actuator, the so-called *influence function* - see section 5.2.3. This can be achieved by using a **S**hack-**H**artmann (SH) wavefront sensor and a beam reflected from the DM that accumulates the deformation in the wavefront change. The SH provides accurate measurements of the wavefront shape. During operation, light is incident on a microlens array, which creates a matrix of focal spots on a CMOS camera sensor. The SH application software analyzes the centroid locations of the focal spots and via integration of the gradients provides wavefront measurements. The SH used has a 1936x1216 pixel CMOS Camera with a rectangular 11.34 mm x 7.13 mm of active area. To couple the DM with the SH a proper optical layout has been devised and put into operation.
The characterization of both DMs was performed using a solid state diod pumped laser emitting at λ =532 nm at $P = 10$ mW. The green laser has been preliminary characterized and the figure 5.5 shows the spotsize as a function of distance, with zero distance representing the laser output. The black and blue points represent the spotsize along the x and y axes, respectively, measured through beam image analysis using a CCD. Meanwhile, the black and blue lines are their fits using the caustic formula for Gaussian beams:

$$w(z) = w_0 \left(1 + \left(\frac{(z - z_0)\,\lambda M^2}{\pi w_{0^2}}\right)^2\right)^{\frac{1}{2}}, \tag{5.1}$$

where z is the distance from the laser head, z_0 is the position of the waist w_0, $w(z)$ is the spotsize at distance z and M^2 is a parameter introduced to include non-diffraction-limited divergence, resulting from deviations from TEM00 - for a pure Gaussian beam $M^2 = 1$.

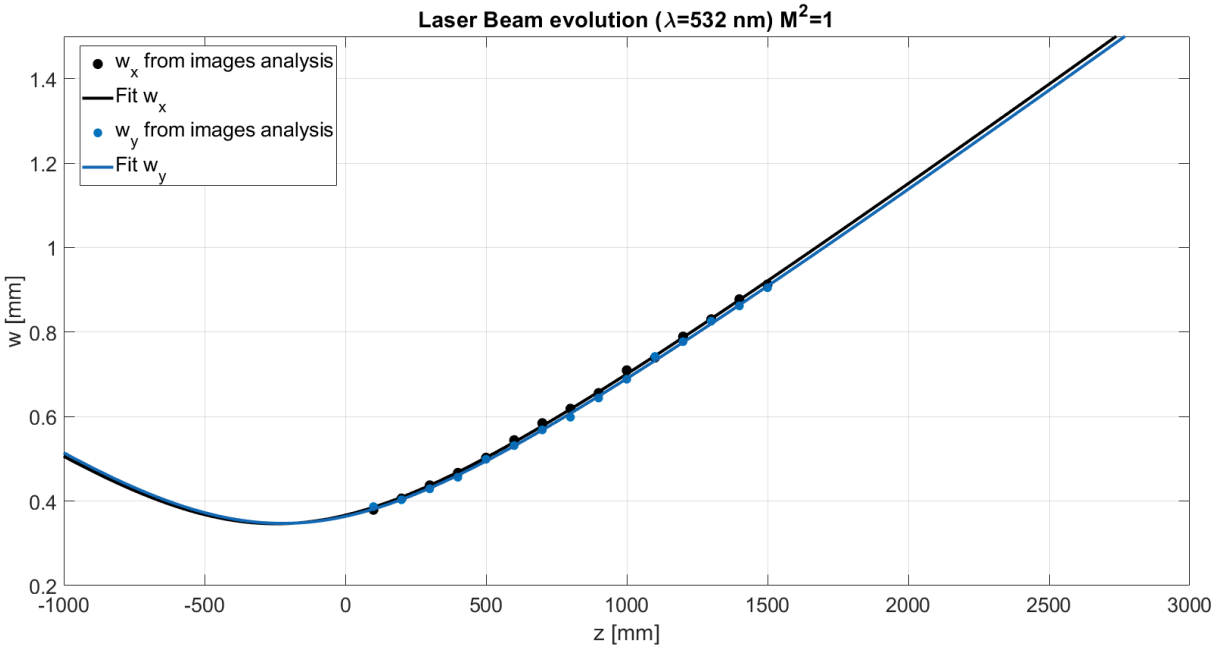

Figure 5.5: *Green laser beam fitted caustic. The black and blue points represent the measured spotsize along the x and y axes, respectively and the black and blue lines are their fits.*

From the performed analysis, the astigmatism is negligible and the beam resulted to

have a spotsize of $w_0 = (0.35 \pm 0.01)$ mm, $z = (-234 \pm 21)$ mm and $M^2 \sim 1$. The sensing optical layout has been designed according to the characterization of the laser and the conceptual layout is shown in figure 5.6. The laser beam first passes through a half-wave plate which in conjunction with the **P**olarizing **B**eam **S**plitter (PBS) is used to enable power adjustment. Subsequently, it is magnified to match the size of the SH using a telescope composed of two lenses, L1 and L2. It proceeds through a PBS and a quarter-wave plate which in conjunction with the PBS serves the purpose of decoupling the forward and return beams, ensuring that only the information reflected from the DM reaches the SH. The beam passes also through a second telescope made up of lenses L3 and L4, which serves to adapt the beam's dimensions to the DM aperture. Upon reflection from the DM, the beam undergoes further shrinking via the second telescope to regain the appropriate dimensions for the SH, and it passes again through the quarter-wave plate.

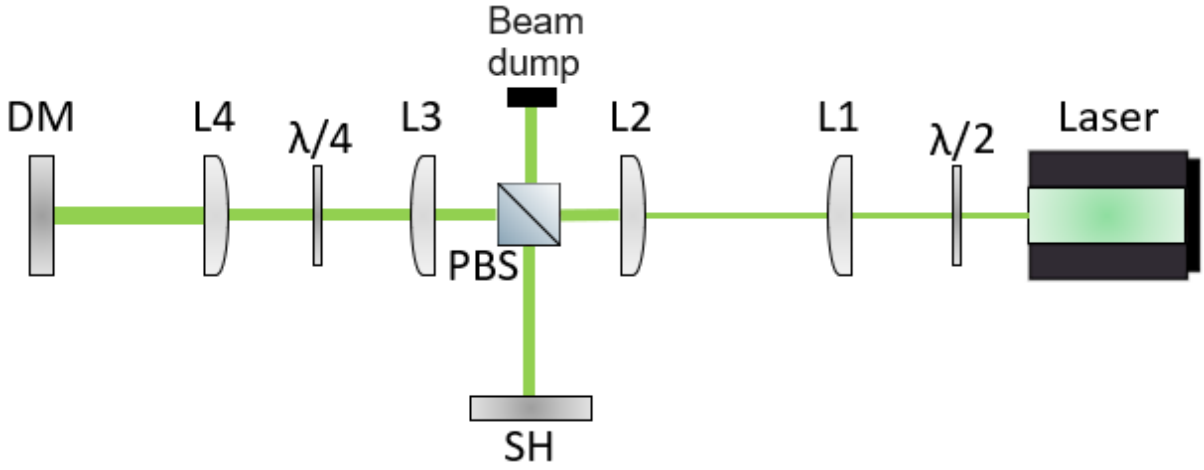

Figure 5.6: *Scheme of the optical layout used for the DMs influence functions characterization.*

Since the diameters of the the Thorlabs DM and the ALPAO DM are different, the dimension of the beam impinging on that should be different, therefore the distances and the focal lengths of the sensing optical layout have been adapted. Table 5.1 presents the focal lengths of the telescope lenses, the magnification M computed as the ratio of the focal lengths and the laser's spotsize on the DM and on the SH, for both sensing optical layouts.

First Telescope	f_1 **[mm]**	f_2 **[mm]**	**M**	w_{SH} **[mm]**	**SH dimension [mm]**
Thorlabs DM	200	1000	5	3.32	11.34 x 7.13
ALPAO DM	50	300	6	2.59	11.34 x 7.13
Second Telescope	f_3 **[mm]**	f_4 **[mm]**	**M**	w_{DM} **[mm]**	**DM diameter [mm]**
Thorlabs DM	100	150	1.5	4.98	10
ALPAO DM	100	200	2	5.19	13.5

Table 5.1: *The design values of the focal lengths of the lenses where the subscripts 1, 2, 3 and 4 refers to L1, L2, L3 and L4 respectively, the magnification M and the laser's spotsize on the DM and on the SH used in the characterization optical layout for both the Thorlabs DM and the ALPAO DM. Also the SH dimension and the pupil diameter of the DMs are reported.*

The SH was placed in the image plane of the DM in order to decouple beam's phase and amplitude propagations. In order to estimate the position of the image plane, the image formed by the lens L4 is used as the object for the lens L3. Knowing that the distance between L4 and the DM is p_1, the other parameters have been evaluated as:

- the L4 image distance $q_1 = \frac{p_1 f_4}{p_1 - f_4}$ where f_4 is the focal length of L4;
- the L3 object distance $p_2 = d_3 - q_1$ with d_3 is the distance between L3 and L4;
- the L3 image distance $q_2 = \frac{p_2 f_3}{p_2 - f_3}$ where f_3 is the focal length of L3. q_2 is precisely the distance from L3 where the SH should be positioned so that it lies in the image plane of the DM.

Table 5.2 presents the parameters p_1, q_1, p_2 and q_2 for both the characterization sensing optical layout.

	p_1 **[mm]**	q_1 **[mm]**	p_2 **[mm]**	q_2 **[mm]**
Thorlabs DM	100	-300	550	122
ALPAO DM	50	-67	367	137

Table 5.2: *The values of the parameters p_1, q_1, p_2 and q_2 used in the characterization sensing optical layout for both the Thorlabs DM and the ALPAO DM.*

Being the SH in the image plane of the DM, the knowledge of the second telescope magnification allows to rescale the wavefront measured by the SH to evaluate the DM deformation. Due to the significance of the magnification value, an experimental verification was also conducted to check whether the SH, positioned at the calculated distance q_2, was actually in the image plane of the DM and whether the magnification value was compliant with that obtained from the focal length ratio, as presented in Table 5.1. The position of the image plane has been checked using a target with a circular hole of known radius positioned in front of the DM. A CCD, placed approximately in the image plane, has been used to acquire the target image for different distances. The SH has been placed where the target appeared optimally focused. As an example of this procedure, the images obtained using the Thorlabs DM layout are depicted in Figure 5.7. The selected ultimate positioning for the SH sensor in both layouts is presented in Table 5.3.

	SH position from L3 [mm]
Thorlabs DM	123 ± 1
ALPAO DM	138 ± 1

Table 5.3: *The selected ultimate positioning for the SH sensor in both layouts. The error ± 1 mm is attributed to the uncertainty during the placement of the SH. The experimental values of the distance between the SH and L3 are in agreement with the q_2 values in Table 5.2*

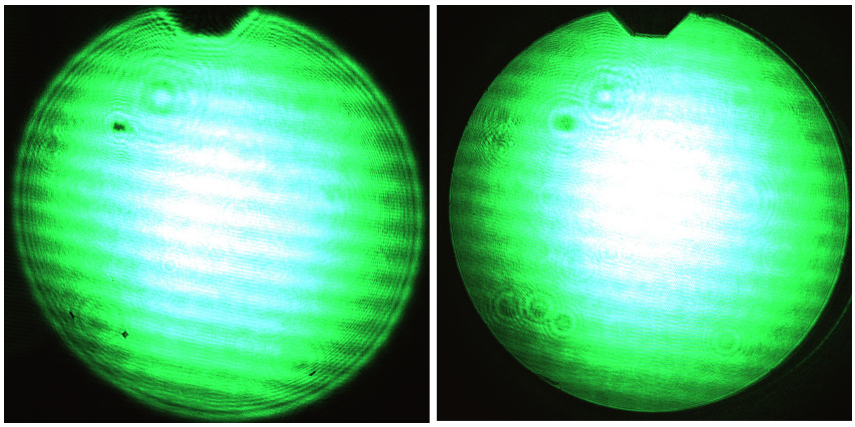

Figure 5.7: *Left: The picture acquired from the CCD at* (193 ± 1) *mm from L3. Right: The picture acquired from the CCD at* (123 ± 1) *mm from L3. The error* ± 1 *mm is attributed to the uncertainty during the placement of the SH.*

The target has also been used to measure the magnification. Ten images have been acquired and the radius of target in the image plane has been computed as the average of all the radii from the ten images. Thus the magnification defined as the ratio between the radius of the image of the target hole in the image plane and that of the target hole in the object plane can be calculated and the results are shown in Table 5.4.

	Commercial DM	**ALPAO DM**
Radius of the target hole in the object plane [mm]	12.00 ± 0.01	5.00 ± 0.05
Radius of the image of the target hole in the image plane [mm]	7.8 ± 0.1	2.6 ± 0.2
Magnification M	1.53 ± 0.02	1.96 ± 0.04

Table 5.4: *The known radius of the target hole, the measured radius of the target image and the magnification defined as the ratio between the two radii are reported for both the optical layouts. The errors of the radii of the target holes are provided by the manufacturer. The error in the measured radius was estimated as the RMS of the ten measured values and the error in magnification is determined by the errors propagation.*

The obtained magnifications are in agreement with the nominal values as computed from the declared focal lengths of the telescope lenses, see M of the second telescope in Table 5.1. During the characterization measurements, the SH has been installed in the measured image plane position shown in Table 5.3. In Figures 5.8 and 5.9 the results of the Matlab simulations of the laser beam propagation through the characterization layouts are shown.

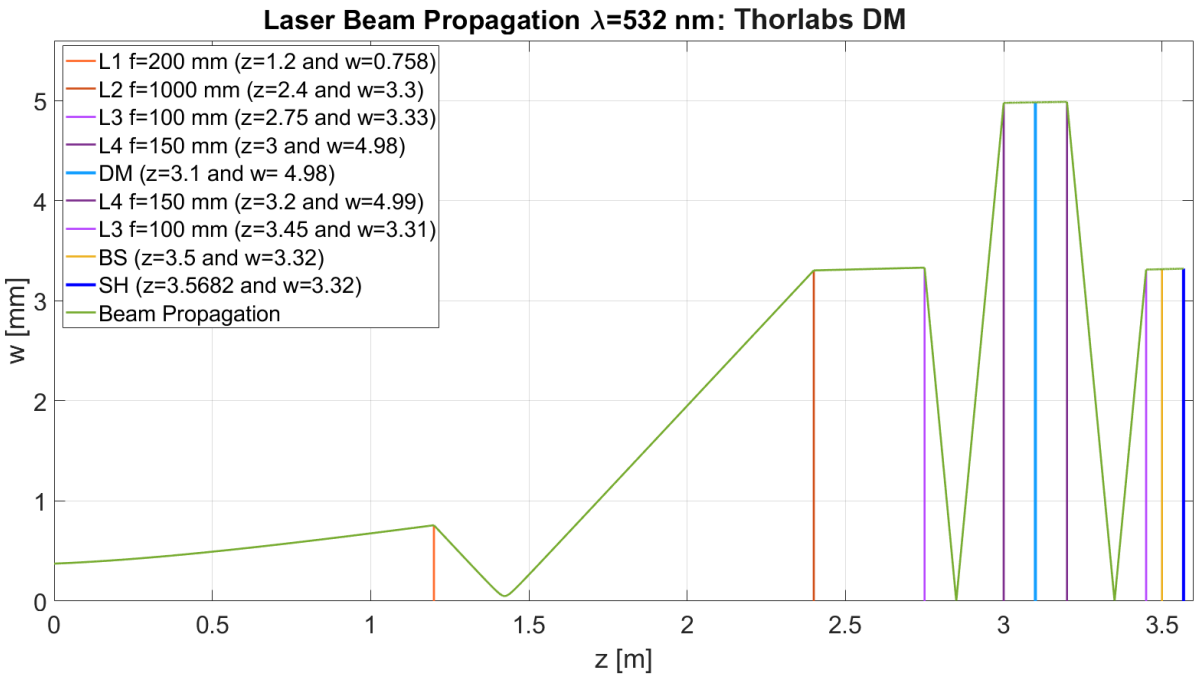

Figure 5.8: *Matlab simulation of the laser beam propagation through the setup dedicated to the Thorlabs DM characterization. In the legend the distances from the laser output and the beam spotsize impinging on each component are reported.*

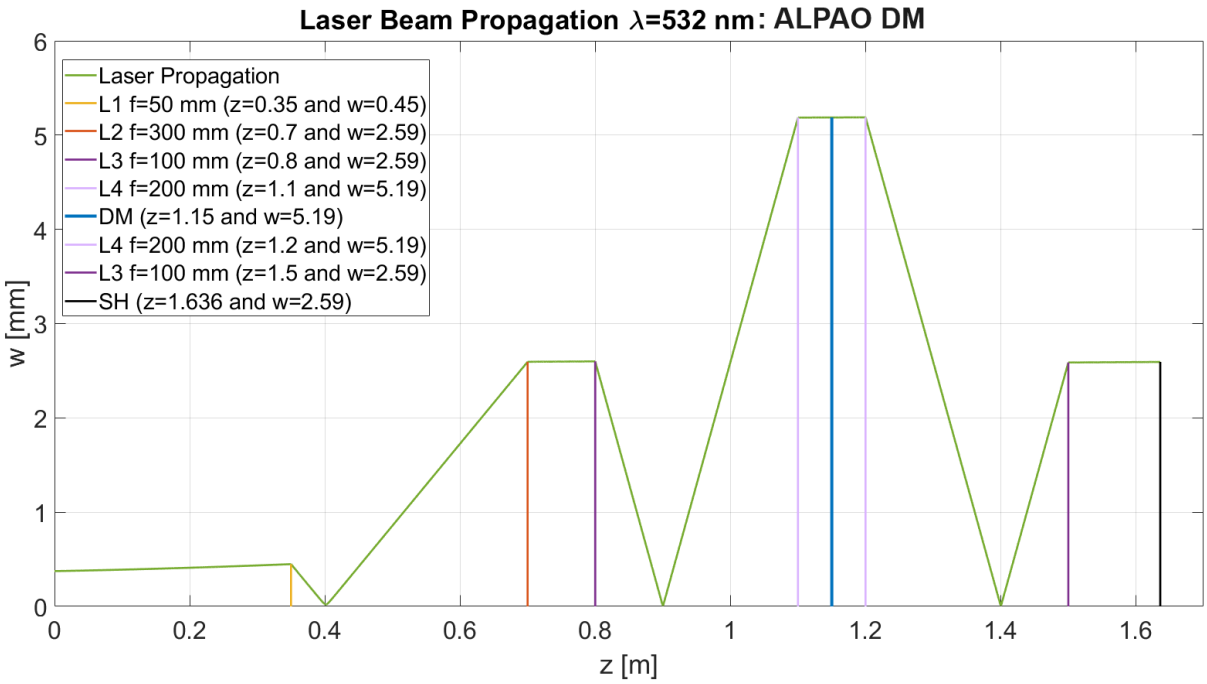

Figure 5.9: *Matlab simulation of the laser beam propagation through the sensing optical layout dedicated to the ALPAO DM characterization. In the legend the distances from the laser output and the beam spotsize impinging on each component are reported.*

To conclude the preliminary characterization of the sensing layout, the sensitivity of the layout was experimentally estimated. The noise limit has been evaluated taking four

wavefront measurements at five-minutes intervals without making any changes to the setup and calculating the RMS of the difference between two consecutive wavefronts, the results are shown in Figure 5.10. Given the RMS of each difference the average value which can be considered as the sensitivity limit is (0.0086 ± 0.0005) μm for the ALPAO DM layout and (0.019 ± 0.001) μm for the Thorlabs DM layout. The noise could be reduced by averaging multiple wavefronts. Nevertheless, this level of sensitivity is sufficient for our purposes.

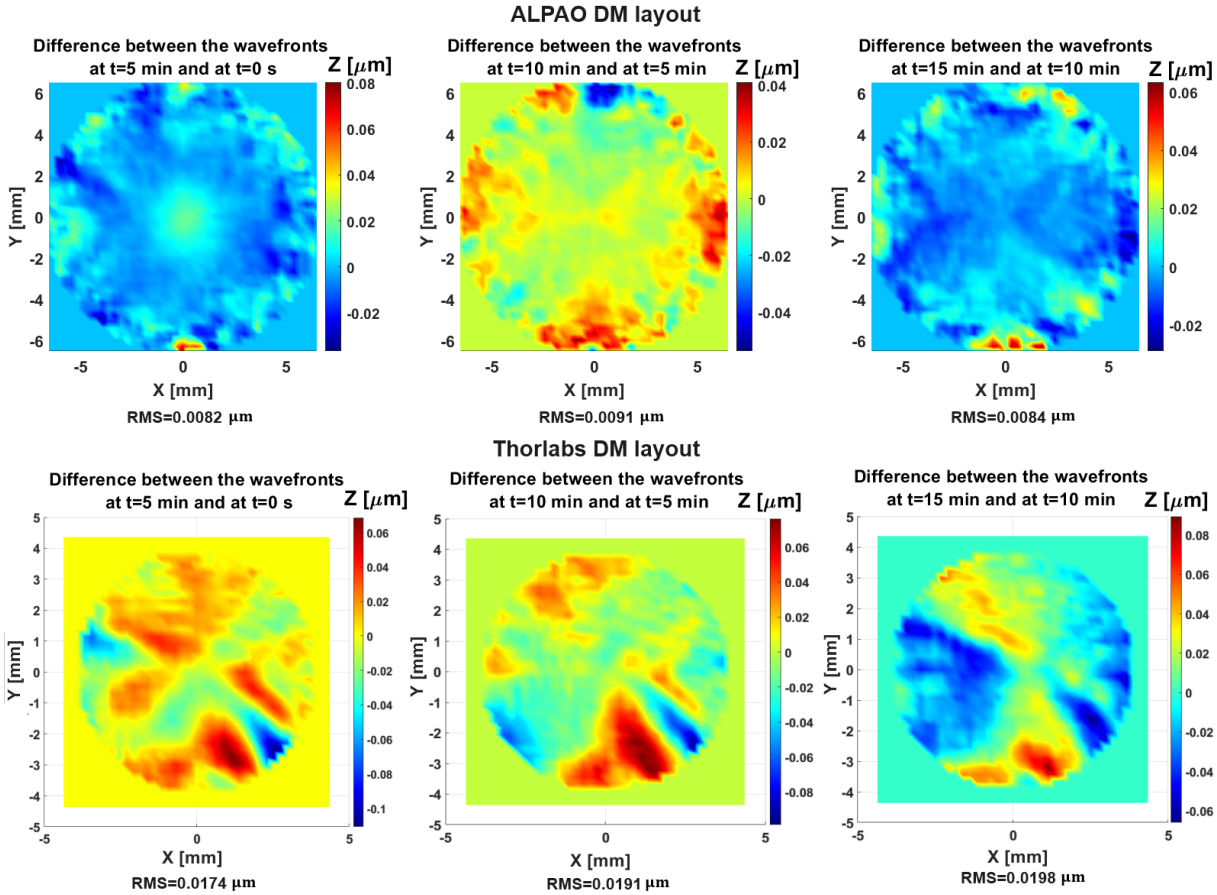

Figure 5.10: *SH maps of the difference between two consecutive wavefronts taken after an interval of five minutes with their RMS.*

5.2.2 Stability in time

Once the sensing optical layout has been defined, the stability in time is evaluated to check the high stability option provided by the ALPAO DM and compare it with the data obtained using the Thorlabs DM. It has been evaluated activating the central actuator in its maximum raising, taking three wavefronts at one-hour intervals and calculating the *RMS* of the difference between two consecutive wavefronts, the results are shown in Figure 5.11. Given the RMS of each difference the average value is (0.012 ± 0.002) μm which can be considered as an upper limit since there is no increase in RMS over time, so if there has been deformation within 2 hours, it is below this value, which has remained approximately constant and is comparable to the value of the sensitivity. Regarding the Thorlabs DM, this value is equal to (0.06 ± 0.01) μm, which is five times larger than the value found for the ALPAO DM and three times larger than the sensitivity.

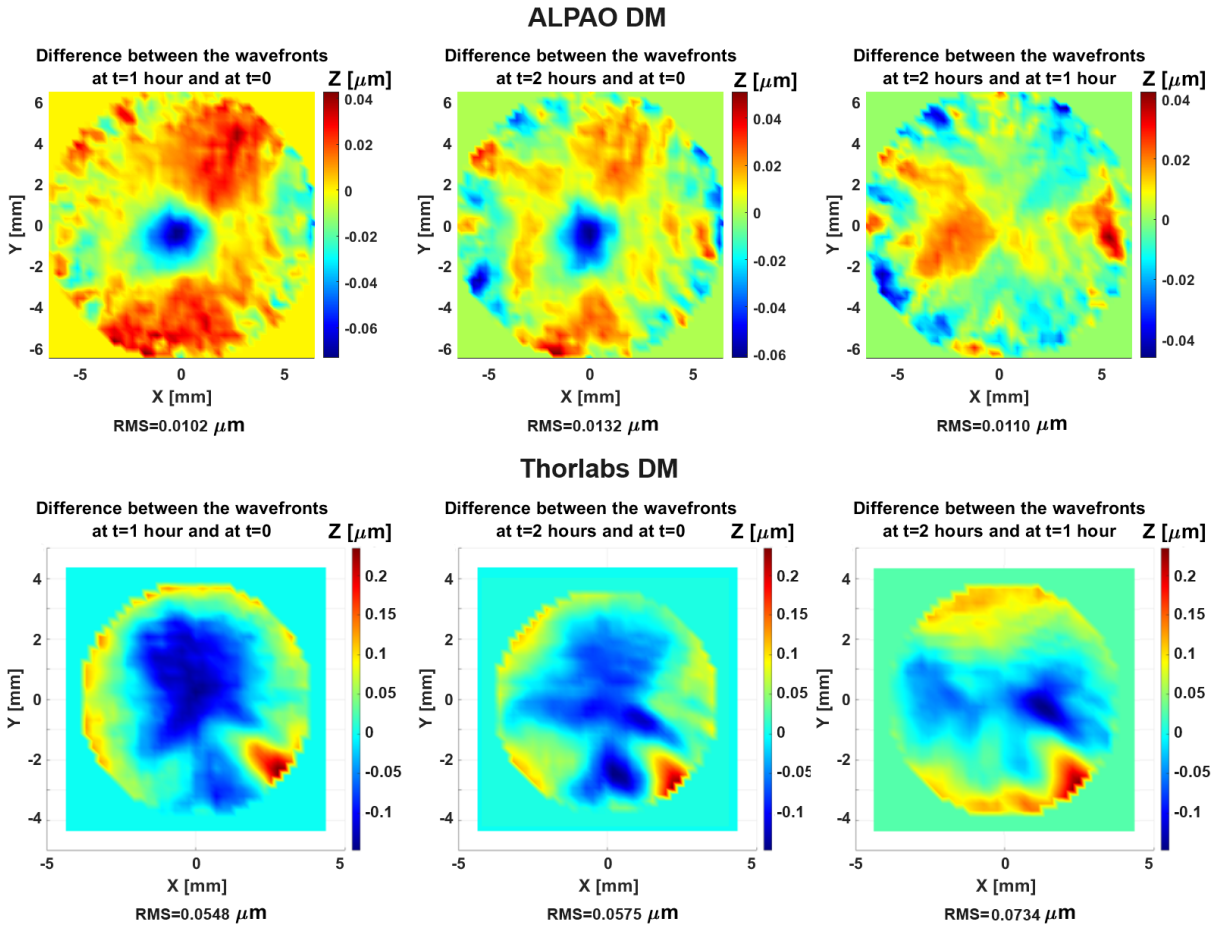

Figure 5.11: *SH maps of the difference between two consecutive wavefronts taken every hour minutes with their RMS for the ALPAO DM and for the Thorlabs DM.*

5.2.3 Influence functions matrix

To determine the actuation signals needed to achieve a desired deformation on the DM, it is necessary to assess a specific parameter for each individual actuator, known as the *influence function*, which represents the deformation generated by individual actuators [136]. Under ideal conditions, which neglect damping effects and finite boundary effects, by linearizing the membrane equation, for small voltages and small deflections, and assuming the absence of external forces and viscous damping, the equation of motion for thin membranes under tension is as follows [137, 138]:

$$\frac{\partial^2 Z}{\partial t^2} = \frac{T}{\sigma}\nabla^2 Z, \tag{5.2}$$

where Z is the vertical displacement, t is the time, T is the tension per unit of length, σ is the mass per unit of area, and ∇^2 is the Laplacian operator. If an external stress $F(r,t)$ is applied to the membrane at position r from the center, the equation 5.2 turns into:

$$\frac{\partial^2 Z}{\partial t^2} = \frac{1}{\sigma}\left(T \cdot \nabla^2 Z + F(r,t)\right). \tag{5.3}$$

The steady-state is therefore described by the Poisson's equation $\nabla^2 Z = -\frac{F(r,t)}{T}$. Considering $F(r,t)$ as a model of the pressure of an electrode and since the solutions of the

Poisson's equation are linear in the electrode pressure [139], it is possible to write:

$$z_i = \sum_{j=1}^{N_e} \mathcal{A}_{ij} P_j, \tag{5.4}$$

where $\mathcal{A}_{ij}$ are the coefficients derived from solutions of the Poisson's equation, z_i is the displacement in position (x_i, y_i) over the membrane surface, Pj is the pressure exerted over the surface of the j-th electrode and N_e the total number of electrodes. By keeping j constant and varying i, the resulting column vector represents the j-th influence function values at surface positions labelled $i = 1, ..., N_p$, where N_p represents the number of surface points. The influence function of each actuator combines linearly with those of all the others to yield the surface displacement z_i. The resulting matrix $\mathcal{A}$ comprising all the elements $\mathcal{A}_{ij}$ is commonly referred to as the *influence function matrix*.
The influence function of each actuator has been evaluated both for raising and lowering following the *relative* mode procedure:

1. a reference image, which means when the DM is in a flat state, is acquired with the SH;
2. the actuator is engaged raising/lowering it at its maximum values;
3. the image is acquired with the SH.

The influence function is derived from the difference between the SH image collected with the actuator activated and the reference one. To minimize the error the raising and lowering influence functions for each actuator have been measured twice in two different days, and the final influence function is computed by averaging these measurements after evaluating the reproducibility of them i.e. the difference RMS between the same influence function measured in two different days. Already from these values, the superior performance of ALPAO DM starts to become evident, given that the average RMS is (0.010 ± 0.004) μm, whereas that of the Thorlabs DM is (0.04 ± 0.03) μm. In Figures 5.12 and 5.13 the measured influence functions for one actuator in its raising and lowering state are shown.

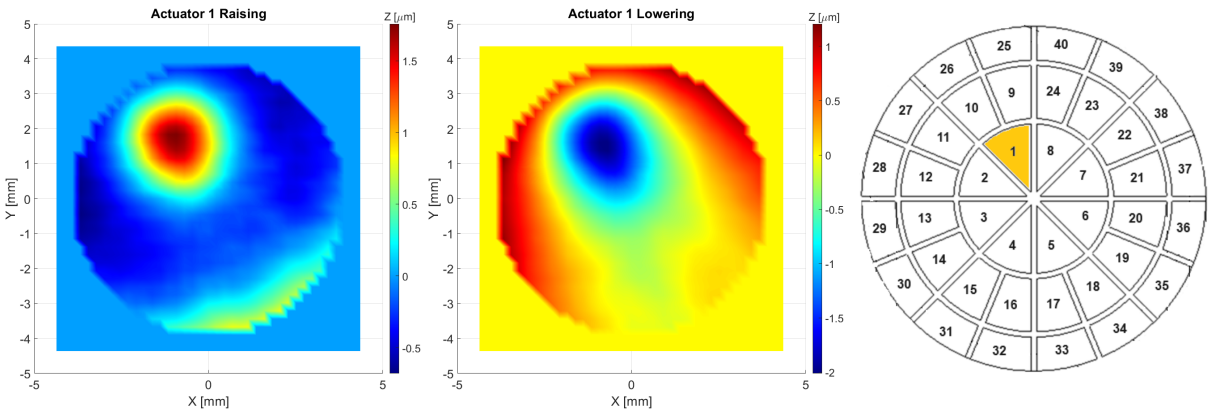

Figure 5.12: *Measured influence functions for the first actuator of the Thorlabs DM engaged in its maximum raising state (on the left) and in its minimum lowering (in the middle). On the right is also reported the actuators mapping with the actuator engaged highlighted.*

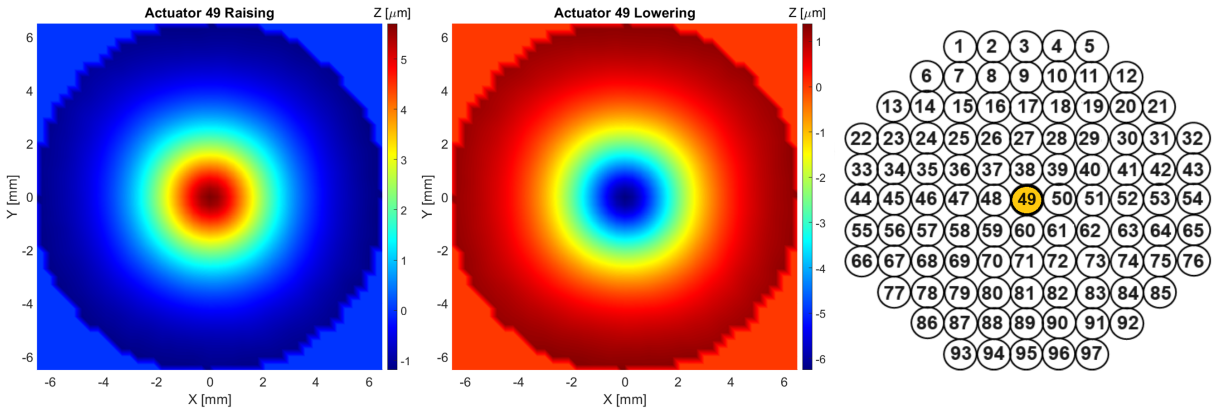

Figure 5.13: *Measured influence functions for the central actuator of the ALPAO DM engaged in its maximum raising state (on the left) and in its minimum lowering (in the middle). On the right is also reported the actuators mapping with the actuator engaged highlighted.*

The actuators display different responses when activated in one direction compared to the other, that means, their behaviour is not perfectly symmetrical for raising and lowering state. This phenomenon is illustrated in Figures 5.14 and 5.15, where the influence function values acquired by fully activating each actuator in both directions are plotted. The maximum difference in the case of the Thorlabs DM is 0.55 μm for the actuator 11 and for the ALPAO DM is 0.74 μm for the actuator 94.

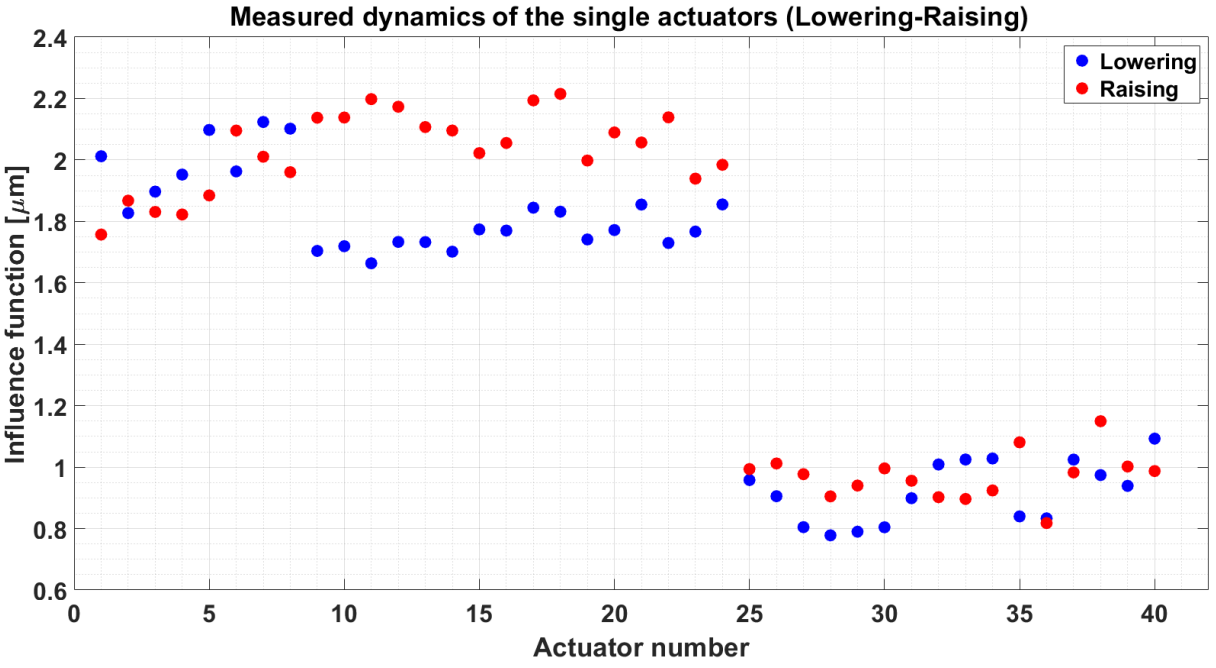

Figure 5.14: *Maximum amplitude value of the influence function of each actuator for engaging it in the raising or lowering state for the Thorlabs DM.*

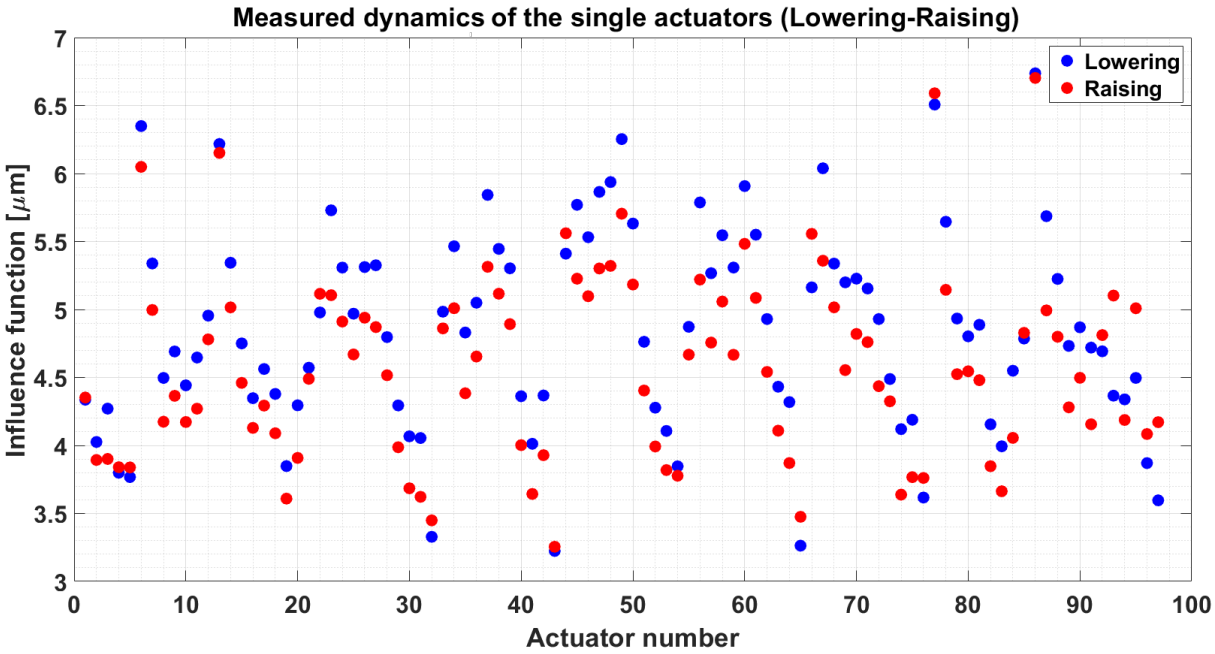

Figure 5.15: *Maximum amplitude value of the influence function of each actuator for engaging it in the raising or lowering state for the ALPAO DM.*

As the data obtained from the SH sensor exhibited irregular shapes with minor size variations across different measurements, due to the intrinsic laser intensity fluctuations causing slight changes in the incident power on the sensor and this affected the SNR. In fact, points at the edges appeared less illuminated and, consequently, more susceptible to noise. For this reason, we computed the influence functions within a central circular area where such effects could be considered negligible. All subsequent influence function computations were performed within this central circular area. For the construction of the influence matrix, the influence function for each individual actuator has been determined as the average of the absolute values of the map in the raising and lowering states. The final influence functions are depicted in Figure 5.16 for the Thorlabs DM and in Figures 5.17, 5.18 and 5.19 for the ALPAO DM.
The average influence functions were utilized to construct the influence function matrix $\mathcal{A}$, which encompasses comprehensive data about the dynamic behaviour of the DM. This matrix is necessary to calculate the optimal voltage values for the actuators to fit the membrane surface z to the target b at selected surface-matching points.

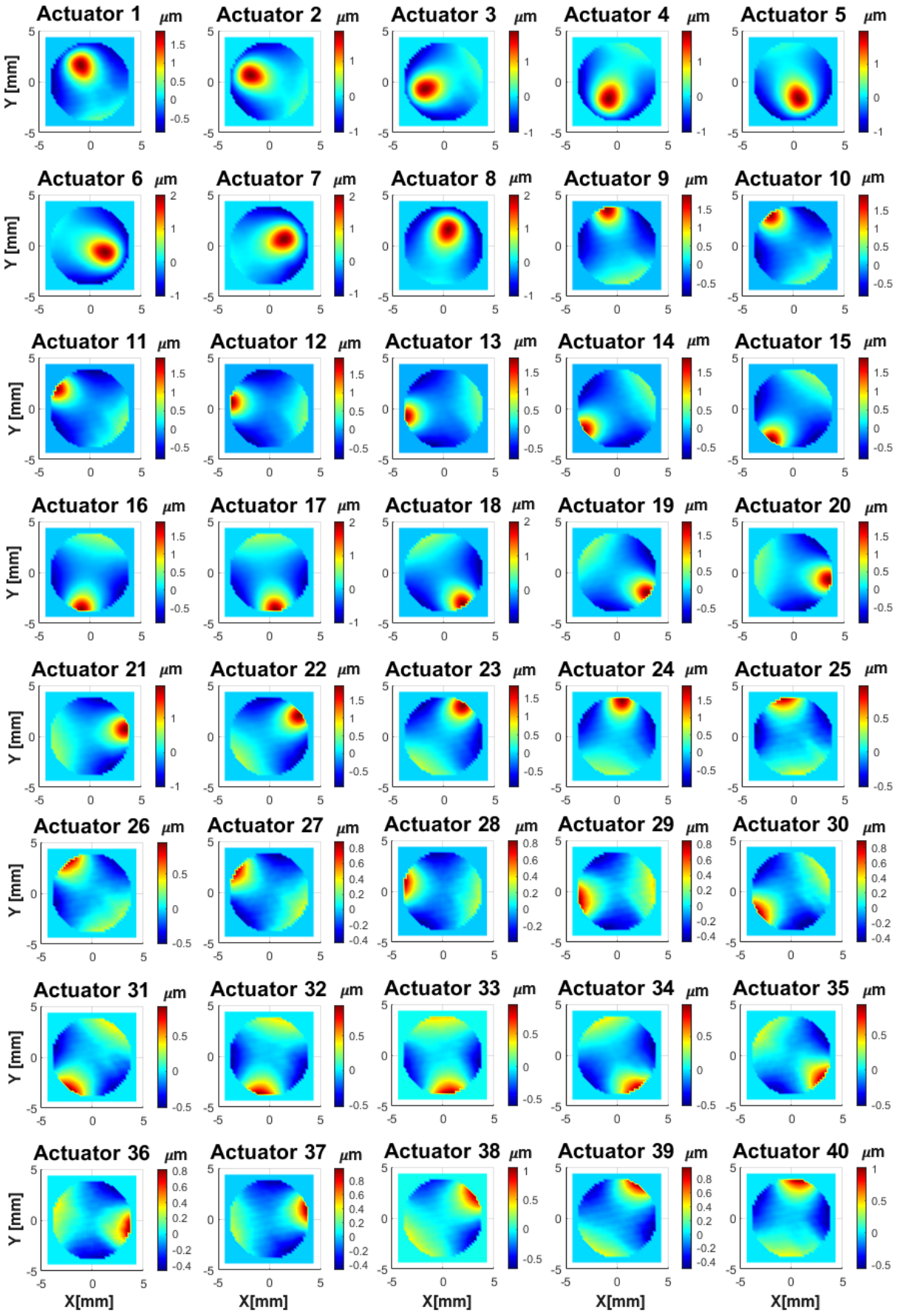

Figure 5.16: *Average influence functions for the Thorlabs DM.*

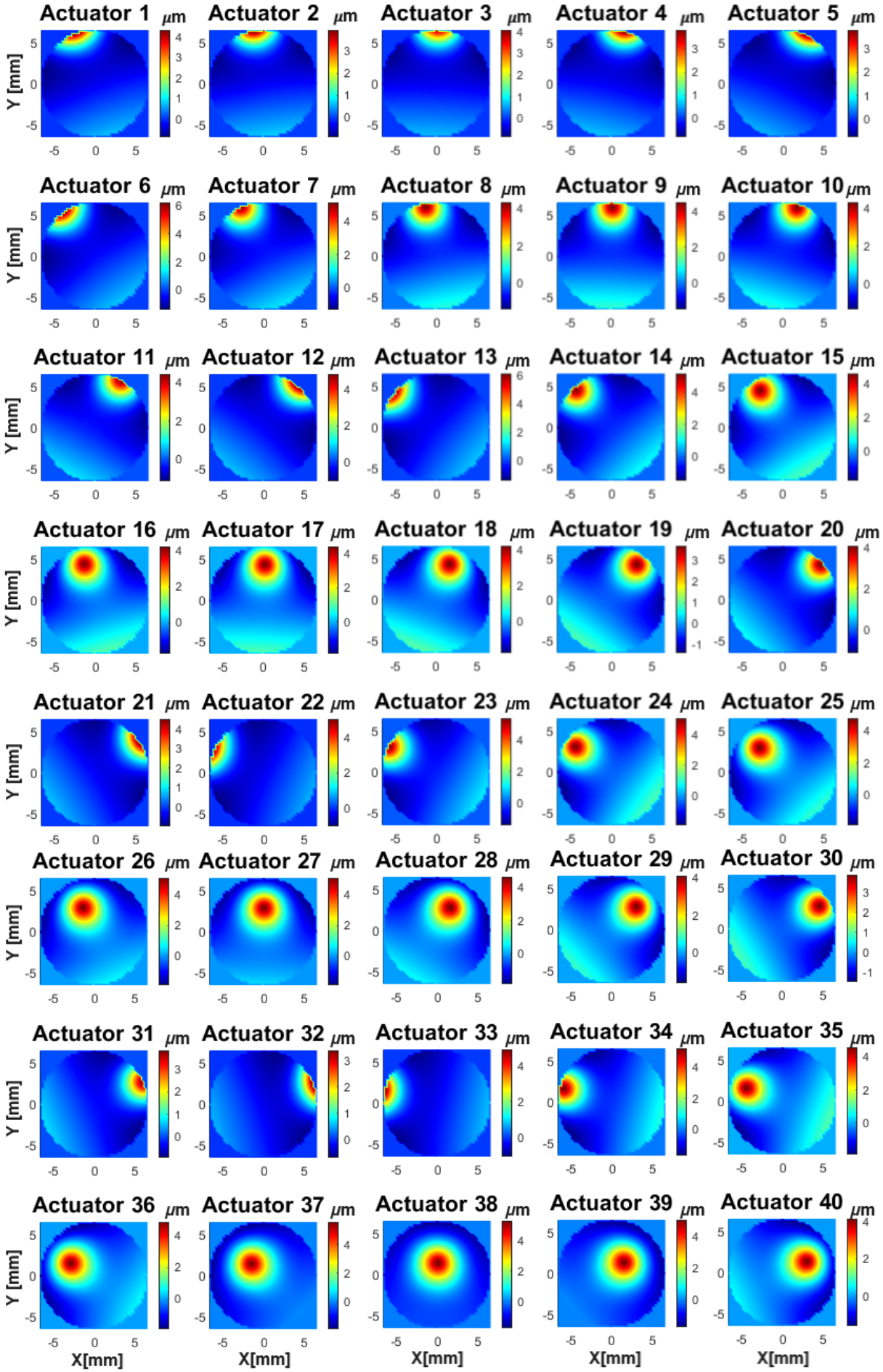

Figure 5.17: *Average influence functions for the ALPAO DM.*

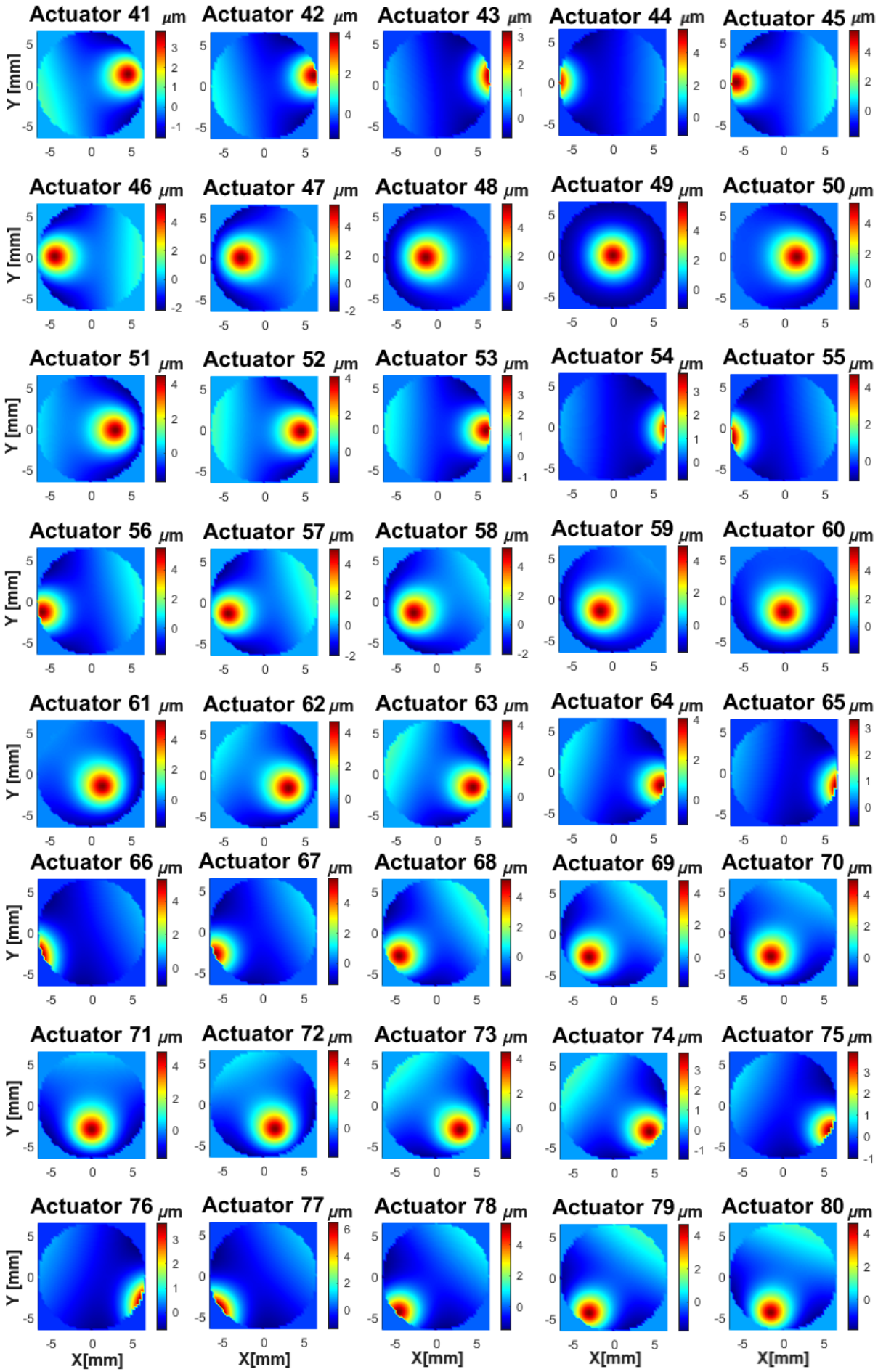

Figure 5.18: *Average influence functions for the ALPAO DM.*

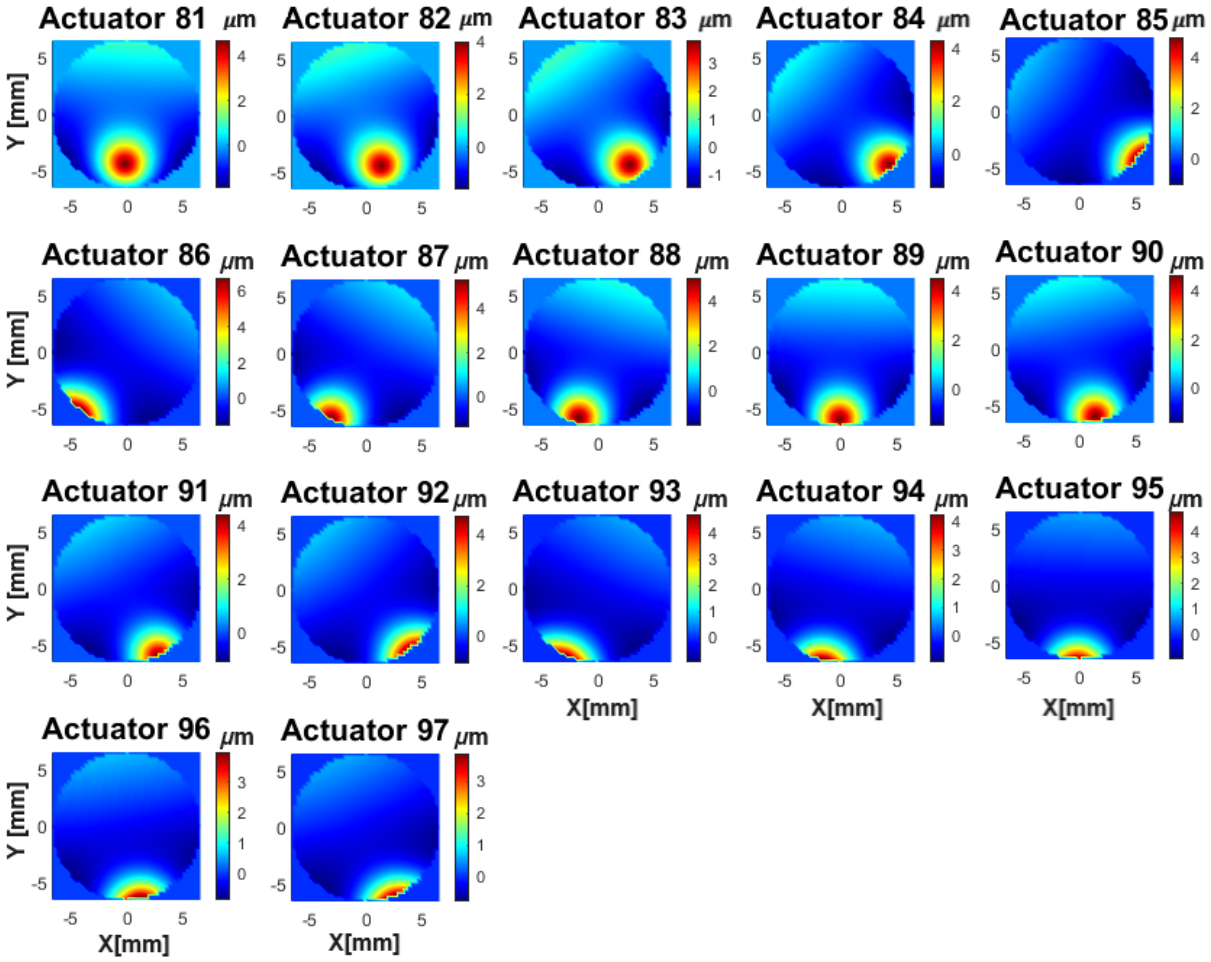

Figure 5.19: *Average influence functions for the ALPAO DM.*

5.2.4 DM actuation performances

Applying a specific pattern to the DM is equivalent to solving a linear problem in the following form:

$$\mathcal{A} \cdot x = b, \tag{5.5}$$

where x is the column vector of the unknown quantity i.e. it is the actuation coefficients for the reconstruction of the pattern and b is the specific pattern converted into a vector. The solution would be unique and given by $x = \mathcal{A}^{-1} \cdot b$ if $\mathcal{A}$ were a square matrix with all its rows being independent. However, in the case of the two studied DMs, $\mathcal{A}$ is not a square matrix because we want the target to be reproduced in a much larger number of points than the number of actuators, making the system overconstrained, and therefore, the matrix inverse does not exist. The equation 5.5 can be solved approximately using the *Moore-Penrose pseudoinverse matrix* [140, 141], denoted as $\mathcal{A}^{+}$. The solution x is given in the least-square sense i.e., it minimizes the quantity $||\mathcal{A}x - b||^2$ and it can be expressed as [142]:

$$x = \mathcal{A}^{+} \cdot b. \tag{5.6}$$

Given that, for the Thorlabs DM, it is possible to activate each of the actuators by applying voltages ranging from 0 V to 200 V to their respective electrodes, and for the ALPAO DM, each actuator requires an actuation value within the range of -1 to 1, the obtained actuation coefficients have been rescaled to fit within the allowable DM actuation

range.
Multiple patterns will be chosen to assess the actuation of the two DMs and evaluate their ability to reproduce the selected pattern. The selected target patterns for testing the DM were chosen to assess the DM's performance across its entire surface and to evaluate how the actuators respond to the lowering/raising instructions. For each target pattern, the following procedure has been used:

- the Moore-Penrose pseudoinverse matrix $\mathcal{A}^+$ has been evaluated;
- the pattern has been converted in a vector b;
- the actuation coefficients for the reconstruction of the pattern have been computed using equation 5.6;
- the obtained coefficients have been rescaled to DM range.

The final result is a vector x with a number of elements corresponding to the number of actuators, 40 for the commercial DM and 97 for the ALPAO one. The computation of the Moore-Penrose pseudoinverse matrix was executed using the Matlab function "*pinv*" and specifying tolerances for each tested pattern. Once we have obtained the vector x, we can proceed with a DM actuation verification. By utilizing Equation 5.5, we multiply the obtained vector x by the influence matrix $\mathcal{A}$, resulting in a vector b that is converted into a pattern. In this manner, we obtain a reconstructed pattern that can be compared to the target pattern. At this point, using the layout shown in Figure 5.6 and the SH, the influence function amplitudes in the vector x has been sent to the DM in order to obtain an experimental pattern to be compared with the target pattern and the reconstructed one. In Figures 5.20, 5.21 and 5.22, the results are depicted, specifically showing the chosen target, the reconstructed one and the experimental data for both the Thorlabs DM and the ALPAO DM. To compare these patterns, the RMS of their difference was evaluated and reported as a percentage error. In the case of the ALPAO DM, the experimental patterns exhibit an agreement with those reconstructed using the pseudoinverse matrix within 1% and an agreement with the target pattern within 4%. The obtained experimental results validate the adopted procedure for computing the actuation vector with the pseudoinverse matrix, demonstrating reliable and reproducible results. Other targets have also been tested, as shown in Figure 5.23, using the ALPAO DM [143]. From this point onward, all further tests will be conducted using only this device.

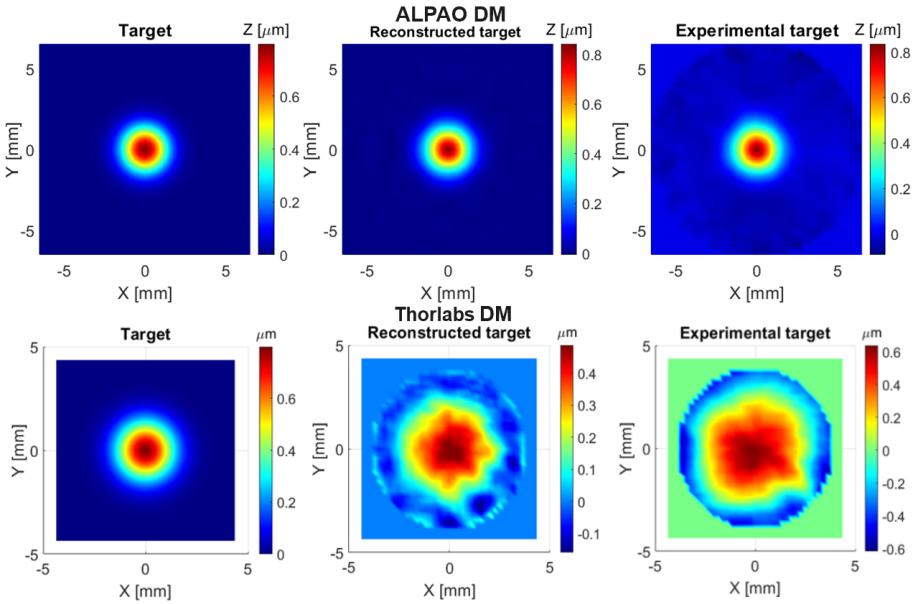

Figure 5.20: *In the first row there are the results from the ALPAO DM and in the second row the results from the Thorlabs DM. On the left: the phase pattern chosen as a target to be reproduced by the DM. In the middle: the reconstructed target computed by the actuation coefficients. On the right: measured phase pattern reproduced by the DM. The target and the experimental patterns agree within 3% for the ALPAO DM and within 17% for the Thorlabs DM.*

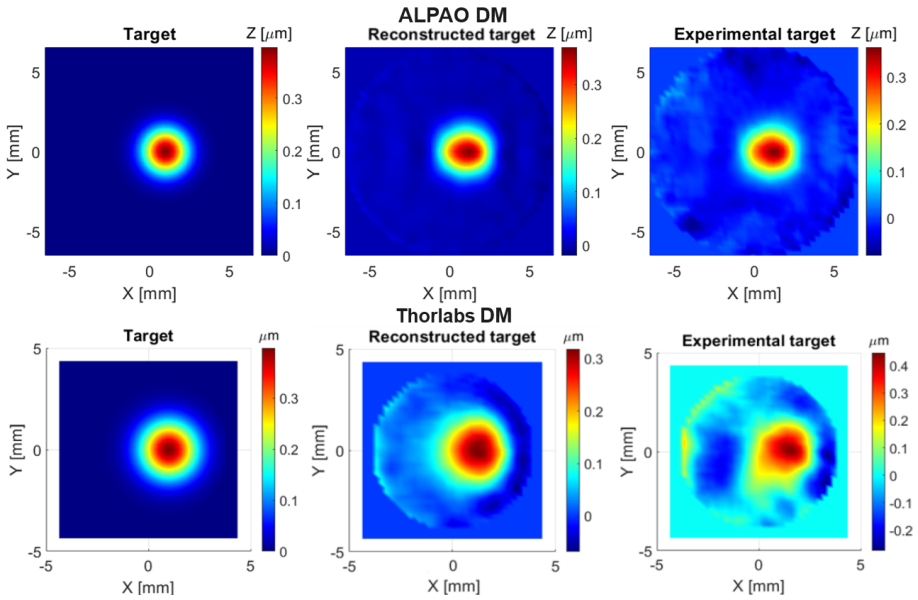

Figure 5.21: *In the first row there are the results from the ALPAO DM and in the second row the results from the Thorlabs DM. On the left: the phase pattern chosen as a target to be reproduced by the DM. In the middle: the reconstructed target computed by the actuation coefficients. On the right: measured phase pattern reproduced by the DM. The target and the experimental patterns agree within 2% for the ALPAO DM and within 8% for the Thorlabs DM.*

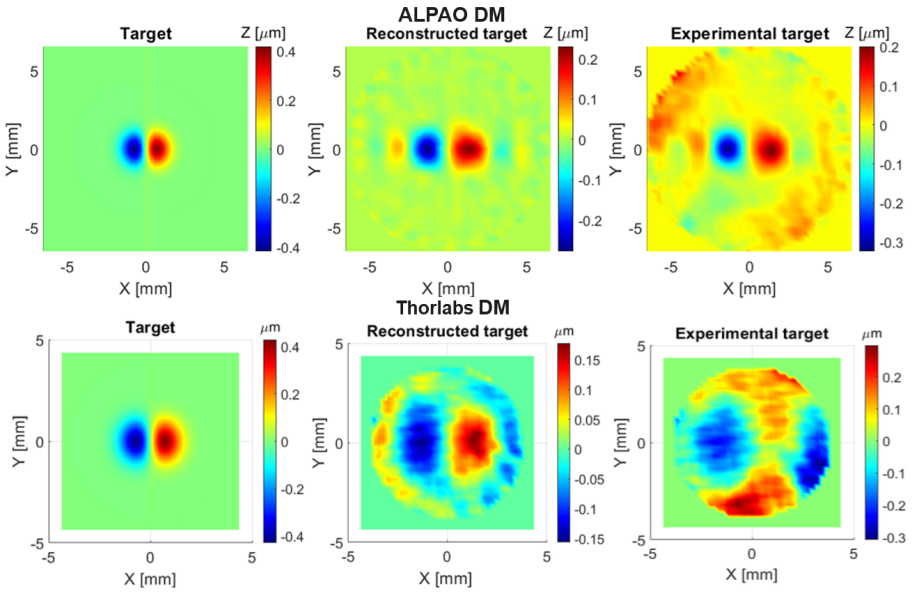

Figure 5.22: *In the first row there are the results from the ALPAO DM and in the second row the results from the Thorlabs DM. On the left: the phase pattern chosen as a target to be reproduced by the DM. In the middle: the reconstructed target computed by the actuation coefficients. On the right: measured phase pattern reproduced by the DM. The target and the experimental patterns agree within 4% for the ALPAO DM and within 19% for the Thorlabs DM.*

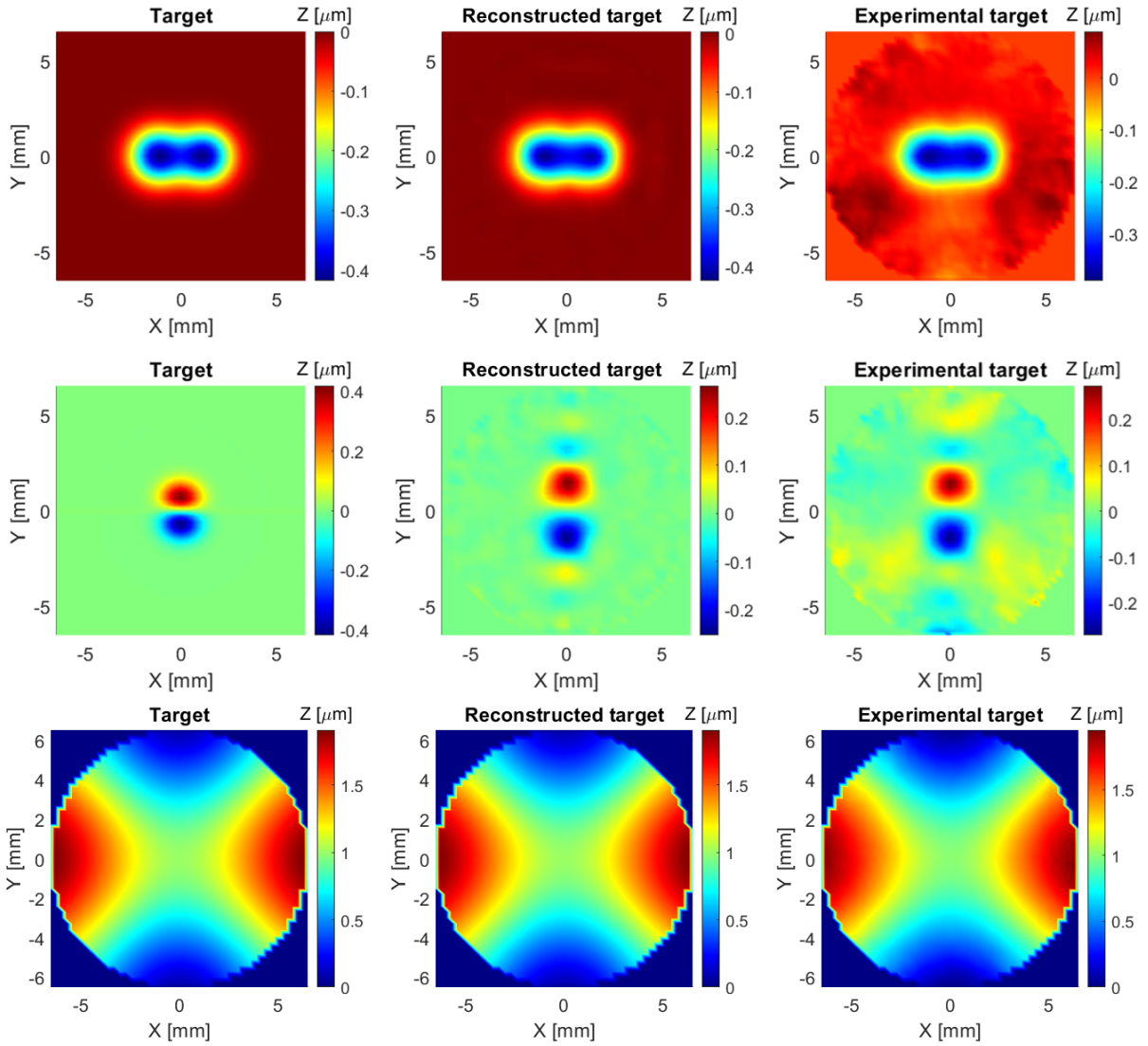

Figure 5.23: *On the left: the phase patterns chosen as a target to be reproduced by the ALPAO DM. In the middle: the reconstructed targets computed by the actuation coefficients. On the right: measured phase patterns reproduced by the DM. The target and the experimental patterns agree within 4% for the fourth pattern, within 4% for the fifth pattern and within 2% for the sixth pattern.*

5.3 Modified Ghergberg-Saxton algorithm

As discussed in section 5.1, the need arises for a method that allows the determination of the phase profile required to achieve the selected target pattern at a specific plane. Subsequently, this phase profile can be used in conjunction with a lens to project the image of this plane onto a CP with the appropriate magnification. This thesis presents the investigation of a prototype of this system, with the study extending up to the image plane. The final optical design, incorporating the projection lens and bench setups, will be addressed in future work. This research addresses a classical phase retrieval problem, wherein the goal is to deduce phase information from intensity measurements at two distinct planes. Standard algorithms within this class are typically derived from the original iterative methods, such as Gerchberg-Saxton algorithm [144, 145], or the **T**ransport-of-

Intensity **E**quation (TIE) method [146].
In the paraxial domain, one of these methods is based on the TIE. Since the relationship between phase and intensity is described by the TIE, it becomes possible to extract phase information through two intensity measurements at different distances. However, its primary drawback is its dependence on the axial intensity derivative in the paraxial direction. Therefore, the distance between intensity measurements must be sufficiently short. Another approach is the Gerchberg-Saxton iterative algorithm. Compared to the TIE, the Gerchberg-Saxton algorithm offers greater flexibility in terms of propagation distance. The Gerchberg-Saxton algorithm is based on a propagator that is the simple Fourier Transform. Therefore, a **Mo**dified **G**erchberg-**S**axton algorithm is proposed in which the propagator is replaced by a fast propagation algorithm, namely, the **Fr**esnel **T**ransform (FRT) [147], which is valid within the paraxial domain. The FRT can be seen as the *Rayleigh-Sommerfeld diffraction* method in the paraxial approximation [148]. For our purposes, a **Mo**dified **G**erchberg-**S**axton algorithm [149] integrated with the measured *influence functions matrix* has been developed.
Let us examine the propagation of monochromatic light originating from a 2D plane, referred to as the source plane, with coordinate variables ξ and η, as illustrated in Figure 5.24.

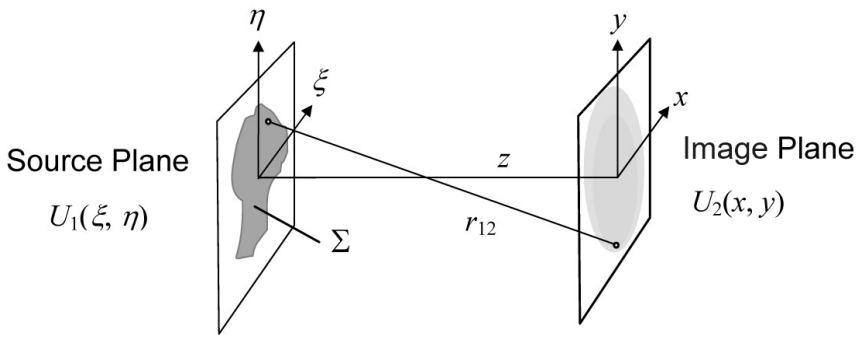

Figure 5.24: *Propagation geometry for parallel source and image planes.*

Within this source plane, an area Σ identifies the boundaries of a source or an illuminated aperture. The *Huygens–Fresnel principle* postulates that the source behaves as an infinite set of hypothetical point sources. Each of these point sources generates a spherical wave associated with the real source field at any given position (ξ, η). The contributions from these spherical waves are aggregated at the observation point (x, y), allowing for interference. The field distribution at the source plane is represented as $U_1(\xi, \eta)$, and we can estimate the field $U_2(x, y)$ in a remote observation plane using the initial Rayleigh–Sommerfeld diffraction solution:

$$U_2(x,y) = \frac{z}{i\lambda} \iint_{\Sigma} U_1(\xi,\eta) \frac{e^{ikr_{12}}}{r_{12}^2} d\xi d\eta, \tag{5.7}$$

where λ is the optical wavelength, $k = \frac{2\pi}{\lambda}$ is the wave number in free space, z is the distance between the centres of the source and image coordinate systems and r_{12} is the distance between a point on the source plane and a point on the image plane. Variables ξ and η serve as integration variables, and the limits of the integral pertain to the source area Σ. When the source and image positions are situated on parallel planes, we can define $r_{12} = \sqrt{z^2 + (x-\xi)^2 + (y-\eta)^2}$. Equation 5.7 represents a superposition integral.

When both the source and image regions are defined on parallel planes, it transforms into a convolution integral, which can be expressed as:

$$U_2(x,y) = \iint U_1(\xi,\eta)\, h(x-\xi, y-\eta)\, d\xi d\eta, \tag{5.8}$$

where the general form of the Rayleigh–Sommerfeld impulse response is $h(x,y) = \frac{z}{i\lambda}\frac{e^{ikr}}{r^2}$ and $r = \sqrt{z^2+x^2+y^2}$. The Fourier convolution theorem is applied to equation 5.8:

$$U_2(x,y) = \Im^{-1}\{\Im\{U_1(x,y)\}\Im\{h(x,y)\}\}, \tag{5.9}$$

where $\Im$ and $\Im^{-1}$ are the Fourier Transform and its inverse, respectively, and the source and image plane variables are re-labeled as x and y. The FRT offers a distinct benefit by exploiting the power of FFT for rapid calculations. To apply the FFT, the source plane is sampled on a grid, the coordinates along one dimension can be represented as $x \to \left[-\frac{L}{2} : \Delta x : \frac{L}{2} - \Delta x\right]$, a notation borrowed from Matlab, signifying that the coordinates span from $-\frac{L}{2}$ to $\frac{L}{2} - \Delta x$ in Δx increments. This same convention is applied to the y-axis coordinates. Assuming the Fourier Transform relationship between spatial and spectral domains, the continuous space of the frequency with coordinates f_X and f_Y inherits a discrete structure described by the substitutions:

- $f_X \to \frac{p}{M\Delta x}$, with $p = -\frac{M}{2}, ..., \frac{M}{2} - 1$;
- $f_Y \to \frac{q}{N\Delta x}$, with $q = -\frac{N}{2}, ..., \frac{N}{2} - 1$,

obtaining M and N evenly spaced coordinates within the intervals:
$f_X \to \left[-\frac{1}{2\Delta x} : \frac{1}{L} : \frac{1}{2\Delta x} - \frac{1}{L}\right]$ and the f_Y coordinates are similar. With this choice, it is possible to derive an equivalent expression for equation 5.9:

$$U_2(x,y) = \Im^{-1}\{\Im\{U_1(x,y)\}H(f_X,f_Y)\}, \tag{5.10}$$

where H is the Rayleigh–Sommerfeld transfer function given by:

$$H(f_X,f_Y) = e^{ikz\sqrt{1-(\lambda f_X)^2-(\lambda f_Y)^2}}. \tag{5.11}$$

The condition $\sqrt{f_X^2}+\sqrt{f_Y}^2 < \frac{1}{\lambda}$ for propagating field components must be met. Assuming scalar diffraction, this solution merely necessitates that the distance between the source and the observation point is significantly larger than the wavelength $r >> \lambda$.
At this point, it is necessary to choose which propagator to use. The TF propagator uses the transfer function H given by $H(f_X,f_Y) = e^{ikz}e^{-i\pi\lambda z\left(f_X^2+f_Y^2\right)}$ and the IR propagator uses the impulse response h given by $\frac{e^{ikz}}{ikz}e^{\frac{ik}{2z}(x^2+y^2)}$. Due to computational artifacts, the IR approach turns out to be more limited in terms of the situations where it should be used than the TF approach, however, it provides a way to simulate propagation over longer distances and is useful for the discussion of simulation limitations and artifacts. The significant artifacts are related to discrete sampling. Two criteria have been considered for the choice of the propagator. A first criterion is that the support of the source field should "fit" within the numerical array. If D is the effective support of the source field (maximum linear width) and L is the array side length, then we usually require $D < L$. This help reduce artifacts at the edges of the array after propagation due to the periodic extension properties of the FFT. The second criterion is derived by considering the effects of sampling the transfer function H and impulse response h expressions. On one hand,

H is adequately sampled (oversampled) when $\Delta x \geq \frac{\lambda z}{L}$, this relationship is derived by considering aliasing of the transfer function in the frequency domain and then converting to the sampled space domain. On the other hand, h chirp is oversampled when $\Delta x \leq \frac{\lambda z}{L}$. These expressions reveal that the oversampling criteria for the transform pair H and h are opposite. With the parameters that will be well described in the section 5.3.1, the TF propagator will be used to maintain the oversampling criteria. This propagator function accepts the source field and generates the image field, ensuring that the dimensions and sample coordinates of both the source and image sides are the same. The TF FRT has been used to develop a model, and therefore, a Matlab code starting from the MoG-S algorithm summarized in Figure 5.25.

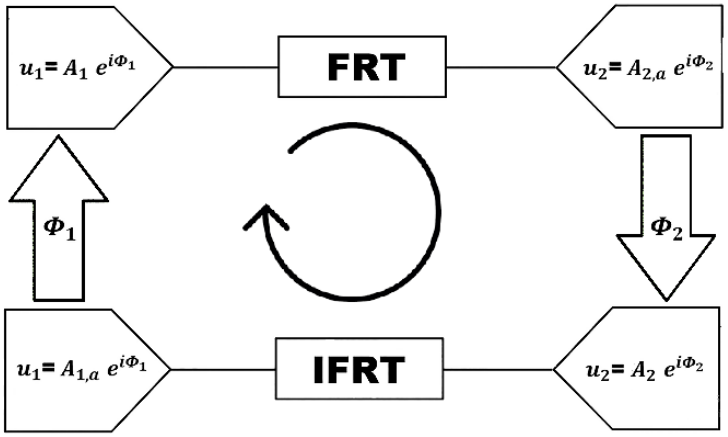

Figure 5.25: *General iterative algorithm of a MoG-S in the Fresnel domain.*

In general, the input and output amplitudes $A_1 = \sqrt{I_1}$ and $A_2 = \sqrt{I_2}$ are given by an intensity measurement. In our case, however, the input field $u_1 = A_1 e^{i\phi_1}$ is given by the CO_2 laser beam impinging on the DM while the image field is represented by the target intensity we want to have at the output. The input field is transformed to the output field u_2 at the distance z with the FRT using the FFT method previously mentioned. The output field amplitude $A_{2,a} = |u_2|$ is replaced using a target intensity $I_2 = A_2^2$ equal to the heating pattern for the wavefront correction while keeping the phase:

$$u_2 = A_{2,a} e^{i\phi_2} \rightarrow u_2 = A_2 e^{i\phi_2}. \tag{5.12}$$

In the algorithm, all intensities have been normalized by dividing them by their maximum value. Then, the inverse FRT is applied on the modified u_2 in order to calculate the input field u_1. Analog to u_2 the input field u_1 is modified by the use of the input field amplitude A_1 as:

$$u_1 = A_{1,a} e^{i\phi_1} \rightarrow u_1 = A_1 e^{i\phi_1}. \tag{5.13}$$

The iteration is repeated until the intensities A_2 and $A_{2,a}$ converge. In our application codes the iteration was performed 400 times, even though it was actually tested that $A_{2,a}$ began to converge with the desired target intensity after just 100 iterations. However, a greater number of iterations was used to refine the convergence as much as possible. In fact, the correlation coefficient converge to 1 after 400 iterations.

5.3.1 Parameters estimation

When implementing the MoG-S algorithm codes in Matlab, the requirement of an experimental validation with dimensions that could be replicated on an actual optical bench has been considered. To evaluate the selection of each parameter mentioned in the previous section, various attempts were undertaken. This section will briefly outline the choice made for each parameter and the reasoning behind the final selection. The parameters will be presented in a particular sequence, yet it is important to note that the optimal outcome was achieved through their collective interaction. During the fine-tuning of the simulation, any changes in one parameter necessitated corresponding adjustments in all the others.
The first parameter considered is the wavelength, which is indeed that of the CO_2 laser, namely 10.6 μm. Furthermore, the initial parameters under investigation are those associated with the source plane - refer to Figure 5.24 - with side length L divided into M samples upon which a Gaussian beam with waist w is incident. In this case the source plane corresponds to the DM plane.

- FFT algorithms are most efficient when M is a power of 2. However, if M is too large, it will slow down the computational speed, but if it is too small, resolution is spoiled. We have found the best compromise with $M = 2^8$, and Figures 5.26 and 5.27 have been created using this value.

- The dimension w of the impinging beam on the DM affects the convergence of the two intensities, the *target intensity* corresponding to I_2, and the *recovered intensity* corresponding to $I_{2,a} = A_{2,a}^2$. Furthermore, w must be large enough to cover the entire surface of the DM to avoid losing the effectiveness of the outermost actuators but cannot be too large to prevent diffraction effects caused by the mirror's edge. In Figure 5.26 we can observe a simple target intensity reproduced for the ideal value of w equal to 4.6 mm and a smaller value equal to 3 mm.

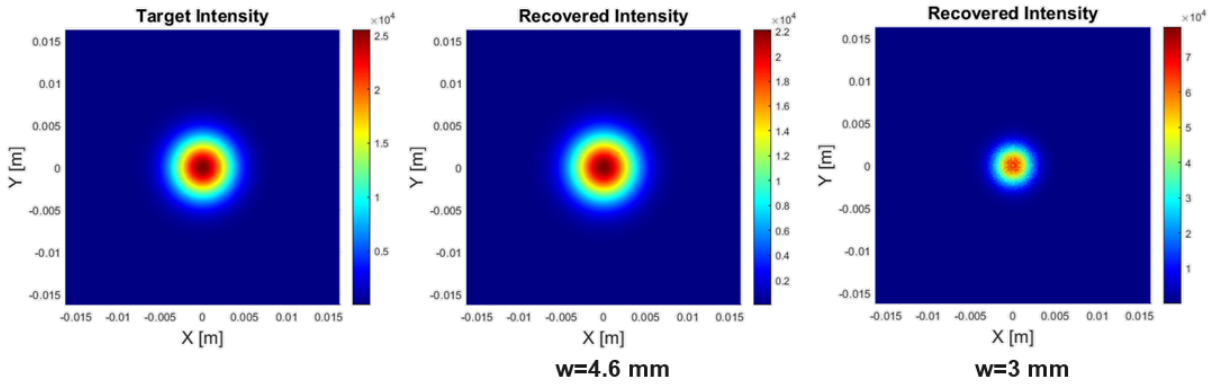

Figure 5.26: *Results of simulating the MoG-S algorithm for two different values of w.*

- The value assigned to L significantly affects the convergence of the two intensities. An example is illustrated in Figure 5.27, where we can observe a random target intensity reproduced for the selected value of M, w and the L value equal to the optimal value of $2.5 \cdot D_{DM}$ where $D_{DM} = 13.5$ mm is the ALPAO DM diameter, equal to a larger value and to a smaller one.

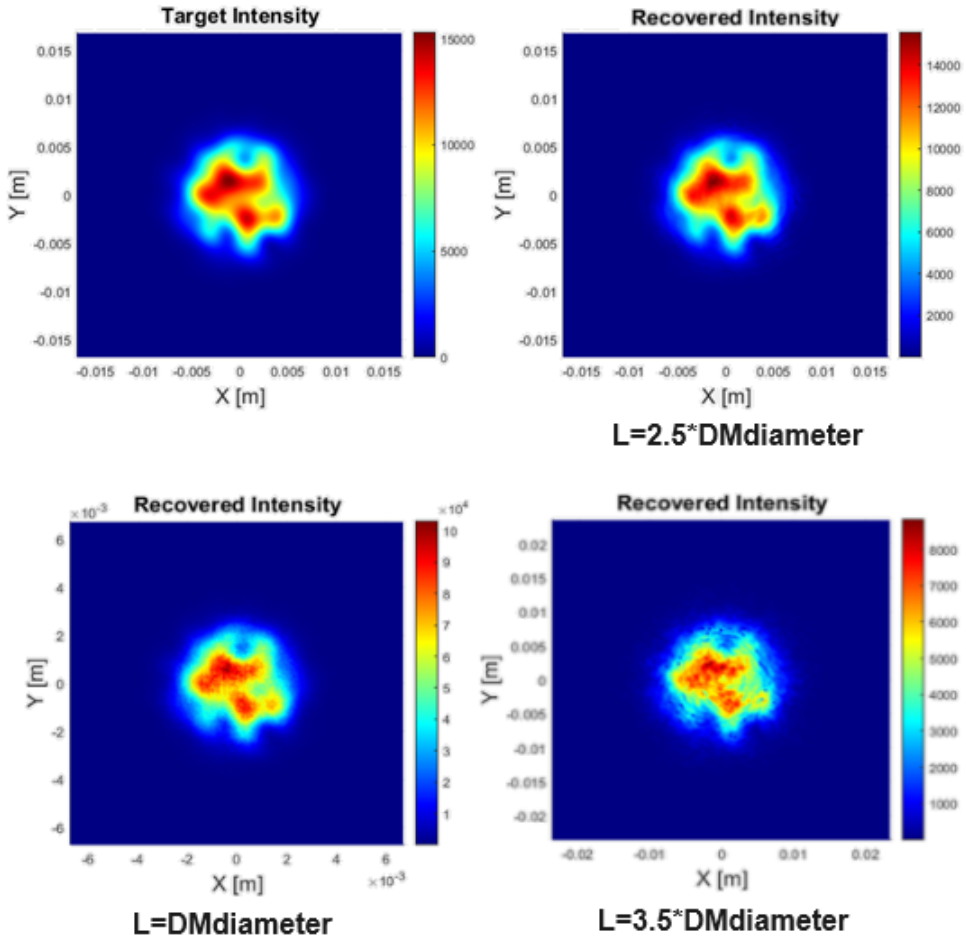

Figure 5.27: *Results of simulating the MoG-S algorithm for various L values and with $M = 2^8$ and $w = 4.6$ mm.*

Once the source plane and the impinging beam on the DM are defined, the next step is to define the image plane and the parameters of the target intensity. To optimize the MoG-S algorithm, a set of test targets has been produced using a random generator that allows the choice of the dimension of the image plane, the support of the target intensity and its spatial frequency.

- The dimension of the image plane must be equal to that of the source, thus we have again a square plane with side length L divided into M samples.
- The optimal distance is constrained by its practical feasibility on the bench, so a range of acceptable distances from 10 cm to 1 m was set, and the best condition was sought within this range. The distance $z = 0.5$ m of the image plane from DM has been found to be the optimal distance at which the target intensity and the recovered intensity converge as closely as possible. From now on, this plane will be referred to as the *Object plane* since it will be the plane where the target is reproduced most accurately.
- It has been observed that the size of the target intensity pattern affects the phase obtained in the DM plane, which is the phase to be applied by the DM. The optimal dimensions are similar to the incident beam on the DM, as shown in Figure 5.28. Significantly different dimensions require the use of dioptre power, which results in

a complex phase wrapping pattern. Since 2D phase unwrapping is complex and inefficient, a preference is given to a result where the phase remains continuous in the area where the intensity is significantly different from zero. Therefore, target intensities with a radius of approximately 4.6 mm have been selected. For comparison, the spot size of the YAG on the CP is ∼5 cm, so we imagine a magnification of about 10 between the image and CP.

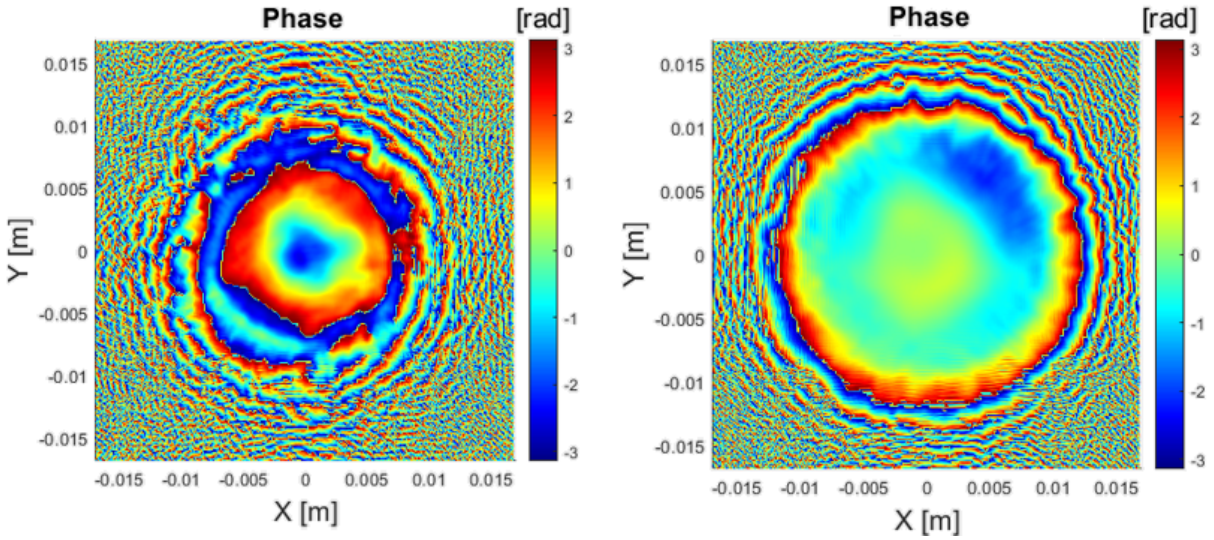

Figure 5.28: *Results of simulating the MoG-S algorithm for two different dimensions of the target intensity. On the left: ϕ_1 with a target intensity dimensions smaller than the optimal ones. On the right: ϕ_1 with the optimal target intensity dimensions.*

- In creating the target, the AdV+ requirement is used, which is 4 cm^{-1} on the DM. This choice produces wrapping effects at the edge, where, as mentioned before, the intensity is negligible. The ideal spatial frequency corresponds to half of the spatial frequency of the ALPAO DM actuators, with a pitch of 1.5 mm, which is approximately 666 m^{-1}. Therefore, the optimal spatial frequency is 333 m^{-1}. For spatial frequencies equal to 400 m^{-1}, the target was perfectly reproduced, but wrapping effects were observed at the edge of the considered region, as shown in Figure 5.29. This can be resolved with a greater number of actuators.

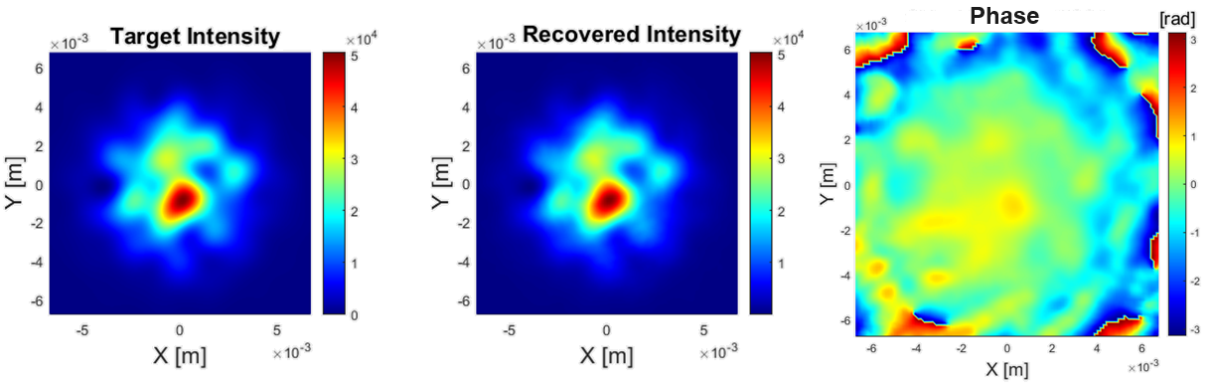

Figure 5.29: *Result from the simulation of the MoG-S algorithm, incorporating all the optimal parameters with a target spatial frequencies equal to 400 m^{-1}.*

Figure 5.30 shows the result from a simulation of the MoG-S algorithm, incorporating all the optimal parameters established thus far. The target intensity and the recovered intensity are in agreement within 1%. This profile has been chosen from those generated randomly to illustrate the complete process, which includes simulation and bench testing. This represents only a starting point for further investigation of other profiles with different and more demanding characteristics.

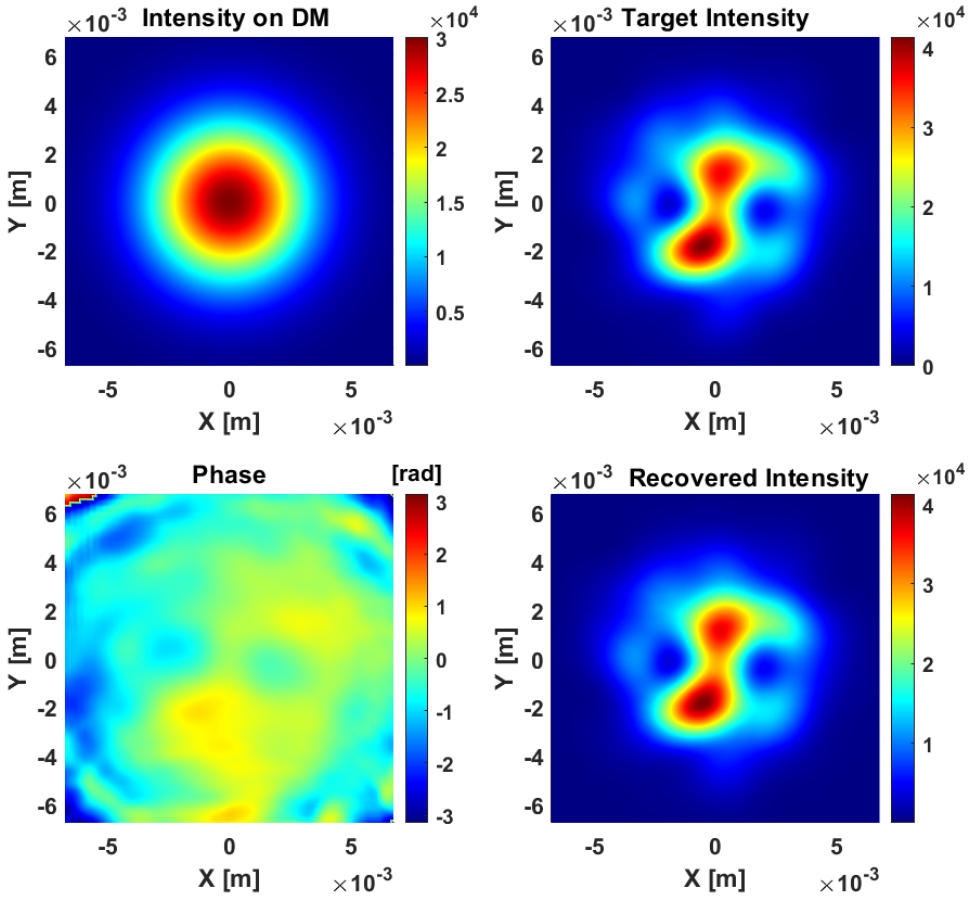

Figure 5.30: *Result from a simulation of the MoG-S algorithm, performed using the optimal set of parameters.*

5.3.2 Optical layout design

Once the parameters have been set, a CO_2 laser has been characterized in order to proceed with the implementation of the optical layout necessary to test the findings of the simulations. Figure 5.31 shows the spotsize as a function of distance, with zero distance representing the laser output. The red and blue points represent the spotsize along the x and y axes, respectively, measured through beam image analysis using a CCD. Meanwhile, the red and blue lines are their fits using the caustic formula for Gaussian beams described by equation 5.1, where the parameter M^2 has been set to be 1.

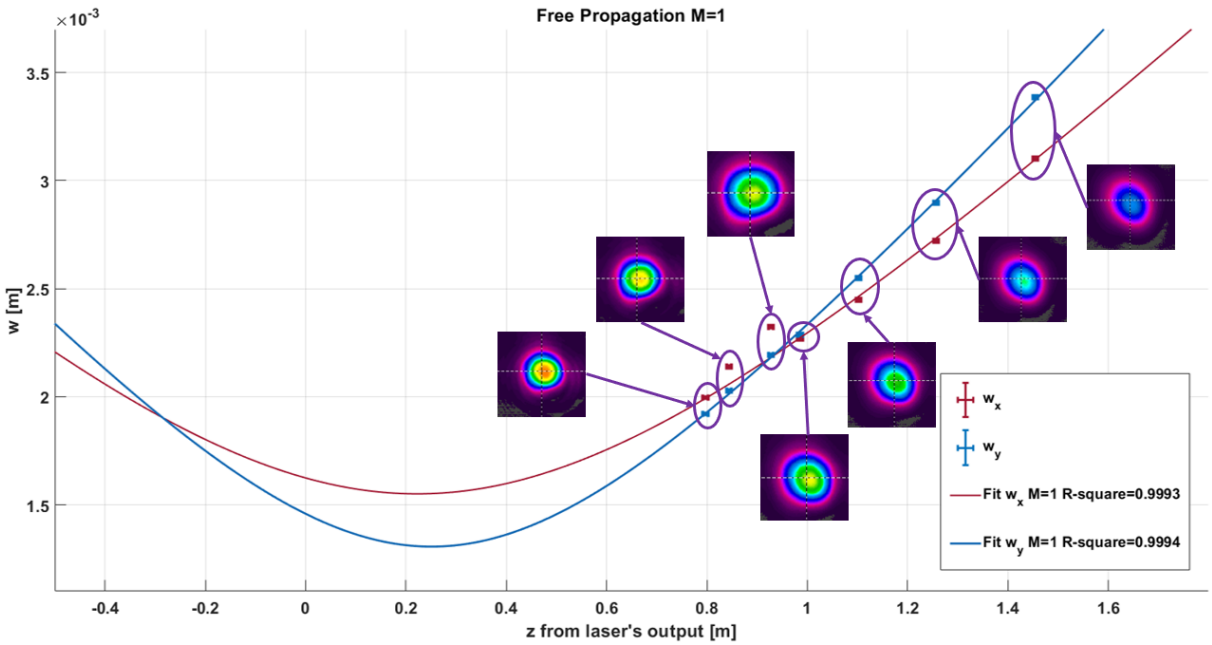

Figure 5.31: *CO_2 laser beam fitted caustic. The red and blue points represent the measured spotsize along the x and y axes, respectively and the red and blue lines are their fits. Images of the beam taken with the CCD for different positions are also shown.*

From the performed analysis, the beam astigmatism is evident and the optical layout has been designed using the average values: $w_0 = (1.35 \pm 0.07)$ mm, $z = (0.23 \pm 0.02)$ mm. The conceptual layout is shown in Figure 5.32.

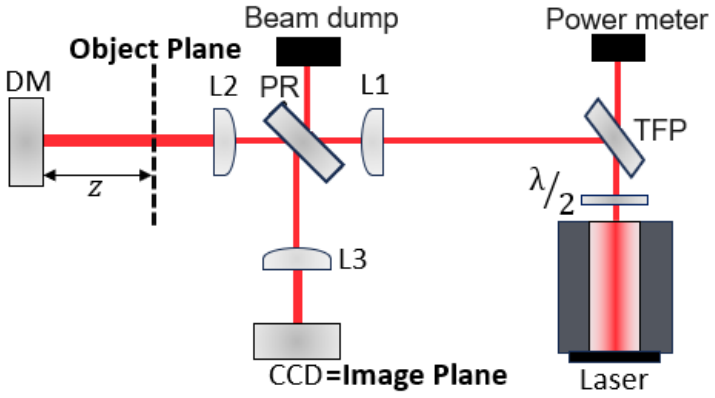

Figure 5.32: *Conceptual layout of the optical layout designed for testing the MoG-S algorithm simulations.*

The laser beam first passes through a **T**hin **F**ilm **P**olarizer (TFP) which splits the beam into two, with the transmitted beam reaching the power meter to monitor the laser power, while the reflected beam passes through the half-wave plate that in combination with the TFP allows to control and manipulate the polarization of light in order to enable power adjustment. Subsequently, it passes through a **P**artial **R**eflector (PR) that reflects 70% and transmits 30% independently of polarization. Then it is magnified to adapt the beam's dimensions to the DM using a telescope composed of L1 with a focal length of f_1 =75 mm and L2 with f_2 =254 mm and finally the beam reaches the DM with a spotsize of about 5.3 mm. Upon reflection from the DM, the beam undergoes further

adaptation via the second telescope composed by L2 and L3 with f_3 =222.25 mm to gain the appropriate dimensions for the CCD and is reflected by the PR reaching the CCD with a spotsize of about 4.6 mm as required by the simulations. The PR is placed at the focal point to reduce the impact of divergence and ensure that the beam is not cut, and the return path after reflection on the DM is slightly misaligned to prevent the beam from re-entering the source. The PR has been employed due to the unavailability[1] of a quarter-wave plate for the CO_2 beam. The CCD is placed in the image plane of the plane located at a distance z from the DM where the simulations accurately reconstructed the chosen pattern intensity. In order to estimate the position of the image plane, the image formed by the lens L2 is used as the object for the lens L3. Knowing that the distance between the object plane and L2 is p_1 =100 mm, the other parameters have been evaluated as:

- the L2 image distance $q_1 = \frac{p_1 f_2}{p_1 - f_2} = -162.34$ mm;
- the L3 object distance $p_2 = d_{2,3} - q_1$ =638.59 mm with $d_{2,3}$ is the distance between L2 and L3;
- the L3 image distance $q_2 = \frac{p_2 f_3}{p_2 - f_3}$ =340.89 mm.

The image plane verification process was carried out as done for the characterization optical layout, as described in section 5.2.1. During the verification process to confirm if the CCD was indeed in the image plane, two issues related to the optical layout were observed -see Figure 5.33:

- the diffraction due to the beam clipping at the edges of the DM;
- the interference produced by the recombination of the secondary PR reflections not completely cancelled by the AR coating.

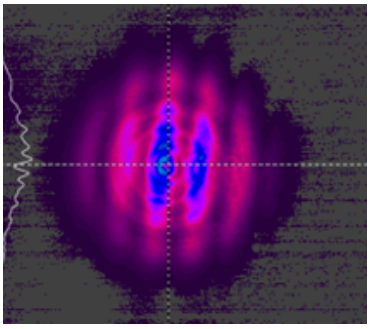

Figure 5.33: *Picture of the image plane beam taken by the CCD.*

To overcome these two issues, two strategies were implemented:

- L1 and L2 have been replaced with two lenses of the same focal length equal to 127 mm and have been placed at a distance of 268 mm greater than the sum of the focal lengths, in order to have a smaller beam impinging on the DM with a spotsize of 2.3 mm. This results in having a waist that is half of what was estimated to be optimal by the simulations, meaning that the simulation parameters have been readjusted to this value and the outermost actuators will have less influence on the pattern reconstruction.

[1] During the research activities, the prices of high-power CO_2 lenses have soared, so a market search is still ongoing.

- a small tilt was applied to the DM to create distinct paths for the incident and return beams. This allowed us to eliminate L3 and PR, and position the CCD directly in the object plane, which is at a distance z from the DM at the price of having a small astigmatism in the obtained profile.

The resulting simplified layout is shown in Figure 5.34.

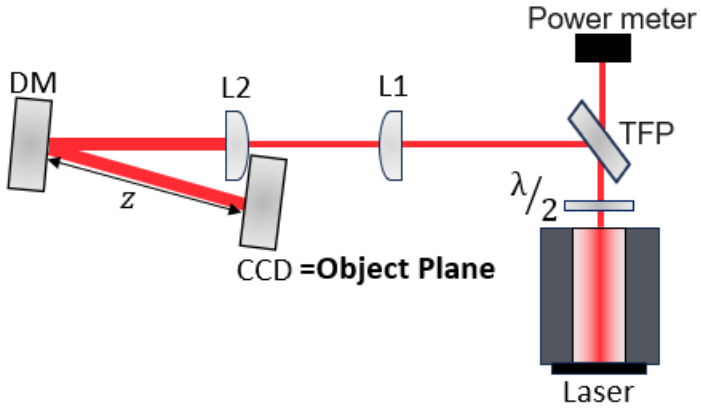

Figure 5.34: *Simplified layout of the optical layout used for testing the MoG-S algorithm simulations.*

5.4 Results and future prospects

Results

Before moving forward with the experimental validation, the phase derived from the MoG-S algorithm is reconstructed by the DM following the procedure outlined in section 5.2.4. Subsequently, this *reconstructed phase* has been combined with the incident field on the DM and then propagated to a distance z to compare the obtained intensity with the expected target intensity. In this instance, they are in agreement - by calculating the percentage error of the RMS of their difference - within 11%. Figure 5.35 illustrates the obtained results.

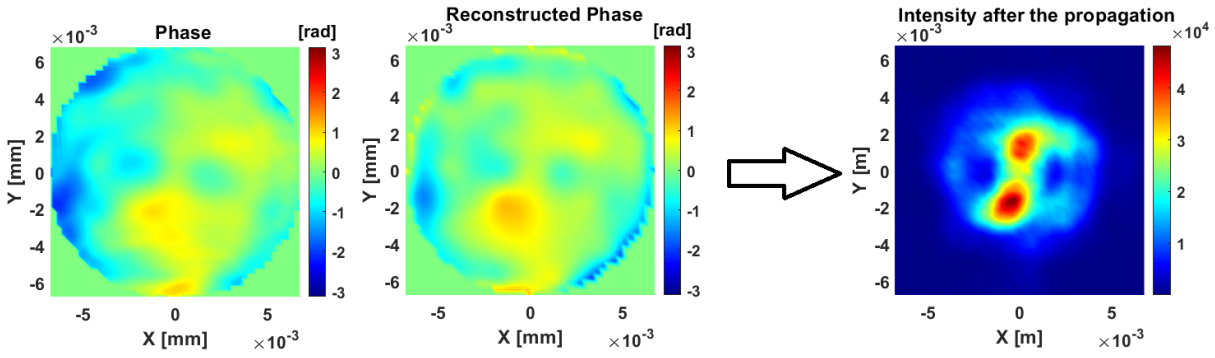

Figure 5.35: *Phase extracted from the MoG-S algorithm (left) and phase reconstructed by the DM (middle) and the intensity obtained after the propagation of the reconstructed phase combined with the incident field on the DM (right).*

The next stage involves experimental verification of our findings. To accomplish this, we utilized the optical layout sketched in Figure 5.34. As outlined in section 5.2.4, from

the phase converted in the vector b, we can derive the actuation coefficients of the influence functions to be sent to the DM using a Matlab code. Subsequently, the intensity image has been captured using the CCD camera and shown in Figure 5.36.
For the purpose of correcting optical defects, what matters in terms of requirements is the residual OPL, thus the comparison should be made on OPL increases rather than intensities. The FEA simulations were carried out to obtain the OPLs generated by these two intensities when applied to the CPs. The OPLs obtained are shown in Figure 5.36 and they are in agreement within 6% calculated again as the percentage error of the RMS of their difference. This number can be used to determine what is the maximum amplitude that could be corrected with this accuracy. In fact, it means that the 2 nm RMS must be within 6%, so the total pattern RMS is $\leq \frac{2 \text{ nm}}{6} * 100) = 33.3$ nm.

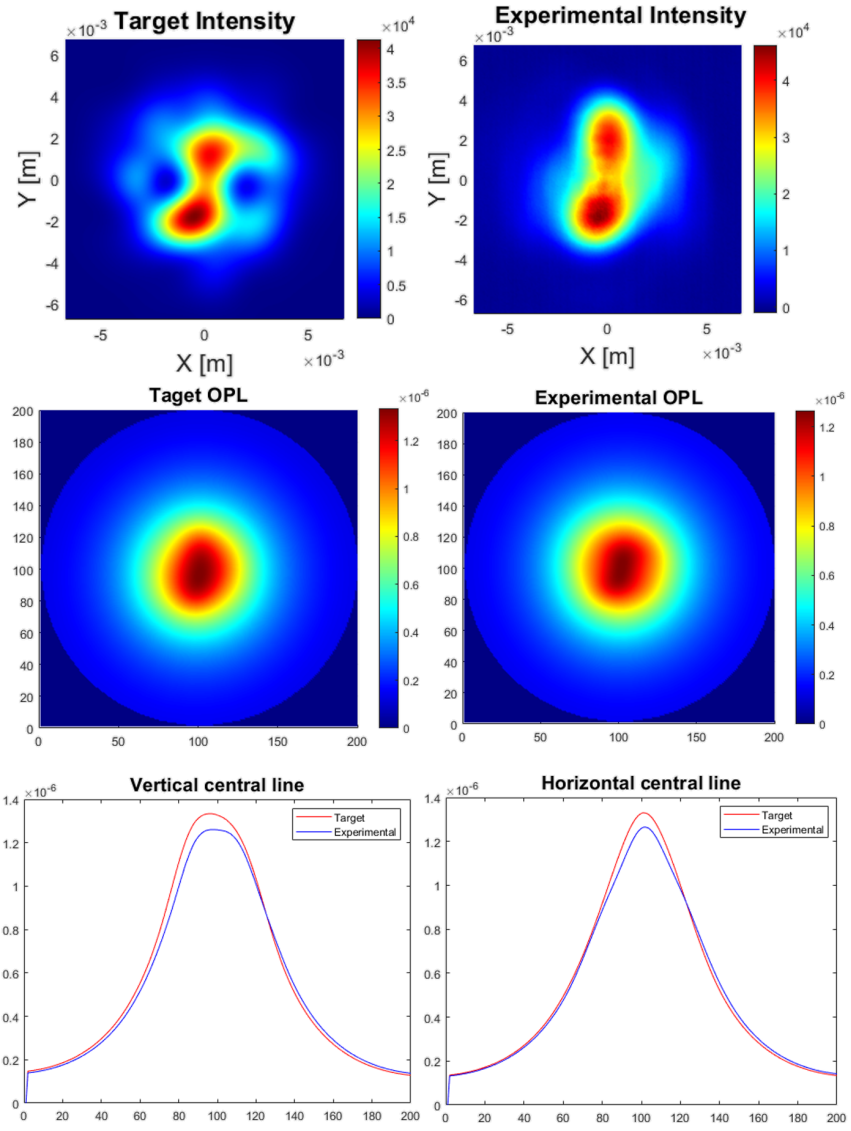

Figure 5.36: *In the first line the target intensity and the experimental one are shown. In the second line the OPLs that would generate these two intensities when applied to the CPs are shown. In the third line the vertical central line of the OPLs and the horizontal one are shown, the blue line is for the experimental OPL and the red one for the target one. The colorbars are in normalized units since all intensities are normalized by dividing them by their maximum value.*

The investigation of this prototype has enabled the development of a characterization procedure, the implementation of simulations based on the MoG-S algorithm, and the validation of the optical layout, which, in turn, allows us to replicate desired experimental results. With these results in hand, we will be equipped to derive complementary compensation once the OPL maps for non-axisymmetric optical aberrations in AdV+'s CPs become available. This will enable us to adjust the optical layout for CO_2 benches by integrating the DM, thereby facilitating the reproduction of complementary compensation.

Future prospects

As previously discussed, a future idea is to test other profiles with different and more demanding characteristics. This will allow us to gain a clearer understanding of the specific features required for acquiring a DM with more specialized characteristic, such as a higher number of actuators to address spatial frequency needs. The simplified layout shown in Figure 5.34 can also be employed in the design of the upgraded CO_2 bench, provided that astigmatism's impact is minimized and a solution to the diffraction issue is found to use the entire set of actuators most efficiently. Furthermore, it is possible to consider the study of a fine intensity feedback adjustment method on the image plane to further reduce the deviation of OPL from the desired compensation. However, this implies the identification of an appropriate error signal to be integrated into the MoG-S algorithm.

Conclusions

In this thesis, the fundamental reasons why the Thermal Compensation System (TCS) plays a pivotal role in maintaining the interferometer at its ideal operational state have been explored. Supported by the detection of ninety gravitational wave signals arising from the mergers of binary systems of black holes, neutron stars, and mixed systems, the first chapter illustrates how continuing research in this domain opens new paths in fundamental physics, astrophysics, and cosmology. To achieve this, it is imperative to continuously enhance the sensitivity of gravitational wave detectors, thereby enabling the observation of a broader range of sources.
The performance of gravitational wave detectors is hampered by wavefront distortion resulting from the absorption of the primary laser beam within their core optics. To counteract these thermal effects, the strategy of introducing a complementary distortion to restore the interferometer's original optical configuration has been employed. Furthermore, the TCS is capable of compensating for non-thermal sources of aberration.
The fourth chapter describes the alignment procedures for the auxiliary beams of the Hartmann wavefront sensors and for the CO_2 laser beams of the TCS actuators and their characterization. These procedures are not only essential for the precise control of actuator operations but also enable us to accurately simulate their effects within the interferometer. This characterization and simulation capabilities have allowed the development of techniques and procedures for compensating not only axisymmetric optical aberrations but also cold defects, as demonstrated in the case of the cold lens within the compensation plate of the North input test mass. Regardless of the input power, following the image analysis techniques from the sensors and the compensation procedures outlined in this thesis, we are capable of achieving effective correction of optical defects, making the enhancement of the interferometer's sensitivity and the binary neutron star detection range possible.
With the projected increase in power for the upcoming O5 observing run, the effects of absorption induced non-axisymmetric optical aberrations will become increasingly critical. To deal with these residual distortions, this thesis investigates the use of a deformable mirror prototype that, by imprinting a phase pattern onto an incident CO_2 laser beam, can recreate a corrective heating profile on a compensation optic. Extensive market research has led to the characterization of a highly promising device developed by the company ALPAO. This device demonstrates remarkable reproducibility of the desired heating profile and stability. The application represents a novel approach, since in astronomy the deformable mirrors are typically used for phase correction in closed-loop systems, connected to sensors providing real-time feedback for mirror surface deformations. For modelling the deformable mirror action, a simulation tool using the modified Ghergberg-Saxton algorithm for phase retrieval has been developed. Since the deformable mirror acts on phase patterns while our focus is on intensity profiles, the aim was to extract the phase by measuring the intensity on the deformable mirror plane and in a specific plane where

we desire the intensity profile to be reproduced.
The final part of the thesis demonstrates the effectiveness of the simulation tool that uses the modified Ghergberg-Saxton algorithm and the agreement between the simulations and the experimental data. This study has defined the procedures for characterization of the deformable mirror and the development of simulations, developing a deformable mirror-based bench-top prototype for the compensation of non-axisymmetric wavefront distortions in Advanced Virgo+. The results obtained pave the way to the integration of this new class of actuators in the design of the TCS for Advanced Virgo+ Phase II upgrade.

List of acronyms and abbreviations

A+ **A**dvanced Ligo +

AdV+ **Ad**vanced **V**irgo +

AR **A**nti-**R**eflective

ASD **A**mplitude **S**pectral **D**ensity

BBH **B**inary **B**lack **H**ole

BH **B**lack **H**ole

BNS **B**inary **N**eutron **S**tar

BS **B**eam **S**plitter

BS-REC **BS** of **R**ecombination

CA **Ca**rrier

CDM **C**old **D**ark **M**atter

CH **C**entral **H**eating

CHRoCC **C**entral **H**eating **R**adius **o**f **C**urvature **C**orrection

CMRF **C**ommon **M**ode **R**ejection **F**actor

CP **C**ompensation **P**late

CW **C**ontinuous **W**aves

DAS **D**ouble **A**xicon **S**ystem

DAS-IN **DAS-In**ner ring

DAS-OUT **DAS-Out**er ring

DE **D**ark **E**nergy

DET **Det**ection

DM **D**eformable **M**irror

DoF **D**egree **o**f **F**reedom

EDB **E**xternal **D**etection **B**ench

EGO **E**uropean **G**ravitational **O**bservatory

EIB **E**xternal **I**njection **B**ench

EM **E**lectro**M**agnetic

EOM **E**lectro **O**ptical **M**odulator

EoS **E**quation **o**f **S**tate

ET **E**instein **T**elescope

ET-HF **E**instein **T**elescope **l**ow-**h**igh

ET-LF **E**instein **T**elescope **l**ow-**f**requency

ETM **E**nd **T**est **M**ass

FC **F**ilter **C**avity

FEA **F**inite **E**lement **A**nalysis

FFT **F**ast **F**ourier **T**ransform

FP **F**abry-**P**erot

FRT **Fr**esnel **T**ransform

GR **G**eneral **R**elativity

GRB **G**amma-**R**ay **B**urst

GW **G**ravitational **W**ave

HM **H**ot **M**irror

HOM **H**igher-**O**rder **M**ode

HP **H**artmann **P**late

HR **H**igh **R**eflectivity

HWS **H**artmann **W**avefront **S**ensor

IMC **I**nput **M**ode **C**leaner

INJ **Inj**ection

ISC **I**nterferometer **S**ensing and **C**ontrol

ITF **I**nt**erf**erometer

ITM **I**nput **T**est **M**ass

KAGRA **Ka**mioka **Gra**vitational Wave Detector

LIGO **L**aser **I**nterferometer **G**ravitational Wave **O**bservatory

LISA **L**aser **I**nterferometer **S**pace **A**ntenna

MEMS **M**icro **E**lectro-**M**echanical **S**ystems

MMT **M**ode-**M**atching **T**elescope

MoG-S **Mo**dified **G**erchberg-**S**axton

MoU **M**emorandum **o**f **U**nderstanding

NE **N**orth **E**nd

NI **N**orth **I**nput

NS **N**eutron **S**tar

OMC **O**utput **M**ode **C**leaner

OPL **O**ptical **P**ath **L**ength

PA **P**oint **A**bsorber

PBH **P**rimordial **B**lack **H**ole

PBS **P**olarizing **B**eam **S**plitter

PC **P**hase **C**amera

PD **P**hoto**d**iode

PDH **P**ound-**D**rever-**H**all

PM **P**ower **M**eter

PN **P**ost-**N**ewtonian

PR **P**artial **R**eflector

PRC **P**ower **R**ecycling **C**avity

PRM **P**ower **R**ecycling **M**irror

PSD **P**ower **S**pectral **D**ensity

PSL **P**re-**S**tabilized **L**aser

RFC **R**eference **F**requency **C**avity

RH **R**ing **H**eater

RIN **R**elative **I**ntensity **N**oise

RMS **R**oot **M**ean **S**quare

RoC **R**adius **o**f **C**urvature

SB **S**ide**B**and

SH **S**hack-**H**artmann

SLED **S**uper**L**uminescent **E**mitting **D**iode

SN **S**uper**N**ovae

SNR **S**ignal-to-**N**oise **R**atio

SRC **S**ignal **R**ecycling **C**avity

SRM **S**ignal **R**ecycling **M**irror

SS **S**canning **S**ystem

TCS **T**hermal **C**ompensation **S**ystem

TFP **T**hin **F**ilm **P**olarizer

TIE **T**ransport-of-**I**ntensity **E**quation

TM **T**est **M**ass

TT **T**ransverse and **T**raceless

WD **W**avefront **D**istortion

WE **W**est **E**nd

WI **W**est **I**nput

Bibliography

[1] Einstein A., *Über Gravitationswellen*, Sitzungsberichte der Königlich Preussischen Akademie der Wissenschaften Berlin (1918);

[2] Maggiore M., *Gravitational Waves, Volume 1, Theory and Experiments*, OXFORD UNIVERSITY PRESS (2008);

[3] Abbott B.P. et al. (LIGO Scientific Collaboration and Virgo Collaboration), *All-sky search for short gravitational-wave bursts in the second Advanced LIGO and Advanced Virgo run*, Phys. Rev. D 100, 024017 (2019);

[4] Brito R., Cardoso V., Pani P., *Superradiance: New Frontiers in Black Hole Physics*, Lect. Notes Phys. 906 (2015);

[5] Regimbau T., *The Quest for the Astrophysical Gravitational-Wave Background with Terrestrial detectors*, Symmetry 14.2 (2022);

[6] Mezzacappa A. et al., *Gravitational-wave signal of a core-collapse supernova explosion of a 15 Solar mass star*, Physical Review D 102, 023027 (2020);

[7] Dai1 Z.G., *Gravitational waves from post-merger radially oscillating millisecond pulsars*, A&A, 622, 5 (2019);

[8] Janka H.-Th., Marek A., Mueller B., Scheck L., *Supernova explosions and the birth of neutron stars*, AIP Conf.Proc.983:369-378 (2008);

[9] Abbott R. et al. (LIGO Scientific and Virgo and KAGRA Collaborations), *The population of merging compact binaries inferred using gravitational waves through GWTC-3*, arXiv:2111.03634 [astro-ph.HE] (2022);

[10] García-Bellido J., *Massive Primordial Black Holes as Dark Matter and their detection with Gravitational Waves*, IOP Conf. Series: Journal of Physics: Conf. Series 840, 012032 (2017);

[11] Miller A.L., *Direct detection of dark matter with gravitational-wave interferometers*, Séminaires LAPP (2021);

[12] Tong H., Galaudage S., Thrane E., *The population properties of spinning black holes using Gravitational-wave Transient Catalog 3*, arXiv:2209.02206 [astro-ph.HE] (2022);

[13] Abbott B.P. et al. (LIGO Scientific Collaboration and Virgo Collaboration), *Gravitational Waves and Gamma-rays from a Binary Neutron Star Merger: GW170817 and GRB 170817A*, The Astrophysical Journal Letters, 848:L13 (2017);

[14] Gill R., Granot J., *Gamma-Ray Bursts at TeV Energies: Theoretical Considerations*, Galaxies, 10(3), 74 (2022);

[15] Burns E. et al., *Identification of a Local Sample of Gamma-Ray Bursts Consistent with a Magnetar Giant Flare Origin*, The Astrophysical Journal Letters 907 (2021);

[16] Rastinejad J. C. et al., *A Kilonova Following a Long-Duration Gamma-Ray Burst at 350 Mpc*, arXiv e-prints, arXiv:2204.10864 (2022);

[17] Abbott R. et al. (LIGO Scientific and Virgo and KAGRA Collaborations), *Search for Gravitational Waves Associated with Gamma-Ray Bursts Detected by Fermi and Swift during the LIGO-Virgo Run O3b*, The Astrophysical Journal 928 (2022);

[18] Chatziioannou K., *Neutron star tidal deformability and equation of state constraints*, arXiv:2006.03168 [gr-qc] (2020);

[19] Aasil J.et al., (The LIGO Scientific Collaboration), *Advanced LIGO*, Classical and Quantum Gravity, 32, 7 (2015);

[20] Abbott R. et al. (LIGO Scientific and Virgo and KAGRA Collaborations), *Searches for Gravitational Waves from Known Pulsars at Two Harmonics in the Second and Third LIGO-Virgo Observing Runs*, arXiv e-prints, 2111.13106 (2021);

[21] Abbott R. et al. (LIGO Scientific and Virgo and KAGRA Collaborations), *Narrow-band searches for continuous and long-duration transient gravitational waves from known pulsars in the LIGO-Virgo third observing run*, arXiv e-prints, arXiv:2112.10990 (2021);

[22] Abbott R. et al. (LIGO Scientific Collaboration and Virgo Collaboration), *Search of the Early O3 LIGO Data for Continuous Gravitational Waves from the Cassiopeia A and Vela Jr. Supernova Remnants*, arXiv e-prints, arXiv:2111.15116 (2021);

[23] Abbott R. et al. (LIGO Scientific Collaboration and Virgo Collaboration), *Searches for Continuous Gravitational Waves from Young Supernova Remnants in the Early Third Observing Run of Advanced LIGO and Virgo*, apj 921.1, 80 (2021);

[24] Zhang Y. et al., *Search for Continuous Gravitational Waves from Scorpius X-1 in LIGO O2 Data*, The Astrophysical Journal Letters 906.2 (2021);

[25] Palomba C., *Gravitational radiation from young magnetars: Preliminary results*, aap 367 (2001);

[26] Dall'Osso S., Stella L., and Palomba C., *Neutron star bulk viscosity, "spin-flip" and GW emission of newly born magnetars*, mnras 480.1 (2018);

[27] Dall'Osso S. and Stella L., *Millisecond Magnetars*, Millisecond Pulsars. Ed. by Sudip Bhattacharyya, Alessandro Papitto, and Dipankar Bhattacharya. Cham: Springer International Publishing (2022);

[28] Lai D. and Shapiro S.L., *Gravitational Radiation from Rapidly Rotating Nascent Neutron Stars*, apj 442 (1995);

[29] Corsi A. and Mészáros P., *Gamma-ray Burst Afterglow Plateaus and Gravitational Waves: Multi-messenger Signature of a Millisecond Magnetar?*, apj 702.2 (2009);

[30] Sur A., Haskell B., *Gravitational waves from mountains in newly born millisecond magnetars*, Monthly Notices of the Royal Astronomical Society, Volume 502, Issue 4 (2021);

[31] Szczepanczyk M. et al., *Detecting and reconstructing gravitational waves from the next galactic core-collapse supernova in the advanced detector era*, Phys. Rev. D 104.10 (2021);

[32] Planck Collaboration et al. *Planck 2015 results. XIII. Cosmological parameters*, aap 594, A13 (2016);

[33] Reid M.J., Pesce D.W., Riess A.G., *An Improved Distance to NGC and Its Implications for the Hubble Constant*, apjl 886.2, L27 (2019);

[34] Abbott R. et al. (LIGO Scientific and Virgo and KAGRA Collaborations), *A Gravitational-wave Measurement of the Hubble Constant Following the Second Observing Run of Advanced LIGO and Virgo*, The Astrophysical Journal, 909, 2 (2021);

[35] Chassande-Mottin E. et al., *Gravitational wave observations, distance measurement uncertainties, and cosmology*, prd 100.8, 083514 (2019);

[36] Euclid Collaboration et al., *Euclid preparation. III. Galaxy cluster detection in the wide photometric survey, performance and algorithm selection*, aap 627, A23 (2019);

[37] Farr W.M. et al., *A Future Percent-level Measurement of the Hubble Expansion at Redshift 0.8 with Advanced LIGO*, apjl 883.2, L42 (2019);

[38] Carr B. and Kuhnel F., *Primordial Black Holes as Dark Matter: Recent Developments*, Annual Review of Nuclear and Particle Science 70 (2020);

[39] D'Agostino R., Giambò R., Luongo O., *Constraining primordial black holes as a fraction of dark matter through accretion disk luminosity*, arXiv:2204.02098 [gr-qc] (2023);

[40] Abbott R. et al. (LIGO Scientific and Virgo and KAGRA Collaborations, *Search for subsolar-mass binaries in the first half of Advanced LIGO and Virgo's third observing run*, arXiv e-prints, arXiv:2109.12197 (2021);

[41] Abbott R. et al. (LIGO Scientific Collaboration and Virgo Collaboration), *Tests of General Relativity with GWTC-3*, arXiv e-prints, arXiv:2112.06861 (2021);

[42] Buonanno A. et al.,*Comparison of post-Newtonian templates for compact binary inspiral signals in gravitational-wave detectors*, prd 80.8, 084043 (2009);

[43] Abbott B.P. et al. (LIGO Scientific Collaboration and Virgo Collaboration), *Tests of General Relativity with GW150914*, prl 116.22, 221101 (2016);

[44] Bertone G., Tait Tim M.P., *A new era in the search for dark matter*, Nature 562, pages 51–56 (2018);

[45] Grote H., Stadnik Y.V., *Novel signatures of dark matter in laser-interferometric gravitational-wave detectors*, Phys. Rev. Research 1, 033187 (2019);

[46] Aiello L., Richardson J.W., Vermeulen S.M., Grote H., Hogan C., Kwon O., Stoughton C., *Constraints on scalar field dark matter from co-located Michelson interferometers*, Phys. Rev. Lett. 128, 121101 (2022);

[47] Brito R., Cardoso V. and Pani P., *Superradiance: New Frontiers in Black Hole Physics*, Lect. Notes Phys. 906 (2015);

[48] Morisaki S. et al., *Improved sensitivity of interferometric gravitational-wave detectors to ultralight vector dark matter from the finite light-traveling time*, Physical Review D 103.5 (2021);

[49] Vermeulen S.M., Relton P., Grote H. et al., *Direct limits for scalar field dark matter from a gravitational-wave detector*, eprint: arXiv:2103.03783v3 (2021);

[50] Miller A.L. et al., *Probing new light gauge bosons with gravitational-wave interferometers using an adapted semicoherent method*, prd 103.10, 103002 (2021),

[51] Brito R. et al. *Gravitational wave searches for ultralight bosons with LIGO and LISA*, Phys. Rev. D 96.6 (2017);

[52] Baumann D., Chia H.S. and Porto R.A., *Probing ultralight bosons with binary black holes*, Physical Review D 99.4 (2019);

[53] Abbott R. et al. (LIGO Scientific Collaboration and Virgo Collaboration), *Constraints on dark photon dark matter using data from LIGO's and Virgo's third observing run*, Phys. Rev. D 105, 063030, (2022);

[54] Abbott B.P. et al. (LIGO Scientific Collaboration and Virgo Collaboration), *GWTC-1: A Gravitational-Wave Transient Catalog of Compact Binary Mergers Observed by LIGO and Virgo during the First and Second Observing Runs*, Phys. Rev. X 9, 031040 (2019);

[55] Abbott B.P. et al. (LIGO Scientific Collaboration and Virgo Collaboration), *GWTC-2: Compact Binary Coalescences Observed by LIGO and Virgo during the First Half of the Third Observing Run*, PHYSICAL REVIEW LETTERS X 11, 021053 (2021);

[56] Abbott B.P. et al. (LIGO Scientific Collaboration and Virgo Collaboration), *GW190425: Observation of a Compact Binary Coalescence with Total Mass* $\sim$*3.4* $M_{\odot}$, The Astrophysical Journal Letters 892 (2020);

[57] Abbott R. et al. (LIGO Scientific and Virgo and KAGRA Collaborations), *GWTC-3: Compact Binary Coalescences Observed by LIGO and Virgo During the Second Part of the Third Observing Run*, arXiv:2111.03606 [gr-qc] (2021);

[58] Abbott B.P. et al. (LIGO Scientific Collaboration and Virgo Collaboration), *Observation of Gravitational Waves from a Binary Black Hole Merger*, Phys. Rev. Lett. 116, 061102 (2016);

[59] Abbott B.P. et al. (LIGO Scientific Collaboration and Virgo Collaboration), *GW170814: A Three-Detector Observation of Gravitational Waves from a Binary Black Hole Coalescence*, Phys. Rev. Lett. 119, 141101 (2017);

[60] Veitch J. et al., *Parameter estimation for compact binaries with ground-based gravitational-wave observations using the LALInference software library*, Phys. Rev. D 91, 042003 (2015);

[61] Abbott B.P. et al. (LIGO Scientific Collaboration and Virgo Collaboration), *GW170817: Observation of Gravitational Waves from a Binary Neutron Star Inspiral*, Phys. Rev. Lett. 119 161101 (2017);

[62] Abbott B.P. et al. (LIGO Scientific Collaboration and Virgo Collaboration), *Multi-messenger Observations of a Binary Neutron Star Merger*, The Astrophysical Journal Letters, 848:L12 (2017);

[63] Abbott B.P. et al. (LIGO Scientific Collaboration, Virgo Collaboration, IM2H Collaboration, Dark Energy Camera GW-EM Collaboration, DES Collaboration, DLT40 Collaboration, Las Cumbres Observatory Collaboration, VINROUGE Collaboration, and MASTER Collaboration), *A gravitational-wave standard siren measurement of the Hubble constant*, Nature (London), in press (2017);

[64] Abbott R. et al. (LIGO Scientific Collaboration and Virgo Collaboration), *GW190412: Observation of a Binary-Black-Hole Coalescence with Asymmetric Masses*, Phys. Rev. D 102, 043015 (2020);

[65] Abbott R. et al. (LIGO Scientific Collaboration and Virgo Collaboration), *GW190521: A Binary Black Hole Merger with a Total Mass of 150 $M_{\odot}$*, PHYSICAL REVIEW LETTERS 125, 101102 (2020);

[66] Sanaea C. Rose et al.,*The Formation of Intermediate-mass Black Holes in Galactic Nuclei*, The Astrophysical Journal Letters, 929, 2 (2022);

[67] Abbott B.P. et al. (LIGO Scientific Collaboration and Virgo Collaboration), *Properties and Astrophysical Implications of the 150 $M_{\odot}$ Binary Black Hole Merger GW190521*, The Astrophysical Journal Letters, Volume 900, Number 1 (2020);

[68] Klimenko S. et al., *Method for detection and reconstruction of gravitational wave transients with networks of advanced detectors*, Phys. Rev. D 93, 042004 (2016);

[69] Abbott R. et al. (LIGO Scientific Collaboration and Virgo Collaboration), *GW190814: Gravitational Waves from the Coalescence of a 23 $M_{\odot}$ Black Hole with a 2.6* $M_{\odot}$ *Compact Object*, The Astrophysical Journal Letters, Volume 896, Number 2 (2020);

[70] Hansen R.O., *Multipole moments of stationary space-times*, J. Math. Phys. 15, 46–52 (1974);

[71] Poisson E., *Gravitational waves from inspiraling compact binaries: The quadrupole-moment term*, Phys. Rev. D 57 (1998);

[72] Muller H., Serot B.D., *Relativistic mean-field theory and the high-density nuclear equation of state*, Nuclear Physics A 606, 508 (1996);

[73] Abbott B.P. et al. (LIGO Scientific Collaboration and Virgo Collaboration), *Search for Gravitational Waves from a Long-lived Remnant of the Binary Neutron Star Merger GW170817*, The Astrophysical Journal, 875, 2 (2019);

[74] Olejak A., Belczynski K., Holz D.E. et al., *The Origin of inequality: isolated formation of a 30+10Msun binary black-hole merger*, arXiv:2004.11866 [astro-ph.HE] (2020);

[75] Abbott R. et al. (LIGO Scientific and Virgo and KAGRA Collaborations), *Observation of Gravitational Waves from Two Neutron Star–Black Hole Coalescences*, The Astrophysical Journal Letters, Volume 915, Number 1 (2021);

[76] Abbott B.P. et al. (LIGO Scientific Collaboration and Virgo Collaboration), *A Gravitational-wave Measurement of the Hubble Constant Following the Second Observing Run of Advanced LIGO and Virgo*, The Astrophysical Journal, 909, 2 (2021);

[77] Fishbach M., Essick R., Holz D.E., *Does Matter Matter? Using the Mass Distribution to Distinguish Neutron Stars and Black Holes*, The Astrophysical Journal Letters, 899, 1 (2020);

[78] Broekgaarden F.S., Berger E., Neijssel C.J. et al., *Impact of Massive Binary Star and Cosmic Evolution on Gravitational Wave Observations I: Black Hole-Neutron Star Mergers*, arXiv:2103.02608 [astro-ph.HE] (2021);

[79] Alsing J., Silva H.O., Berti E., *Evidence for a maximum mass cut-off in the neutron star mass distribution and constraints on the equation of state*, Monthly Notices of the Royal Astronomical Society, 478 (2018);

[80] The Virgo Collaboration, *Advanced Virgo Plus Phase I - Design Report*, Internal note VIR-0596A-19 (2019);

[81] Cerdonio M., Losurdo G., *Gravitational waves: From discovery to astronomy*, RIVISTA DEL NUOVO CIMENTO Vol. 35, N. 8 (2012);

[82] Beccaria M. et al., *Relevance of newtonian seismic noise for interferometer sensitivity*, Class. Quantum Grav., 15 (1998);

[83] Callen H.B and Welton T.A., *Irreversibility and generalized noise*, Phys. Rev. (1951);

[84] Fritschel P., *DC Readout for Advanced LIGO*, LSC meeting Hannover (2003);

[85] Fricke T., *An Introduction to DC Readout*, Internal note LIGO-G080405-00-L (2008);

[86] Maggiore M., *Gravitational Wave Experiments and Early Universe Cosmology*, arXiv:gr-qc/9909001 (2000);

[87] The Virgo Collaboration, *Advanced Virgo: a second-generation interferometric gravitational wave detector*, Class. Quantum Grav., 32 (2015);

[88] Nardecchia I., *Detecting Gravitational Waves with Advanced Virgo*, Galaxies, 10(1), 28 (2022);

[89] Drever R.W.P., Hall, J.L., Kowalski F.V., Hough J., Ford G.M., Munley A.J., Ward H., *Laser phase and frequency stabilization using an optical resonator*, Appl. Phys. B (1983);

[90] Black E.D., *An introduction to Pound-Drever-Hall laser frequency stabilization*, Am. J. Phys. (2001);

[91] Allocca A. et al., *Interferometer Sensing and Control for the Advanced Virgo Experiment in the O3 Scientific Run*, Galaxies 8.4 (2020);

[92] Chiummo A., *AdV INJ and SLC presentation - KIT visit @EGO*, Internal note VIR-0283A-19 (2019);

[93] Cleva F., Coulon JP., Kefelian F., *Characterization, Integration and Operation of a 100-W Solid State Amplifier in the Advanced-VIRGO Pre-Stabilized Laser System*, Conference on Lasers and Electro-Optics Europe & European Quantum Electronics Conference (2019);

[94] Hild S., *A Basic Introduction to Quantum Noise and Quantum-Non-Demolition Techniques*, Advanced Interferometers and the Search for Gravitational Waves - Lectures from the First VESF School on Advanced Detectors for Gravitational Waves, editor Bassan M. (2014);

[95] Caves C.M., *Quantum-mechanical noise in an interferometer*, Phys. Rev. D23, 1693-1708 (1981);

[96] The Virgo Collaboration, *Increasing the Astrophysical Reach of the Advanced Virgo Detector via the Application of Squeezed Vacuum States of Light*, Phys. Rev. Lett. 123, 231108 (2019);

[97] The Virgo Collaboration, *Virgo nEXT: beyond the AdV+ project - A concept study*, Internal note VIR-0497A-22 (2022);

[98] Abernathy M. et al.(The ET Science Team), *Einstein gravitational wave Telescope - Conceptual Design Study*, https://tds.ego-gw.it/itf/tds/file.php?callFile=ET-0106C-10.pdf (2011);

[99] https://sci.esa.int/web/lisa/-/61367-mission-summary;

[100] https://www.lisamission.org/?q=articles/lisa-mission/lisa-mission-proposal-l3;

[101] Anderson G. et al., *Experimental results from the ST7 mission on LISA Pathfinder*, Phys. Rev. D 98, 102005 (2018);

[102] Brooks A.F., Fafone V., *Thermal Adaptive Optics in Interferometric Gravitational Wave Detectors*, World Scientific, Reitze D., Saulson P.R. editors (2016);

[103] Lawrence C.R., *Active Wavefront Correction in Laser Interferometric Gravitational Wave Detectors*, Ph.D. Thesis, (2003);

[104] Touloukian Y.S. et al., *Thermal expansion metallic elements and alloys*, Thermophysical properties of matter - the TPRC data series, volume 12 (1975);

[105] Ballard S.S., Browder J.S., *Thermal Expansion and Other Physical Properties of the Newer Infrared-Transmitting Optical Materials*, Appl. Opt. 5.12 (1966);

[106] Vinet J.Y., *On Special Optical Modes and Thermal Issues in Advanced Gravitational Wave Interferometric Detectors*, Living Rev. Relativity, Vol. 12 (2009);

[107] Vinet J.Y.,Thermal issues in mirrors, Internal note, VIR-0224A-10 (2010);

[108] Bathe K.J., Wilson E.L., *Numerical methods in finite element analysis*, Prentice-Hall (1976);

[109] Moaveni S., *Finite element analysis - Theory and Applications with Ansys*, Prentice-Hall (1999);

[110] Fischer R.F., *Optical Systems Design*, Second Edition, McGraw-Hill Professional (2007);

[111] https://it.mathworks.com/products/matlab.html

[112] Degallaix J., *OSCAR a Matlab based optical FFT code*, Journal of Physics: Conference Series. Vol. 228. 1. IOP Publishing (2010);

[113] Rocchi A. et al., *Thermal effects and their compensation in advanced Virgo*, J. Phys. Conf. Ser. 363 (2012);

[114] Brooks A.F., *Hartmann Wavefront Sensors for Advanced Gravitational Wave Interferometers*, Ph.D. Thesis (2007);

[115] Hartmann J., *Objektuvuntersuchungen*, Zt. Instrumentenkd., vol. 24, p. 1 (1904);

[116] Van Der Schaaf L., *The Phase Cameras of Advanced Virgo*, Ph.D. Thesis (2020);

[117] Nardecchia I. et al., *Optimized radius of curvature tuning for the virgo core optics*, Class. Quantum Grav. 40, 055004 (2023);

[118] Rocchi A., *Thermal effects and other wavefront aberrations in recycling cavities*, Advanced Interferometers and the Search for Gravitational Waves - Lectures from the First VESF School on Advanced Detectors for Gravitational Waves, editor Bassan M. (2014);

[119] Fafone V., Rocchi A., *TCS noise: general concepts and application to the Virgo/Virgo+ case*, Internal note VIR-0615B-09 (2009);

[120] Giri P., *Optimisation of CO2 laser-based aberration control in Advanced Virgo +*, Ph.D. Thesis (2023);

[121] Mudadu L., *Realization and characterization of a laser scanning system for correction of optical asymmetrical aberrations in Advanced Virgo*, Master thesis, University of Rome Tor Vergata (2013);

[122] Allocca A., Chiummo A., Ruggi P., Yamamoto H., *Transient power drop in dark fringe lock acquisition during the commissioning before O3*, Internal note VIR-1047A-19 (2019);

[123] Brooks A.F. et al., *Point absorbers in Advanced LIGO*, Appl. Opt. 60.13, pp. 4047–4063 (2021);

[124] Lorenzini M. for the TCS group, *Satus of TCS commissioning*, Internal note VIR-0070A-23 (2023);

[125] Cifaldi M., *Mitigation of anomalous absorptions in the Virgo core optics*, Ph.D. Thesis (2023);

[126] Brooks A.F. et al., *Ultra-sensitive wavefront measurement using a Hartmann sensor*, Opt. Express 15(16), 10370-10375 (2007);

[127] Bersanetti D., Boldrini M., Casanueva Diaz J., Freise A., Maggiore R., Mantovani M. and Valentini M., *Simulations for the locking and alignment strategy of the DRMI configuration of the advanced virgo plus detector*, Galaxies, 10(6), (2022);

[128] Cifaldi M., Fafone V., Lumaca D., Nardecchia I., Rocchi A., Taranto C., *TCS: actuators characterization*, Internal note VIR-0047A-22 (2022);

[129] Fafone V., Lumaca D., Lorenzini M., Nardecchia I., Rocchi A., Taranto C., *TCS simulations*, Internal note VIR-1365A-21 (2021);

[130] Rocchi A., Coccia E., Fafone V., Malvezzi V., Minenkov Y., Sperandio L., *Thermal effects and their compensation in Advanced Virgo*, Journal of Physics: Conference Series, 363(1):012016 (2012);

[131] Ianni M., *Modeling of thermally-induced optical aberration in the current and future GW detectors*, Master Thesis (2023);

[132] Nardecchia I. for the TCS group, *Update on TCS: YAG absorption measurements and stability of DAS powers*, Internal note VIR-0898A-22 (2022);

[133] Porcelli E., *Actuation time optimization in the Advanced Virgo mirror thermo-elastic correction*, Master Thesis (2021);

[134] Fafone V. and Rocchi A., *AdV TCS: Considerations on actuation and sensing for the correction of high order aberrations in MSRC*, Internal note VIR-0373A-11 (2011);

[135] https://www.alpao.com/

[136] Clain E.S., Bareket N., *Configuring an electrostatic membrane mirror by least-squares fitting with analytically derived influence functions*, J. Opt. Soc. Am. A 3 (1986);

[137] Grosso R.P., Yellin M.J., *The membrane mirror as an adaptive optical element*, J. Opt. Soc. Am. 67 (1977);

[138] Morse P.M., *Vibration and Sound*, 2nd ed., McGraw-Hill, New York (1948);

[139] Morse P.M., Feshbach H., *Methods of Theoretical Physics*, Part I, McGraw-Hill, New York (1953);

[140] Moore E.H., *On the reciprocal of the general algebraic matrix*, Bulletin of the American Mathematical Society, 26 (1920);

[141] Penrose R., *A generalized inverse for matrices*, Proceedings of the Cambridge Philosophical Society, 51 (1955);

[142] James M, *The generalised inverse*, Mathematical Gazette, 62, 420 (1978);

[143] Taranto C. et al., *Mitigation of non-axisymmetric optical aberrations in Advanced Virgo*, Nuovo Cim. C, 45, 5, 155 (2022);

[144] Gerchberg R.W. and Saxton W.O., *Phase determination for image and diffraction plane pictures in the electron microscope*, Optik 34, 275–284 (1971);

[145] Gerchberg R.W. and Saxton W.O., *A practical algorithm for the determination of phase from image and diffraction plane pictures*, Optik 35, 237–246 (1972);

[146] Teague M.R., *Deterministic phase retrieval: a Green's function solution*, J. Opt. Soc. Am. A 73, 1424-1411 (1983);

[147] Goodman J.W., *Introduction to Fourier Optics*, McGraw-Hill (2017);

[148] Voelz D.G., *Computational Fourier Optics - A MATLAB Tutorial*, SPIE PRESS, Tutorial Texts in Optical Engineering, Vol. No. TT89 (2010).

[149] Mehrabkhani S., Kuester M., *Optimization of phase retrieval in the Fresnel domain by the modified Gerchberg-Saxton algorithm*, arXiv1711.01176 (2019);

Ringraziamenti

Ci tengo a ringraziare tutte le persone che, direttamente o indirettamente, hanno contribuito a questa tesi.

Grazie...
... alla *prof.ssa Viviana Fafone*, per avermi accompagnato nel mio percorso accademico, dalla triennale al dottorato.
... ad *Alessio*, per aver sempre risposto alle chiamate, ai messaggi ed alle mille domande sensate e non.
... a *Matteo*, per aver alimentato la mia curiosità verso il mondo e per l'ispirazione ad essere una "visionaria".
... ad *Elisabetta*, per aver contribuito alla mia crescita come scienziata e come donna.
... ad *Ilaria* e *Diana*, per essere state come delle sorelle maggiori e un sostegno prezioso soprattutto nei periodi di commissioning intenso.
... a tutte le persone passate per il PP1, in particolare *Lorenzo*, *Pier Paolo*, *Matteo* ed *Andrea*, per essere stati un aiuto nei momenti di necessità.
... a tutte le *persone di EGO* con cui ho condiviso non solo gli shifts, ma anche i momenti informali che hanno reso il percorso più leggero e piacevole e per aver imparato qualcosa di nuovo da ognuno di voi. Un ringranziamento particolare va a *Manuel*, per il continuo supporto e una birra sempre pronta.

... a *Marco*, per essere la parte migliore di me e per gli occhi con cui da sempre mi guardi.
... a *papà Romano*, per te ho sempre voluto fare il meglio possibile.
... ad *Arianna*, per essere cane e gatto ma avere lo stesso modo di camminare e lo stesso sguardo di chi non ci sta.
... a *mamma Roberta*, per essere l'abbraccio sicuro di cui ho bisogno.
... alla *mia famiglia* complicata e contorta e a *Chiara, Annamaria e Pietro*, per l'incoraggiamento costante, anche quando non capivate appieno cosa stessi facendo e per essere sempre presenti in ogni passo del mio cammino.
... a *nonno Nando*, speranzosa di renderti ancora una volta fiero di me, ovunque tu sia.

... a tutti i *miei amici*, perché siete tantissimi e questo vuol dire che non sono proprio una brutta persona...
... a *Maria*, per essere la Testimone di tutta la mia vita, di ogni momento bello e di ogni momento difficile, nonostante tutto, sempre al mio fianco.
... a *Valentina, Monica, Livia e Giulia*, perché la vostra presenza riempie la mia vita.
... a *Noemi, Elena, Irene, Francesca, Alessandro, Gaetano, Gianluca, Giulia, Benedetta e Melissa*, per essere sempre presenti in ogni passo importante.
... a *Francesca*, per avermi scelto come sorella e per il nostro capirci senza parlare.

... a *Chiara, Giulia e Martina*, per essere sempre un punto di riferimento in qualsiasi parte del mondo.
... a *Sara*, per la tua attenzione e la cura nel raccontarci le nostre vite.
... a *Giulia*, perché con te ho imparato la parola "amicizia", per aver camminato con me da sempre e per sempre.
... a *Barbara ed Eleonora*, non posso fare a meno di riflettere su quanto sia stato prezioso il nostro legame iniziato per caso tra i banchi di scuola elementare.
... a *Gianmarco, Silvia ed Emanuele*, per la vostra gioia contagiosa e per l'amicizia che avete generosamente donato nel corso degli anni.
... ad *Elisa*, per i nostri discorsi sedute sul divano, per le cene improvvisate, per gli appuntamenti fissati e disdetti, semplicemente, perché ci sei.
... a *Matteo e Roberta*, per la nostra amicizia genuina, iniziata per caso e proseguita per scelta.
... ad *Irene*, perché tra una tinta e un taglio di capelli, sei diventata un'amica.
.. alla grande famiglia del *COR*, per avermi accolta che ero una ragazzina e per avermi accompagnato nella mia crescita.

L'ultimo grazie va alla *Claudia* che ha iniziato questo percorso, per aver mantenuto la stessa passione, nonostante tutto, *fino alla fine*.